THE UNIVERSITY OF QUEENSLAND

AUSTRALIA

The Dynamic Response of β Titanium Alloys to High Strain Rates at Room and Elevated Temperatures

Hongyi Zhan

B. Eng.

A thesis submitted for the degree of Doctor of Philosophy at

The University of Queensland in 2016

School of Mechanical and Mining Engineering

Abstract

Titanium and its alloys fulfil a wide range of applications involving aerospace, biomedical, chemical and petroleum industries due to their extraordinary properties such as high specific strength, excellent biocompatibility and corrosion resistance. Among different types of titanium alloys, β titanium alloys have a unique range of properties such as an excellent combination of high strength and fracture toughness and low Young's modulus. Therefore, the usage of β titanium alloys in the manufacturing of some key components in aerospace and biomedical industries has continually increased in the past decade.

Nowadays many commercial manufacturing processes for metallic materials such as machining, explosive welding, hot forging and extrusion employ high strain rates and are conducted at elevated temperatures. Also, high-strain-rate deformation can be encountered in collisions such as in car crashes, bird strikes on airplanes and micrometeorite impacts on space structures. Hence a large number of studies have been conducted on the dynamic response of metallic materials including copper, steels, tantalum, Ti-6Al-4V alloy and commercially pure titanium to high strain rates. Due to limited knowledge of the dynamic behaviour of β titanium alloys, this thesis mainly investigates the stress-strain behaviour and microstructural evolution of β titanium alloys under high strain rates at room and elevated temperatures.

Split Hopkinson Pressure Bar compressive tests were carried out on two new types of β titanium alloys with different levels of β phase stability, the Ti-6Cr-5Mo-5V-4Al (wt. %) and Ti-25Nb-3Zr-3Mo-2Sn (wt.%) alloys, at strain rates ranging from 10^{-3} s^{-1} to 10^{4} s^{-1} and temperatures ranging from 293K to 1173K. The Ti-6Cr-5Mo-5V-4Al alloy, with relatively high β phase stability, represents an alloy type which can be engineered through heat treatment or thermo-mechanical processing to achieve a superior combination of strength and fracture toughness. While the Ti-25Nb-3Zr-3Mo-2Sn alloy with relatively low β phase stability represents an alloy type which can be applied in biomedical applications due to their low Young's modulus and superelastic properties.

For the Ti-6Cr-5Mo-5V-4Al alloy, dislocation slip is dominant at all testing strain rates and temperatures in this research. The flow stress increases with increasing strain rate but decreasing temperature. Also, it is more sensitive to temperature than strain rate. At ambient temperatures, the strain hardening rate exhibited by the Ti-6Cr-5Mo-5V-4Al alloy at high strain rates is much lower than that at quasi-static strain rates, which is attributed to the thermal softening effect brought by

adiabatic heating. While for the Ti-25Nb-3Zr-3Mo-2Sn alloy, multiple deformation mechanisms including dislocation slip, {332} <113> and {112} <111> mechanical twinning, stress-induced martensitic α" and ω phase transformations can be activated simultaneously and among them {332} <113> twinning is dominant at 293K regardless of strain rate. A strong strain hardening rate is maintained at high strain rates at 293K due to dynamic Hall-Petch effects induced by extensive mechanical twinning. As the stability of the β phase increases with increasing temperatures, the dominant deformation mechanism in the Ti-25Nb-3Zr-3Mo-2Sn alloy gradually transforms to dislocation slip with increasing temperatures. The comparison between the dynamic behaviours of the Ti-6Cr-5Mo-5V-4Al and Ti-25Nb-3Zr-3Mo-2Sn alloys demonstrates that the β phase stability has great effects on the dynamic response of β titanium alloys to high strain rates.

In this research, adiabatic shear bands were only observed in the Ti-6Cr-5Mo-5V-4Al alloy deformed at $4000s^{-1}$ and $10000s^{-1}$ at 873K. The tendency for shear bands to form at an elevated temperature is potentially related to the formation of features with string-like morphologies. The string-like morphologies are ~30-100 μm in length and ~300-500 nm in width according to optical and scanning electron microscopic observations. The grain refinement process of microstructures within the shear bands was studied by the observation of morphologies and misorientations of microstructures in different locations across the shear bands. Dynamic recovery and rotational dynamic recrystallization mechanisms were employed to explain the formation of ultrafine subgrains (~100-300 nm) and recrystallized nanograins (~50-100 nm) observed in the core area of the shear bands, respectively. It is also noticed that the initiation of adiabatic shear bands did not induce a significant drop in flow stress for the Ti-6Cr-5Mo-5V-4Al alloy.

In this thesis, the Johnson-Cook model and a modified Zerilli-Armstrong model have been established for the Ti-6Cr-5Mo-5V-4Al alloy and a comparative study on their predictability is made. Both the Johnson-Cook model and modified Zerilli-Armstrong model have good capacities to describe the flow behaviour of the Ti-6Cr-5Mo-5V-4Al alloy at high strain rates and elevated temperatures. The average absolute errors calculated between the predicted data and experimental data for the Johnson-Cook model and modified Zerilli-Armstrong model are 6.0% and 5.7%, respectively. Although the Johnson-Cook model has a poor track of strain hardening behaviour of the Ti-6Cr-5Mo-5V-4Al alloy, it has been proved to be suitable for implementation in Ti-6Cr-5Mo-5V-4Al alloy machining SPH/FE simulations for cutting force studies. The modified Zerilli-Armstrong model is able to capture the strain hardening behaviour better as it incorporates the coupled effects of strain and temperature. However, for the modified Zerilli-Armstrong model the

dynamic recovery or dynamic recrystallization that may occur at elevated temperatures should be taken into consideration when selecting data for parameter fitting. Also, the modified Zerilli-Armstrong model requires more stress-strain data for the parameter fitting than the Johnson-Cook model.

The discoveries and discussion made in this thesis can be directly applied to the understanding of the dynamic behaviours of β titanium alloys and other body-centred cubic structured metallic materials during manufacturing processes or collisions where high strain rates and elevated temperatures are involved.

Declaration by author

This thesis is composed of my original work, and contains no material previously published or written by another person except where due reference has been made in the text. I have clearly stated the contribution by others to jointly-authored works that I have included in my thesis.

I have clearly stated the contribution of others to my thesis as a whole, including statistical assistance, survey design, data analysis, significant technical procedures, professional editorial advice, and any other original research work used or reported in my thesis. The content of my thesis is the result of work I have carried out since the commencement of my research higher degree candidature and does not include a substantial part of work that has been submitted to qualify for the award of any other degree or diploma in any university or other tertiary institution. I have clearly stated which parts of my thesis, if any, have been submitted to qualify for another award.

I acknowledge that an electronic copy of my thesis must be lodged with the University Library and, subject to the policy and procedures of The University of Queensland, the thesis be made available for research and study in accordance with the Copyright Act 1968 unless a period of embargo has been approved by the Dean of the Graduate School.

I acknowledge that copyright of all material contained in my thesis resides with the copyright holder(s) of that material. Where appropriate I have obtained copyright permission from the copyright holder to reproduce material in this thesis.

Publications during candidature

Journal Articles:

1. **H. Zhan**, G. Wang, D. Kent, M. Dargusch. The dynamic response of a metastable β Ti–Nb alloy to high strain rates at room and elevated temperatures, **Acta Materialia, 105 (2016) 104-113**.

2. **Zhan H**, Zeng W, Wang G, Kent D, Dargusch M. On the deformation mechanisms and strain rate sensitivity of a metastable β Ti–Nb alloy, **Scripta Materialia, 107 (2015) 34-37**.

3. **H. Zhan**, G. Wang, D. Kent, M. Dargusch, Constitutive modelling of the flow behavior of a beta titanium alloy at high strain rates and elevated temperatures using the Johnson-Cook and modified Zerilli-Armstrong models, **Materials Science and Engineering: A, 612 (2014) 71-79.**

4. **H. Zhan**, W. Zeng, G. Wang, D. Kent, M. Dargusch, Microstructural characteristics of adiabatic shear localization in a metastable beta titanium alloy deformed at high strain rate and elevated temperatures, **Materials Characterization, 102 (2015) 103-113.**

5. **H. Zhan**, D. Kent, G. Wang, M.S. Dargusch, The dynamic response of a β titanium alloy to high strain rates and elevated temperatures**, Materials Science and Engineering: A, 607 (2014) 417-426**.

6. M.J. Bermingham, D. Kent, **H. Zhan**, D.H. StJohn, M.S. Dargusch, Controlling the microstructure and properties of wire arc additive manufactured Ti–6Al–4V with trace boron additions, **Acta Materialia, 91 (2015) 289-303.**

7. Y. Xi, **H. Zhan**, R.A. Rahman Rashid, G. Wang, S. Sun, M. Dargusch, Numerical modeling of laser assisted machining of a beta titanium alloy, **Computational Materials Science, 92 (2014) 149-156.**

Conference Presentations:

1. **Oral Presentation**, Constitutive modelling of the flow behaviour of a β titanium alloy at high strain rates and elevated temperatures using the Johnson-Cook and modified Zerilli-Armstrong models, **Ti-2015: The 13th World Conference on Titanium**, San Diego, U.S. 19th Aug, 2015.

2. **Oral Presentation,** The dynamic response of a β titanium alloy to high strain rates and elevated temperatures**, Combined Australian Materials Sciences Conference 2014 (CAMS2014)**, Sydney, Australia. 28th November 2014.

3. **Oral Presentation**, Dynamic behavior of β-Ti alloys at high strain rates and elevated temperatures, **Engineering Postgraduate Conference**, The University of Queensland. 3rd June, 2013.

Publications included in this thesis

1. H. Zhan, D. Kent, G. Wang, M.S. Dargusch, The dynamic response of a β titanium alloy to high strain rates and elevated temperatures, Materials Science and Engineering: A, 607 (2014) 417-426.– incorporated as Paper 1 in Chapter 3.

Contributor	Statement of contribution
H. Zhan (Candidate)	Conception and design (70%) Experimental (90%) Data analysis and interpretation (80%) Drafting and writing (80%)
D. Kent	Data analysis and interpretation (20%) Drafting and writing (10%)
G. Wang	Conception and design (20%) Experimental (10%)
M. Dargusch	Conception and design (10%) Drafting and writing (10%)

2. H. Zhan, W. Zeng, G. Wang, D. Kent, M. Dargusch, Microstructural characteristics of adiabatic shear localization in a metastable beta titanium alloy deformed at high strain rate and elevated temperatures, Materials Characterization, 102 (2015) 103-113. – incorporated as Paper 2 in Chapter 3.

Contributor	Statement of contribution
H. Zhan (Candidate)	Conception and design (80%) Experimental (90%) Data analysis and interpretation (80%) Drafting and writing (85%)
W. Zeng	Experimental (10%) Data analysis and interpretation (10%)
G. Wang	Conception and design (10%) Drafting and writing (5%)
D. Kent	Data analysis and interpretation (10%) Drafting and writing (5%)
M. Dargusch	Conception and design (10%) Drafting and writing (5%)

3. H. Zhan, G. Wang, D. Kent, M. Dargusch, Constitutive modelling of the flow behaviour of a beta titanium alloy at high strain rates and elevated temperatures using the Johnson-Cook and modified Zerilli-Armstrong models, Materials Science and Engineering: A, 612 (2014) 71-79. – incorporated as Paper 3 in Chapter 3.

Contributor	Statement of contribution
H. Zhan (Candidate)	Conception and design (80%) Experimental (90%) Data analysis and interpretation (80%) Drafting and writing (80%)
G. Wang	Conception and design (10%) Experimental (10%) Data analysis and interpretation (10%)
D. Kent	Data analysis and interpretation (10%) Drafting and writing (10%)
M. Dargusch	Conception and design (10%) Drafting and writing (10%)

4. Zhan H, Zeng W, Wang G, Kent D, Dargusch M. On the deformation mechanisms and strain rate

sensitivity of a metastable β Ti–Nb alloy, Scripta Materialia, 107 (2015) 34-37. – incorporated as Paper 4 in Chapter 3.

Contributor	Statement of contribution
H. Zhan (Candidate)	Conception and design (80%) Experimental (80%) Data analysis and interpretation (80%) Drafting and writing (85%)
W. Zeng	Experimental (10%) Data analysis and interpretation (10%)
G. Wang	Conception and design (10%) Experimental (10%)
D. Kent	Data analysis and interpretation (10%) Drafting and writing (10%)
M. Dargusch	Conception and design (10%) Drafting and writing (5%)

5. H. Zhan, G. Wang, D. Kent, M. Dargusch. The dynamic response of a metastable β Ti–Nb alloy to high strain rates at room and elevated temperatures, Acta Materialia, 105 (2016) 104-113.
– incorporated as Paper 5 in Chapter 3.

Contributor	Statement of contribution
H. Zhan (Candidate)	Conception and design (80%) Experimental (90%) Data analysis and interpretation (90%) Drafting and writing (85%)
G. Wang	Conception and design (10%) Experimental (10%)
D. Kent	Data analysis and interpretation (10%) Drafting and writing (10%)
M. Dargusch	Conception and design (10%) Drafting and writing (5%)

6. Y. Xi, H. Zhan, R.A. Rahman Rashid, G. Wang, S. Sun, M. Dargusch, Numerical modeling of laser assisted machining of a beta titanium alloy, Computational Materials Science, 92 (2014) 149-156.- incorporated as Appendix.

Contributor	Statement of contribution
Y. Xi	Conception and design (70%) Model development (70%) Data analysis and interpretation (60%) Drafting and writing (70%)
H. Zhan (Candidate)	Constitutive model development (20%)
R.A. Rahman Rashid	Data analysis and interpretation (20%)
S. Sun	Data analysis and interpretation (10%)
G. Wang	Conception and design (15%) Model development (10%) Data analysis and interpretation (10%)
M. Dargusch	Conception and design (15%) Drafting and writing (30%)

Contributions by others to the thesis

No contributions by others

Statement of parts of the thesis submitted to qualify for the award of another degree

None

Acknowledgements

First and foremost, I would like to express my deepest gratitude to my two principle supervisors, Dr. Gui Wang and Dr. Damon Kent. It is Dr. Gui Wang who helped me prepare paperwork for scholarship applications to the Chinese Scholarship Council and The University of Queensland. The preliminary design and conception of this project was firstly made by Dr. Gui Wang. Without his foresight in this project, I may not have had this precious chance to pursue my PhD degree at The University of Queensland. For Dr. Damon Kent, especially thank him for his invaluable instructions on the experimental design, data analysis and paper drafting. I really learned a lot through discussion with him and without his help I would not be able to become a qualified researcher. I would also like to thank my two principle supervisors for their encouragement, support and guidance not only for my PhD study but also for my future career development.

Then I would like to thank my associate supervisor, Associate Professor Matthew Dargusch. He always shows support to me, whether for my participation into workshops and international conferences or repeating experiments. His outstanding capacity in project management, hard-working and sense of humour really impressed me a lot.

Sincere appreciation is extended to my milestone review committee members: Dr. Bill Daniel and Dr. Stuart McDonald for their rigorous suggestions made for my every milestone.

I would also like to thank my senior colleagues Dr. Michael Bermingham, Dr. R.A. Rahman Rashid, Dr. Yao Xi and Dr. Yaowu Zhang for their experimental assistance and extensive discussions. Then I would like to extend my thanks to fellow postgraduate students seating in the same building with me, Dr. Guang Zeng, Dr. Zhilin Liu and Dr. Shenglu Lu. They made the atmosphere in our office suitable for studying and sometimes inspired me with their ideas.

Many thanks go to Dr. Dong Qiu for his instructions on TEM sample preparation and TEM analysis. Also, Ms. Glenda Zemanek in the School of Mechanical and Mining Engineering in the University of Queensland, Mr. Ron Rush, Ms. Eunice Grinan, Dr. Kim Swell, Mr. Graeme Auchterlonine, Ms. Ying Yu and Dr. Hui Diao in the Centre of Microscopy and Microanalysis are acknowledged for their training and technical support to my research. Special thanks to Mr. Saifei Zhang in the North-western Polytechnic University for his help in the Split Hopkinson Pressure Bar tests.

The scholarship from China Scholarship Council and The University of Queensland and the research funding from Defence Materials Technology Centre and Centre for Advanced Materials Processing and Manufacturing are gratefully acknowledged.

Lastly, I would like to acknowledge my families, my mother Ms. Canyun Zhou, my father Mr. Tuqiang Zhan and my wife Ms. Yue Ma. My parents gave birth to me and their endless love always drives me forward. My wife brightens my life in Australia and always accompanies me when I feel frustrated or perplexed. You three are invaluable treasures to me.

Keywords

metastable β titanium alloys, high strain rate, split Hopkinson pressure bar (SHPB), adiabatic shear band, grain refinement, transmission electron microscopy (TEM), electron backscattered diffraction (EBSD), constitutive model, mechanical twinning, stress-induced martensitic transformation

Australian and New Zealand Standard Research Classifications (ANZSRC)

ANZSRC code: 091207, Metals and Alloy Materials, 80%

ANZSRC code: 091307, Numerical Modelling and Mechanical Characterisation, 20%

Fields of Research (FoR) Classification

FoR code: 0912, Materials Engineering, 80%

FoR code: 0913, Mechanical Engineering, 20%

Contents

List of Figures

List of Tables

List of Abbreviations

HCP	Hexagonal Close Packed
BCC	Body-Centred Cubic
FCC	Face-Centred cubic
SHPB	Split Hopkinson Pressure Bar
SPH	Smoothed Particle Hydrodynamics
SE	Superelasticity
SME	Shape Memory Effect
SIM	Stress-Induced Martensitic
SFE	Stacking Fault Energy
TWIP	Twinning-Induced Plasticity
TRIP	Transformation-Induced Plasticity
DSA	Dynamic Strain Aging
FEA	Finite Element Analysis
JC	Johnson-Cook
ZA	Zerilli-Armstrong
ASB	Adiabatic Shear Band
TEM	Transmission Electron Microscopy
EBSD	Electron Backscatter diffraction
PrisM	Progressive Subgrain Misorientation
Ti6554	Ti-6Cr-5Mo-5V-4Al
Bo	Bond Order
Mo_{eq}	Equivalent Binary Ti-Mo Alloy
Md	D-Orbital Method Concentration

Chapter 1

Introduction

1.1 Introduction to Titanium and Its Alloys

Titanium is the fourth most abundant structural metal following Al, Fe and Mg, and is also the ninth most abundant element on the Earth. Titanium and its alloys fulfil a wide range of applications in aerospace, biomedical, chemical, military and petroleum industries due to their extraordinary properties such as high specific strength and excellent corrosion resistance [1, 2]. The general characteristics and typical applications of titanium alloys are shown in Figure 1 [3].

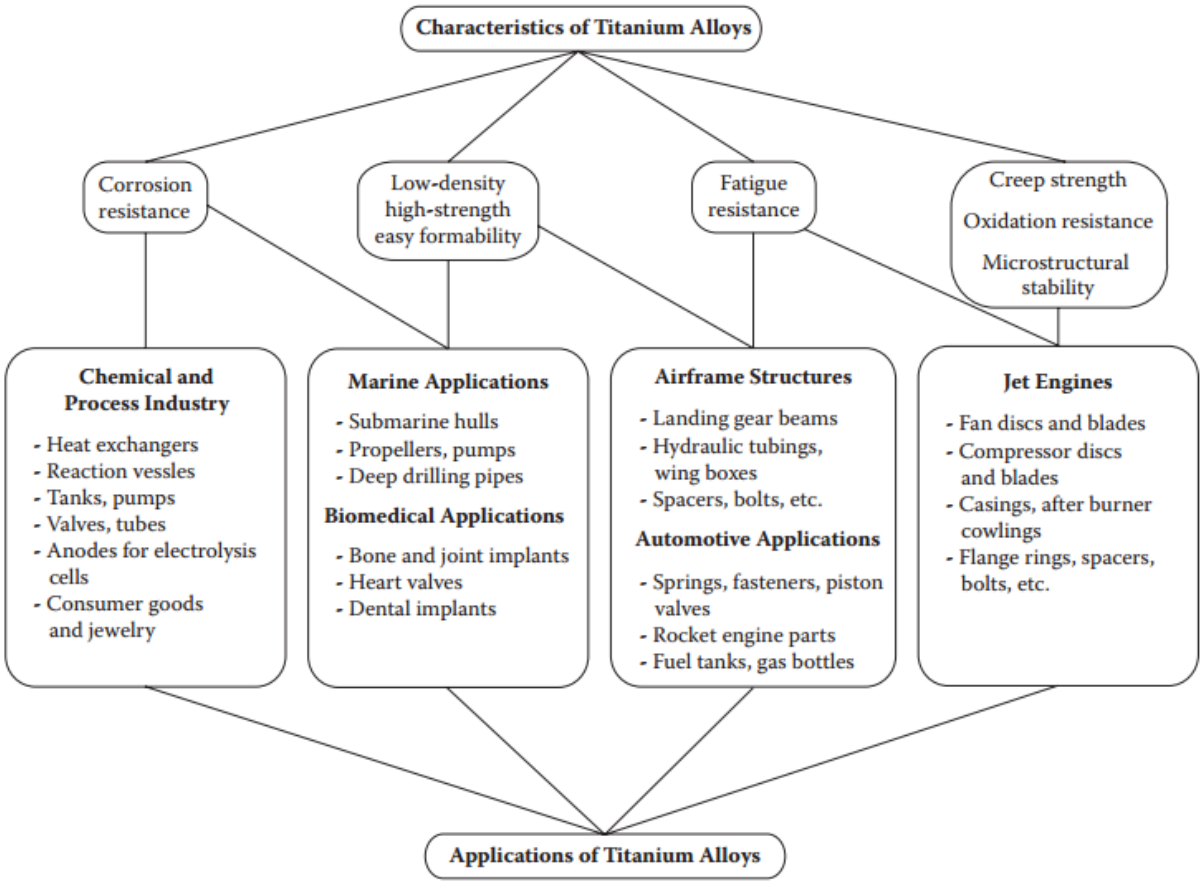

Fig.1. General characteristics and typical applications of titanium alloys [3].

The crystalline structure of pure titanium will transform from the hexagonal close packed (HCP) structure referred to as α phase to the body centred cubic (BCC) structure referred to as β phase at the temperature around 882 ℃ (Figure 2 [2]). This temperature is called the β transus. It will increase by adding α stabilizer such as Al, O, N, Ga, and C while it will decrease by adding β stabilizers such as Mo, V, Ta, Cu, Cr, Fe, Mn, Ni, Co and H to the pure titanium [4]. According to the composition and predominant phase of titanium alloys at ambient temperature, they are conventionally divided into four categories [5-9]:

1. Commercially Pure (CP) titanium: CP titanium is mainly used in the chemical industry due to its excellent corrosion resistance. But its strength is comparatively lower than other types of titanium alloys.

2. α alloys and near α alloys: α alloys only contain α stabilizers while near α alloys contain α stabilizers and a limited quantity of β stabilizers. Both are preferred in high temperature and cryogenic applications due to their excellent creep resistance at elevated temperatures up to 300 ℃ ("between 400 and 520 ℃ for near-α alloys" as indicated in Ref.[10]). They are intrinsically weldable as they are insensitive to heat treatment, but their forgeability is rather poor.

3. α-β alloys: This group contains both α stabilizers and β stabilizers. They have a wide processing window through which different microstructures and properties can be obtained, providing a good opportunity to adjust the properties of the alloys through processing. Their strength can be increased greatly through solution treating and aging heat treatments. As reported by Yang et al. in Ref. [4], "α-β alloys account for 70% of all titanium used, among which Ti-6Al-4V is the most common used one". To date, Ti-6Al-4V has been extensively used in the aerospace industry.

4. β alloys: β alloys have the ability to retain a fully β phase structure when cooled from above the β transus to room temperature as large amounts of β stabilizers are added to these alloys. They are characterised by high hardenability, improved forgeability and excellent cold formability in the solution-treated condition. Their disadvantages mainly lie in lower creep strength, tensile ductility and poor oxidation resistance thus they are rarely considered appropriate for elevated temperature applications. A more detailed description of β alloys will be produced in the Literature Review.

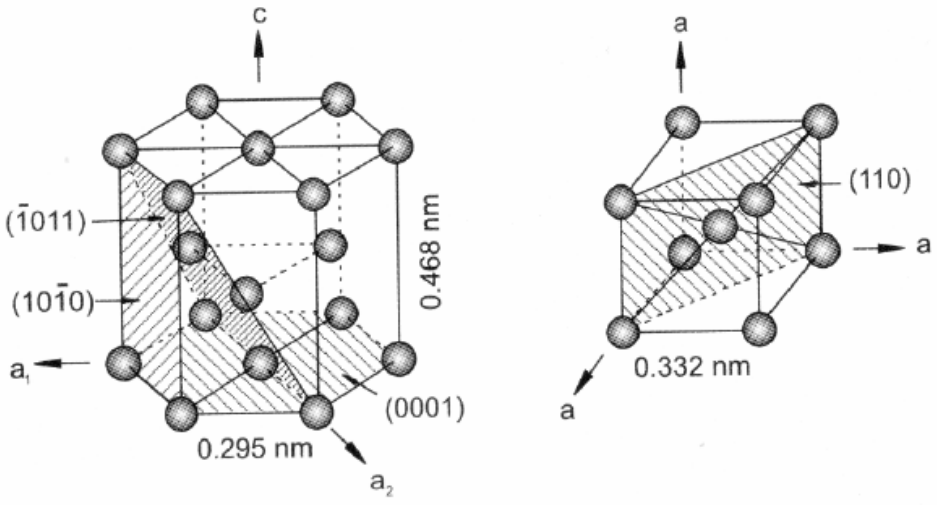

Fig.2. Crystal structures of HCP α-Ti and BCC β-Ti [2].

1.2 Dynamic Behaviour of Materials

The definition of strain rate ($\dot{\varepsilon}$) is the rate of change in strain with regard to time in materials. Conventional mechanical tensile or compressive tests are carried out under quasi-static conditions where strain rates are slower than 1×10^{-3} s^{-1}. Rohde et al. [11] related strain rate to dislocation motion and proposed that only when the dislocation velocities are of the same or even larger order than the shear wave velocity can the strain rate be defined to be high. The baseline for high strain rate is calculated by Rohde et al. [11] to be 10^4 s^{-1}. However, the strain rates obtained by various mechanical testing methods, such as torsion of thin walled tubes [12], thick walled cylinder implosion tests [13] and Split Hopkinson Pressure Bar (SHPB) [14] are not larger than 10^4 s^{-1}. For SHPB testing, the most widely used method for high strain rate tests, the strain rates achieved typically lie in a range of 10^2-10^4 s^{-1} [15]. Therefore, the "high strain rate" mentioned in most literatures refers to strain rates ranging from 10^3s^{-1} to 10^4s^{-1}. In this strain rate range, deformation is fundamentally different from that in quasi-static conditions. At quasi-static strain rates, a static equilibrium state is maintained as any element in the specimens has a summation of forces acting on it approximating to zero. However, in high strain rate deformations stress travels through materials, resulting in different loading states for different regions. Also, high strain rates affect thermally-activated mechanisms and may result in microstructural change through adiabatic heating [16]. In this context, the response of materials to high strain rates has attracted researchers' interest and formed a new area of study [17].

1.3 Applications involving high strain rate

The high strain rates and elevated temperatures experienced by metallic materials during commercial manufacturing processes or extreme service environments also motivate the investigation of the dynamic behaviour of metals and alloys at room and elevated temperatures. Industrial applications such as explosive welding, explosive forming and machining always occupy very high strain rates. Explosive welding is an excellent method for joining metals and alloys with very different melting points through producing a weld joint by high velocity impact aided by controlled detonation with an explosive charge. This technique has been investigated for welding titanium/stainless [18], titanium/steel [19] and titanium/magnesium alloys [20]. Other explosive metalworking techniques, like explosive forming [21], have also been developed to take advantages of explosive impacts. Machining is the most common manufacturing process and is widely used in

industrial production. Typical strain rates for machining processes lie in the range of 10^3-10^6 s^{-1} [15]. Understanding the dynamic behaviour of materials during machining is helpful for obtaining superior surface quality [22] and improving tool life [23]. High strain rate deformation is also encountered in car crashes, bird strikes on airplanes and micrometeorite impact on space structures, etc. The dynamic response of materials to high strain rates in these instances is tied to life safety. In addition, military applications such as protective armour [24] for prevention of ballistic penetration also involve high strain rate deformations.

1.4 Thesis Outline

Currently, most studies on the dynamic response of metals and alloys to high strain rates focus on copper, steel, tantalum, Ti-6Al-4V and commercially pure titanium. There is no well-established research on the dynamic behaviour of β titanium alloys. Complicated phase transformations and various deformation mechanisms may occur in β titanium alloys during deformations, which make the investigation of the dynamic response of β titanium alloys to high strain rates challenging. The aim of this project is to develop a comprehensive understanding of the high strain rate properties of new types of β titanium alloys at room and elevated temperatures and to characterize the microstructural evolution and deformation mechanisms of the alloys with differing levels of β phase stability. This work will be directly applied to optimise the high speed machining of β titanium alloys and will also contribute to a better understanding of the dynamic behaviours of BCC structured metallic materials.

Chapter 2 provides a literature review concerning the dynamic response of metals and alloys to high strain rates. A detailed description of the complex phase transformations and multiple deformation mechanisms that may occur in β titanium alloys is given followed by an introduction to the most widely applied high strain rate testing method-Split Hopkinson Pressure Bar testing. The dynamic flow behaviours of materials with different crystalline structures at high strain rates are summarized. Constitutive models applied to predict flow behaviour of metallic materials, especially the most widely used Johnson-Cook and Zerilli-Armstrong models, are reviewed in sequence. Finally, microstructural evolution including precipitation, stress-induced phase transformations and adiabatic shear banding which may occur during high strain rate deformations are discussed.

Chapter 3 covers the research findings presented as a series of publications. These papers describe the methods, results, discussions and conclusions and were published during the course of

candidature. An overview of these papers provides readers with an insight into how these papers relate to each other and contribute to an improved understanding of the dynamic behaviour and microstructures of β titanium alloys. The final chapter summarizes the research and outlines future work.

Chapter 2

Literature Review

2.1 Beta Titanium Alloys

Over the past decade, β titanium alloys have attracted significant attentions due to their extraordinary mechanical properties along with complex phase transformations and deformation mechanisms which may occur during plastic deformations. Currently, the investigations on β titanium alloys mainly focus on two types of alloys: 1. β titanium alloys for aircraft structural applications; 2. β titanium alloys for biomedical applications.

2.1.1 β titanium alloys for aircraft structural applications

In terms of damage tolerance, β titanium alloys with an excellent combination of high specific strength and superior fracture toughness are promising for structural applications in aerospace industry. For instance, forgings of the Ti-10V-2Fe-3Al alloy are increasingly used in the hub of the main rotor system in helicopters and forgings of the Ti-5Al-5Mo-5V-3Cr (Ti5553) alloy have been used for fabrications of the landing gears in the Boeing-787 and Airbus-350 [25, 26]. Other similar β titanium alloys such as Ti-7Mo-3Nb-3Cr-3Al (Ti7333) [27] and Ti-6Cr-5Mo-5V-4Al (Ti6554) [28, 29], with ultrahigh strength and excellent ductility, have also been developed recently for aerospace applications. As the volume fraction, distribution and morphology of α phase precipitates have great effects on the mechanical properties of β titanium alloys [30], a large number of experiments have been conducted on the effects of heat treatment on the microstructures and tensile properties of this category of alloys.

Shekhar et al. [31] studied the structure-property correlation in thermo-mechanically processed Ti5553 alloy as a function of solution treatment temperature and aging time and temperature. Ahmed et al. [32] studied the effect of aging time on the structure-property correlation of the thermo-mechanically processed powder Ti-5Al-5V-5Mo-1Cr-1Fe (TC18) alloy at 923 K. The influences of solution treatment on microstructure and mechanical properties of the Ti7333 and Ti6554 alloys have been investigated by Fan et al. [33] and Li et al. [34], respectively. As refined dispersions of secondary α phase precipitates play a critical role in the improvement of the mechanical properties of β titanium alloys, experiments on α phase nucleation sites and influence of ω phase on the refinement of the α phase precipitates have been conducted by Zheng et al. [35], Ahmed et al. [36], Coakley et al. [37] and Nag et al. [38]. As thermo-mechanical processing has been considered as a suitable fabrication approach for titanium alloys, another important topic is their flow behaviours and microstructural evolutions during hot deformations. The dynamic softening behaviour of the TC18 alloy during hot deformations has been studied by Ning et al. [39]

and Liang et al. [40], respectively. Meanwhile, the response of the TC18 alloy to strain, strain rate and temperature during hot deformations has been investigated by Nan et al. [41]. Hua et al. [42] reported that deformation parameters, such as temperature and strain rate, in hot mechanical compressive tests significantly affect the microstructural evolution of the Ti5553 alloy. The hot deformation behaviour of the Ti7333 alloy in the temperatures ranging from 770 to 970 ℃ and the strain rates ranging from 10^{-3} to 10 s^{-1} has been investigated by Fan et al. [43].

2.1.2 β titanium alloys for biomedical applications

Though Ti-Ni shape memory alloys have superior superelasticity (SE), shape memory effect (SME) and biocompatibility [44, 45], the use of Ni, which may cause human allergies and hypersensitivity [46], has pushed researchers to find replacement for Ti-Ni based alloys. Recently, a range of Ni-free β titanium alloys with ultralow Young's modulus, good biocompatibility and superelastic properties have been developed for biomedical implant applications [47]. Compared with the Ti-6Al-4V alloy, the workhorse in biomedical implantations [48], these β titanium alloys can be engineered to achieve a much lower Young's modulus, ~50 GPa as shown in Table 1 [49]. As the Young's modulus of human bone is ~30 GPa, the reduced mismatch in modulus between human bone and the implantation can help alleviate "stress shielding effect" [50]. It is generally accepted that the metastable β phase has the lowest modulus compared with α" and ω phases. The origin of low Young's modulus in Ti-Nb-Ta-Zr alloys [51] and cold worked Ti-Nb-Ta-Zr-O alloys [52] have been studied and it is reported that "Young's modulus is lowest near the Martensite start temperature (M_s)". Chang et al. [53] investigated the effect of microstructures on the Young's modulus for Ti-Nb based alloys with different Nb contents and concluded that the Young's modulus depends directly on the chemical compositions of the alloy and its heat treatments.

In addition, transformations from β phase to martensitic α" phase or ω phase can be induced by applied stress when the M_s temperature can be suppressed to around room temperature, which can yield alloys with superelasticity and shape memory properties [54-58]. Kim et al. [59, 60] studied the effects of Mo and Nb on the superelasticity and shape memory properties of Ti-Nb based biomedical alloys and reported that increment in the critical stress for dislocation slip will lead to a larger superelastic strain. Umer et al. [61] investigated the effects of Al content on the microstructures and superelasticity of the Ti-Nb-Al alloys. Fu et al. [62] developed a new Ti-Zr-Nb-Sn alloy system and demonstrated a large superelastic recovery strain of 6.0% which was related to a strong recrystallization texture. Experiments on the relationship between cyclic deformation and superelasticity were conducted for a Ti-26 at% Nb alloy by Tahara et al. [63].

Table 1 Mechanical properties of a range of biomedical β-type Ti alloys [49].

Biomedical β titanium alloys	Chemical comp. (wt.)	E(GPa)	YS(MPa)	UTS(MPa)	El. (%)
TMZF	Ti–12Mo–6Zr–2Fe	74–85	1000–1060	1060–1100	18–22
Ti-15-5-3	Ti–15Mo–5Zr–3Al	75	870–968	882–975	25
Ti–30Ta	Ti–30Ta (ST)	69	~430	587	21
TNZT	Ti–35Nb–5Ta–7Zr	55	547	597	19
Ti-30Ta	Ti-30Ta (Aged)	76		892	9.3
TNZTO	Ti–35Nb–5Ta–7Zr–0.4O	66	976	1010	
Ti-24-Nb-4Zr-7.9Sn	Ti–24–Nb–4Zr–7.9Sn	42	~350	850	
Ti–35–4	(Ti–35Nb)–4Sn	42–55	619–787	673–846	7–12
TNTZ	Ti-29Nb-13Ta-4.6Zr	55-65	864	911	13.2
Ti–13Nb–13Zr	Ti–13Nb–13Zr (Aged)	79–84	836–908	973–1037	10–16
Ti25Nb3Zr3Mo2Sn	Ti–25Nb–3Zr–3Mo–2Sn	50–80	440–500	708–715	15.3–31.3
TNZF	Ti–28Nb–13Zr–0.5Fe	58–120	780–1050		7–13

2.1.3 Design Strategy for β titanium alloys

The dominant deformation mechanism for β titanium alloys will change from dislocation slip to twinning and/or stress-induced martensitic (SIM) transformation with decreasing levels of β phase stability [54, 64-66]. β phase stability is commonly gauged by Mo_{eq}, an equivalent binary Ti-Mo alloy concentration [66]. In recent years, bond order (Bo) and d-orbital energy (Md) have been applied to predict the relationship between plastic deformation behaviour and β phase stability [67, 68]. Decreasing β phase stability is reflected by an increase in Md or a decrease in Bo. A Bo-Md plot [69] over the range of 2.35 to 2.60 in Md and 2.78 to 2.96 in Bo has been developed based on numerous experimental results as shown in Fig.3. Based on variations in deformation mechanisms with β phase stability in β titanium alloys, "d-electron alloy design method" has been highlighted as a strategy to design β titanium alloys. This alloy design concept was firstly proposed for the superelastic properties of β titanium alloys [68, 70, 71]. Sun et al. [47, 72] and Marteleur et al. [73] have proved that "d-electron alloy design method" can also be extended to the plastic properties of β titanium alloys. It is observed that when β titanium alloys are designed to be located within a specific zone in the Bo-Md diagram (Fig.3), different deformation modes including stress-induced martensitic transformation, various types of twinning and/or dislocations slip will be activated simultaneously and their interactions significantly contribute to enhanced strain hardening and

improved ductility [73, 74]. The Ti-15Mo-5Zr alloy[75, 76] and Ti-10Mo-2Fe alloy [76] are also designed to combine {332}<113> mechanical twinning and dislocation slip together to achieve large uniform elongation and high yield strength.

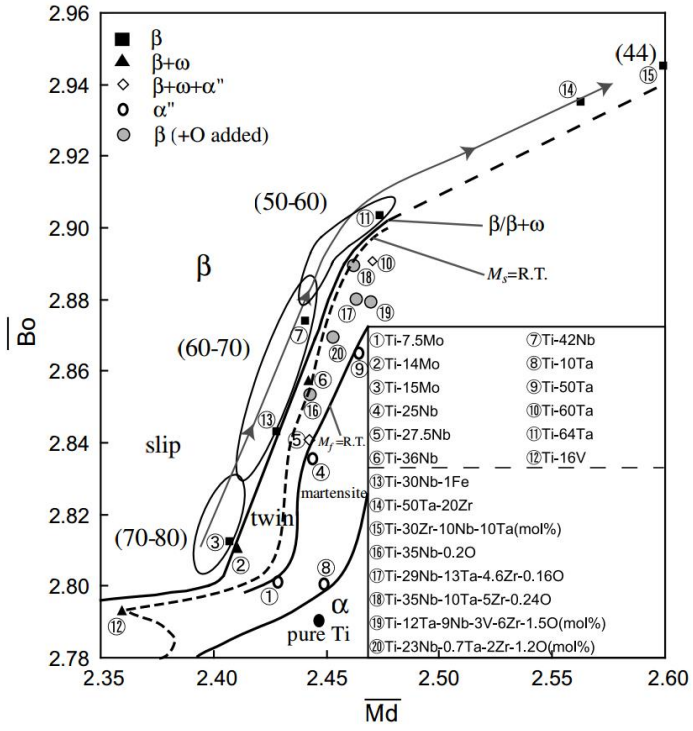

Fig.3. Extended Bo-Md diagram in which the β/β+ω phase boundary is shown together with the boundaries for M_s=RT and for M_f= RT. The Young's modulus (GPa) is given in parentheses for typical alloys [69].

2.2 High Strain Rate Testing

Traditional mechanical testing methods like screw-driven or servo-hydraulic machines render some limitations at high strain rates like oscillations and stress waves which can affect the interpretation of data [77]. The most crucial limitation is that the maximum strain rate reached by these machines is quite low. The highest strain rate for testing in servo-hydraulic machines reported in the past literature was only $100s^{-1}$ [78]. In order to characterize the mechanical response of materials under high strain rate deformations more accurately, several high strain rate experimental techniques have been applied; torsion of thin walled tubes [12], thick walled cylinder implosion tests [13], modified double shear tests and shear-compression specimen tests [79], etc. Among these techniques, Split Hopkinson Pressure Bar (SHPB) is the most widely established and accepted.

Fig.4. Scheme of SHPB device [80].

Instead of using conventional screw-driven or servo-hydraulic methods, SHPB has been used extensively to test the dynamic stress-strain behaviour of materials at high strain rates ranging from 10^2 to $10^4 s^{-1}$ [30]. The data obtained by SHPB can be used to fit constitutive models. The prototype of SHPB was first built by Bertrand Hopkinson to measure the detonation energy of explosives in 1914 [14]. Then in 1948, Davies et al. [81] mounted a condenser on the bar to measure the strains. One year later, Kolsky et al. [82] completed the basic form of SHPB testing by adding a second bar to the prototype developed by Hopkinson and hence the SHPB is also commonly referred to as Kolsky bar. In 1970, Hauser et al. [80] added strain gauges to the SHPB and then surface displacements can be measured. From then on, the typical scheme of SHPB device was established as shown in Fig.4. It consists of a striker bar, an input (or incident) bar and an output (or transmitted) bar. Specimen is sandwiched between the input and output bar. Once the striker bar impacts the input bar, a pulse referred to as incident pulse will be created going through the input bar into the specimen. When the incident pulse reaches the interface between the input bar and the specimen, part of the pulse (reflected pulse) will be reflected back to the Input bar while the rest (transmitted pulse) will be transmitted to the output bar through the specimen. These pulses will be recorded by the strain gages mounted on the bars [30]. The flow stress σ, strain ε and strain rate $\dot{\varepsilon}$ are calculated using equations as follow:

$$\sigma = E\frac{A_b}{A_s}\varepsilon_t \tag{2.1}$$

$$\dot{\varepsilon} = -2\frac{C_0}{L}\varepsilon_R \tag{2.2}$$

$$\varepsilon = -2\frac{C_0}{L}\int \varepsilon_R \, dt \tag{2.3}$$

ε_R and ε_t represent the reflected pulse and transmitted pulse, respectively. A_b is the cross-sectional area of the bars, A_s is the cross-sectional area of the specimen and L is the gauge length of the specimen. C_0 is the elastic wave speed in the bars which can be calculated by equation $\sqrt{E/\rho}$ where E and ρ correspond to Young's modulus and density of the specimen. As the dimensions used in the calculation are all initial values before deformation, the computed stress and strain are engineering values [80]. However, engineering values of stress and strain do not describe the real behaviour of materials during deformations. Thus it is necessary to transfer engineering values into true values to acquire true stress-strain response for the material.

The theory and calculation of SHPB experimental data above are based on several assumptions listed below [77, 80]:

(1) The pulse propagating in the bars obey the one-dimensional elastic wave propagation theory.

(2) Strain pulses do not exceed the elastic limitation of the bars.

(3) The specimen maintains a state of dynamic equilibrium.

(4) The plastic deformation in the specimen is uniform.

Unfortunately, it is almost impossible to satisfy the first assumption above in practice. The pulse tend to disperse when moving down the bar as the higher frequency component of the pulse travel slower than the low frequency component as shown in Fig.5 [83]. The dispersion of the pulse will produce oscillations on the stress-strain curve and distort the true response of the material in deformations [83]. Up to this stage, Fast Fourier Transform (FFT) has been used to correct the dispersion.

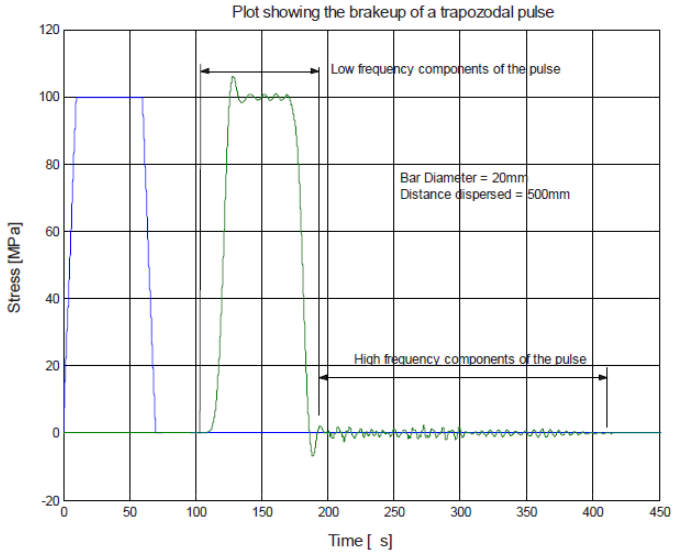

Fig.5. Plot showing the break-up of a trapezoidal pulse due to dispersion [83].

Recently, the SHPB technique was extended from compressive tests to tensile [79, 84] and torsion tests [79, 84-86]. Setup and corresponding specimens for these tests are different as shown in Fig.6. Under the same conditions, tensile tests allow a higher effective strain rate than compression tests. However, the state of tri-axial stress and non-uniform strain in tensile tests make the stress-strain curve obtained deviate from the real response of the material [80]. Advantages involved in torsional tests are relatively uniform strain distribution and pure shear stress state [79]. Compared with the former two tests, the biggest advantage of compressive tests is that a higher shear strain can be reached before fracture, which enables researchers to observe the microstructural changes that may occur in deformations. Especially, when using hat-shaped specimens which were first used by Meyers et al. [87], the largest shear strain can reach 4 or even higher. The basic theory for using

hat-shaped specimen in compressive SHPB tests to achieve large strains is shown in Fig.7.

In order to investigate the effects of high temperature on the dynamic deformation behaviour of materials, a high temperature SHPB test system has been developed in the experiments conducted by Seo et al. [88] as shown in Fig.8. It has been verified that the effect of thermal gradient and oxidation on the flow behaviour of Ti6Al4V at high strain rates can be neglected [88]. Barrelling becomes more serious with increasing temperature, thus the lubrication between the two ends of the specimen and the two pressure bars is important to dampen negative effects caused by barrelling.

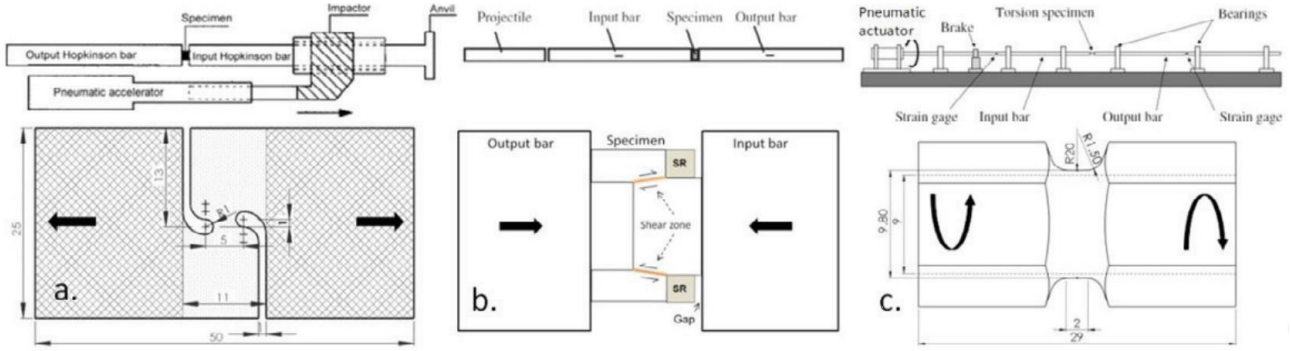

Fig.6. (a) Tensile test with planar shear specimen; (b) Compressive test with hat-shaped specimen; (c) Torsional test with thin-walled tubular specimens [89].

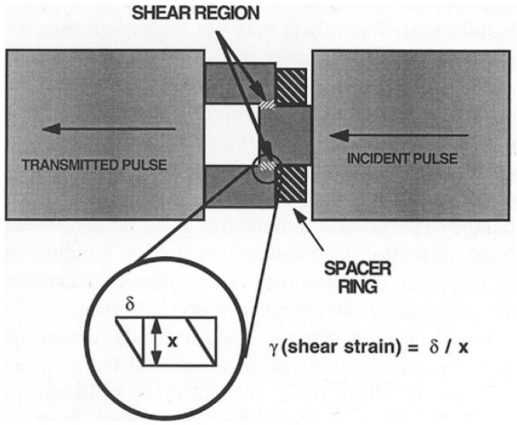

Fig.7. Schematic illustration of a cross-section in the "hat-shaped" sample within the Hopkinson bar testing apparatus and the enlarge view show the region of shear deformation within the sample [90].

Though widely used for high-strain-rate mechanical tests, limitations of SHPB tests are still very evident when compared with practical conditions in manufacturing processes. It can be seen in Table 2 and Table 3 that the strain and strain rate which can be obtained in SHPB tests are significantly lower compared with those in manufacturing processes. Although strain is a function of specimen size, large strains cannot be achieved by reducing the specimen size without limitations. When determining the size and slenderness ratio of cylindrical specimen for SHPB compressive

tests, friction between the specimen and bars, stress equilibrium within the specimens and radial inertia should be taken into consideration in order to obtain a dynamic stress-strain relationship in good agreement to the real condition for tested materials. Therefore ratio of length-to-diameter of cylindrical specimen has been determined to be in the range of 0.5-1 for SHPB compressive tests [91, 92]. Also, it has been reported that "the number of oscillations in the stress-strain curve increases considerably when the specimen diameter is reduced, probably due to an increase in the triaxiality of the stress state in the bars for smaller diameters. Part of the bar end is free, and thus is in zero-stress condition. Therefore, differences between the bar axis and its lateral surface, near the end, will be higher if the specimen diameter is reduced [93]." In a summary, reducing the size of cylindrical specimen cannot help us achieve a strain larger than 0.6 without distorting the obtained stress-strain curves. Therefore it is still difficult to use data obtained by SHPB tests to acquire satisfactory characterization of the flow behaviour of materials in manufacturing process. Currently stress-strain data from SHPB tests are mostly applied in the establishment of constitutive models which can be applied into finite element simulations.

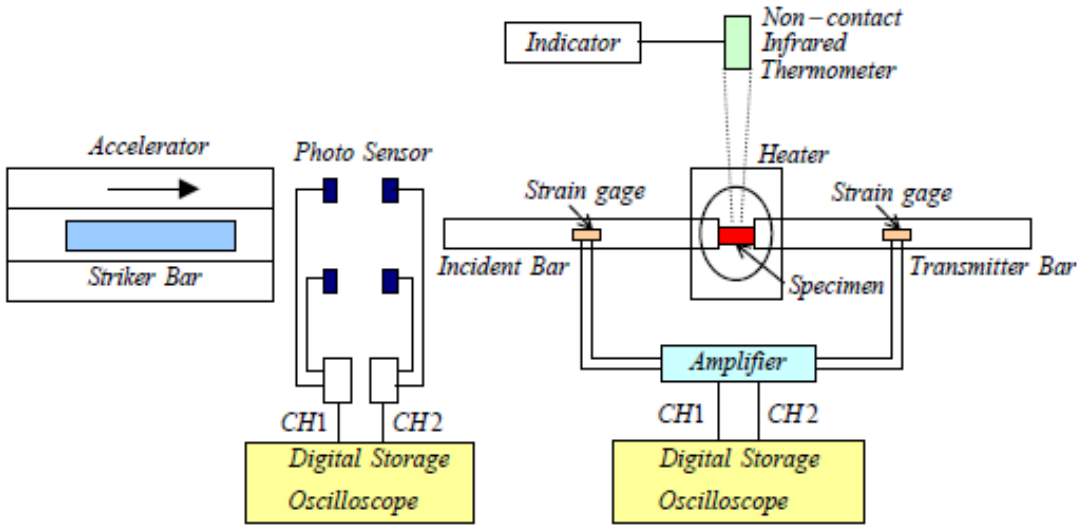

Fig.8. Scheme of the high-temperature compressive SHPB apparatus [88].

Table 2 Typical strains, strain rates, and temperatures (T_h=T/T_{melt}) of some manufacturing processes [15].

Process	Strain	Strain rate (/s)	T_h
Extrusion	2-5	10^{-1}-10^{2}	0.16-0.7
Forging/rolling	0.1-0.5	100-10^{3}	0.16-0.7
Sheet-metal forging	0.1-0.5	100-10^{2}	0.6-0.7
Machining	1-10	10^{3}-10^{6}	0.16-0.9

Table 3 Typical SHPB test conditions[15]

Testing parameters	Largest strain	Largest strain rate(/s)	Highest temperature (℃)
Khan et al.**[94]**	0.25	1700	482
Lesuer et al.**[95]**	0.28	4500	25
Macdougall et al.**[96]**	0.12	577.4	20
Nemat-Nasser et al.**[97]**	0.6	3700	725
Johnson et al.**[98]**	-	-	-
Songwon Seo et al.**[99]**	0.3	1400	1000
Lee et al.**[100]**	0.28	3000	1100

2.3. Dynamic Flow Behaviour at High Strain Rates

2.3.1 Mechanical Properties at High Strain Rates

Mechanical properties exhibited by metallic materials during high strain rate deformations are quite different from those under quasi-static deformations. They are highly dependent on crystal lattice configuration, matrix phase stability and stacking fault energy (SFE). For heavily stabilized body-centred cubic (BCC) structured and high-SFE face-centred cubic (FCC) structured metallic materials, dislocation movement is generally accepted as the dominant deformation mechanism. According to dislocation dynamics [101, 102], flow stress σ consists of a thermal component σ_{th} and an athermal component σ_a. Thermal component, controlled by shot-range barriers such as dislocation forest and Peierls stress, is sensitive to temperature and strain rate while athermal portion, controlled by long-range barriers such as grain boundaries and secondary precipitates, is always regarded as independent of temperature and strain rate. According to Harding et al. [103], thermal component becomes relatively more important at low temperatures and high strain rates as thermal vibration can help to overcome short-range barriers. The rate equation for the plastic flow controlled by thermal vibration can be written as [104]:

$$\dot{\gamma} = \dot{\gamma}_0 \, exp\left(-\frac{G^*}{kT}\right) \tag{2.4}$$

where G^* is activation energy, which is strongly dependent on σ_{th} , $\dot{\gamma}$ represents shear strain rate, $\dot{\gamma}_0$ is a parameter which depends mainly on dislocation density, vibrational frequency and strain per successful activation, k is Boltzmann's constant and T absolute temperature [104].

Activation volume v^* is a concept defined to describe the work done by external stress during

thermal activation. Its format can be derived from the rate equation (2.4), as shown below:

$$v^* = -\left(\frac{\partial G^*}{\partial \sigma_{th}}\right)_T = kT\left(\frac{\partial ln\frac{\dot{\gamma}}{\dot{\gamma}_0}}{\partial \sigma_{th}}\right)_T \quad (2.5)$$

For most single-phase BCC structured materials, the thermal activation of dislocation slip is mainly controlled by Peierls stress. Therefore the yield strengths of BCC metals and alloys increase with increasing strain rates but decrease with increasing temperatures as Peierls stress is a kind of short-range barrier sensitive to strain rate and temperature [16]. For the same reason, the activation volume of BCC structured materials is constant irrespective of strain and much smaller than that for pure FCC structured materials [102, 104, 105]. Unlike yield stress, the strain hardening rate of BCC metals and alloys is mainly controlled by long-range barriers [103]. As long-range barriers are insensitive to temperature and strain rate, the strain hardening behaviour of BCC metals and alloys is always regarded as rate- and temperature-independent. Meyers et al. [106] conducted a sequential interrupted compressive test to establish the isothermal curve for tantalum (BCC structured metal) deformed at 3500 s^{-1} as shown in Fig. 9(a). Comparing the isothermal stress-strain curve at 3500 s^{-1} with the curves at very low strain rates in Fig. 9(b), the parallelism between these curves indicates that the evolution of strain hardening of tantalum is insensitive to strain rate.

The thermal activation for pure FCC structured materials is primarily controlled by dislocation forests rather than Peierls stress [105]. Therefore the strain hardening behaviour of FCC metallic materials is highly dependent on strain rate and temperature as high strain rates will contribute to an enhanced rate of multiplication of dislocations with straining and elevated temperature will induce recovery of dislocation structures. Another characteristics of FCC metals and alloys is that strain rate and temperature have a small influence on their yield strength [16]. The most representative FCC metal with these features is OFHC Cu [107]. FCC structured Inconel 690 superalloy [108] also showed similar characteristics though mechanical twinning was observed in it. Aluminium alloys AA5754 and AA5182 [109], typical high-SFE FCC materials, showed low rate-dependency for yield strength and strain hardening rate at room temperature. At high strain rates, their yield stress remained constant at different temperatures, while strain hardening rates decreased with increasing temperatures as shown in Fig. 10.

The dynamic response of hexagonal-close packed (HCP) structured metallic materials to strain rate and temperature is similar to BCC structured metallic materials as reviewed by Gray et al. [16]. One important characteristics of HCP structured materials is that the shapes of stress-strain curves are highly dependent on the relative orientation between loading axis and crystallographic c-axes due to

the nature of crystallographic anisotropy in HCP lattice as shown in Fig.11 [110]. Therefore the influence of strain rate and temperature on their yield strengths and strain hardening rates can also be anisotropic. Multiple deformation mechanisms including different forms of slip (basal, prismatic and pyramidal) and different twinning systems (extension and contraction) may be activated under different loading conditions, leading to different responses to high strain rates. Ulacia et al. [110] reported that for a Mg AZ31 sheet the yield strength did not vary with strain rate when testing the material in compression along rolling direction due to the preferential activation of twinning. However, when prismatic and basal slips are dominant in the deformation, there was a significant variation in the yield strength with strain rate in the AZ31 alloy. Shen et al. [111] observed that the strain hardening responses of magnesium alloy AMX602 to differing loading rates were in variances when loading direction was kept constant. Gurao et al. [112] found that the strain hardening behaviour of pure titanium in high-strain-rate deformations was complicated due to enhanced twinning behaviour and the variance between strain hardening rates for differently oriented samples was reduced at high strain rates.

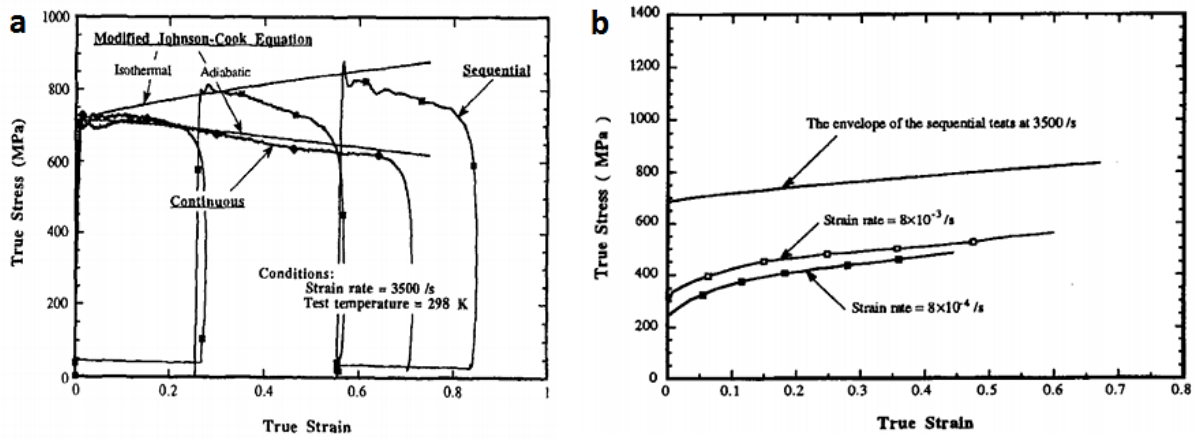

Fig.9. (a) Continuous and sequential (isothermal) stress-strain response of tantalum at nominal strain rate of 3500 s^{-1} in room temperature; (b) Comparison of stress-strain curves at different

It is worth noting that the understanding of flow behaviour of metastable BCC structured materials and low-SFE FCC structured materials as a function of temperature and strain rate becomes relatively complex as temperature and strain rate will affect the activation of different mechanisms including dislocation slip, mechanical twinning and martensitic phase transformations. Twinning-induced plasticity (TWIP) and transformation-induced plasticity (TRIP) are two similar but competing mechanisms for enhancing plasticity, which have been reported in less stabilized BCC structured materials and low-SFE FCC structured materials. Lee et al. [113] studied the influence of strain rate on the TRIP-TWIP transition in Austenitic Fe12Mn0.6C steel and qualitatively described

SFE dependence and strain rate dependence of the strengthening mechanism in the Fe12Mn0.6C steel as shown in Fig.12. Yang et al. [114] and Bintu et al. [115] reported that the strain hardening rate decreases at high strain rates in TWIP steels as adiabatic heating brought by high strain rate deformations will retard twinning. Russel et al. [116] observed that in the Fe85Cr4Mo8V2C1 alloy higher strain rates promoted formation of martensite at the onset of deformation. Whether martensitic transformation will increase the flow stress or not depends on the hardness of martensite in relation to parent phase. Kim et al. [78] reported that the flow stress under quasi-static loading conditions is larger than that in deformations at higher strain rates in the early plastic strain range **strain rates [106].**

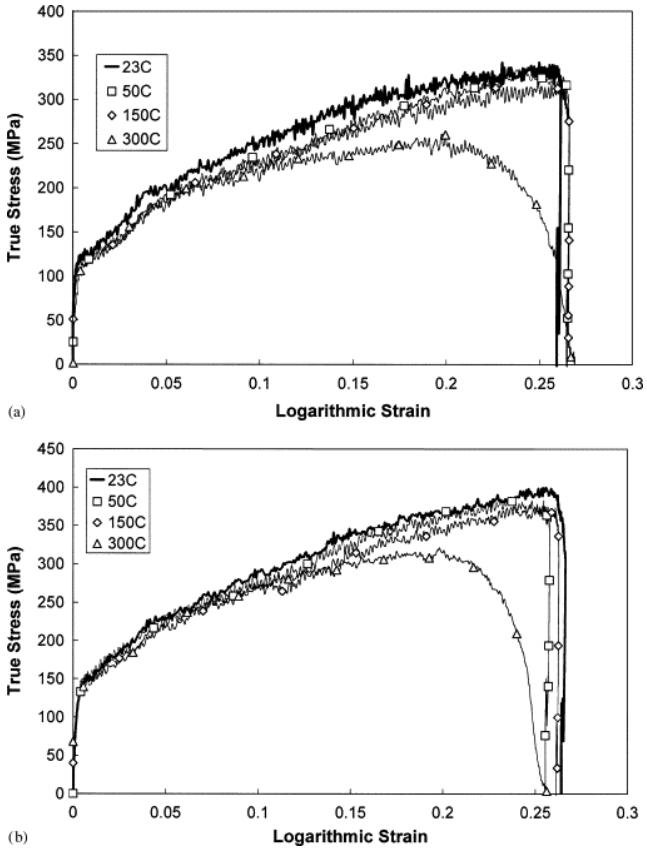

Fig.10. Effects of initial temperature on flow stress at a strain rate of 1500 s^{-1} for (a) AA5754 and (b) AA5182 [109].

for the TRIP780 steel. As the martensitic phase is harder than the austenite in the TRIP780 steel, a potential reason for this flow softening at high strain rates is that high strain rates retard the martensitic transformation. For an FCC structured AlCrFeCoNi high entropy alloy with low SFE, an exceptional strain hardening rate was observed irrespective of strain rate [117]. This is speculated to be due to secondary nano-twins occurring during high strain rate deformations. Though TRIP and TWIP phenomena have been reported in BCC structured β titanium alloys [54,

64, 65], no study has systematically studied their mechanical behaviour at high strain rates over a wide range of temperatures.

The ductility and fracture resistance of materials also depend on strain rate and temperature. Studies on biomedical titanium [85, 118] and Al-Sc alloys [119] suggest that the ductility of materials increase with increasing strain rates. However, similar studies conducted on Inconel 690 superalloy [120] and 316L stainless steel [121, 122] indicated that the ductility and fracture resistance decreased with increasing strain rate. El-Magd et al. [123] reported that when strain rates exceeded 1000 s^{-1}, the ductility of AA7075 aluminium alloy and AZ80 Mg alloy increased significantly with increasing strain rates while the Ti6Al4V alloy rendered a contrary behaviour. In the study conducted by Ryttberg et al. [124] on high strength aluminium alloys, it was concluded that for failure by tensile cracks at low loading rates the impact fracture toughness decreases with increasing loading rates; for failure by adiabatic shear bands at higher loading rates the fracture toughness increases with increasing loading rates. In summary, the effects of strain rate on ductility are material-dependent. As to the dependence of ductility of materials on temperature, the ductility will generally be improved with elevated temperature due to enhanced thermal softening effects [85, 120, 121].

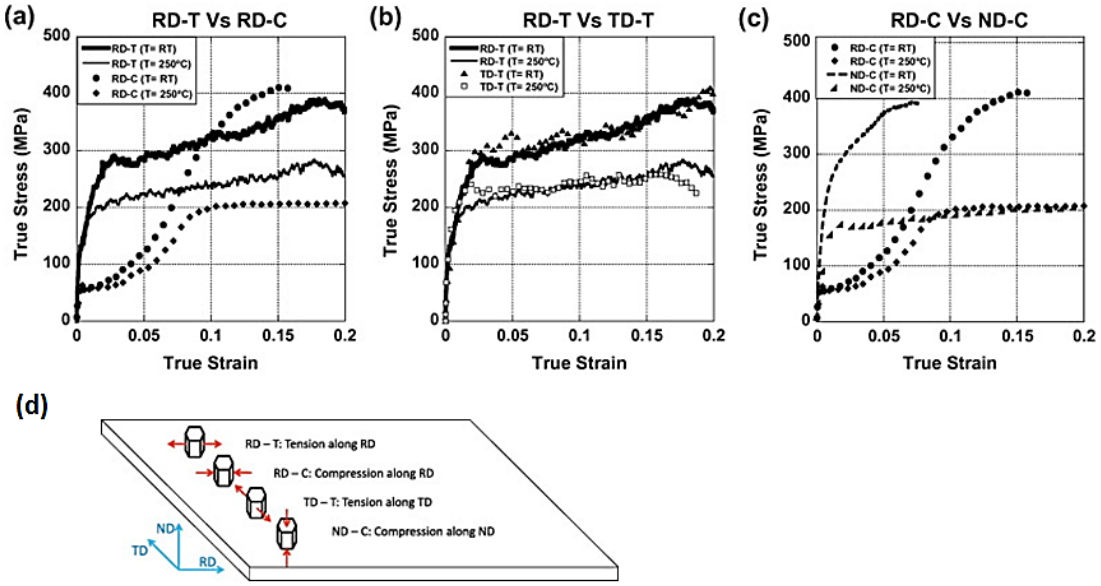

Fig. 11. True stress–true strain curves corresponding to high-strain-rate (10^3 s^{-1}) tests performed on the Mg AZ31 alloy at room temperature and at 250 ℃: (a) RD-T vs. RD-C; (b) RD-T vs. TD-T; and (c) RD-C vs. ND-C; (d) Schematic illustrating the relative orientation of the tension and compression axes with respect to the *c*-axes and the sheet reference system (RD, TD, ND) for all the tests carried out in the present investigation [110].

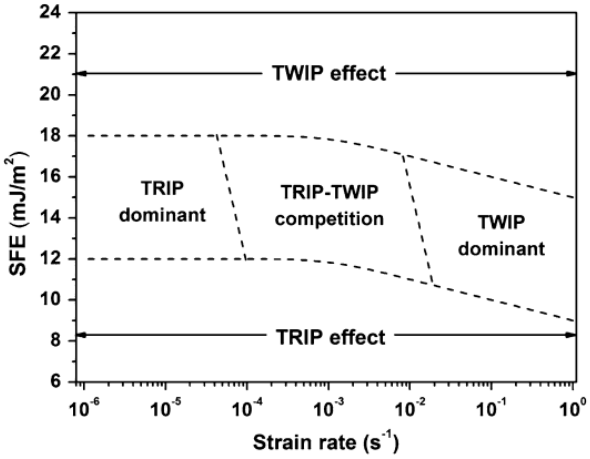

Fig. 12. Effect of strain rate on plasticity-enhancing mechanisms in austenitic alloys with SFE ranging from 12 to 18 mJ/m^2 [113].

2.3.2 Strain Rate Sensitivity and Temperature Sensitivity

The dependence of strain rate effect and temperature effect on strain rate, strain and temperature are always quantified by strain rate sensitivity, β, and temperature sensitivity, n_a. Calculations for them are listed below:

$$\beta = (\sigma_2 - \sigma_1)/ln(\dot{\varepsilon}_2 - \dot{\varepsilon}_1) \tag{2.6}$$

$$n_a = |(\sigma_2 - \sigma_1)/(T_2 - T_1)| \tag{2.7}$$

In equation (2.6), the stresses σ_1 and σ_2 are obtained from tests conducted at average strain rates of $\dot{\varepsilon}_1$ and $\dot{\varepsilon}_2$, respectively. In equation (2.7), the stresses σ_1 and σ_2 are obtained from tests conducted at temperatures of T_1 and T_2, respectively [118, 125]. It is generally observed that strain rate sensitivity will increase with increasing strain rate and decrease with increasing temperature for most metallic materials [85, 118, 120-122]. In addition, some experimental results show that strain rate sensitivity tends to increase greatly beyond a strain rate of $10^3 s^{-1}$ as shown in Fig.13 [108]. This large increment in flow stress beyond $10^3 s^{-1}$ has been interpreted as a transition from thermally controlled activation mechanisms to dislocation drag controlled mechanisms at higher strain rates according to Meyer et al. [17]. However, Fallansbee et al. [126] suggested that improved strengths should be attributed to the enhanced rates of dislocation multiplication, instead of the change in deformation mechanism. This alternative view was supported by Lee et al. [127] and Zerill et al. [128] in their studies on 304L stainless steel and OFHC copper, respectively. As to temperature sensitivity, there exist some contradictions. In Refs [85, 118, 121, 129], the temperature sensitivity of the investigated metals was interpreted to increase with increasing strain, strain rate and

decreasing temperatures. However, Lee et al. [120] reported that in 690 superalloy temperature sensitivity increases with decreasing strain rate, while in 304L stainless steel [125] temperature sensitivity increases with increasing temperature. It is worth noting that when dynamic strain aging (DSA) occurs, the influence of temperature on stress will reverse. DSA is caused by the interaction between moving dislocations and mobile point defects and appears at certain suitable combinations of strain rate and temperature. DSA has been observed in commercially pure titanium [130], AL-6XN stainless steel [131] and Ti-6Al-4V [132] and it becomes more pronounced with increasing strain and less pronounced with increasing strain rates.

2.3.3 Dynamic Flow Behaviour of Titanium Alloys

Khan et al. [133], Nemat-Nasser et al. [132], Hokka et al. [134] and Lee et al. [85, 118, 129] have performed dynamic mechanical tests on titanium alloys and observed that flow stress was sensitive to high strain rate and elevated temperature. Furthermore, for the Ti6Al4V [129] and Ti15Mo5Zr3Al alloys [85] researchers found that flow stress was more sensitive to changes of temperature than strain rate. In the study on the dynamic behaviour of the Ti6Al4V alloy with three different microstructures [132], it was found that initial microstructures only affected the athermal portion of flow stress while the thermal part depends on temperature and strain rate. Song et al. [135] have conducted dynamic compressive tests on the β Ti-Nb-Zr-Mo-Sn alloy and found that the flow stress decreased slightly when the strain rate was raised to 1000 s^{-1} as shown in Fig.14. It may be attributed to the fact that high strain rates increased the volume fraction of α" martensitic phase which has a lower hardness than β phase. Negative strain rate sensitivity is also reported by Farghadany et al. [136] in the β Ti-Nb-Ta-Zr alloys and is likely due to the increased volume fractions of softer martensitic phase as the strain rate increased.

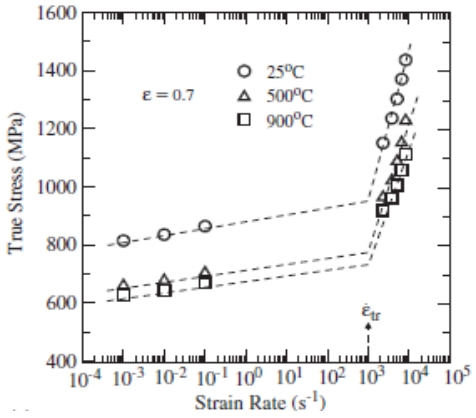

Fig.13. Influence of strain rate on flow stress at different temperatures for inconel 690 superalloy [108].

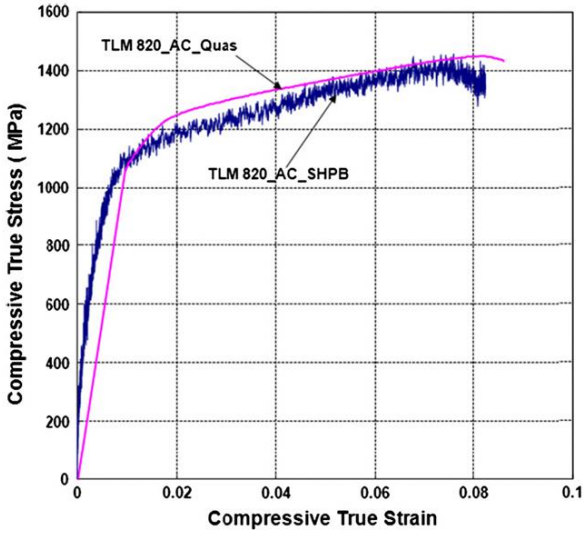

Fig.14. Experimental results from quasi static and dynamic compression testing for the near β titanium alloy (TLM 820_AC_Quas: 10^{-3} s^{-1}, TLM 820_AC_SHPB: 10^{3} s^{-1}) [135].

2.4 Constitutive Modelling

2.4.1 Introduction to Constitutive Models

Materials constitutive models are used to describe the relationship between flow stress, strain, strain rate and temperature of materials. This forms the foundation for finite element analysis (FEA) modelling of their deformation behaviours. Several constitutive models, based on differing theories, have been proposed and can be categorised into three different types: phenomenological, semi-empirical based and physically based models, respectively. Physically based models, such as the Mechanical Threshold Stress (MTS) model [126] and the Bammann-Chiesa-Johnson (BCJ) model [137], are based on specific physical theories and can provide good agreement to experimental results. However, parameters for these models are difficult to obtain as they always require some data from strictly controlled experimental tests. In addition, the accuracy of some material property constants used in these physically based models is still in doubt. Moreover, these physically based models are not readily available in FEA code. Compared with physically based models, the Johnson-Cook (JC) model [138], one of the most frequently used empirical models, is more preferred by investigators because parameters for the JC model can be obtained using fewer stress-strain curves due to its simple mathematical form. Also, the JC model can be applied directly to the major commercial FEA packages. The main drawback of the JC model lies in its simple mathematical form as it neglects the coupled effects of strain rate, strain and temperature on flow stress. Also, being an empirical model the average absolute error will increase with increasing

deviation of strain, temperature or strain rate from the reference condition defined by users [139]. Another frequently used constitutive model available in commercial FEA package is the Zerilli-Armstrong (ZA) model [101]. Although the ZA model is based on dislocation dynamics, the parameters for the model are still determined by fitting the model to stress-strain curves of materials in a similar manner to the JC model. Therefore, the ZA model is a kind of semi-empirical model. Some researchers prefer the ZA model to the JC model as the former not only incorporates the coupled effects of strain rate and temperature but also considers dislocation characteristics for particular crystalline structures.

One challenge involved in the application of constitutive models is that it is almost impossible to verify their effectiveness at strains larger than 0.5 when the strain rate is higher than 10^3 s^{-1}. This is because that the stress-strain curves used for parameter fitting are obtained from conventional SHPB testing and the strains reached rarely exceed 0.6 due to equipment limitation [15]. Unfortunately, the strain typically reached in some manufacturing processes such as machining and extrusion [15] can exceed 1. Moreover, for some constitutive models which are established on the basis of dislocation dynamics, the activation of mechanical twinning in specimens during high strain rate deformations will affect their fitting process and predictions. In current work, we decided to model the dynamic stress-strain behaviour of the β titanium alloys at high strain rates and elevated temperatures based on the JC and ZA models in consideration of the convenience of input into FEA packages.

2.4.2 Johnson-Cook Model

The Johnson-Cook (JC) model, firstly proposed in 1983 [138], is one of the most frequently used phenomenological model. The basic form of the JC model is defined by the product of three distinct mathematical terms:

$$\sigma = (\mathrm{A} + \mathrm{B}\varepsilon^{\mathrm{n}})\left(1 + \mathrm{C}\ln\frac{\dot{\varepsilon}}{\dot{\varepsilon}_0}\right)\left[1 - \left(\frac{\mathrm{T}-\mathrm{T_r}}{\mathrm{T_m}-\mathrm{T_r}}\right)^{\mathrm{m}}\right] \tag{2.8}$$

in which σ is equivalent flow stress, ε is equivalent plastic strain, $\dot{\varepsilon}$ is equivalent plastic strain rate and $\dot{\varepsilon}_0$ is the reference equivalent plastic strain rate defined by users (usually defined as 1.0 s^{-1}). T, T_r and T_m are workpiece temperature, room temperature and materials melting temperature, respectively. There are five parameters in this model in which A represents yield stress, B and n are strain hardening constant and exponent, C accounts for strain rate hardening and m accounts for thermal softening. Instead of being based on any physical theory, the JC model just considers the independent effects of strain hardening, strain rate hardening and thermal softening on flow stress

and multiplies them together to calculate the flow stress [140]. The parameters can be obtained by fitting the model to stress-strain curves over different temperatures and strain rates.

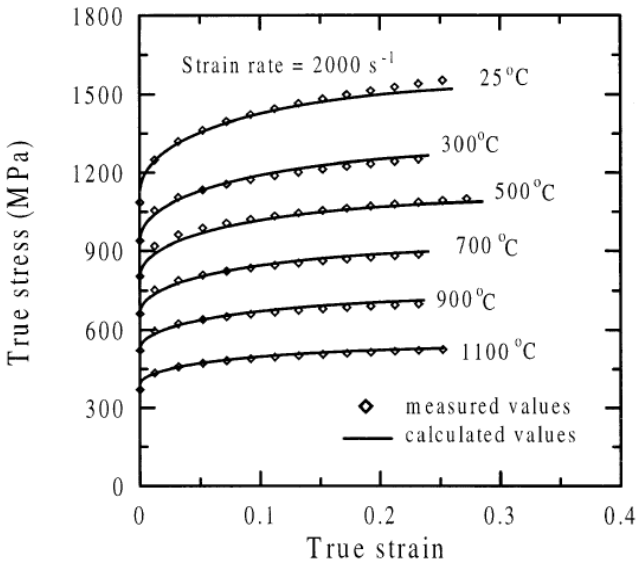

Fig.15. Comparison between the predicted and measured stress–strain curves for Ti6Al4V specimens deformed at 2×10^3 s [141].

It is important to include the temperature change caused by adiabatic heating in the process of fitting. In 1998, Lee et al. [141] calculated a set of parameters for the JC model for Ti6Al4V and included the adiabatic temperature elevation in the parameter fitting. They added an increment to the initial testing temperature to obtain the actual temperature which was used to calculate the parameter for thermal softening i.e. *m*. The comparison between the predicted and measured stress–strain curves is shown in Figure 15. They also estimated the temperature elevation in the specimens deformed under different circumstances, as listed in Table 4, from which the temperature elevation is particularly evident, especially for low initial testing temperatures. One equation has been extensively used to estimate temperature change during high strain rate deformations over the past decade:

$$\Delta T = \frac{\eta}{\rho c}\int_{\varepsilon_i}^{\varepsilon_{i+1}} \sigma(\varepsilon_i, \dot{\varepsilon}_i, T_i)\, d\varepsilon \tag{2.9}$$

in which ρ and c are the density and specific heat of material, respectively. The integral is plastic work i.e. the area under the stress-strain curve. η is heat fraction coefficient which is usually defined as 0.9 or 1 [15, 80, 85, 132, 142]. The heat produced by plastic deformation hardly dissipates under the circumstance of high strain rate deformations, especially when the strain rate is higher than 1×10^3 s^{-1}. There exists a controversy on the value of η. Macdougall et al. [84] observed that η varied from 0.2 to 0.7 with increasing strains by using infrared radiometry. The potential reason for

this discrepancy may be that the infrared radiometer used by Macdougall et al. only detected the surface temperature of the specimens and its accuracy is uncertain. Therefore, the value of η used in current work is still generally defined as 0.9.

In order to make the JC model more accurate in the prediction of flow stress for structural materials, some modifications have been proposed. Meyer et al. [143] paid attention to the obviously softer predictions of the JC model in comparison to experimental results at high strain rates. They reasoned that this was due to the unreasonable choice of 1 s^{-1} as the reference strain rate in the calculation of strain rate parameter *C* [143] and thereby suggested that a higher strain rate should be selected as the reference for high strain rate deformations. Holmquist et al. [144] also found similar phenomenon and concluded that it is due to the change of deformation mechanism at a higher strain rates. They suggested an exponential function of the natural log to replace the linear function of the natural log in Equation 2.8.

Table 4 [141]

Increases in temperature for Ti6Al4V specimens deformed at a strain rate of $2\times10^{3}s^{-1}$ and strains ranging from 0.05 to 0.25 at six initial testing temperatures.

Initial tested temperature(℃)	ΔT(℃)				
	ε=0.05	ε=0.1	ε=0.15	ε=0.2	ε=0.25
25	26.6	55.7	85.9	117.0	148.9
300	22.4	46.4	71.2	96.6	122.5
500	19.5	40.4	61.9	84.0	106.5
700	15.9	33.0	50.7	68.7	87.0
900	12.6	26.1	40.0	54.2	68.7
1100	9.3	19.3	29.6	40.2	50.0

As the dynamic stress-strain behaviour of metallic materials are closely related to their microstructural evolution during deformations, constitutive equations fail to predict the flow stress of materials well when further deformations result in significant microstructural change [145]. Although the JC model is an empirical model, many efforts have been made to relate it to the microstructural change that may occur at large strains or high temperatures during manufacturing processes in order to make more accurate predictions [88, 146, 147]. Lin et al. [148] developed a modified JC model incorporating the coupled effects of temperature and strain rate on the flow behaviours and the effectiveness of this modified JC model have been demonstrated for high-strength alloy steels [149, 150]. Tan et al. [151] found that for 7050-T7451 aluminium alloy the value of strain rate parameter *C* varies with strain and strain rate, therefore they modified the

original JC model and made *C* a function of strain and strain rate.

2.4.3 Zerilli-Armstrong Model

The Zerilli-Armstrong(ZA) model [105], which is based on dislocation dynamics, is a semi-empirical model. There are two different forms for FCC metals and BCC metals, respectively. They are given as below:

$$\sigma = C_0 + C_1 e^{(-C_3 T + C_4 T \ln\dot{\varepsilon})} + C_5 \varepsilon^{n} \qquad \text{(BCC)} \qquad (2.10)$$

$$\sigma = C_0 + C_2 \varepsilon^{0.5} e^{(-C_3 T + C_4 T \ln\dot{\varepsilon})} \qquad \text{(FCC)} \qquad (2.11)$$

σ, ε, $\dot{\varepsilon}$ and T have the same meaning as for the JC model. $C_{0\text{-}5}$ and n are parameters of the model. Unlike the JC model, strain rate hardening and thermal softening are coupled in the ZA model.

In view of its mathematical form, the ZA model has a better capacity to describe the behaviour of materials as it incorporates the coupled effects of strain rate and temperature. Meyer and Kleponis's study [143] on comparing the effectiveness of the JC and ZA models in the simulations of ballistic experiments on Ti6Al4V also verifies this perspective. Even though some sets of parameters for the ZA model for the Ti6Al4V alloy and different steels [84, 96, 143, 152-156] have been proposed in recent years, some materials constants for the ZA model are very difficult to validate as they require the critical resolved stress at 0 K and the athermal stress of materials. Thus, the ZA model does not necessarily describe the mechanical response of materials more accurately than the JC model.

Also, it is not appropriate to apply the ZA model at temperatures above the half of the melting temperature of materials [2]. In order to overcome these barriers, the reference condition has been introduced into the original ZA model for FCC structured metals and alloys and succeeded in using this modified model to predict the mechanical behaviour of a titanium-modified austenitic stainless steel [157] and a modified 9Cr-1Mo steel [158] at low strain rates at elevated temperatures. He et al. [159] and Shamsolhodaei et al. [160] have applied the modified ZA model developed in predicting hot deformation behaviour of 20CrMo alloy steel and NiTi shape memory alloy, respectively. However, there is still uncertainty as to whether this modified version can be used in high strain rate domain (strain rate $>10^3$ s^{-1}). Therefore, further investigations are required to test its applicability. In addition, Zhang et al. [161] considered the parameter C_3 in the original ZA model strain and temperature dependent and developed a modified ZA model for alloy IC10 over a wide range of temperatures and strain rates.

2.4.4 Constitutive Models for Titanium Alloys

In recent years, constitutive modelling for the dynamic behaviour of titanium alloys has mainly focused on the Ti6Al4V alloy and several sets of parameters for the JC model have been determined, as listed in Table 5. It is obvious that there exist large discrepancies between different sets of parameters. Sun et al. [15] concluded that there are three potential reasons for this discrepancy:

(1) Differences in alloy composition.

(2) Different preparation procedures for specimens.

(3) Different testing methods.

Variations in alloy composition and preparation procedure will lead to differences in the microstructure of specimens. Khan et al. [133] reported that different amounts of α and β phases in the Ti6Al4V alloy will affect the calculation of parameters for the JC model, therefore they controlled the SHPB experimental temperature below 873K to make sure that the microstructure of specimens would remain similar. To date very few works have been done on the calculation of parameters for constitutive models for the dynamic stress-strain behaviour of β titanium alloys. As far as we know, only Hokka et al. [134] has calculated a set of parameters for the JC model for the β Ti-15V-3Sn-3Al-3Cr alloy.

Table 5 Parameters for the JC model for the Ti6Al4V alloy.

JC model parameter	A(MPa)	B(MPa)	n	C	M
Lee and Lin[141]	728.7	498.4	0.28	0.028	1
Lee and Lin[129]	724.7	683.1	0.47	0.035	1
Seo and Min[88]	997.9	653.1	0.45	0.0198	0.7
Calamaz et.al[147]	968	380	0.421	0.0197	0.577
Meyer et.al[143]	896	656	0.0128	0.8	0.5
Meyer et.al[143]	862.5	331.2	0.012	0.8	0.34
Lesuer et al.[162]	1098	1092	0.93	0.014	1.1
S.Khan et.al[133]	1104	1036	0.6349	0.0139	0.7794
S.Khan et.al[133]	1080	1007	0.5975	0.01304	0.7701
S.Khan et.al[133]	1119	838.6	0.4734	0.01921	0.6437
S.Khan et.al[133]	984	520.3	0.5102	0.015	0.8242

2.5. Microstructural Evolution

2.5.1 Precipitation, Phase Transformation and Mechanical Twinning

Over the past years, researchers have investigated the microstructural evolution in metals and alloys in high strain rate deformations. They observed that strain rate and temperature have effects on the fraction and morphology of precipitates, products from stress-induced phase transformations and the evolutions of substructures in metallic materials.

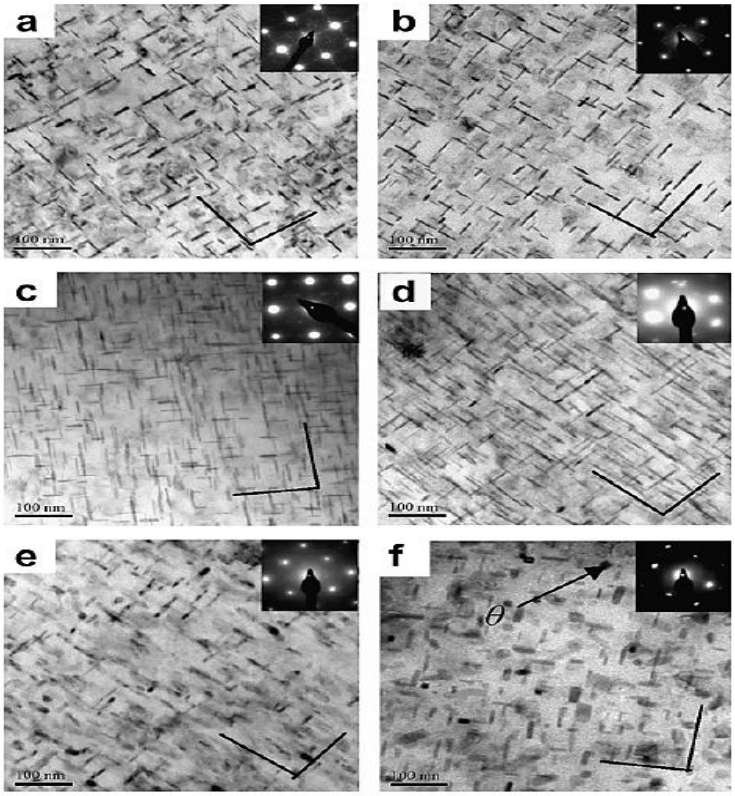

Fig.16. TEM bright-field images and corresponding SAD patterns of aluminium alloy impacted at different strain rates of: (a) 667 s^{-1}, (b) 1287 s^{-1}, (c) 3560 s^{-1}, (d) 4353 s^{-1}, (e) 5730 s^{-1}, (f) 7050 s^{-1} (The line indicates the {100} Al habit plane.) [163].

The influence of strain rate and temperature on precipitation is material dependent. Gao and Zhang [163] investigated the influence of strain rate on the precipitation behaviour in an impacted aluminium alloy and found that both the fraction and aspect ratio of θ' precipitates within the matrix changed drastically when the specimens were deformed at strain rates higher than 5730 s^{-1} as shown in Figure 16. In addition, high strain rates can lower the temperature of the phase transformation from θ' phase to θ phase. Lee et al. [118] investigated the microstructural evolution of a biomedical titanium alloy deformed at strain rates ranging from 8×10^{2} s^{-1} to 8×10^{3} s^{-1} and temperatures ranging from 25℃ to 900℃. It was reported that the proportion of α phase was insensitive to high strain

rates but decreased as the deformation approached the β transus temperature. As significant stress concentrations will form at α phase boundaries, the fracture strain is reduced as the amount of α phase is increased. To date, reports of the changes in precipitation during high strain rate deformations are few and this topic requires further investigation.

In some materials, such as TRIP steels and metastable β titanium alloys, stress-induced martensitic (SIM) phase transformations potentially occur at high strain rates at temperatures higher than martensite start temperature. It is generally accepted that high temperatures will stabilize parent phase, hence delaying SIM transformation [164]. However, the influence of strain rate on SIM transformation remains controversial. For metastable β titanium alloys: in the SHPB experiments [135] on the Ti-25Nb-3Zr-3Mo-2Sn alloy, it was observed that the deformations at a higher strain rate of 10^3 s^{-1} increased the amount of α″ martensite phase as shown in Figure 17. However, Ahmed et al. [165] reported that the SIM transformation was diminishing with increasing strain rates in a metastable β Ti-10V-3Fe-3Al-0.27O alloy, which was explained by the free energy change associated with the phase transformation. Li et al. [166] also found that the triggering stress for the SIM transformation in the β Ti-V-(Cr,Fe)-Al alloys increased with increasing strain rates as the adiabatic heating induced by higher strain rates can stabilize the β matrix, thereby retarding the initiation of SIM.

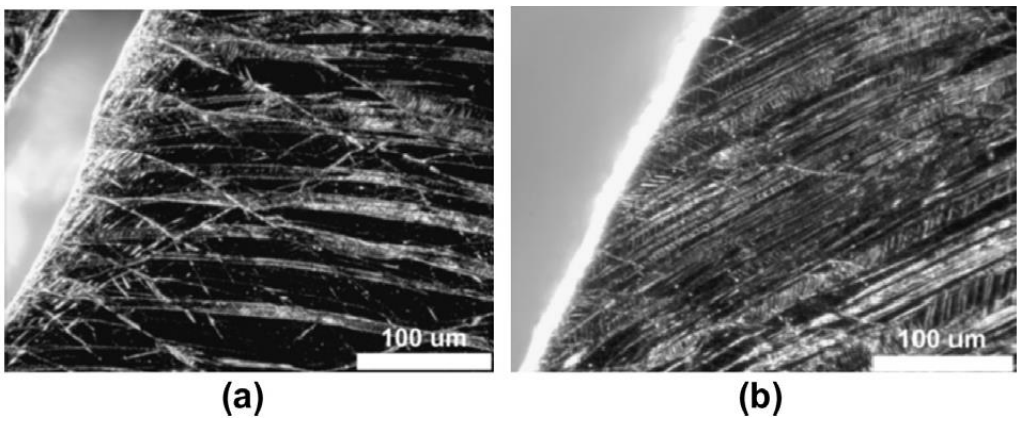

Fig.17. (a) Orthorhombic α" phase distributed across the β phase matrix after deformation at a strain rate of 10^{-3} s^{-1}; (b) orthorhombic α" phase distributed throughout the β phase matrix in the Ti25Nb3Zr3Mo2Sn alloy deformed at a strain rate of $10^3 s^{-1}$ [135].

For TRIP steels: The results of experiment conducted by Russel et al. [116] on the Fe85Cr4Mo8V2C1 alloy indicate that although high strain rates can promote the formation of martensite at the onset of deformation, the accompanying adiabatic heating will decrease the transformation rate with further straining. Lee et al. [167] summarized the results of several dynamic experiments on steels where a contradiction aroused about the effects of strain rate on the

martensitic transformations. Impact process can induce SIM transformation in deformed specimens, but the increment in strain rate and temperature will reduce the volume fraction of martensite.

The substructure evolutions in metals and alloys during high-strain-rate loading also strongly depend on strain rate and temperature. It is generally recognized that the density of dislocations and mechanical twins will increase with increasing strain rate but decreasing temperature [110, 118, 120, 167, 168]. In addition, the morphology and distribution of dislocations and mechanical twins are also strain-rate and temperature dependent. Lee et al. [118, 120, 169] concluded that with increasing strain rate the size of dislocation cells is reduced but the cell walls become thicker, while elevated temperatures will contribute to larger dislocation cells and thinner cell walls, as shown in Fig.18. According to Dudamell et al. [170], thermal activation is critical for dislocation rearrangement. This explains that why high strain rates have adverse influence on the dislocation rearrangement and retard dynamic recovery.

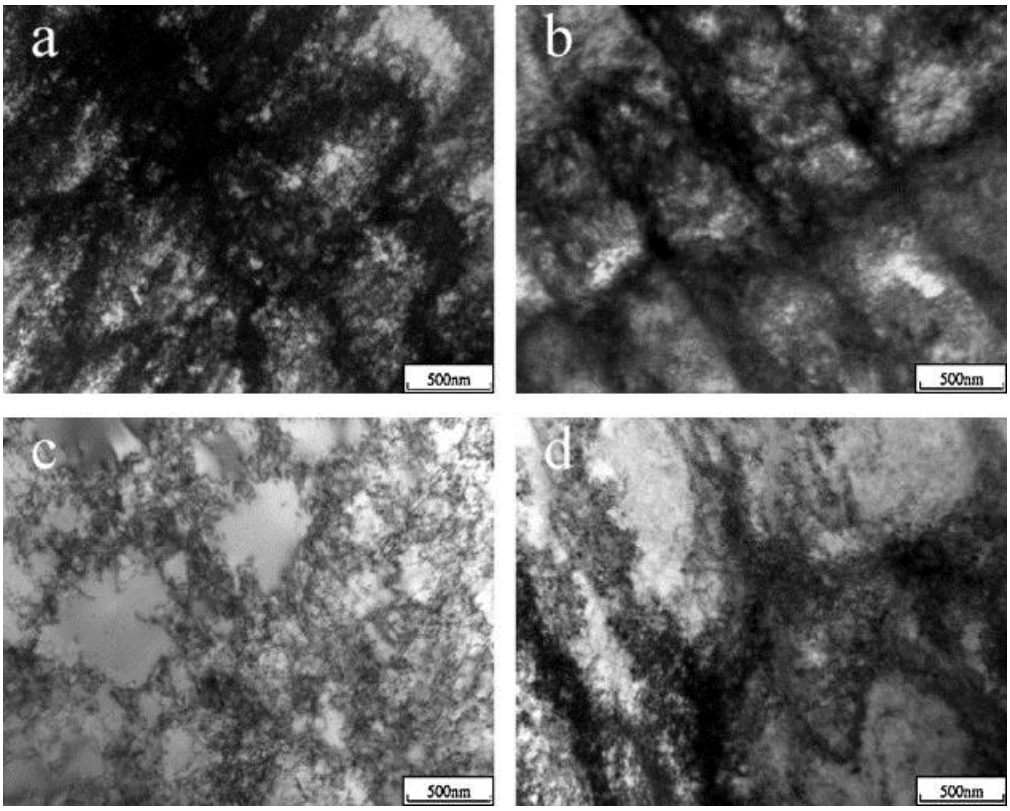

Fig.18. Dislocation substructures of 0.15 pre-strained 304L stainless steel deformed at: (a) 300 ℃, $\dot{\varepsilon}$=2000 s^{-1}; (b) 300 ℃, $\dot{\varepsilon}$=6000 s^{-1}; (c) 800 ℃, $\dot{\varepsilon}$=2000 s^{-1}; (d) 800 ℃, $\dot{\varepsilon}$=6000 s^{-1}[169].

Li et al. [171] observed pin-like deformation twins in the microstructure of TWIP steel after high strain rate deformations. Podurets et al. [172] reported that the deformation twins in copper were grouped into packets with widths of 2 to 15μm when certain threshold values of pressure (20GPa) and strain rate (>10^6 s^{-1}) were exceeded. Below these thresholds, the deformation twins were more

uniformly distributed in the matrix. Ahmed et al. [165] investigated the strain rate dependence of mechanical twinning in a metastable titanium alloy and found that the volume fraction of twins increased with increasing strain rate as the higher density and faster movement rate of dislocations induced by high strain rates will assist the nucleation and propagation of twins.

For HCP structured materials, the influence of strain rate on twinning activity is more pronounced and complicated than BCC and FCC structured materials. In the Mg AZ31 alloy, $\{10\bar{1}2\}$ extension twin nucleation and propagation were reported to be dramatically enhanced at high strain rates [170]. In pure titanium, $\{11\bar{2}4\}$ twinning, absent in quasi-static conditions, was activated in high strain rate deformations [173]. In experiments conducted on commercial pure titanium [174], the volume fraction of $\{11\bar{2}2\}$ twinning increased with increasing strain rate while the volume fraction of $\{11\bar{2}1\}$ twinning decreased slightly. This twin-type selection behaviour was attributed to the twinning energy and short time of deformation. The enhanced twinning activity in HCP structured materials at high strain rates can not only accommodate plastic strain but also affect texture evolution. For example, the activation of the $\{10\bar{1}2\}$ extension twins in HCP structured materials, such as the Ti-6Al-4V alloy [175], pure titanium [175] and Zr [176], reorients the c-axis by 94.8 ° and therefore result in a direct change of the (0001) texture. In addition, the matrix reorientation by twinning will also change the tendency for the activation of slip systems. Wang et al. [174] suggested that as the grains around the $\{10\bar{1}2\}$ extension twin have a high Schmid factor for $\{10\bar{1}1\}$ $<11\bar{2}3>$ slip system, an increase in the volume fraction of $\{10\bar{1}2\}$ extension twinning will stimulate more extensive activation of this slip system in deformed samples.

Furthermore, the review on the influence of strain rate on substructure evolution by Gray et al. [177] concluded that dislocation slip and deformation twins are two competing deformation modes and the latter form more readily as temperature decreases or strain rate increases. Also, the high stresses and dislocation jog movement, enhanced by high strain rates during shock loading, will lead to an increased production of point defects in the matrix.

2.5.2 Adiabatic Shear Band

Adiabatic shear band (ASB), firstly observed by Zener and Hollomon [178] in steels in 1944, is an important deformation mode mainly occurring under high strain rate deformations. Materials may crack at the site of shear bands with low ductility once the shear bands forms [179-183]. During high strain rate deformations, the heat generated by plastic deformation fails to dissipate thus the elevated temperature will contribute to outweigh thermal softening effects over that of strain and

strain rate hardening, which leads to the initiation of shear localization. Because of their low strain hardening rates and poor thermal conductivity, titanium alloys are recognized to be very susceptible to adiabatic shear bands [184, 185] and an optical image of an adiabatic shear band in the Ti-6Al-4V alloy is shown in Fig.19. Most studies on the ASBs in titanium alloys focus on Ti-6Al-4V [186-189] and commercially pure titanium [190, 191] and few focus on β-Ti alloys. In this section, we do not focus on any specific metals or alloys in order to give a complete perspective of ASB formation.

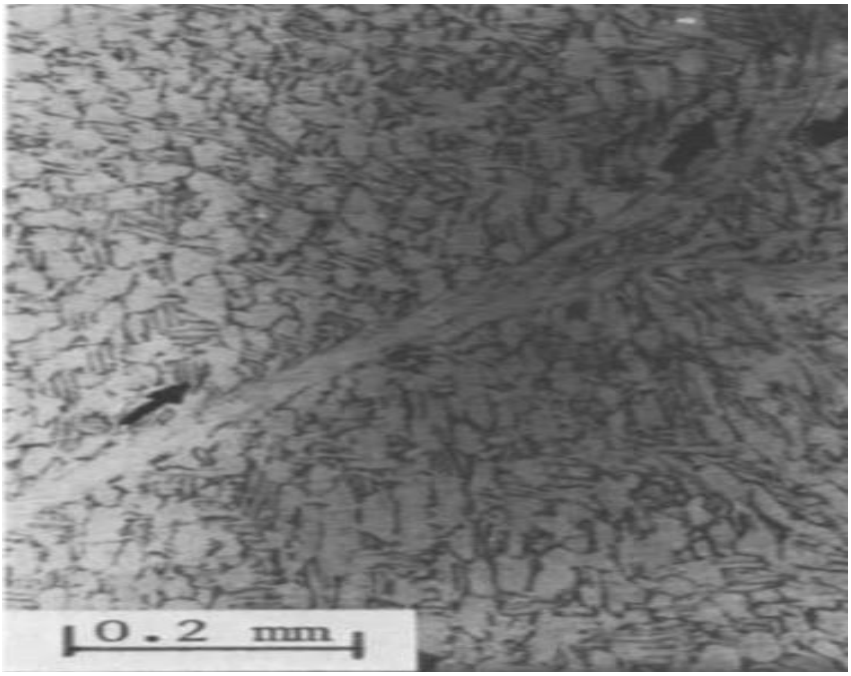

Fig.19. Optical micrograph of an adiabatic shear band in Ti-6Al-4V [192].

As adiabatic shear bands lead to the catastrophic failure of materials, the criterion for the occurrence of shear bands has aroused the interest of researchers in order to design strategies to mitigate their effects. Xu et al. [193] summarized their experimental results and concluded that both a critical strain and strain rate is required for band formation. They cited Roger's [194] words to explain that ''large strain can be achieved quasi-statically in steel without transformed band formation; hence, provided that a minimum strain is achieved, there must exist a strain rate above which the removal of heat from the region of deformation is sufficiently limited that the temperature can rise above that needed for transformation to occur-at a critical strain rate.'' In Ref. [118], the results indicated that the tendency toward adiabatic shearing increases with increasing strain rate and reducing temperature. Boakye et al. [195] conducted systematic observations of the evolution of ASBs with different impact momentum (strain rate/strain) and concluded that the shear band structure evolved gradually and became more defined with increasing strain rate/strain. Aside from strain, strain rate and temperature, the initial microstructure of the materials under impact also have great influence on the formation of ASBs. Lee et al. [129] found that "the nucleation and formation of the shear

band were influenced significantly by the initial microstructure and hardness of the matrix material". In Refs [196, 197], the experiments on steels with different microstructures indicate that for the same strain rates, different microstructures in the same kind of alloy will lead to different degrees of susceptibility to ASBs. It was explained that the presence of defects like second-phase particles, precipitates or other inhomogeneity in the microstructure of metallic materials can increase their susceptibility to strain localization and formation of ASBs. Similar studies conducted by Boakye et al. [198] also confirms that "the initiation of ASBs in AISI 4340 steel during impact occurs when the microstructure is highly inhomogeneous".

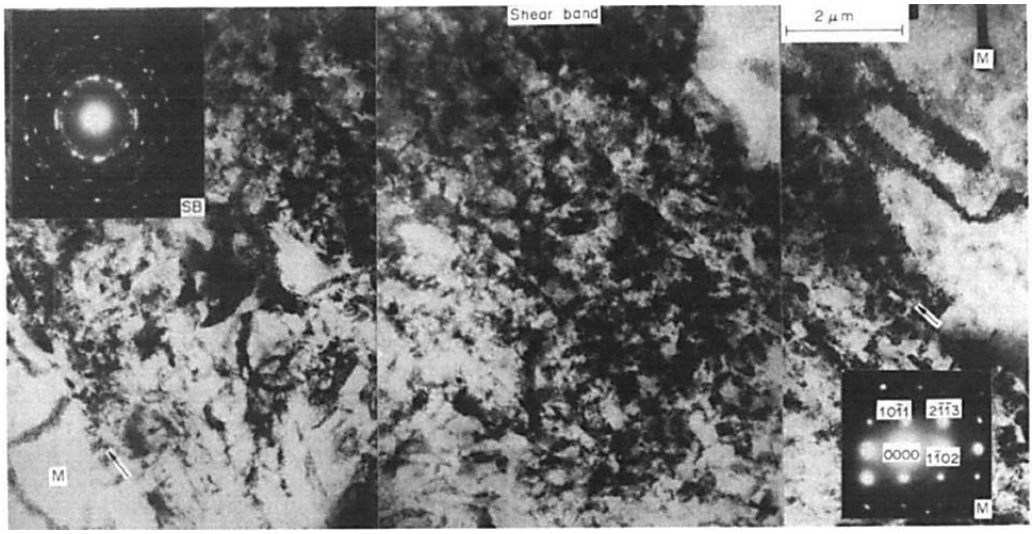

Fig.20. High-voltage electron micrograph showing an adiabatic shear band bounded by the matrix (M) in commercial pure titanium (The black arrows represent boundaries) [199].

In the past thirty years, many studies have been conducted on the microstructure of adiabatic shear bands in different metals and alloys. Early in 1983, Mebar et al. [192] studied adiabatic shearing in four types of Ti-6Al-4V alloys with different microstructures and concluded that all the observed shear bands have the same microstructure which consists of fine transformation products with arbitrary orientations. Meyers et al. [199] characterized the microstructure within the shear band and adjoining matrix in commercial pure titanium using transmission electron microscopy (TEM) as shown in Figure 20. Sharp boundaries and well-defined small grains can be observed within the shear bands. Andrade et al. [200] investigated the microstructural evolution of copper deformed at high strain rates by showing a sequence of TEM micrographs and corresponding diffraction patterns from different positions near or inside the shear band as shown in Figure 21. It was concluded that towards the centre of the shear band, the elongated dislocation cells break down and are replaced by fine equiaxed grains. Nasser et al. [201] and Meyers et al. [106] reached a consensus that in high-strain-rate deformed tantalum, the microstructure changes from the vicinity of shear bands to the

centre of shear bands in the following order; arrays of dislocation lines, dislocation groupings, formation of elongated dislocation cells and subgrains, and recrystallized micro-grains. As TEM can only observe a limited area of microstructure, electron backscatter diffraction (EBSD) has been applied to characterize the microstructure within ASBs in the past decade [202-205]. A series of EBSD maps of the adiabatic shear bands in Ti-6Al-4V specimens are shown in Figure 22 [204].

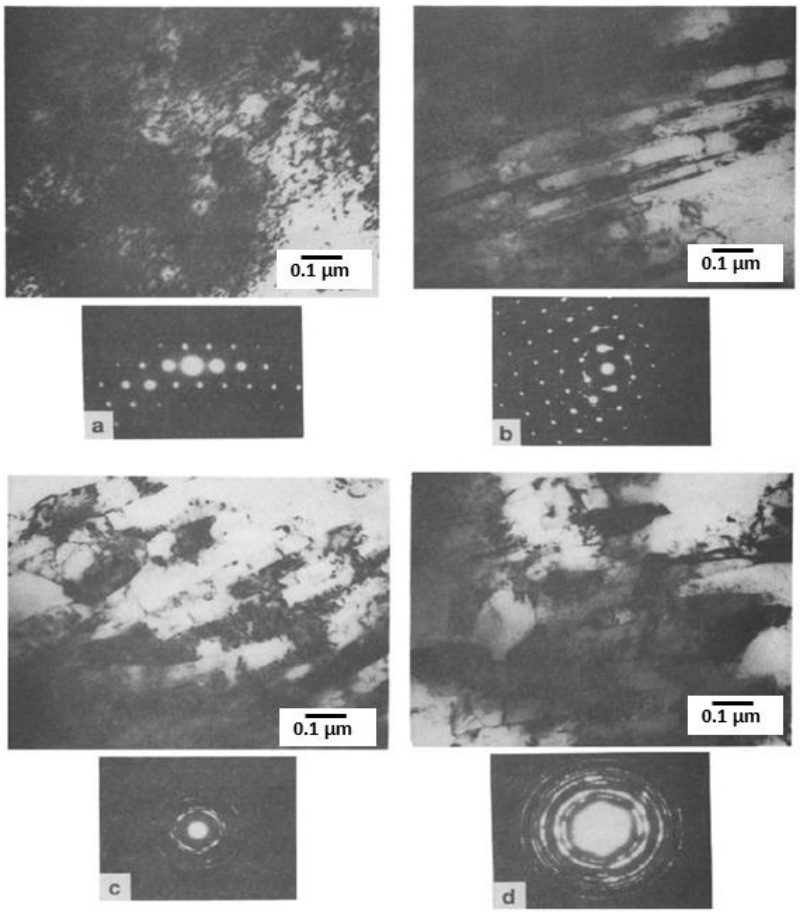

Fig.21. Transmission electron micrographs and diffraction patterns from specimen of copper subjected to shear strain of 5: (a) region outside shear localization area; (b) region adjacent to shear localization area; (c) region at onset of shear localization area; (d) region at centre of shear localization area [200].

In 2000, Meyers et al. [206] proposed a sequence of events that may occur to form the microstructure within ASBs as shown in Figure 23. With increasing strains, randomly distributed dislocations will firstly interact with each other to form elongated cells. Then these cells will rearrange into subgrains as misorientation increases. Eventually the subgrains will be refined to form equiaxed micrograins. This process has been accepted extensively. In the past decade, a sequence of experiments has been conducted on the microstructural evolution in the shear bands of titanium alloys formed under high strain rate deformations [142, 207, 208] and the observed

phenomena agreed well with the model proposed by Meyers et al. [206]. In general, the ASBs in titanium alloys are tens of microns wide. Elongated cell structures (0.2-0.5μm wide) with thick dislocation walls are located near the boundaries and micrograins (0.05-0.2μm wide) with low dislocation density towards the centre.

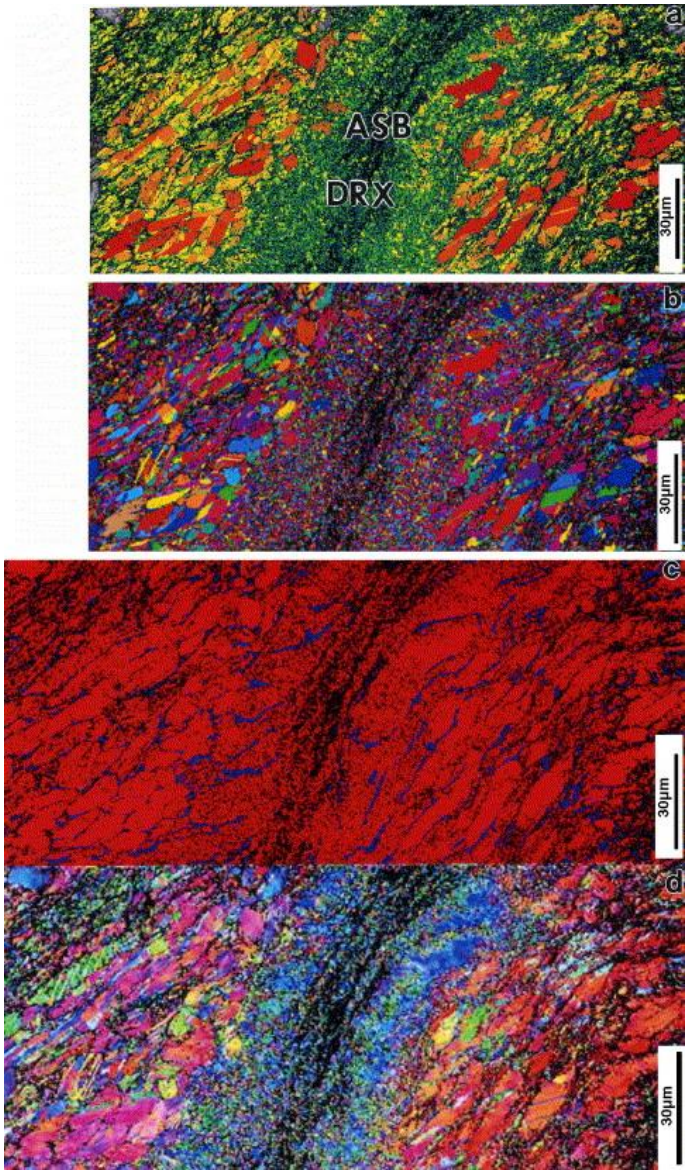

Fig.22. EBSD images of an ASB in Ti-6Al-4V specimen: (a) and (b) show grain-color maps. The black striations at the ASB center represent grains sizes below the resolution limit. (c) Phase map. Red represents α-phase grains, blue β-phase. Black represents grains below the resolution limit. (d) Orientation map. Same colors are the same orientation. Black represents grains below the resolution limit. (For interpretation of the references to color in this figure legend, the reader is referred to the web version of the article.) [204].

In the investigations of microstructural evolution within ASBs, the formation mechanism of micro-

grains in the centre of shear bands has attracted a significant attention from researchers. Xue et al. [209] suggested that twinning plays a critical role in the formation of micro-grains in stainless steels. On the basis of the TEM results, it is surmised that "secondary twins directly led to the formation of elongated subgrains. Microtwins inside shear bands promoted division and break-down of the subgrains, which further refined microstructures [209]" as plotted in Figure 24. For HCP and FCC structured metals and alloys, twin intersections have been reported to play an important role in the formation of ASBs [210-212]. The recrystallization mechanism is much more frequently used to explain the formation of micrograins. Early in 1986, Meyers et al. [5] concluded that the recrystallized grains within shear bands of titanium should occur during the process of plastic deformation and also pointed out that some types of grain-boundary sliding mechanism might be operational in this process. The study of Hines and Vecchio [90] confirmed that the recrystallized grains in the shear bands of copper should be attributed to dynamic recrystallization because the kinetics of static recrystallization mechanisms are too slow. After 2000, researchers focused on answering two questions: "(1). do the observed recrystallization features occur during or after plastic deformation? (2). what is the mechanism of recrystallization? [206]" The calculation and modelling in studies conducted by Meyers et al. [206] excluded the probability of migrational dynamic recrystallization and strongly supported a rotational dynamic recrystallization mechanism [199]. It was surmised that the broken down subgrains transfer to recrystallized micrograins through diffusive rotation of grain boundaries, which is driven by reduction in interfacial energy.

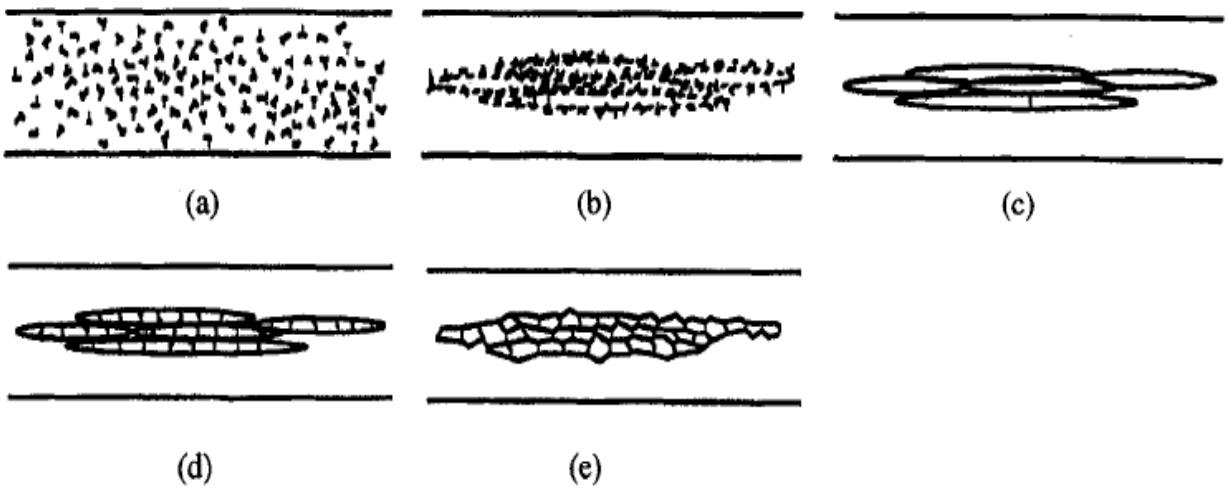

Fig.23. Schematic illustration of microstructural evolution during high-strain-rate deformation. (a) Randomly distributed dislocations; (b) Elongated dislocation cell formation (i.e. dynamic recovery); (c) Elongated subgrain formation; (d) Initial break-up of elongated subgrains; and (e) Recrystallized microstructure [206].

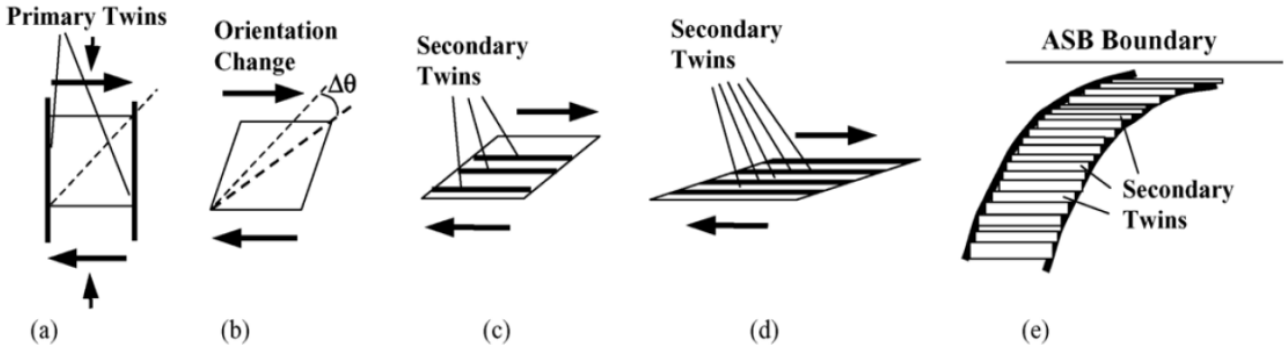

Fig.24. The formation mechanism of substructure though secondary twin multiplication (a) a typical unit area sandwiched by two primary twin boundaries and (b)continuous shear deformation changes the crystalline orientation. (c) The shear stress and the continued crystalline rotation activate some twin systems and (d) more twin systems are activated and aligned in the same direction as the shear band. (e) A saturation of secondary twins near a shear band [209].

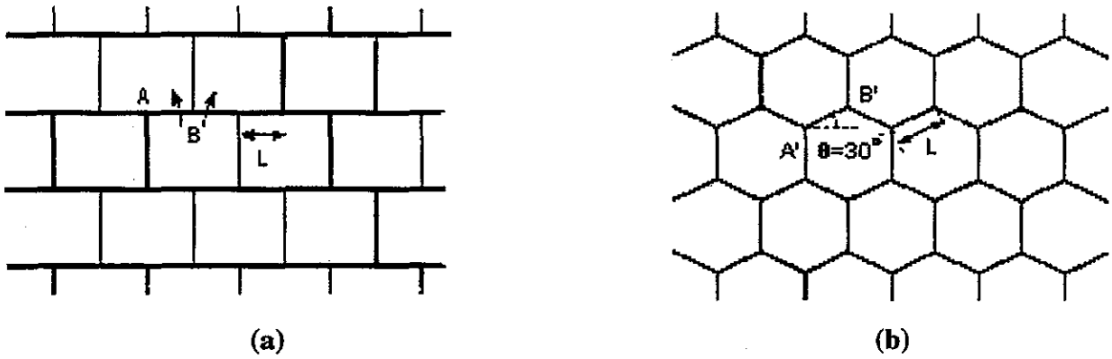

Fig.25. Rotation of grain boundaries leading to equiaxed configuration: (a) broken down subgrains; (b) rotation of boundaries [206].

The rotation process is shown in Figure 25. A large number of results from experiments in the last decade support the rotational recrystallization mechanism: Yang et al. [10-12] validated the availability of the rotational recrystallization mechanism based on kinetic calculations and estimated the peak temperature in the centre of shear bands of titanium alloys deformed at high strain rates. Tang et al. [213] and Zou et al. [214] also attributed the formation of ultrafine grains in copper and zirconium alloys at high strain rates to rotational dynamic recrystallization. Another similar mechanism named progressive subgrain misorientation (PrisM) was proposed by Hines and Vecchio [215]. In PrisM, recrystallized grains "occur by the formation and mechanical rotation of subgrains during deformation, coupled with boundary refinement via diffusion during shear band cooling [215]". The distinct textured equiaxed grain structure within the adiabatic shear bands along with aligned elongated subgrains and grains in hot rolled interstitial-free steels observed by Lins et

al. [216] support PriM. Though the rotational recrystallization mechanism has been widely used to explain recrystallization in the shear bands, the exact roles played by temperature and mechanical assistance in the formation of micrograins is still unclear due to the limited experimental data and knowledge. Temperature seems to play an important role as proved by Nasser et al. [201] and Meyer et al. [106] in the high-strain-rate deformed tantalum. They observed that when temperature was below 0.4-0.5 of the melting temperature of tantalum, dynamic recovery occurred within the shear bands instead of dynamic recrystallization. As mentioned by Rhim et al. [217], most researchers defined the critical dynamic recrystallization temperature as 0.4-0.5 of the melting temperature of metals and then tried to determine whether the peak temperature within the shear band can reach this level. However, Hines and Vecchio [13] found that the role of temperature seemed less important in the formation of shear bands as the calculated peak temperature within the shear bands of copper is less than the expected recrystallization temperature. Nesterenko et al. [218] also noted that rotational recrystallization is primarily caused by dislocation reorganization and does not require temperatures on the order of one-half the melting temperature. The coupled effects of temperature and mechanical assistance require further investigation.

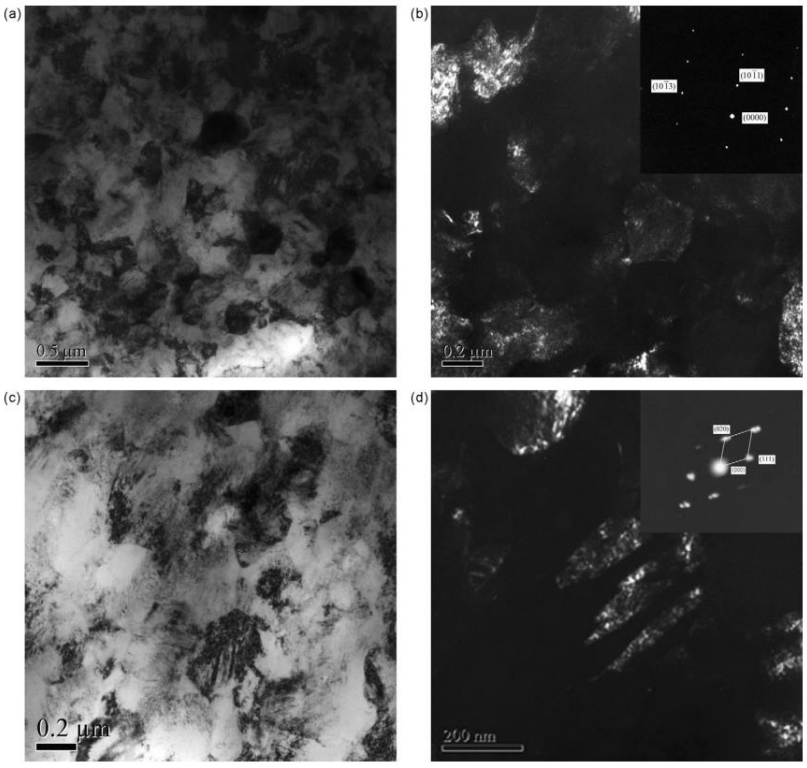

Fig.26. TEM micrographs and SAD patterns showing the microstructure in the centre of shear band in TC 16 alloy: (a) and (b) are the bright field images of the microstructure in the centre of a shear band and (c) and (d) are the dark field images and their corresponding SAD patterns showing α-phase and α''-phase in (a), respectively [208].

In addition to dynamic recrystallization, phase transformation is another phenomenon that may occur along with the formation of adiabatic shear bands. α′ martensitic phase transformation has been observed in the shear bands in stainless steel [219] and Fe-Cr-Ni single crystals [220]. Similar phase transformations have also been observed in adiabatic shear bands of titanium alloys. In the experiments conducted by Bayoumi et al. [221] , X-ray diffraction techniques identified that a non-diffusional phase transformation occurred, leading to the loss of β structure in the shear bands of the Ti-6Al-4V alloy. It is reported that β phase with BCC structure transformed into α″ phase with orthorhombic structure within the shear bands of the TC16 alloy [208] and the Ti-5Al-5Mo-5V-1Cr-1Fe alloy [222] and the corresponding selected area diffraction is shown in Figure 26 [208]. Yang et al. [142] firstly observed β-to-ω transformation in the Ti-1300 alloy and confirmed that the high alloy content of this alloy, necessary thermodynamic and kinetic conditions contribute to this kind of phase transformation. Though Timothy et al. [223] reported that there was no clear evidence to suggest that martensitic transformation occur in the shear bands of the Ti6Al4V alloy, it was proved that the peak temperature within the shear bands reached the β transus and lasted tens of microseconds. Me-Bar et al. [192] reported that the temperature elevation induced by adiabatic heating within shear bands can lead to transformations from α phase to β phase in the Ti6Al4V alloy. Also, the cooling rate of materials within shear bands can be as high as 10^7 s^{-1} [192], which is consistent with calculations in later studies [10,12]. It is widely accepted that this extreme temperature history offers necessary thermodynamic and kinetic conditions for martensitic transformation to occur in the adiabatic shear bands in titanium alloys.

The temperature elevation within adiabatic shear bands concomitant with the tensile stress perpendicular to the shear face contributes to the initiation of voids. Me-Bar et al. [192] found that there were two shapes of voids within adiabatic shear bands, namely spherical and elliptical. It is summarized that the shape of voids depends on the state of materials when the tensile stress is applied. When the material in shear bands is melted, voids will be spherical while if it is just softened the voids will be elliptical. This view was supported by Lee et al. [129, 141] and the voids and cracks in shear bands observed by Lee et al. are shown in Figure 26**.** They [129, 141] also described the process of the formation of cracks. The width of voids will increase until they reach the thickness of the shear band. Then the voids begin to coalesce and extend along the shear band to form cracks. Zhang et al. [224] reported that the temperature rise in adiabatic shear bands contributed to the generation of voids and the voids will transform into elongated dimples. This explains why dimples are dominant on the fracture surface with low ductility under the condition of high strain rates.

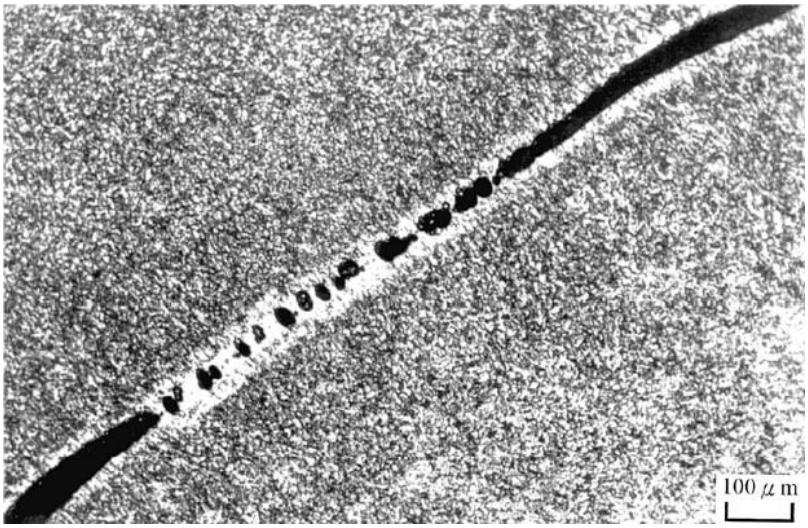

Fig.27. Voids and cracks in an adiabatic shear band of a Ti-6Al-4V specimen deformed at 700 ℃ at 2×10^{3} s^{1} [138].

2.6 Summary of the Literature Review and Research Gaps

Some conclusions can be summarized based on the literature review:

1. β titanium alloys have been shown to be promising in aircraft structural and biomedical applications due to their extraordinary properties such as an excellent combination of strength and fracture toughness, low Young's modulus and good biocompatibility.
2. Hopkinson Split Pressure Bar testing is the most widely applied laboratory method for the systematic investigations of the high-strain-rate response of materials to date despite limitations in the highest strains which can be reached in experiments.
3. Factors such as the crystalline structure, matrix phase stability and stacking fault energy of materials will influence the deformation mechanisms activated during high strain rate deformations and therefore affect the dynamic response of materials to high strain rates at room and elevated temperatures.
4. Among the reported constitutive models, the Johnson-Cook model and Zerilli-Armstrong model are the two most widely used and can easily be applied to commercial finite element code. Some modifications have been made to the models in order to make them more accurate and valid.
5. Precipitation, stress-induced phase transformation and substructure evolution occurred in materials during high strain rate deformations are influenced by strain rate and temperature. Adiabatic shear band is an important microstructural feature mainly occurring under high

strain rate deformations and is closely related to cracking of materials. A large number of studies have been conducted on the microstructures within adiabatic shear bands and their corresponding formation mechanisms.

Research gaps identified based on the literature review are also summarized as follows:

1. The dynamic response of β titanium alloys to high strain rates at room and elevated temperatures has not been systematically investigated.
2. β phase stability will affect the deformation mechanisms activated in β titanium alloys during the deformations at quasi-static strain rates. However, its influence on the dynamic behaviour of β titanium alloys at high strain rates has not been investigated.
3. The constitutive models which can be applied to commercial finite element code should be established for β titanium alloys and their reliability should be tested and analysed.
4. The microstructural evolution in β titanium alloys during high strain rate deformations should be investigated and related to the stress-strain behaviour of the alloys.
5. The microstructures within the adiabatic shear bands in β titanium alloys require investigations and the formation mechanisms of the microstructures within shear bands need to be understood.

Chapter 3

The Papers

3.1 Overview of the Papers

The current work was conducted to gain a better understanding of the dynamic response of β titanium alloys to high strain rates at room and elevated temperatures. Two new types of β titanium alloys with different levels of β phase stability were selected. One is the Ti-6Cr-5Mo-5V-4Al (Ti6554) alloy developed for heavy section structural aerospace applications. This alloy is optimized to provide high levels of strength and toughness based on the similar composition to the Ti-5Al-5Mo-5V-3Cr (Ti5553) alloy which has been applied to the manufacture of the landing gear for Airbus. The Mo_{eq}, a measure of β phase stability, of the Ti6554 alloy is calculated to be ~16. The other alloy is the Ti-25Nb-3Zr-3Mo-2Sn alloy developed for biomedical applications. The Mo_{eq} for this alloy is calculated to be ~10, indicating significantly lower β phase stability relative to the Ti6554 alloy.

In this research, the hot rolled rods of the Ti6554 and Ti-25Nb-3Zr-3Mo-2Sn alloys were solution treated in a protective Argon atmosphere for 1 h at 1100K and 1023K, respectively. After being solution treated, the Ti-25Nb-3Zr-3Mo-2Sn rods were water quenched while the Ti6554 rods were air cooled. An extra aging heat treatment was conducted on the Ti6554 rods at 833K for 8 h followed by air cooling. Individual cylindrical specimens were cut from these rods using electrical discharged machining. The dimension of the cylindrical specimens was ϕ5mm×4mm for the Split Hopkinson Pressure Bar (SHPB) tests. To diminish the effects of texture in the hot rolled rods on the deformation behaviour of materials, all specimens were taken from the rods along the rolling direction. Quasi-static compressive tests were performed using an Instron hydraulic testing machine and high strain rate compressive tests were undertaken using a SHPB machine. The details of the experiments are covered in the corresponding papers.

In Paper 1, the stress-strain behaviour and microstructural evolution of the Ti6554 alloy deformed at high strain rates ranging from $10^3 s^{-1}$ to $10^4 s^{-1}$ and temperatures ranging from 293K to 1173K were investigated. It is the first time that the dynamic behaviour of a β titanium alloy has been studied systematically over such a wide range of strain rates and temperatures. According to the microstructures observed in the deformed specimens, dislocation slip was proposed as the dominant deformation mechanism for the Ti6554 alloy during high strain rate deformations. Therefore, the influence of strain rate and temperature on the flow stress behaviour of the Ti6554 alloy was evaluated on the basis of dislocation mechanics. The influence of adiabatic heating on the strain hardening was emphasized. Furthermore, features with string-like morphologies were observed in

the Ti6554 alloy under specific conditions along with adiabatic shear bands. The potential correlation between this feature and shear localization was also discussed.

The microstructures within the adiabatic shear bands observed in Paper 1 and their corresponding formation mechanism were further investigated in Paper 2. A high degree of grain refinement was observed by TEM in the adiabatic shear bands, which results in significant increase in the hardness within the shear bands as reported in Paper 1. The grain refinement process was inferred by the TEM observations of morphologies and misorientations of substructures at different locations across the shear bands. The role played by dislocation movement and dynamic recovery was discussed in detail. The Rotational Dynamic Recrystallization (RDRX) mechanism was adopted to explain the occurrence of recrystallized nanograins in the core region of the shear bands. Calculations of the kinetics were also undertaken to explore the function of RDRX mechanism.

In Paper 3, two phenomenological constitutive models, the Johnson-Cook (JC) model and a modified Zerrilli-Armstrong (ZA) model were adopted to predict the flow behaviour of the Ti6554 alloy based on the stress-strain curves obtained by SHPB tests in Paper 1. As microstructural changes, including the features of string-like morphologies and adiabatic shear bands, did not significantly affect the flow behaviour of the Ti6554 alloy, they were neglected in the constitutive modelling in order to simplify the establishment of constitutive models. Detailed procedures for the establishment of the JC model and modified ZA model were described in Paper 3. The stress-strain curves for conditions not used in the fitting process were employed to validate the reliability of the obtained constitutive models. Both the JC model and modified ZA model are found to be effective in predicting the stress-strain behaviour of the Ti6554 alloy at high strain rates. The efficiency and deficiency of these two models were also discussed in detail. The parameters obtained for the JC model in Paper 3 have been applied to finite element simulations of laser-assisted machining of the Ti6554 alloy and have proven to be effective in this capacity (Appendix).

The first three papers focused on a β titanium alloy with relative high β phase stability. It can be inferred that for the β titanium alloys with similar or higher Mo_{eq} values to that of the Ti6554 alloy, dislocation slip will be the dominant deformation mechanism even at very high strain rates due to their very stable β matrix phase and their mechanical properties can be mainly engineered by controlling the size, morphology and distribution of precipitates through heat treatment or hot deformation. As microstructural changes occurred during deformation over the range of testing temperatures and strain rates did not significantly affect the flow behaviour of the Ti6554 alloy in

this research, empirical models such as the JC model and modified ZA model were shown to be effective in describing the stress-strain behaviour of the Ti6554 alloy.

In Paper 4, the deformation mechanisms and strain rate sensitivity of the Ti-25Nb-3Zr-3Mo-2Sn alloy were studied. Microstructural characterization and stress-strain curve analyses were conducted for the Ti-25Nb-3Zr-3Mo-2Sn alloy deformed at $10^{-3}s^{-1}$ and $10^{3}s^{-1}$ at ambient temperatures. Based on the microstructural observations multiple deformation mechanisms were activated simultaneously to accommodate the plastic strain at both quasi-static and high strain rates. Unlike the Ti6554 alloy, the influence of adiabatic heating on the strain hardening rate of the Ti-25Nb-3Zr-3Mo-2Sn alloy was marginal. One potential reason for this is that the temperature increase induced by adiabatic heating after the high strain rate deformation of the Ti-25Nb-3Zr-3Mo-2Sn alloy was only 38 K, which is obviously lower than that for the Ti6554 alloy (~100K) for a similar strain rate and strain. Another factor is that the main deformation mechanism in the Ti-25Nb-3Zr-3Mo-2Sn alloy is {332} <113> mechanical twinning, which is relatively insensitive to the strain rate.

Paper 5 investigated the dynamic response of the Ti-25Nb-3Zr-3Mo-2Sn alloy at room and elevated temperatures. The strain rate employed in the research was 10^{3} s^{-1} and temperatures were 293K, 573K and 873K. To the authors' best knowledge, this is the first time that a Ti-Nb based β titanium alloy has been systematically studied at high strain rates over a wide range of temperatures. Though it was already reported in Paper 4 that the strong strain hardening rate exhibited by the Ti-25Nb-3Zr-3Mo-2Sn alloy in high strain rate deformation at 293K is caused by the intensive mechanical twinning, the hardening effect induced by the mechanical twinning was quantitatively analysed in Paper 5. One important inference proposed in Paper 5 is that thick twins cannot produce significant hardening, which was supported by the aid of a physical argument. The variations in the deformation mechanisms activated in the Ti-25Nb-3Zr-3Mo-2Sn alloy with temperatures were analysed. Furthermore, the influence of mechanical twinning on the strain hardening behaviour of the Ti-25Nb-3Zr-3Mo-2Sn alloy at high strain rates at elevated temperatures was discussed. Yield behaviour and texture development were related to the deformation mechanisms activated during plastic deformation.

The combined results from Papers 1, 4 and 5 demonstrated that β phase stability has a significant influence on the microstructural evolution and flow behaviour of β titanium alloys during high strain rate deformation. Compared to the Ti6554 alloy, the Ti-25Nb-3Zr-3Mo-2Sn alloy is less stable and the deformation mechanisms active under different conditions (strain rate, temperature and strain) are more complicated. On the one hand, the Ti6554 alloy exhibited much higher strength

due to its aged microstructure. On the other hand, the Ti-25Nb-3Zr-3Mo-2Sn alloy exhibited a much stronger strain hardening rate at high strain rates due to the dynamic Hall-Petch effect induced by extensive mechanical twinning. In addition, parameters for empirical constitutive models for applications in finite element simulations were not calculated for the Ti-25Nb-3Zr-3Mo-2Sn alloy in this research as the influence of strain rate, temperature and strain on the flow behaviour of the Ti-25Nb-3Zr-3Mo-2Sn alloy is too complicated and different deformation mechanisms may be activated under different deformation conditions.

PAPER 1

The dynamic response of a β titanium alloy to high strain rates and elevated temperatures

Hongyi Zhan, Damon Kent, Gui Wang, Matthew S. Dargusch

Materials Science and Engineering A

2014, Volume 607, Pages 417-426

The Dynamic response of a β titanium alloy to high strain rates and elevated temperatures

Hongyi Zhan[a,*], Damon Kent[a], Gui Wang[a,b], Matthew S. Dargusch[a,b]

[a]Queensland Centre for Advanced Materials Processing and Manufacturing (AMPAM), School of Mechanical and Mining Engineering, The University of Queensland, Brisbane, QLD 4072, Australia

[b]Defence Materials Technology Centre, The University of Queensland, Brisbane, QLD4072, Australia

*h.zhan@uq.edu.au

Abstract

The stress-strain behaviour and microstructural evolution of the Ti-6Cr-5Mo-5V-4Al (Ti6554) alloy was systematically investigated using Split Hopkinson Pressure Bar (SHPB) tests over a wide range of strain rates from 1000 s^{-1} to 10000 s^{-1} and initial temperatures from 293K to 1173K. Dislocation slip is the main deformation mechanism for plastic flow of the Ti6554 alloy at high strain rates. The flow stress increases with increasing strain rate and decreasing temperature. Also the flow stress is more sensitive to temperature than to strain rate. For high strain rate deformations, the strain hardening rate is found to be negative at 293K and increases with increasing temperatures. Flow softening observed at 293K is potentially caused by adiabatic heating. The increment in the strain hardening rate with increasing temperatures may be the result of interactions between thermally activated solute Cr atoms and mobile dislocations. When the temperature is raised to 873K, a novel α precipitate morphology consisting of globular α aligned in strings was observed in specimens deformed at strain rates of 4000 and 10000 s^{-1}. It has hardening effects on the β matrix and is purported to nucleate on dislocations introduced by the high strain rate deformation. Adiabatic shear bands were observed in specimens deformed at higher temperatures (873K). The microstructure inside the shear bands is harder than that outside of the shear bands in the Ti6554 alloy.

Key Words:

Titanium alloys; Precipitation; Shear bands; Split Hopkinson Pressure Bar; Flow softening

1. Introduction

Beta titanium alloys have been developed for use in large section structural aerospace components due to their high hardenability and improved forgeability [2, 9, 225, 226]. The Ti-6Cr-5Mo-5V-4Al (Ti6554) alloy is a newly-developed metastable beta alloy which has an excellent combination of strength and ductility. An ultimate tensile strength (UTS) of around 1250MPa and fracture toughness (KIC) from 80 to 90 MPa $m^{1/2}$ can be obtained for the Ti6554 alloy through proper solution and aging heat treatments [28, 29]. Under quasi-static conditions, the dominant deformation mechanism for β titanium alloys will change from stress-induced martensitic transformation to twinning to dislocation slip with increasing levels of β phase stability [54, 64, 65]. Due to its relative high stability, the main deformation mode for the Ti6554 alloy under the quasi-static conditions is dislocation slip. In order to understand and optimize the mechanical properties of the Ti6554 alloy through controlling the microstructure, Li et al. and Pinghui et al. have investigated the relationship between microstructures and tensile properties of the Ti6554 alloy [227, 228]. Kent et al. have investigated the influence of aging temperature and heating rate on the mechanical properties and microstructure of the Ti6554 alloy [229]. In general, the published information on the Ti6554 alloy is limited and no one has investigated its mechanical properties and microstructure evolution over a wide range of strain rates and temperatures. However, processing technologies involving hot forging, machining and extrusion employ high strain rates even over 1000 s^{-1}. Under conditions of ballistic impact, the strain rate for the deformation of the target can be as high as 10^6 s^{-1}. Therefore, it is important to understand, evaluate and predict the dynamic response of β titanium alloys over a wide range of strain rates and temperatures.

The response of metals at high strain rates is quite different to that of quasi-static deformation. Over the past decade, researchers have investigated the dynamic response of various metals under the conditions of strain rates ranging from 10^{-3} to 10^4 s^{-1} over a wide range of temperatures. It was observed that the dependence of flow stress on strain rate and temperature is material-dependent. For most metals the flow stress increases with increasing strain rate but decreases with increasing temperature. However, for TWIP steel [171] and some aluminium alloys [230], flow stress is mildly sensitive or essentially insensitive to the strain rate. In addition, a strain rate softening behaviour was observed for a kind of high manganese steel in the range of ~500-1700 s^{-1} [231]. Khan et al. [133], Nemat-Nasser et al. [132], Hokka et al. [134] and Lee et al. [85, 118, 129] have done similar dynamic experiments on titanium alloys and observed that the flow stress is sensitive to high strain rates and elevated temperatures. For the Ti6Al4V [129] and Ti15Mo5Zr3Al [85] alloys, it was observed that the flow stress is more sensitive to temperature than strain rate. In addition, when

dynamic strain aging (DSA) occurs, the flow stress will increase with increasing temperature. DSA is caused by the interaction between moving dislocations and mobile point defects and appears at certain combinations of strain rate and temperature. Nemat-Nasser and his colleagues have observed DSA in commercially pure titanium [130] and Ti-6Al-4V [132]. It is concluded that DSA becomes more pronounced with further straining and less pronounced with increasing strain rate.

It is generally accepted that the volume fraction, distribution and morphology of α phase precipitates will have effects on the mechanical properties of β titanium alloys. The Ti6554 alloy is able to be strengthened by large numbers of uniformly distributed fine lath-like α precipitates formed through solution and aging heat treatment at suitable temperatures [229]. The strain, strain rate and temperature during dynamic testing can have effects on the volume fraction, distribution and morphology of α precipitates. Consequently, it is essential to investigate the relationship between the mechanical properties of β titanium alloys and their microstructural evolution over a wide range of strain rates and temperatures. In addition, adiabatic shear bands are an important phenomenon which mainly occurs during high strain rate deformations. Materials may crack at the site of a shear band once the shear band initiates [179-183, 232]. During high strain rate deformations, the heat generated by the deformation fails to dissipate and thus the elevated temperatures cause thermal softening which is dominant over strain and strain rate hardening, leading to the initiation of shear localization. Because of their low strain hardening rate and poor thermal conductivity, titanium alloys are recognized to be very susceptible to adiabatic shear bands [184, 185]. Most studies on the adiabatic shear bands in titanium alloys focus on Ti-6Al-4V and commercially pure titanium and few have focused on β-Ti alloys. As adiabatic shear bands can lead to catastrophic failures, the criterion for their occurrence is of interest such that it can be avoided.

In this work, the stress-strain behaviour of the Ti6554 alloy was investigated under high strain rates ranging from $1000s^{-1}$ to $10000s^{-1}$ and temperatures ranging from 293K to 1173K. The microstructural evolution of the Ti6554 alloy during high strain rate deformations was observed and the correlation between the microstructure evolution and stress-strain behaviour was analysed.

2. Experimental

Hot rolled cylindrical rods of the Ti6554 alloy were solution treated at 1100 K for 1 h in a protective Argon atmosphere and then air cooled. Aging treatments were conducted on the solution treated Ti6554 rods at 833 K for 8 h under ambient atmospheres and then air cooled. The chemical composition of the Ti6554 alloy is shown in Table 1. Individual cylindrical specimens were cut

from rods using electrical discharge machining. The general dimensions of cylindrical specimens were ϕ5 mm × 4mm. For testing at a strain rate of 10^4 s^{-1}, smaller dimensions of ϕ2 ×1.5 mm were required due to equipment limitations. As the aspect ratio is almost the same, the effect of specimen geometry does not affect the experimental results.

The high strain rate tests were achieved using a Split Hopkinson Pressure Bar (SHPB) arrangement at strain rates ranging from 1000s^{-1} to 10000s^{-1} and temperatures ranging from 293K to 1173K. SHPB tests have been extensively used to test the dynamic behaviour of materials at high strain rates ranging from 10^2 to $10^4 s^{-1}$. The apparatus consists of a striker bar, an input (or incident) bar and an output (or transmitted) bar as shown in Fig.1. The specimen is sandwiched between the input and output bar. Once the striker bar impacts the input bar, a pulse referred to as the incident pulse will be created going through the input bar into the specimen. When the pulse reaches the interface between the input bar and the specimen, part of the pulse (reflected pulse) will be reflected back to the input bar while the rest (transmitted pulse) will be transmitted to the output bar through the specimen. These pulses are recorded by strain gages mounted on the bars. The flow stress σ, strain ε and strain rate $\dot{\varepsilon}$ are then calculated using the following equations

$$\sigma = E\frac{A_b}{A_s}\varepsilon_t \tag{1}$$

$$\dot{\varepsilon} = -2\frac{C_0}{L}\varepsilon_R \tag{2}$$

$$\varepsilon = -2\frac{C_0}{L}\int \varepsilon_R \, dt \tag{3}$$

ε_R and ε_t represent the reflected pulse and transmitted pulse, respectively. A_b is the cross-sectional area of the bars, A_s is the cross-sectional area of the specimen and L is the gauge length of the specimen. C_0 is the elastic wave speed in the bars which can be calculated by the equation $\sqrt{E/\rho}$ where E and ρ correspond to Young's modulus and the density of the specimen, respectively.

For the experiments at elevated temperatures, the specimens were heated by an in-situ induction coil and the temperature was regulated by a thermocouple not in contact with the specimen. After heating, the specimen was maintained at the designated temperature for approximately 2 minutes to ensure a uniform temperature distribution. Then the incident and transmitted bars were assembled by a pushing support. The striker bar was launched with the assembly of incident and transmitted bars synchronously to avoid temperature drops in the specimen. The assembly must be completed before the stress wave arrives at the incident bar. The contact time should also be controlled to within 500 ms as the contact between the bars and the specimen will lead to a temperature drop in

the specimen. In order to decrease the friction between the contact surfaces of the bars and specimen, molybdenum sulphide was used as a lubricant. Quasi-static compressive tests were done using an Instron hydraulic testing machine.

Specimens for microstructural observation and X-ray diffraction were wet ground using silicon carbide papers, mechanically polished and ultrasonically cleaned. Specimens for Scanning Electron Microscopy (SEM) were etched using Kroll's Reagent (2% hydrofluoric acid, 6% nitric acid and 92% distilled water). SEM was performed on a XL30 instrument. XRD was conducted on a D8 Advance X-ray diffractometer equipped with a graphite monochromators and a Ni-filtered Cu K_α source. Hardness testing was conducted on polished specimens using a Struers Vickers microhardness testing machine.

3. Results

3.1 Dynamic stress-strain response

The true stress-strain curves of Ti6554 at different strain rates and temperatures are shown in Fig.2. The intense oscillations in the curves at high strain rates are due to the technical limitations of the Split Hopkinson Bar Tests [77]. None of the deformations resulted in fracture hence the ends of the curves represent unloading rather than fracture. The strain hardening rate is pronounced in the stress-strain curve performed under quasi-static conditions as shown in Fig.2a. However, the flow stress at strain rates higher than $1000s^{-1}$ is mildly sensitive to strain. At 293K, stress-strain curves at high strain rates show a negative slope. When the temperature is raised, the slope becomes positive as shown in Fig.2b, c, d. The strain hardening rate increases with increasing temperature for strain rates higher than 1000 s^{-1}. Hokka et al. observed similar strain hardening behaviour in another metastable beta titanium alloy, Ti-15V-Sn-3Al-3Cr [134]. However, when the temperature is raised to 1173K, the stress-strain curve at $4000s^{-1}$ shows an almost zero slope for small strains and a negative slope for strains larger than 0.15. The flow stress of the Ti6554 alloy increases with increasing strain rate and decreasing temperature as shown in Fig.3. It is observed that the effect of temperature on the flow stress is more obvious than that of strain rate for the Ti6554 alloy. In addition, it is observed that the relationship between flow stress and logarithmic strain rate is not linear and flow stress tends to increase to a greater degree beyond a strain rate of 10^3 s^{-1} as shown in Fig.3a.

The dependence of the strain rate hardening and thermal softening effects on the strain rate and

temperature are always quantified by strain rate sensitivity, β, and temperature sensitivity, n_a. The equations to calculate these are listed below:

$$\beta = (\sigma_2 - \sigma_1)/\ln(\dot{\varepsilon}_2/\dot{\varepsilon}_1) \quad (4)$$

$$n_a = \left|\ln\left(\frac{\sigma_2}{\sigma_1}\right)/\ln\left(\frac{T_2}{T_1}\right)\right| \quad (5)$$

In equation (4), stresses σ_1 and σ_2 are obtained from tests conducted at average strain rates of $\dot{\varepsilon}_1$ and $\dot{\varepsilon}_2$ respectively. In equation (5), stresses σ_1 and σ_2 are obtained from tests conducted at temperatures of T_1 and T_2, respectively. For Ti6554, the strain rate sensitivity decreases with increasing temperature as shown in Fig.4a, which is also observed for most other metals [85, 118, 120-122]. The temperature sensitivity of Ti6554 increases with increasing temperature. An important observation is that when the temperature is raised to 1173K, the temperature sensitivity experiences a significant increment. Strain also has effects on the strain rate and temperature sensitivity for the Ti6554 alloy. According to Fig.4, the strain rate sensitivity increases slightly with increasing strain while the temperature sensitivity decreases with increasing strain.

3.2 Microstructural Observation

The undeformed specimens of the Ti6554 alloy are solution treated and aged. According to the XRD analysis shown in Fig.5a, the spectra can be indexed to α and β phases. An image of the microstructure of the undeformed specimen is shown in Fig.5b. It shows the β phase matrix and intragranular clustered α phases. The black areas represent α phase precipitates, which cluster inside the matrix and nucleate along the grain boundaries. The SEM image of the clustered α precipitates inside β grains is shown in Fig.5c. They are mainly composed of a mesh of fine Widmanstätten plates. Similar morphologies of α precipitates have been observed in the Ti-5Al-5Mo-5V-3Cr (Ti5553) alloy aged at 673K or higher temperatures [233].

Optical images of samples deformed at the strain rate of $4000s^{-1}$ by SHPB are shown in Fig.6. Microhardness testing was performed on these samples and results are shown in Fig.6h. It is found that the samples deformed at temperatures from 293K to 873K all exhibit typical aged microstructure for the Ti6554 alloy. Though the volume fraction of clustered α precipitates in the β matrix varies with experimental temperatures, the hardness of these samples is maintained around 345 HV as shown in Fig.6h. When the temperature is raised above 1000K, α precipitates begin to dissolve into the matrix and the hardness begins to drop. When deformed at 1173 K, which is higher than the β transus of the Ti6554 alloy, it can be seen in Fig.6f and g that all the α phase has dissolved into the β matrix. Also, full recrystallization occurs in the sample deformed at a strain rate

of 4000s^{-1} and the temperature of 1173K as shown in Fig.6f. Partially recrystallized grains can be observed in the sample deformed at the strain rate of 1000s^{-1} and 1173K in Fig.6g because of comparatively smaller maximum strain.

The dominant morphology of intragranular α precipitate in the specimens deformed at temperatures of 293K and 573K is almost the same as shown in Fig.5c. An important microstructure observation is that a string-like morphology stretching across some grains appeared in the samples deformed at strain rates of 4000 and 10000s^{-1} when the temperature is raised to 873K as shown in Fig.7a and b. These morphologies are confined to individual β grains and the space between them is reduced with increasing strain rate. The string-like morphologies are 30-100μm in length (Fig7a, b) and developed from aligned globular α precipitates (Fig.7c). The size of the individual α precipitate is approximately 300-500 nm. Each precipitate grows along a specific orientation until they pin each other to form a continuous morphology as shown in Fig.7d. Within some β grains two distinct orientations of the aligned α precipitates have been observed as shown in Fig.7c. The angle between different orientations is always approximately 60˚. As the aligned α precipitate morphology is absent at 1000s^{-1} under the same temperature as shown in Fig.7e, this indicates that strain rate may play an important role in its formation. The hardness of the area containing aligned α precipitate morphologies is approximate 50 HV harder than that of the area without them in the sample deformed at 873K and 4000 s^{-1} as shown in Fig.7f.

Adiabatic shear bands were only observed in the samples in which the aligned α precipitate morphologies have been observed as shown in Fig8. When viewed along the transverse section of the cylinder specimens, more than one adiabatic shear bands formed in a circular shape around the edge of the specimens. It is concluded that shear bands will form two coaxial and symmetrical hemispherical-shaped shells inside the cylindrical specimens during the high strain rate testing in the study of Odeshi et al. on a dual-phase steel [196]. In general, the flow stress will drop from the maximum value with the formation of adiabatic shear bands [15, 142, 200, 234]. However, no such flow softening is observed in the stress-strain curves of specimens in which shear bands are observed. This indicates that the initiation of ASBs will not lead to the drop of flow stress from the peak value in the Ti6554 alloy. SEM images in Fig.9 show the adiabatic shear bands in the Ti6554 alloy. With increasing strain rate, the width of the shear bands decreases. Microhardness testing has been done on the samples deformed at 873K and 4000s^{-1}. The area of indent inside the band is smaller than that outside as shown in Fig.9a, indicating that the microstructure inside the band is harder. A comparison of hardness of areas inside and outside ASB is shown in Fig.9c. The hardening effect within ASBs is related to the grain refinement and phase transformations that may

occur inside the shear bands [193].

4. Discussion

Considering the high stability of the β phase in the Ti6554 alloy and the absence of twinning and martensite through microstructural observation, it can be confirmed that the dominant deformation mode of the Ti6554 alloy during high strain rate deformations is dislocations slip. According to dislocation dynamics [105], the flow stress of materials consists of a thermal part and an athermal part. The thermal part is controlled by shot-range barriers such as the intersection of dislocations and the Peierls stress which is sensitive to temperature and strain rate. A higher strain rate can accelerate the multiplicity of dislocations, leading to the formation of dislocation tangles [53-55] which will retard the movement of dislocations. In addition, a higher temperature will supply dislocations with sufficient thermal energy to help them overcome dislocation tangles [33, 41]. Therefore, the flow stress increases with increasing strain rate while decreases with increasing temperature. The athermal part of the flow stress is controlled by long-range barriers such as grain boundaries and secondary precipitates which are regarded as independent of temperature and strain rate during high strain rate deformations. Therefore, the dissolution of α phase in the specimens deformed at temperatures higher than 1023K leads to a drop in hardness as shown in Fig.6h, which can explain the significant increment in temperature sensitivity for Ti6554 at 1173K shown in Fig.4b. The large increment of flow stress beyond a strain rate of 10^3 s^{-1} in Fig.3a has been interpreted as a transition from a thermally activated controlled mechanism to a dislocation drag controlled mechanism at higher strain rates according to the three different mechanisms governing plastic flow proposed by Meyer et al. [17]. However, Fallansbee and Kocks [126] suggest that the improved strength can be attributed to enhanced rates of dislocation multiplication, instead of a change in the deformation mechanism. This alternate view was supported by studies of Lee et al. [127] and Zerilli et al. [128] in studies on 304L stainless steel and OFHC copper, respectively.

4.1 Strain hardening behaviour

The strain hardening rate is dependent on the competition between strain and strain rate hardening and thermal softening effects. Under quasi-static conditions, the heat generated by deformation can dissipate quickly thus the thermal softening effects can be neglected. This explains why the strain hardening rate in the stress-strain curve performed under quasi-static conditions is pronounced in Fig.2a, while under high strain rate conditions the heat generated by deformation cannot dissipate due to the short deformation duration. Hence thermal softening effects play an important role in

high strain rate deformations of the Ti6554 alloy, leading to an insensitivity of flow stress to strains.

The negative slope of curves performed at strain rates higher than 1000 s^{-1} and at a temperature of 293K in Fig. 2a is typically interpreted as flow softening. Flow softening is attributed to the initiation of adiabatic shear bands [15, 142, 200, 234], break-up of high aspect ratio lath-like precipitates [235] or adiabatic heating. As the former two microstructural features are absent in the specimens deformed at 293K, it is supposed that thermal softening effects caused by adiabatic heating are responsible for the flow softening behaviour of the Ti6554 alloy deformed at high strain rates at a temperature of 293K. The adiabatic temperature elevation in these specimens during high strain rate deformations has been calculated using the formula:

$$\Delta T = \frac{\eta}{\rho c}\int_{\varepsilon_i}^{\varepsilon_{i+1}} \sigma(\varepsilon_i, \dot{\varepsilon}_i, T_i)\, d\varepsilon \qquad (6)$$

in which ρ and c are the density and specific heat of the material, respectively. The integral is the plastic work i.e. the area under the stress-strain curve. η is the heat fraction coefficient which is always defined as 0.9. The result is shown in Fig.10. It is found that the adiabatic heating leads to a significant increment of the sample temperature during high strain rate deformation. Therefore, the flow softening phenomenon in the Ti6554 alloy at 293K during high strain rate deformations is likely caused by thermal softening effects which outweigh the effects of the strain rate and strain hardening.

The strain hardening rate for tests performed at temperatures higher than 293K increases compared to those performed at 293K especially at a strain rate of 1000 s^{-1}, as shown in Fig.2. According to dislocation dynamics, the microstructure only has influence on the athermal part of the flow stress (initial yield stress) [132] and has almost no influence on the thermally activated part. It is reasoned that gross microstructural features do not affect dislocation-dislocation interactions [132]. Therefore, there is no obvious relationship between the strain hardening rate and the microstructure during high strain rate deformations of the Ti6554 alloy. An alternative explanation for this abnormal increment in the strain hardening rate with increasing temperature are dynamic strain aging (DSA) effects caused by the activation of solute Cr atoms in the β phase. The small atomic radius and high diffusivity of Cr compared with the other alloying elements make it possible for the mobile Cr atoms to pin dislocations. The interaction between solute atoms and dislocations reduces the mobile dislocation density, resulting in an increment in the strain hardening rate at higher temperatures. The issue of DSA has been analysed in detail in a study on commercially pure titanium by Nemat-Nasser et al. [130]. As for the negative slope at strains larger than 0.15 for the test performed at 1173K and 4000 s^{-1}, this is attributed to the full recrystallization of the β phase.

4.2 Novel α precipitate morphologies and strain localization

To our knowledge, this is the first time that the continuous morphology consisting of globular α precipitates has been observed in a metastable β titanium alloy. A similar string-like morphology consisting of chevron α precipitates has been observed in the Ti5553 alloy [236], which was hypothesized to develop through multiple site nucleation from ω particles. However, it has not been explained why these aligned α precipitates shared two or three distinct orientations in the Ti5553 alloy. In our study, it is supposed that dislocations act as the preferential nucleation sites for the formation of the aligned α precipitates. It has been observed that α precipitates nucleate along dislocations within slip bands during aging treatments of a cold rolled Ti-15V-3Cr-3Sn-3Al alloy [237, 238]. During high strain rate deformations, structural defects like dislocations and vacancies will multiply in a much faster manner and the influence of networks of localized dislocations may increase. This explains why the aligned α precipitates formed in a short duration for the high strain tests conducted at 873K. The development of the aligned α precipitates is accompanied with an increment in the hardness of the specimens as shown in Fig.7e. Precipitates with high aspect ratios can act as barriers to dislocation movement, resulting in pile-up of dislocations at the α/β interface [239].

Adiabatic shear bands were absent in the sample deformed at $1000s^{-1}$ and 873K. This indicates that shear bands tend to form at higher strain rates. It has been reported that high strain rates and low temperatures are beneficial for the formation of shear bands in titanium alloys [118]. However, in this study it was observed that the adiabatic shear bands prefer to form at higher temperatures. This phenomenon may be attributed to the occurrence of the aligned α precipitate morphologies, which may contribute to strain localization. The aligned α precipitate morphology has hardening effects, leading to variations in the hardness distribution within specimens. As the areas absent of aligned α precipitate morphologies are softer, the deformation is likely to proceed more readily in these areas.

5. Conclusion

The dynamic response of the β titanium alloy, Ti6554, has been characterized at strain rates ranging from 1000 s^{-1} to 10000 s^{-1} and temperature ranging from 293K to 1173K using split Hopkinson pressure bar tests. The following conclusions can be drawn from the study.

1. The dominant deformation mode for the Ti6554 alloy during high strain rate deformations is dislocation slip. The flow stress of the Ti6554 alloy is more sensitive to temperature than strain rate.

It increases with increasing strain rate and decreasing temperature.

2. Flow softening observed in tests performed at 293K is potentially due to thermal softening effects caused by adiabatic heating during the high strain rate deformations. The increment of the strain hardening rate with increasing temperatures may be attributed to the interaction between thermally activated solute Cr atoms and mobile dislocations.

3. When the temperature is raised to 873K, aligned α precipitate morphologies formed in the specimens deformed at the strain rates of 4000 and 10000s^{-1}. These precipitates have hardening effects on the matrix and are proposed to nucleate on dislocations introduced by the high strain rate deformations.

4. Adiabatic shear bands tend to form in specimens deformed at higher temperatures (873K), which may be attributed to the presence of the aligned α precipitate morphologies. The microstructure inside the shear bands is harder than that outside the bands in the Ti6554 alloy.

Acknowledgement

The authors would like to acknowledge the support of the Queensland Centre for Advanced Material Processing and Manufacturing (AMPAM) and the Defence Materials Technology Centre (DMTC). The authors also acknowledge the facilities and technical assistance of the Australian Microscopy and Microanalysis Research Facility at the Centre for Microscopy and Microanalysis, The University of Queensland. The authors also acknowledge BaoTi Group Ltd., Baoji, China for the provision of the Ti6554 alloy and China Scholarship Council for the scholarship support.

Table 1

Chemical composition table (mass %)

Materials	Cr	Mo	V	Al	O
Ti6554	6.05	4.95	5.09	4.20	0.19

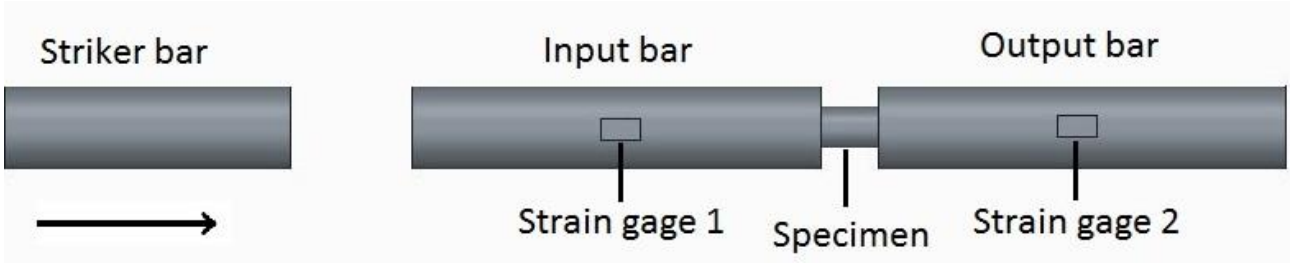

Fig.1. Schematic showing the arrangement of the SHPB device**.**

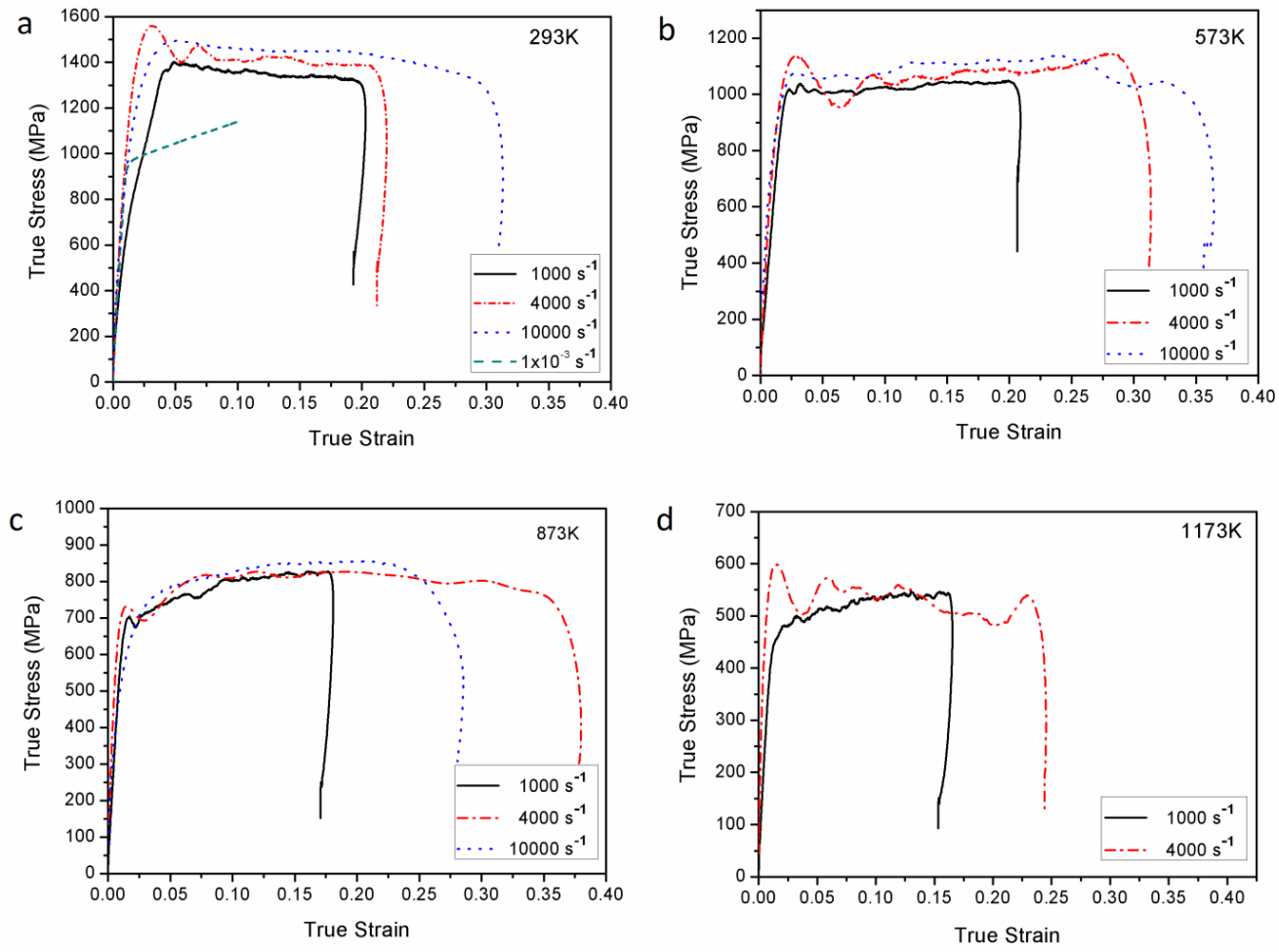

Fig.2. True stress-strain curves of the Ti6554 alloy deformed at different temperatures: (a) 293K (b) 573K (c) 873K (d) 1173K.

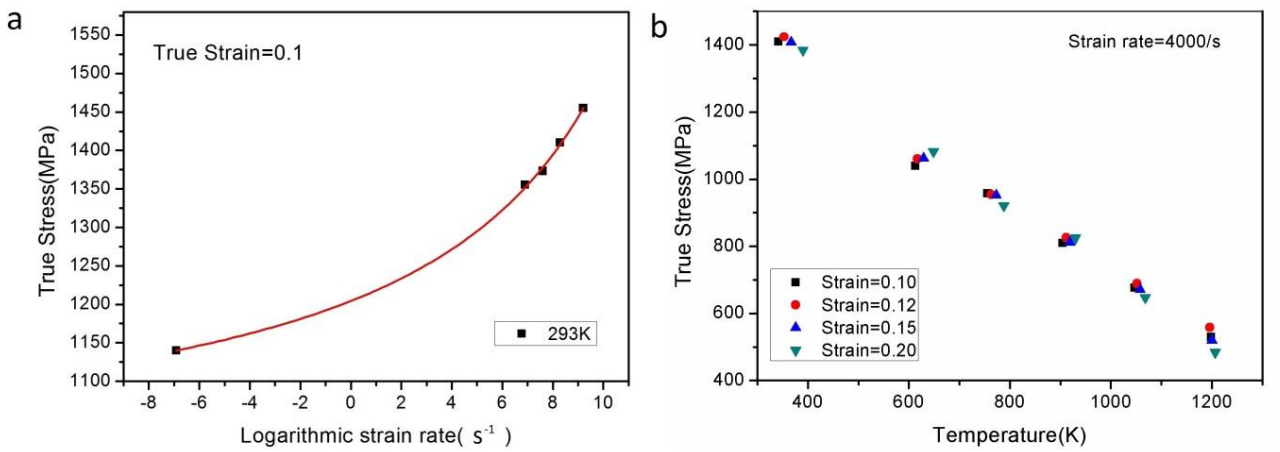

Fig.3. (a) Flow stress for a strain of 0.10 at different strain rates. (b) Flow stress for a strain rate of 4000 s^{-1} at different temperatures.

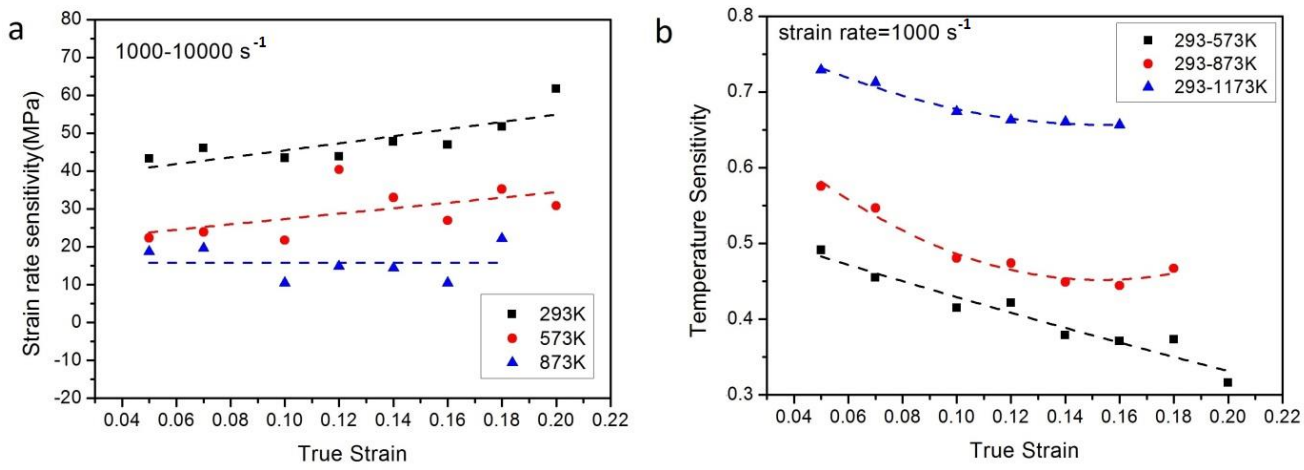

Fig.4. (a) Strain rate sensitivity for strain rate of 1000-10000s^{-1}at different temperatures (b) Temperature sensitivity at a strain rate of 1000s^{-1}

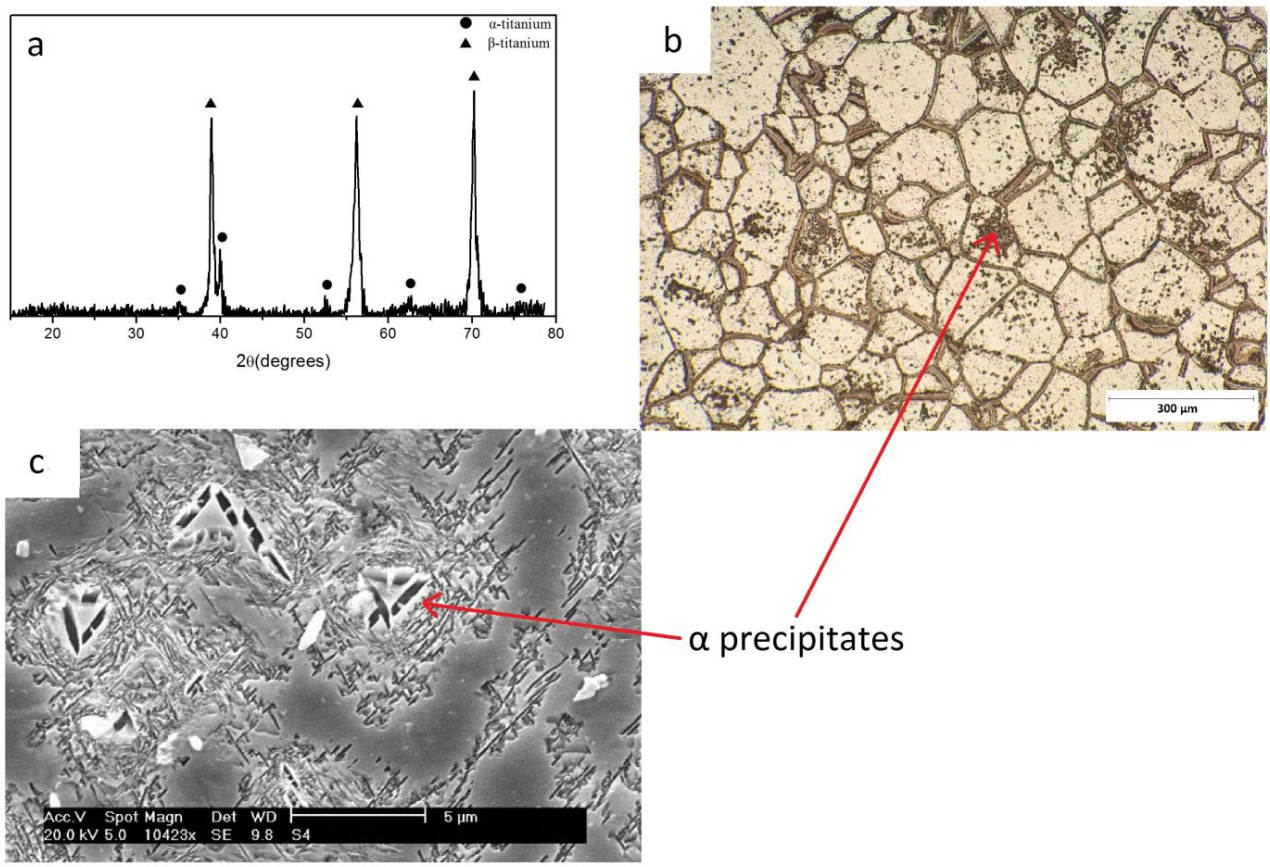

Fig.5. (a) XRD spectra, (b) Optical image and (c) SEM image of solution treated and aged Ti6554 alloy

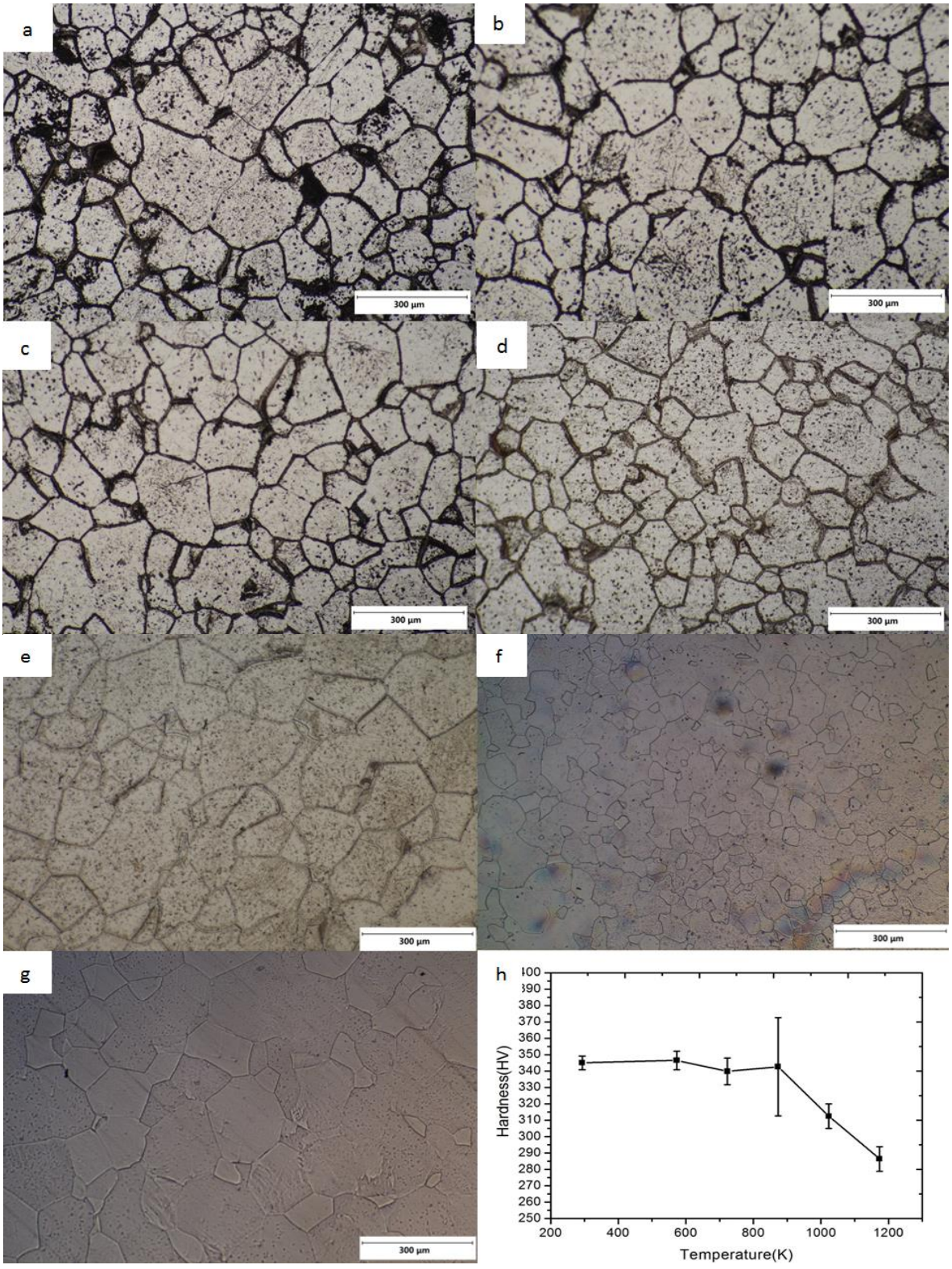

Fig.6. Optical images of samples deformed at: (a) $4000s^{-1}$, 293K (b) $4000s^{-1}$, 573K (c) $4000s^{-1}$, 723K (d) $4000s^{-1}$, 873K (e) $4000s^{-1}$, 1023K (f) $4000s^{-1}$, 1173K (g) $1000s^{-1}$, 1173K, and (h) Microhardness of specimens deformed at $4000s^{-1}$.

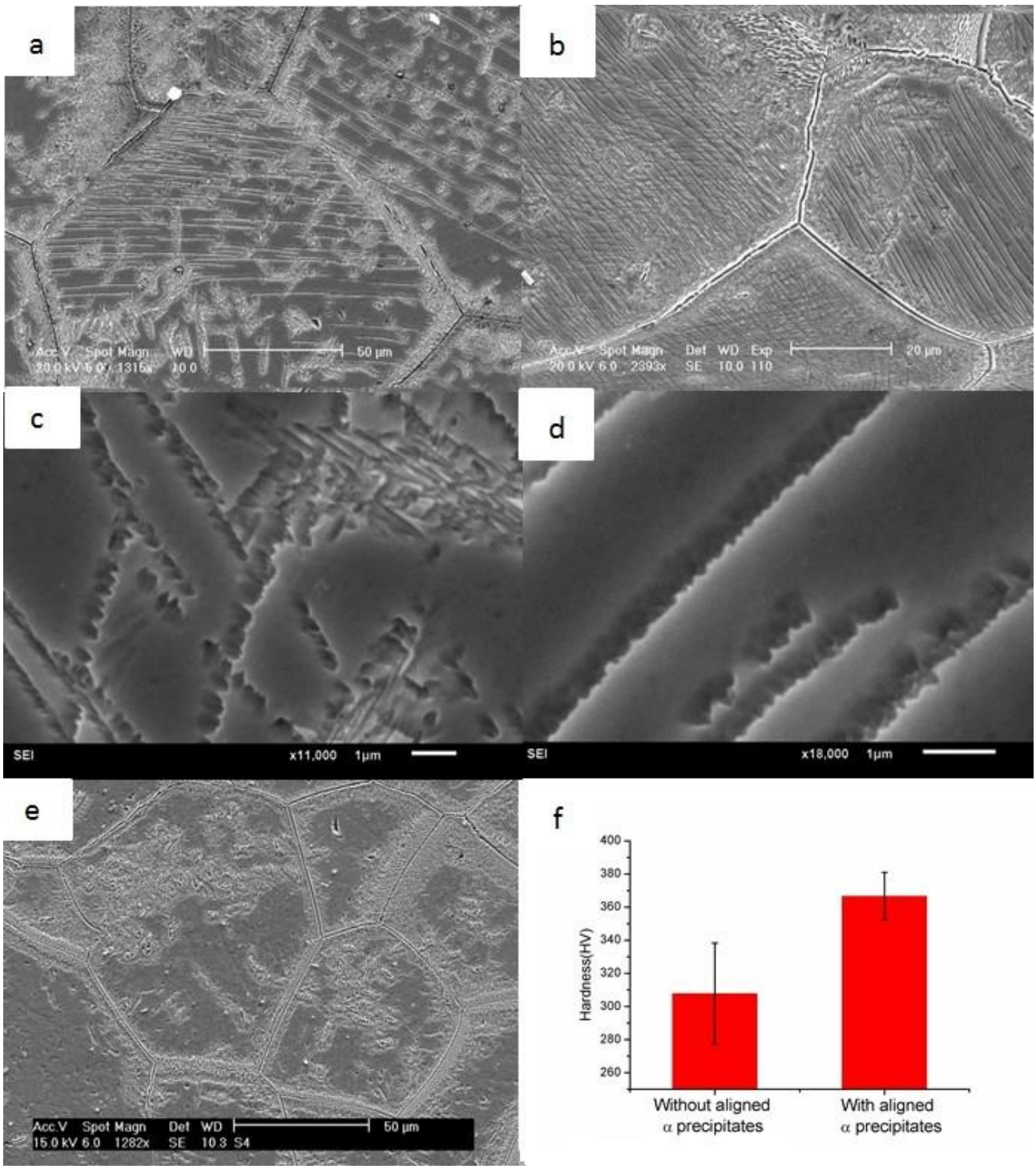

Fig.7. SEM images of samples deformed at: (a) 873K, 4000 s^{-1} (b) 873K, 10000 s^{-1}, (c) and (d) higher magnification SEM images of the aligned α precipitate morphologies (e) SEM image of the sample deformed at 873K and 1000 s^{-1} (f) Microhardness of microstructure with and without aligned α precipitates in the specimen deformed at 4000s^{-1} and 873K.

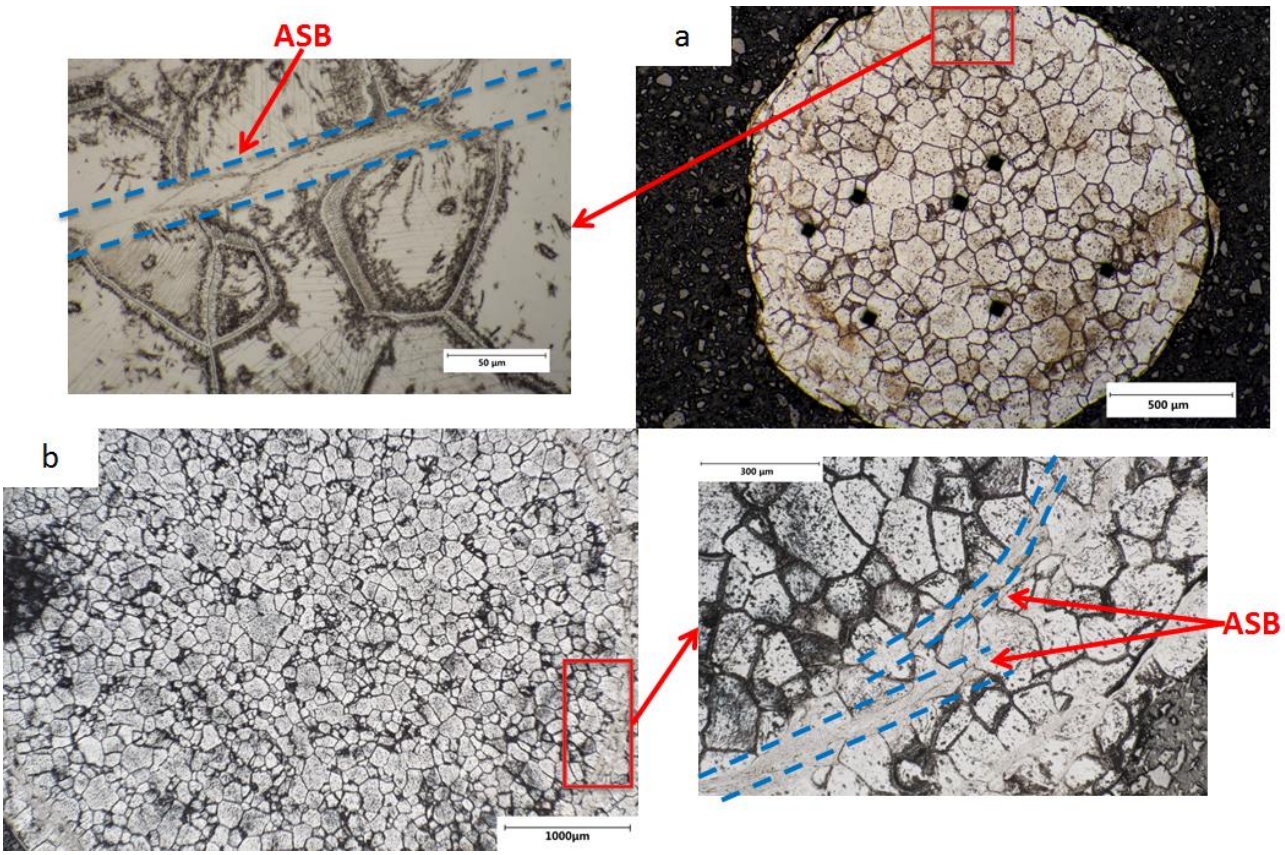

Fig.8. Optical images of adiabatic shear bands in samples deformed at: (a) 873K, 10000s^{-1} (b) 873K 4000s^{-1}.

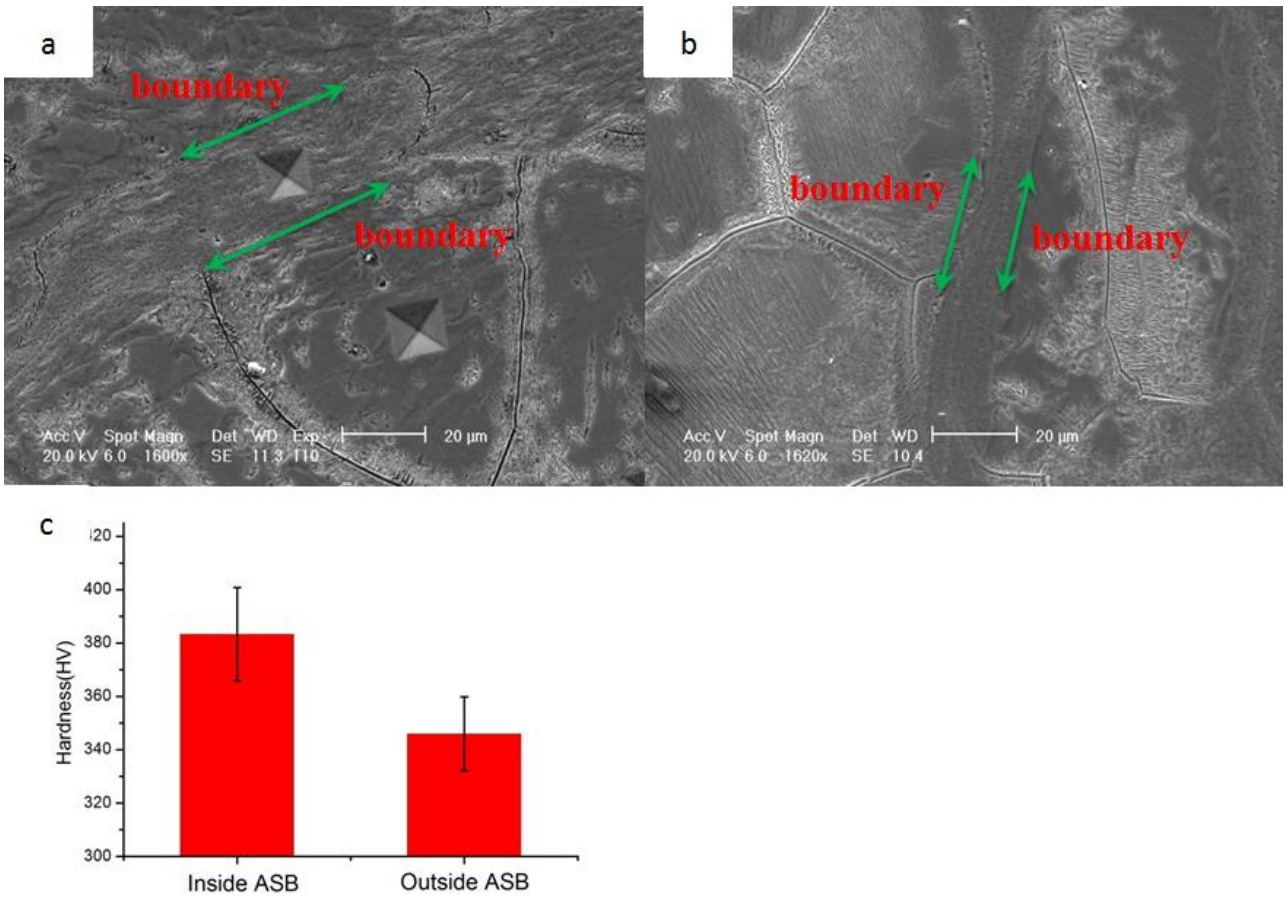

Fig.9. SEM images of adiabatic shear bands in samples deformed at: (a) 873K, $4000s^{-1}$ (b) 873K $10000s^{-1}$, and (c) Microhardness inside and outside ASB in the specimen deformed at $4000s^{-1}$ and 873K.

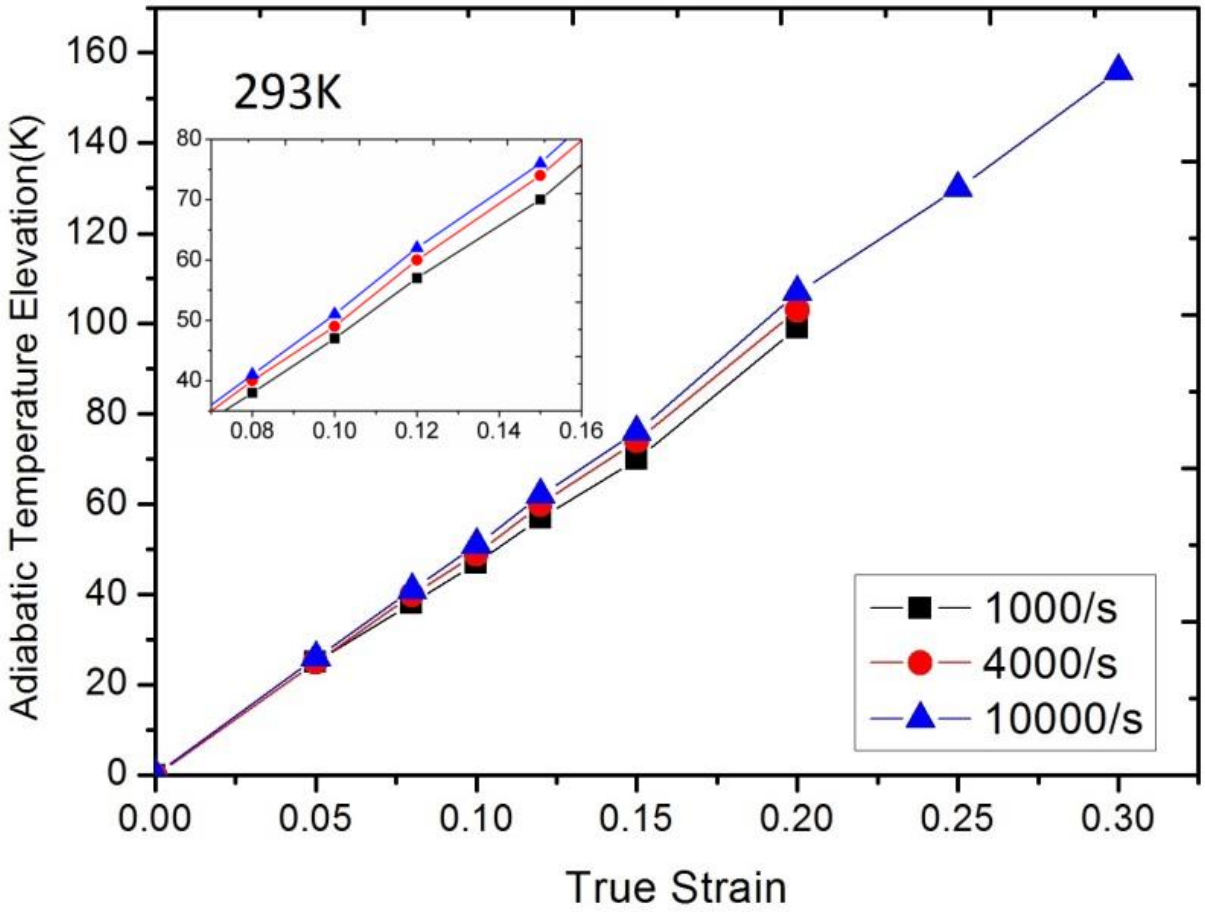

Fig.10. Adiabatic temperature elevation as a function of the true strain.

PAPER 2

Microstructural Characteristics of Adiabatic Shear Localization in a Metastable Beta Titanium Alloy Deformed at High Strain Rate and Elevated Temperatures

Hongyi Zhan, Weidong Zeng, Gui Wang, Damon Kent, Matthew Dargusch

Materials Characterization

2015, Volume 102, Pages 103-113

Microstructural characteristics of adiabatic shear localization in a metastable beta titanium alloy deformed at high strain rate and elevated temperatures

Hongyi Zhan[1,*], *Weidong Zeng*[2], *Gui Wang*[1,3], *Damon Kent*[4], *Matthew Dargusch*[1, 3]

[1]Centre for Advanced Materials Processing and Manufacture, School of Mechanical and Mining Engineering, The University of Queensland, St Lucia, Queensland 4072, Australia

[2]State Key Laboratory of Solidification Processing, School of Materials, Northwestern Polytechnical University, Xi'an 710072, China

[3]Defence Material Technology Centre, Level 2, 24 Wakefield St, Hawthorn VIC 3122, Australia

[4]School of Science and Engineering, University of the Sunshine Coast, Sippy Downs, Queensland 4575, Australia

Corresponding Author: Hongyi Zhan

E-mail: h.zhan@uq.edu.au

Abstract

The microstructural evolution and grain refinement within adiabatic shear bands in the Ti6554 alloy deformed at high strain rates and elevated temperatures have been characterized using transmission electron microscopy. No stress drops were observed in the corresponding stress-strain curve, indicating that the initiation of adiabatic shear bands does not lead to the loss of load capacity for the Ti6554 alloy. The outer region of the shear bands mainly consist of cell structures bounded by dislocation clusters. Equiaxed subgrains in the core area of the shear band can be evolved from the subdivision of cell structures or reconstruction and transverse segmentation of dislocation clusters. It is proposed that dislocation activity dominates the grain refinement process. The rotational recrystallization mechanism may operate as the kinetic requirements for it are fulfilled. The coexistence of different substructures across the shear bands implies that the microstructural evolution inside the shear bands is not homogeneous and different grain refinement mechanisms may operate simultaneously to refine the structure.

Key Words:

Adiabatic shear band; Beta titanium alloy; Grain refinement mechanism; TEM

1. Introduction

Adiabatic shear bands (ASB), first observed by Zener and Hollomon [178] in steel in 1944, are an important deformation mode that mainly occur under high strain rate deformation conditions. During high strain rate deformations, the heat generated by deformation fails to dissipate thus elevated temperatures will contribute to thermal softening which outweighs the effects of strain and strain rate hardening, leading to the initiation of shear localization. Materials with low ductility may crack at the site of shear bands soon after their initiation [179-183]. As the adiabatic shear bands lead to catastrophic failure of materials, the criterion for the occurrence of shear bands has aroused the interest of researchers in order to alleviate their negative effects on the performance of materials. Xu et al. [193] summarized the experimental results of past investigations and concluded that both a critical strain and strain rate are required for ASB formation. The results of Lee's study [118] indicate that the tendency toward adiabatic shearing increases with increasing strain rate and reducing temperatures. Kim et al. [240] solved coupled non-linear governing equations by which they showed that an increase in the initial temperature of the specimens would delay the initiation and growth of shear bands. It is found that the nucleation and formation of the shear bands are also influenced significantly by the initial microstructure [196, 197, 241]. It was explained that the presence of defects like second-phase particles, precipitates or other inhomogeneities in the microstructure of metallic materials can increase their susceptibility to strain localization.

In the past thirty years, a lot of studies have been conducted on the microstructure within ASBs in different metallic materials. Early in 1983, Mebar et al. [192] studied adiabatic shearing in four types of Ti-6Al-4V alloys with different microstructures and concluded that all the observed shear bands had the same microstructure which consisted of fine transformation products with arbitrary orientations. Andrade et al. [200] investigated the microstructural evolution of high-strain-rate deformed copper by transmission electron microscopy (TEM) and observed that towards the centre of the shear bands, the elongated dislocation cells break down and are replaced by fine equiaxed grains. In 2000, Meyers et al. [206] proposed a sequence of events that may occur prior to the formation of adiabatic shear bands. With increasing strain, randomly distributed dislocations will firstly interact with each other to form elongated cells. These cells become elongated subgrains as their misorientation increases. Eventually these subgrains break up into equiaxed micrograins to form a recrystallized structure. This process has been demonstrated by TEM observations of different metallic materials including tantalum [201], Zirconium [242], Ta and Ta-W alloys [243], steels [219, 244] and aluminium alloys [245]. The formation mechanism of equiaxed micrograins in the centre of ASBs has attracted significant attention from researchers. Currently, the rotational

dynamic recrystallization (RDR) mechanism postulated by Meyer et al. [199] is widely used to explain the formation mechanism of micrograins as the static recrystallization and migrational dynamic recrystallization mechanisms have been numerically shown to be too slow in terms of kinetics [90, 246]. However, the exact role that temperature and mechanical assistance play in the formation of micrograins is still unclear due to limited information of the exact temperature and strain history within the ASBs.

Because of their low strain hardening rates and poor thermal conductivity, titanium alloys are very susceptible to adiabatic shear bands [184, 185]. Most studies of adiabatic shear bands in titanium alloys focus on Ti-6Al-4V [186-189] and commercially pure titanium [190, 191] but few focus on β-Ti alloys. Yang et al. [142] conducted an experiment on the microstructural evolution in the shear band of a near beta titanium alloy under high strain rate deformations. In general, adiabatic shear bands in titanium alloys are tens of microns wide. Elongated cell structures (0.2-0.5μm wide) with thick dislocation walls are located near the boundaries and micrograins (0.05-0.2μm wide) with low dislocation density towards the centre. The Ti-6Cr-5Mo-5V-4Al (Ti6554) alloy is a newly-developed metastable β alloy with an ultimate tensile strength (UTS) of around 1250MPa and fracture toughness (KIC) from 80 to 90 MPa $m^{1/2}$ after solution and aging treatments [28, 29]. In terms of damage tolerance, the Ti6554 alloy is promising for applications in the aerospace industry. The objective of the present work is to perform a systematic characterization of the microstructure within the ASBs in the Ti6554 alloy deformed at high strain rates and elevated temperatures. The temperature history and grain refinement mechanisms are also evaluated with regard to the microstructural observations.

2. Experimental procedure

The Ti–6Cr–5Mo–5V–4Al alloy was cast by multiple vacuum arc melting. Ingots of 620 mm diameter were forged to 60% strain at around 1323 K, and then forged with further 70% deformation at around 833K, reducing the diameter to 110 mm. The chemical composition of the alloy is listed in Table 1. Hot rolled cylindrical rods of the Ti6554 alloy were solution treated at 1100 K for 1 h in a protective Argon atmosphere and then air cooled. Aging treatments were conducted on the solution treated Ti6554 rods at 833 K for 8 h under an ambient atmosphere and then air cooled. The solution treated and aged microstructure of the Ti6554 alloy, consisting of β phase matrix with α phase precipitates interspersed, is shown in Fig.1. The average grain size is around 150 μm.

Cylindrical specimens for the high strain rate tests were 5 mm in diameter and 4 mm in height. They were cut from rods using electrical discharge machining with a slow cutting speed to minimise heat effects on the samples. The mechanical behaviour of the Ti6554 alloy at high strain rates was tested using a Split Hopkinson Pressure Bar (SHPB) arrangement [80] at the strain rate of 4000 s^{-1} and temperatures ranging from 293K to 1173K. For the experiments at elevated temperatures, the specimens were heated by an in-situ induction coil and the temperature was regulated by a thermocouple not in contact with the specimen. After reaching the designated temperature, the specimen was maintained at the designated temperature for approximately 2 minutes to ensure a uniform temperature distribution. In order to decrease the friction between the contact surfaces of the bars and specimen, molybdenum sulphide was used as a lubricant.

Specimens for microstructural observation were all first wet ground using silicon carbide papers, mechanically polished and ultrasonically cleaned. Specimens for optical microscopy (OM) and scanning electron microscopy (SEM) were etched using Kroll's reagent (2% hydrofluoric acid, 6% nitric acid and 92% distilled water). Scanning electron microscopy observation was performed on a XL30 and JEOL 6610 instruments. Hardness testing was conducted on polished specimens using a Struers Vickers microhardness testing machine. For transmission electron microscopy sample preparation, in order to target the location of adiabatic shear bands a particular method similar to that described in the literature [242, 247] was applied. By optical observation of etched specimens as shown in Fig.3 (b), the location of the shear bands were determined (200~400μm away from the edge). Then a slice of the specimen was cut perpendicular to the compressive direction followed by mechanical thinned to ~60 μm. Then discs of 3 mm in diameter were punched out near the edge of the slice (with shear band in them) and were twinjet polished using Struers A_3 electrolyte (50 ml perchloric acid, 300 ml butylcellosolve and 500 ml methanol) at an applied voltage of 20V and a temperature of 233 K. As the shear band is located off the centre in the discs, the perforation produced by twinjet polishing was gradually enlarged by ion milling at low angles in a Gatan Precision Ion Polishing System until it intersected the shear bands

3. Results

3.1 Optical and SEM observation of shear localization

From optical microscopic images shown in Fig.2 (a)-(d), it is found that the specimens deformed at the temperature ranging from 293K to 873K all show very typical aged microstructures. When the temperature is raised higher than 1023K, the α precipitates begins to be dissolved into β matrix

(Fig.2 (e)) as the β transus for the Ti6554 alloy is around 1000K [248]. Obvious recrystallization happened in the specimen deformed at 1173K as shown in Fig.2 (f). The true stress-strain curves of Ti6554 deformed at 4000 s^{-1} over a wide range of temperatures from 293K to 1173K are shown in Fig.3 (a). The strain hardening behaviour is weak for all these curves.

It is found that a well-developed adiabatic shear band can only be observed in the specimen deformed at 873K as shown in Fig.3 (b) and no rapid reduction in stress can be found in the corresponding stress-strain curve in Fig.3 (a). When viewed along the transverse section of the specimen, the shear bands are circular in shape. This shape of the ASB is in accordance with the report that shear bands typically form two coaxial and symmetrical hemispherical-shaped shells inside cylindrical specimens during the high strain rate tests [196]. It is also reported that the diameter of the circular shear band on the transverse section will decrease with distance from the diametrical surface to the centre of the cylinder. It is worth noting that the ASBs only formed at 873K in the SHPB tests conducted over a wide range of temperatures under high strain rates conditions. It is unusual that the ASB should form at a high initial temperature. With thermal softening effects due to the high initial temperature the deformation should tend to be more homogeneous within the specimen, which retards shear localization [240]. The conditions required for the occurrence of ASBs should be studied with more controlled experiments taking factors such as strain, temperature and microstructure into consideration. The present study will only focus on the microstuctural evolution and grain refinement mechanisms which took place within the ASB in the Ti6554 alloy.

SEM images in Fig.4 show the microstructure of the ASB in the Ti6554 alloy. The shear band is 10 to 25 μm wide with sharp boundaries distinguished from the surrounding matrix. Stretched and curved flow lines can be observed within the shear band along with residual grain boundary α phase and intragranular α precipitates marked by arrows in Fig.4. The residual grain boundary α phase marked in Fig.4 (a) has been broken up and rotated along the shear direction while the intragranular α precipitates marked in Fig.4 (b) remain intact. This implies that the shear strain within the shear band is not homogeneous. Microhardness testing has been conducted inside and outside of the shear band. The area of indent inside the band is smaller than that outside as shown in Fig.4 (a), indicating that the microstructure inside the band is harder. A comparison of hardness inside and outside the ASB is shown in the inset of Fig.4 (a). The hardening effect within the ASB has always been attributed to grain refinement or phase transformations that occur within the shear bands [249].

3.2 TEM observation of shear localization

The ASB has been observed in the framed area as shown in Fig.5 (a). A sharp boundary marked by a dashed line can be observed in Fig.5 (b) dividing the ASB and surrounding matrix. As shown in Fig.5 (c), the matrix outside the shear band mainly consists of high-density dislocations tangles. The selected area diffraction (SAD) pattern in the inset of Fig.5 (c) exhibits a typical pattern along the [0 0 1] zone axis of the β phase bcc crystal indicating that the misorientations across these dislocations structures are small. Inside the shear band, the microstructure is finer than that outside by several orders of magnitude as shown in Fig.5 (d) and (f). The SAD patterns in the insets of Fig.5 (d) and (f) both show diffusive arcing spots which indicate the presence of a large amount of randomly misorientated subgrains. A less deformed area interspersed in the severely deformed area has been shown in Fig.5 (e). From a comparison of the SAD patterns in the insets of Fig.5 (c) and Fig.5 (e), it is found that although the less deformed area maintains a coarse grain structure it has been rotated tens of degrees by the shear strain. A lath-like morphology has been marked by an arrow in Fig.5 (b) within the ASB, the details of which are presented in Fig.6. This lath morphology, about 500 nm wide and several microns long, is surrounded by dense dislocations as shown in Fig.6 (a). Similar morphologies have been observed in the severely shear localized area in cold-rolled titanium [250] and a surface mechanical attrition treated Mg alloy [210], which were attributed to twinning. However, the SAD patterns in Fig.6 (b) and (c) both show typical patterns of a hcp crystal observed along different zone axis indicating that the lath morphology is α phase precipitate. The zone axis of the SAD pattern in Fig.6 (b) is the $[1\bar{2}1\bar{3}]$ while the zone axis of the SAD pattern in Fig.6 (c) has rotated to be very close to $[1\bar{2}1\bar{6}]$, indicating that this lath-like α phase precipitate has been broken up and twisted by the shear strain. According to the dimensions and morphologies observed by TEM, it is reasonable to presume that this broken and twisted lath structure is grain boundary α phase which was observed in Fig.4 (a).

The neighbouring area of the residual grain boundary α phase maintained a comparatively less deformed crystal structure than the area far from the grain boundary α phase as shown in Fig.7. The shear direction can be inferred by the elongation direction of the dislocation structures in Fig.7 (a). The SAD pattern of Fig.7 (a) exhibits clustering which implies some degree of texture in this area. Also some satellite spots are observed indicating minor changes of orientation of small segments. The size of the grains decreases to 50-300 nm gradually over several microns away from the residual grain boundary and the shear direction cannot be discerned in this area as shown in Fig.7 (c). The SAD pattern of Fig.7 (c) exhibits an approximate ring pattern indicating the existence of randomly orientated fine subgrains. This pattern has been indexed to the α and β phases. The diffraction ring of the α (100) reflection is too weak and also too close to that of the β (110) reflection to form clear dark field images of the nanocrystalline α phase even using the smallest

objective lens. These nanocrystalline α phase may be formed by the breakdown and recrystallization of the original α precipitates or the transformation of the unstable β phase caused by the adiabatic temperature elevation.

3.3 TEM investigation of the grain refinement process

The microstructures within the ASB observed in other metallic materials always follow a gradient of structural refinement across the ASB as aforementioned in the introduction [219, 244, 251]. The grain refinement process can then be inferred by the morphology and misorientations of microstructures in different locations within the ASB. Bundles of lamellar/lath structures are observed to be characteristic of the outer region of the shear band, especially in metallic materials with intermediate or lower stacking fault energies (SFE) [210, 251, 252]. In our experiments, similar lamellar/lath structures of 100-200 nm width are also observed in the outer region of the ASB as shown in Fig.8 though the volume fraction of these is quite low. The boundaries of the lamella in Fig.8 (a) are curved and blurred in association with the high density of dislocations. The trace of the shear direction can be discerned by the elongation direction of these lamella. Also some transverse dislocation walls have been marked by arrows as shown in Fig.8 (a) and it is supposed that these lamella will break down along these transverse dislocation walls with further straining. A more typical microstructure observed in the outer regions of the ASBs is the cell structure enclosed by high-density dislocation clusters marked by the black arrow as shown in Fig.9. The density of dislocations within the interior of the cell structure is quite low and the size of cell structures is around 300-800 nm. A straight subboundary has been marked by the white arrow in Fig.9. The subboundary typically formed through the annihilation and rearrangement of dislocations tangles in order to minimize the total system energy.

A typical microstructure observed in the intermediate region of the ASB reveals blocks in association with equiaxed subgrains as shown in Fig.10. The size of the blocks is around 300-500 nm and the size of the equiaxed subgrains is 100-300 nm. The corresponding SAD pattern in the inset of Fig.10 indicates that these blocks and equiaxed subgrains are separated by high-angle boundaries with random orientations. It is speculated that the “clean” blocks evolve from the subdivision of the cell structures shown in Fig.9. Some elongated subgrains are also observed surrounding the blocks in this area as shown in Fig.11. The width of these elongated subgrains is 100-300 nm which is in accordance with the size of the equiaxed subgrains. Thus the equiaxed subgrains surrounding the blocks in Fig.10 may be formed through breakdown and refinement of these elongated subgrains. The possible routes for the breakdown of these elongated subgrains have been delineated by dashed lines in Fig.11 (a) and (b). According to Fig.11 (c), it is observed that the

lateral boundaries of these elongated subgrains always show medium to high misorientation angles as marked by the white arrow while the transvers dislocation walls along the shorter axis are at low misorientation angles as marked by the black arrow. The transverse dislocation walls can form by the accumulation and rearrangement of dislocations via dynamic recovery and act as the route for the breakdown of the elongated subgrains. These elongated subgrains may evolve from the dislocation clusters surrounding the cell structures shown in Fig.9.

In the core region of the ASB, a mixture of elliptical nanograins with sharp boundaries and equiaxed subgrains is present as shown in Fig.12. The size of the equiaxed subgrains is 100-300 nm and the size of the nanograins is 50-100 nm. Traces of the shear direction have been completely eliminated in this area. The equiaxed subgrains may evolve in two ways: (1) the breakdown of elongated subgrains as shown in Fig.11 and (2) the subdivision of blocks shown in Fig.10 by further straining. The "clean" nanograins shown in Fig.12 (c) eliminate the defects introduced by the severe plastic deformation and exhibit the characteristics of dynamic recrystallization (DRX). Some refined subgrains have also been observed in the core region as shown in Fig.13. The size of the cluster of these refined subgrains marked by arrows in Fig.13 (a) is around 200 nm which is almost the same as the equiaxed subgrains nearby. Thus it is speculated that these refined subgrains might be formed by the further subdivision of the equiaxed subgrains. The possible routes of this further subdivision of equiaxed subgrains can be inferred by the dashed lines indicated in Fig.13 (a). Also the size of refined subgrains marked is 50-100 nm which is in accordance with the size of DRX nanograins shown in Fig. 12 (c). It is reasonable to believe that the DRX nanograins shown in Fig.12 (c) were evolved from these refined subgrains. The volume fraction of the DRX nanograins in the core region is quite low indicating that recrystallization did not play a dominant role in the grain refinement process within the ASB.

4. Discussion

It is always reported that the flow softening would happen with the formation of adiabatic shear bands [185, 186, 250, 253] in the high strain rate deformation. However, the curve shown in Fig.3 (a) maintains a plateau trend after yielding until the unloading. Similar results have been found in a series of interrupted SHPB tests on Ti-6Al-4V [254] and 316L stainless steel [255]. It was suggested that it is the coalescence of cracks, instead of the formation of ASBs, which leads to the steep drop of stress and the loss of load capacity of these materials. An alternative explanation for the absence of the drop of peak stress is that the ASB observed in our specimen is only in the early

stages of formation considering the existence of residual grain boundary α phase within the ASB.

4.1 Temperature estimation within the ASB

It is usually impossible to detect and record the temperature rise directly during the SHPB tests due to the equipment limitation. Up to now, equation (1) has been extensively used to estimate the temperature change during high strain rate deformation [15, 80, 85, 132, 142]:

$$\Delta T = \frac{\eta}{\rho c}\int_{\varepsilon_i}^{\varepsilon_{i+1}} \sigma(\varepsilon_i, \dot{\varepsilon}_i, T_i)\, d\varepsilon \quad (1)$$

in which ρ and c are the density and specific heat of the material, respectively. The integral is the plastic work i.e. the area under the stress-strain curve. η is the heat fraction coefficient. For the Ti6554 alloy, ρ=4670 kg/m^3, c=550 J kg/K. The integral can be calculated by introducing the constitutive relation (modified Zerilli-Armstrong model [157]) shown in equation (2) into equation (1).

$$\sigma = (C_1 + C_2\varepsilon^n)\exp\{-(C_3 + C_4\varepsilon)T^* + (C_5 + C_6 T^*)\ln\dot{\varepsilon}^*\} \quad (2)$$

Where $C_1, C_2, C_3, C_4, C_5, C_6$ and n are seven parameters of the model. Their values for the Ti6554 alloy have been determined to be 1397.5 MPa, -569.47 MPa, 0.0012 K^{-1}, -0.00222 K^{-1}, 0.03136 K^{-1}, -3.21×10^{-5} K^{-1} and 1.215 [26]. The prevalent perspective is to define η as 0.9 [15, 80, 85, 132, 142] when the strain rate is higher than 1000 s^{-1}. The temperature versus strain curve of the cylinder specimen deformed at 4000 s^{-1} and 873K has been plotted in Fig.14 (a). The highest temperature that can be reached in this specimen is 967 K assuming that the deformation is homogenous within the specimen. However, the strain within the ASB can be much higher than the average true strain shown in the stress-strain curve (Fig.3 (b)). Xue et al. [255] measured the shear strain during forced shear tests on 316L stainless steel by using curved inclusions as fiducial lines. It is found that the maximum shear strain within the ASB can be as high as 6.9. Therefore, it is reasonable to believe that the highest temperature within the ASB in our experiment was higher than 967K. The deformation time can be obtained by examining the transmitted wave pulse recorded by the strain gage mounted on the output bar [90]. The deformation of specimen began from the first peak valve of the pulse to the last one. It is found that the duration for the whole deformation process is 50μs as shown in Fig.14 (b).

4.2 Grain refinement mechanisms

As the volume fraction of DRX nanograins observed within the ASB is quite low, dynamic recovery which controls the formation of subgrains is speculated to play a dominant role in the

grain refinement process for the Ti6554 alloy. For β titanium alloys with high SFE, dislocation activity is very important for the grain refinement as twinning is difficult. According to our TEM investigation on the microstructure within the ASB, the detailed process can be described below. Before the initiation of the ASB, coarse grains are subdivided into fragments by dense dislocation structures. In order to minimize the total system energy, more dislocations will rearrange and annihilate with each other to form subboundaires as the deformation proceeds. It is reported that lamellar structures (Fig.8) form from dislocations walls with preferred orientations while cell structures (Fig.9) form from dislocation tangles without preferred sliding orientation [256]. The volume ratio of lamellar structures observed within the ASB is quite low indicating that the dislocations tend to entangle each other instead of sliding along the same orientation to form dislocations walls in the Ti6554 alloy. For cell structures, a large amount of dislocations may cluster at their lateral dislocation walls. The elongated subgrains (Fig.11) may result from the reconstruction of the thick dislocation clusters, which has been reported in the development of ASBs in 316L stainless steel [257]. Meanwhile, subboudaries can form inside the cell structure dividing it into several blocks with size of 300-500nm with increasing strains (Fig.10). The increment of misorientations between different blocks can be realized by accumulations and annihilations of more dislocations at the subboundaries. Also transverse dislocation walls will form along the short axis of the elongated subgrains as shown in Fig.11(c). The equiaxed subgrains with grain size of 100-300 nm (Fig.12) can be obtained by transverse segmentation of elongated subgrains or subdivision of blocks. Equiaxed subgrains can be further subdivided into finer subgrains with size of 50-100 nm following a similar mechanism as shown in Fig.13.

Low-angle subboundaries of subgrains can transfer to large-angle grain boundaries through diffusive rotation, which is driven by the reduction of interfacial energy. This process is termed rotational dynamic recrystallization (RDRX) [142, 213, 219, 242]. The kinetic calculation of Meyers et al. [206] excludes the probability of migrational dynamic recrystallization in adiabatic shear bands and strongly supports the rotational dynamic recrystallization mechanism [199]. The process of RDRX can be described using the following equation:

$$t = \frac{TL_1 k f(\theta)}{4\delta\eta D_{b0}\exp(-Q_b/RT)} \quad (3)$$

where t is the time; T is the temperature, L_1 is the average diameter of subboundaries; k is the rate constant; δ is the grain boundary thickness; η is the grain boundary energy; D_{b0} is the grain boundary diffusion coefficient; Q_b is the activation energy for grain boundary diffusion which is about 0.4-0.6 of that for lattice diffusion; f (θ) can be expressed as:

$$f(\theta) = \frac{3\tan\theta - 2\cos\theta}{3 - 6\sin\theta} + \frac{2}{3} - \frac{4\sqrt{3}}{9} ln \frac{2+\sqrt{3}}{2-\sqrt{3}} + \frac{4\sqrt{3}}{9} ln \frac{\tan(\theta/2) - 2 - \sqrt{3}}{\tan(\theta/2) - 2 + \sqrt{3}} \quad (4)$$

In RDRX, it is presumed that subboundaries of broken-down subgrains have to rotate by an angle of 30 degrees to generate recrystallized grains [206]. The time required for the rotation of boundaries with a specific size at a specific temperature can be calculated through the equations (3) and (4). It is found that the time for the rotation will decrease with increasing temperature and reducing size of subgrains. The parameters required in equation (3) for the Ti6554 alloy are unknown. Therefore, parameters used for another type of metastable β titanium alloy, Ti-1300, will be applied into our kinetic calculations [142]: k =1.38×10^{-23} J/K; δ = 6.0×10^{-10} m; η = 1.19 J/m^2. D_{b0} = 1.0×10^{-5} m^2/s; Q_b = 132 kJ/mol. In the conservative estimation, the temperature (T) within the ASB during the high strain rate deformation lies in the range from 873K to 967K. Also, the size (L_1) of most subgrains within the ASB is around 100-300 nm according to the TEM observation. Therefore, the corresponding curve for the rotation of subgrain boundaries has been plotted using these parameters and is shown in Fig.15. It is found that when the temperature is higher than 873K and the size of subgrains is smaller than 300 nm, the rotation of subboundaries by an angle of 30 degrees can be accomplished within 10 μs. Especially when the size of subgrain is reduced to 100 nm, this rotation can be accomplished within 3 μs at 873K as shown in Fig.15 (b). As shown in Fig.14 (b), the duration for the high strain rate deformation is found to be 50μs. It is reasonable to believe that the duration of shear localization is no less than 10μs. In summary, the occurrence of the RDRX mechanism within the ASB is possible in kinetics.

As different substructures, such as cell structures, blocks, subgrains and recrystallized grains were always observed to coexist across the ASB, the microstructural evolution within the ASB in the Ti6554 alloy is not homogeneous and several different grain refinement mechanisms, such as transverse segmentation, subdivision and RDRX, operate simultaneously during the shear localization.

5. Conclusion

The microstructural evolution within adiabatic shear bands (ASBs) observed in the Ti6554 alloy deformed at high strain rates and elevated temperatures has been systematically investigated in our study. TEM examinations of the microstructures within the ASB reveal a sequence of events that may occur during the grain refinement. The major results can be summarized as below:

1. The observation of residual grain boundary α phase within the adiabatic shear band indicates

that the shear band observed was not fully developed and the initiation of the shear band will not induce a steep drop of stress in the Ti6554 alloy.

2. Microstructures in the outer region mainly consist of cell structures bounded by thick dislocation clusters and microstructures in the core region mainly consist of equiaxed subgrains and recrystallized nanograins. The transition area consists of the mixture of blocks, elongated subgrains and equiaxed subgrains, which indicates that the strain is not uniformly distributed inside the ASB.

3. Dynamic recovery played a dominant role in the grain refinement process. Equiaxed subgrains in the core region of the ASB may either evolve from the transverse segmentation of elongated subgrains or from subdivision of cell structures.

4. Trough calculation of the kinetics it was established that the transition from low-angle subboundaries to high-angle boundaries can be accomplished by rotational dynamic recrystallization (RDRX) mechanism within the deformation time (50μs).

Acknowledgement

The present research is supported by the fund of the State Key Laboratory of Solidification Processing in NWPU, project number: SKLSP201207. The authors would like to acknowledge the support of the Queensland Centre for Advanced Material Processing and Manufacturing (AMPAM) and the Defence Materials Technology Centre (DMTC), the facilities and technical assistance from the Australian Microscopy and Microanalysis Research Facility at the Centre for Microscopy and Microanalysis, The University of Queensland. The authors also acknowledge BaoTi Group Ltd., Baoji, China for the provision of the Ti6554 alloy and China Scholarship Council for the scholarship support.

Table 1

Chemical composition (wt. %) of the Ti6554 alloy

Materials	Cr	Mo	V	Al	O
Ti6554	6.05	4.95	5.09	4.20	0.19

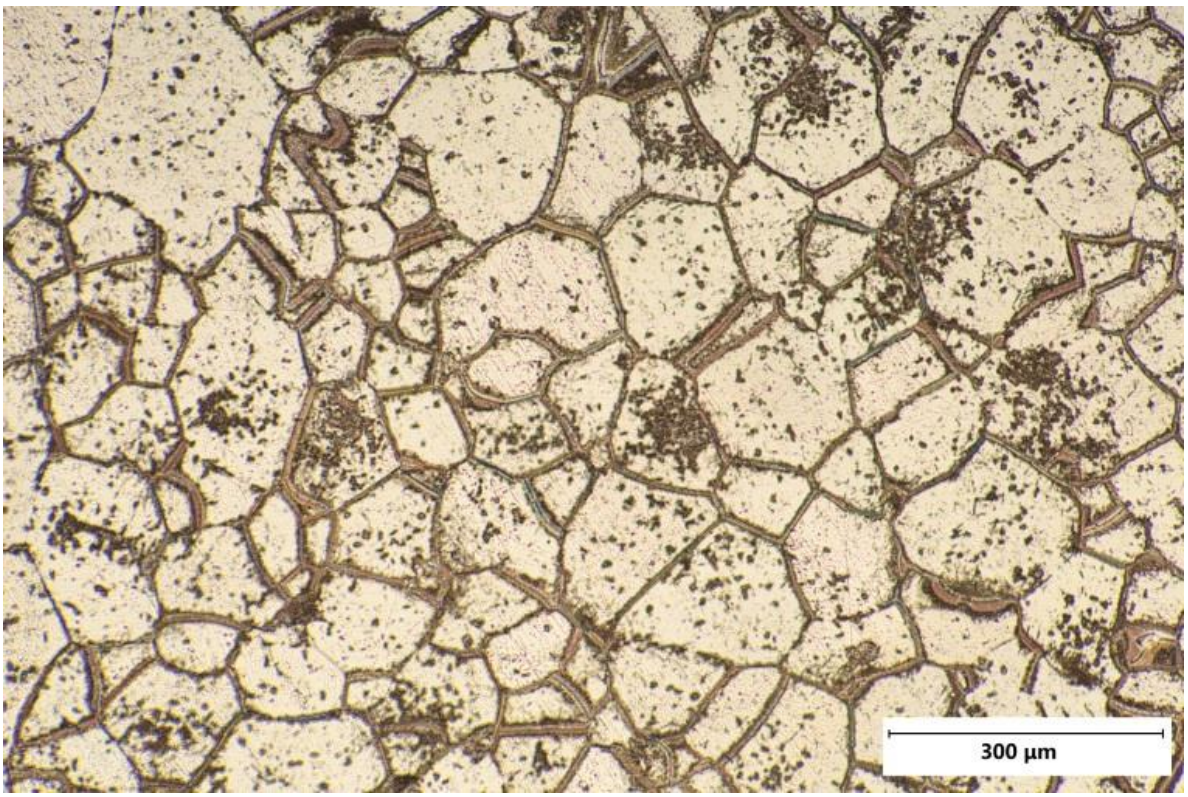

Fig.1. Optical micrograph of the solution and aging treated microstructure of the Ti6554 alloy

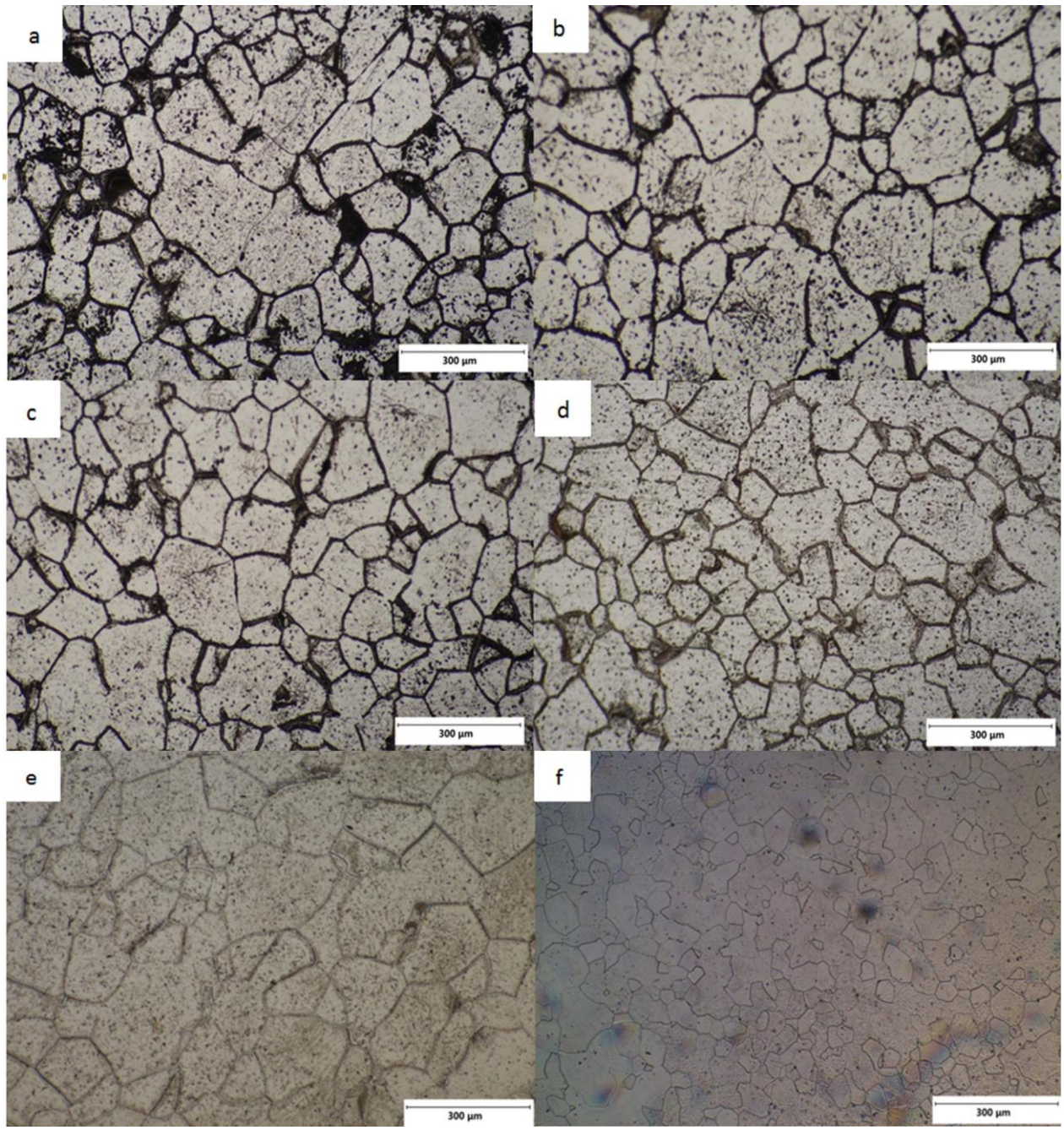

Fig.2. Optical microscopic images of samples deformed at $4000s^{-1}$ over a wide range of temperatures: (a) 293K (b) 573K (c) 723K (d) 873K (e) 1023K (f) 1173K

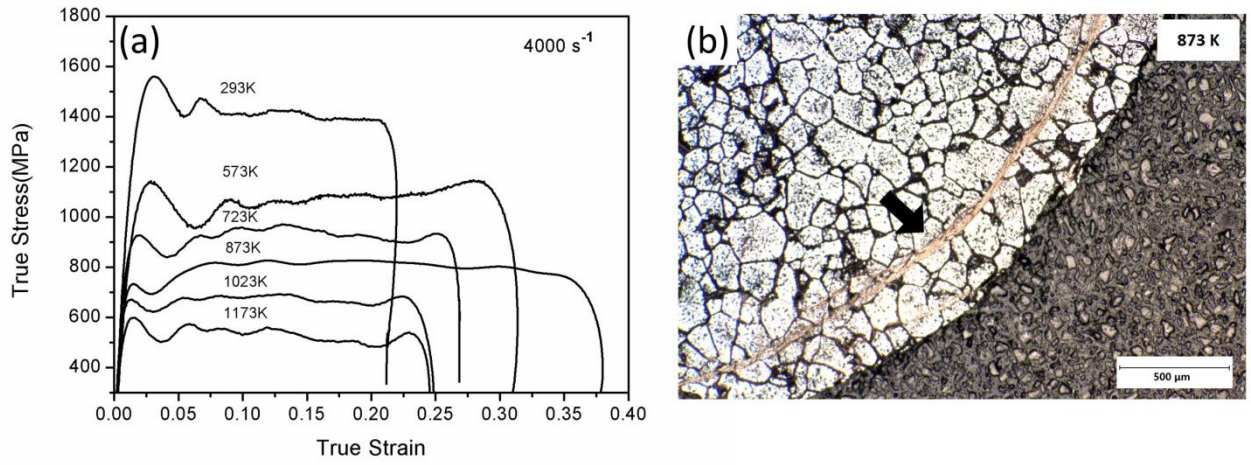

Fig.3. (a) True stress-strain curves of the Ti6554 alloy deformed at 4000 s^{-1} (b) An optical micrograph showing the adiabatic shear band viewed along the transverse section of the cylinder specimens deformed at 873K and 4000 s^{-1}

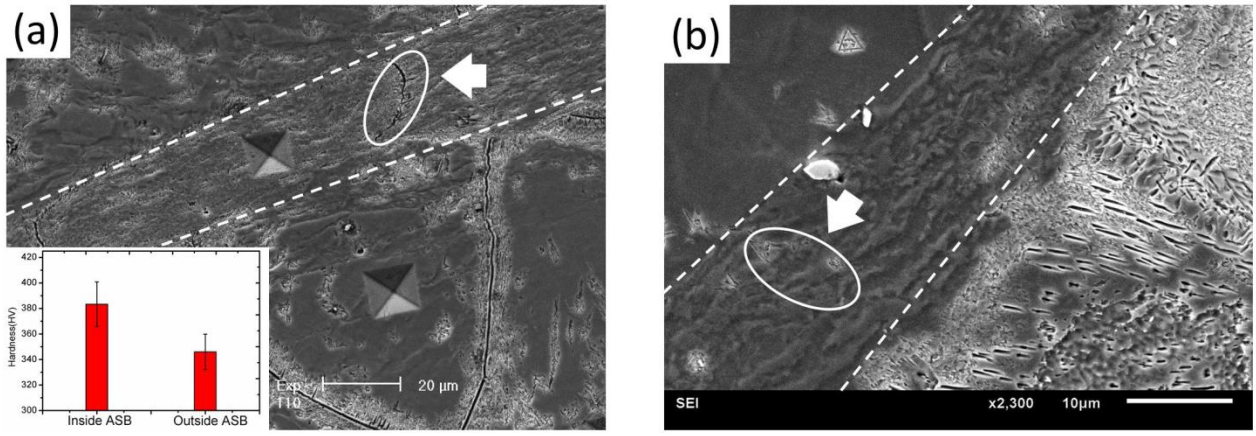

Fig.4. SEM micrographs showing the adiabatic shear band delineated by dashed lines in the Ti6554 alloy (residual grain boundary and intragranular α precipitates have been marked by arrows), the inset in (a) shows microhardness inside and outside of the ASB.

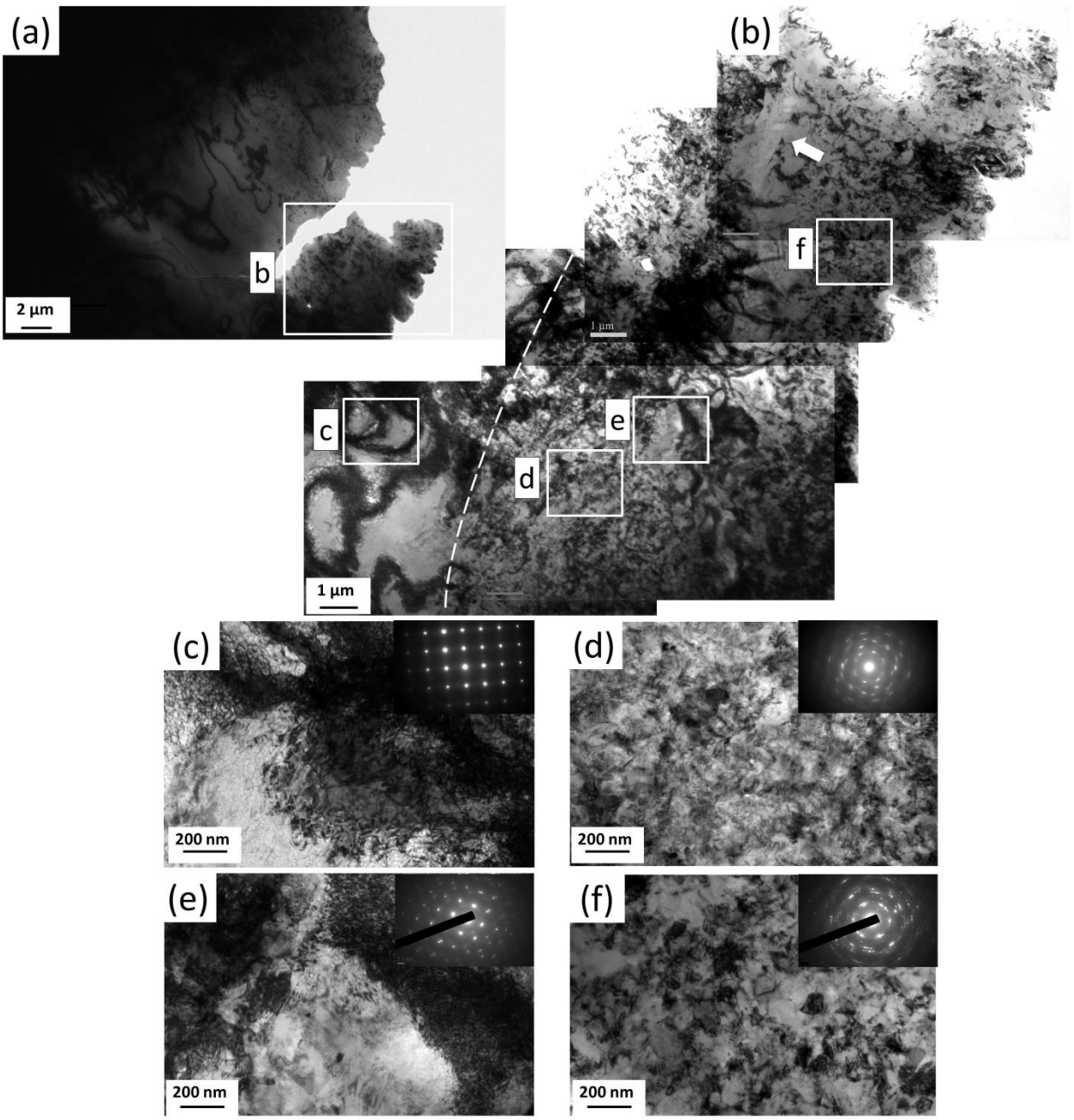

Fig.5. (a) Microstructure within the adiabatic shear band, (b) A montage of TEM micrographs of the shear band (delineated by dashed lines) within the area marked in (a) (The lath morphology is marked by an arrow), (c), (d), (e), (f) TEM micrographs with higher magnification showing the microstructure within the area marked in (b) (The insets show the corresponding SAD patterns).

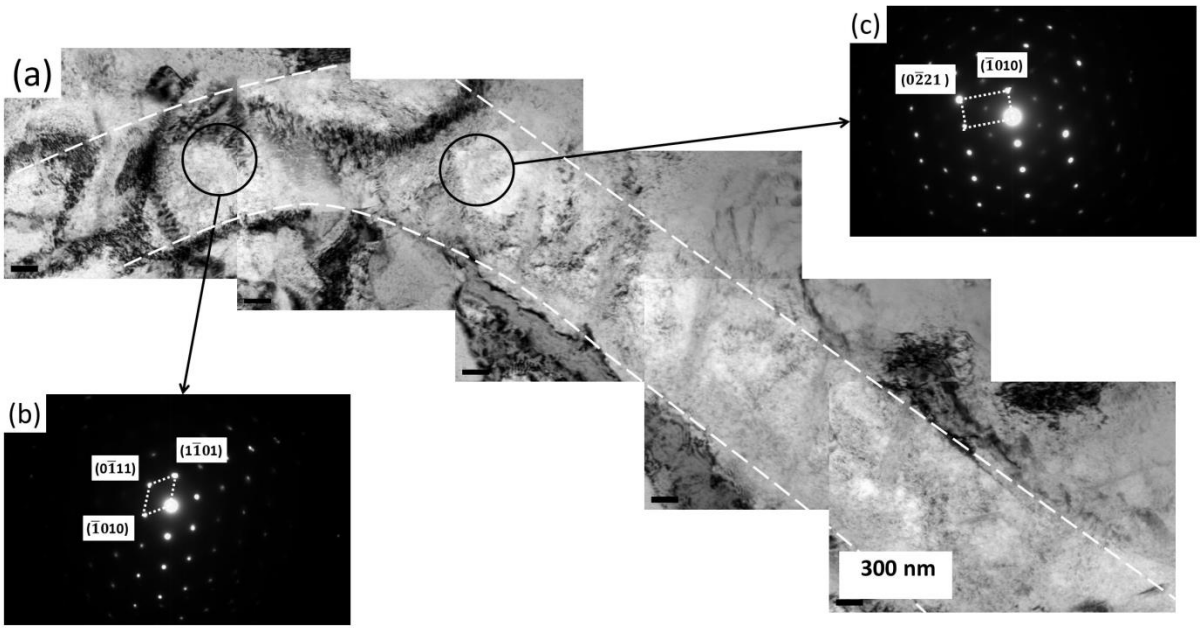

Fig.6. (a) Montage of TEM bright field images of α precipitate (marked by the arrow in Fig.6 (b)). (b) and (c) SAD patterns corresponding to the circled area. (The zone axis for (b) is $[1\bar{2}1\bar{3}]$, the zone axis for (c) is close to $[1\bar{2}1\bar{6}]$.)

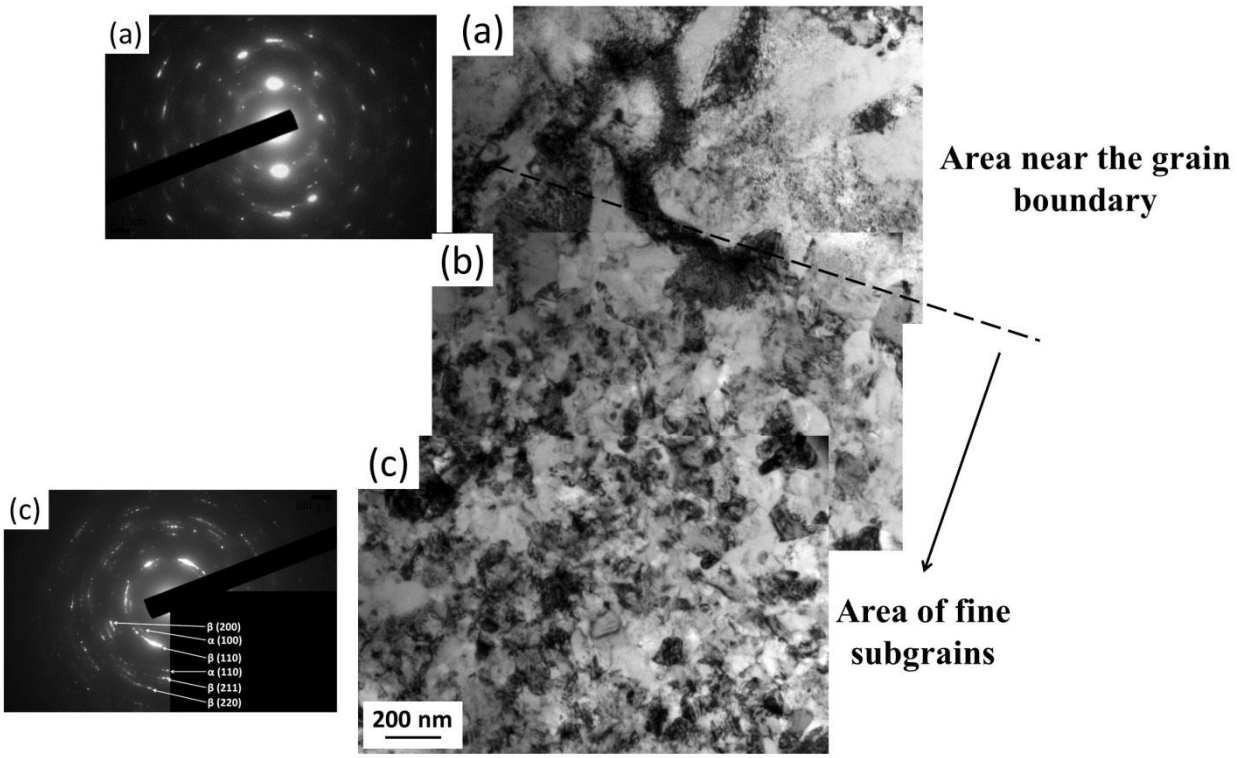

Fig.7. TEM bright-field micrographs of microstructures near the grain boundary α phase and corresponding SAD patterns (The SAD pattern of (c) has been indexed to the α and β phases).

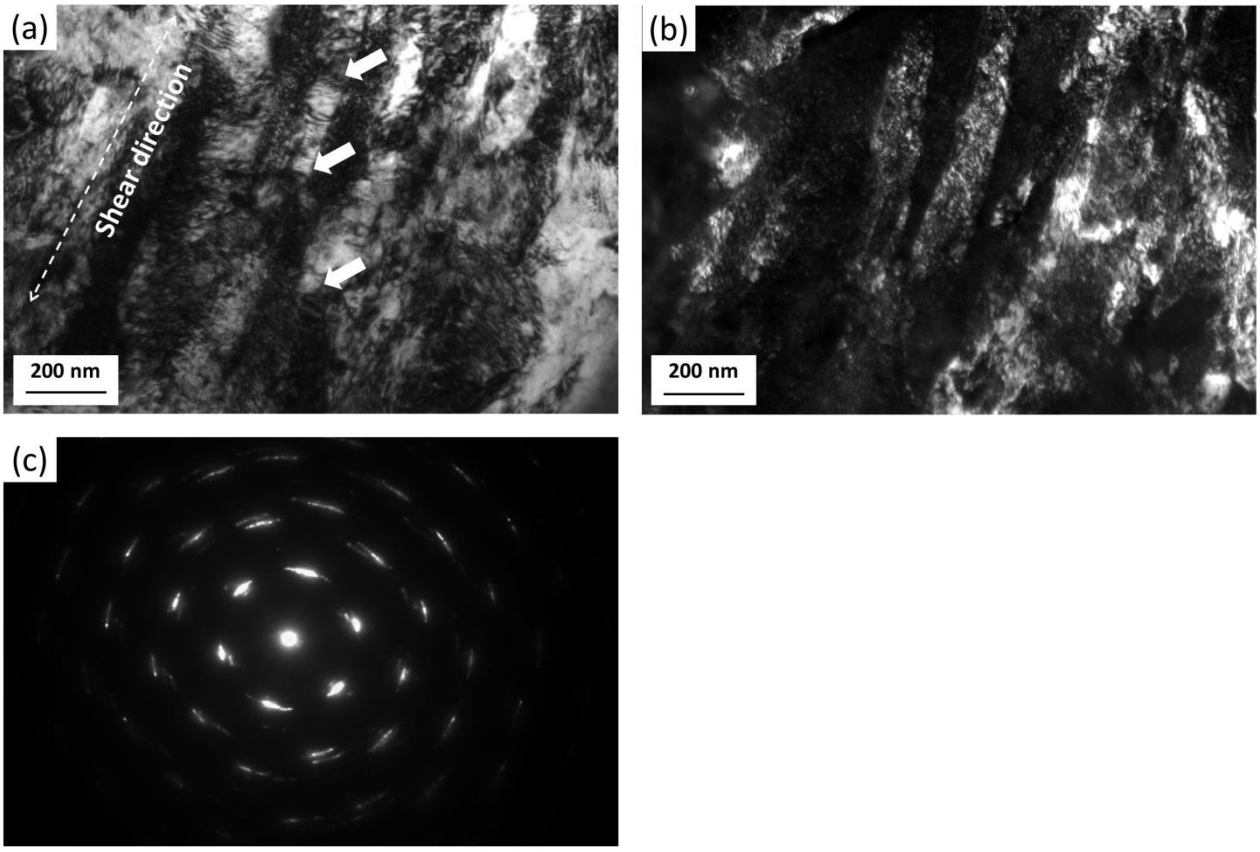

Fig.8. (a) Bright-field and (b) Dark-field micrographs of lamellar structures in the outer region of the ASB (dashed arrow denotes the shear direction and white arrows denote the transverse dislocation walls), (c) SAD pattern corresponding to (a).

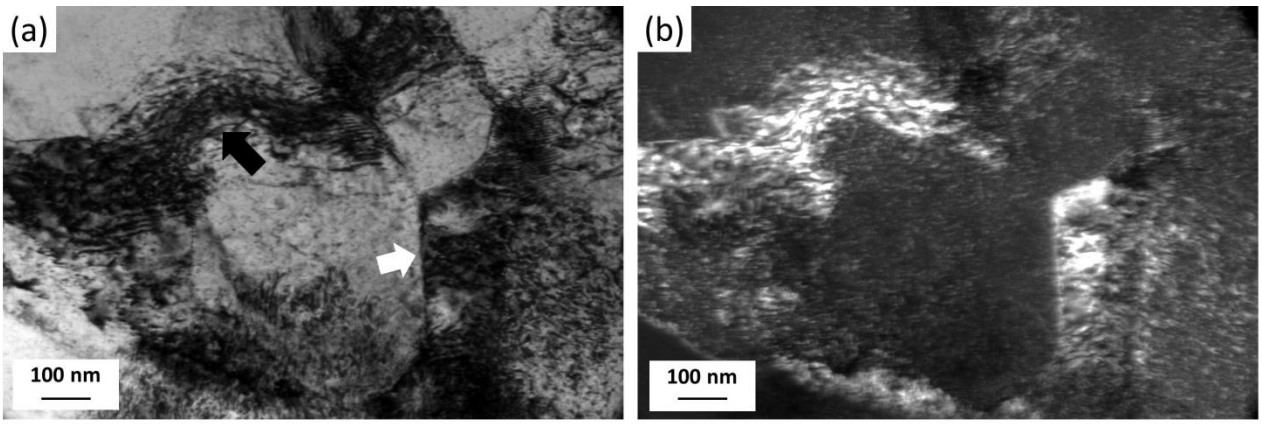

Fig.9. TEM (a) Bright-field and (b) Dark-field micrographs of cell structures in the outer region of the ASB. (A straight subboundary is marked by the white arrow and dislocation clusters marked by the black arrow.)

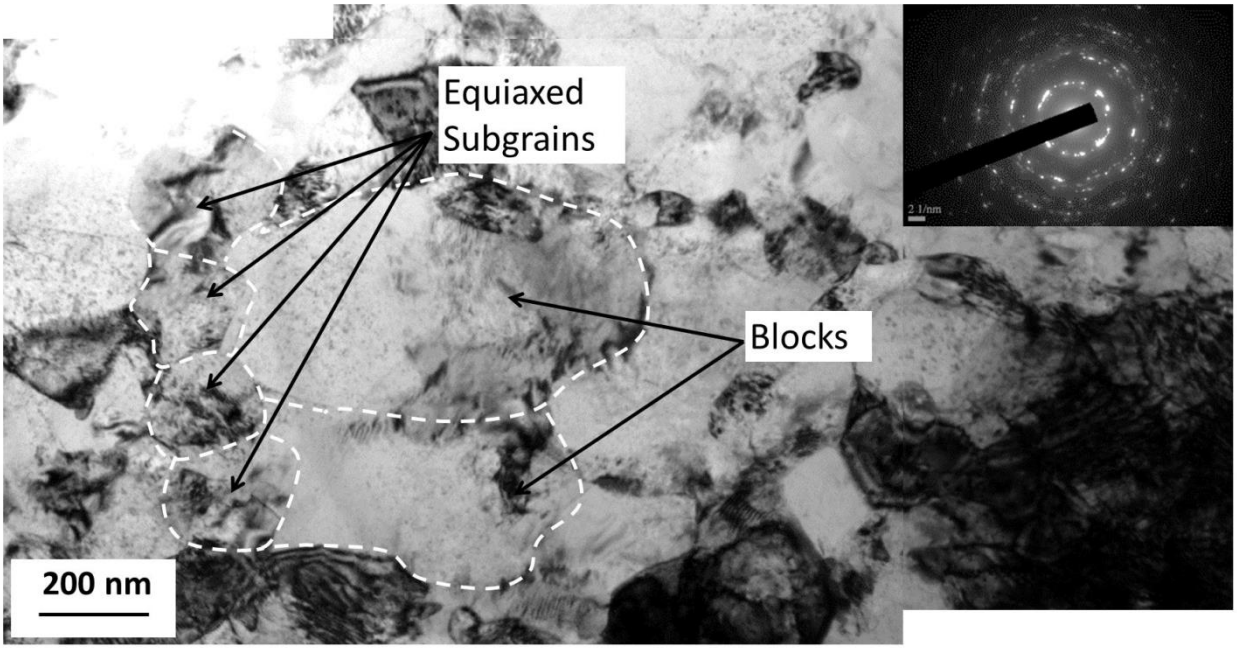

Fig.10. TEM bright-field micrograph showing the blocks surrounded by equiaxed subgrains with few dislocations in their interior. (Subboundaries of equiaxed subgrains and blocks have been delineated by dashed lines. The inset shows the corresponding SAD pattern.)

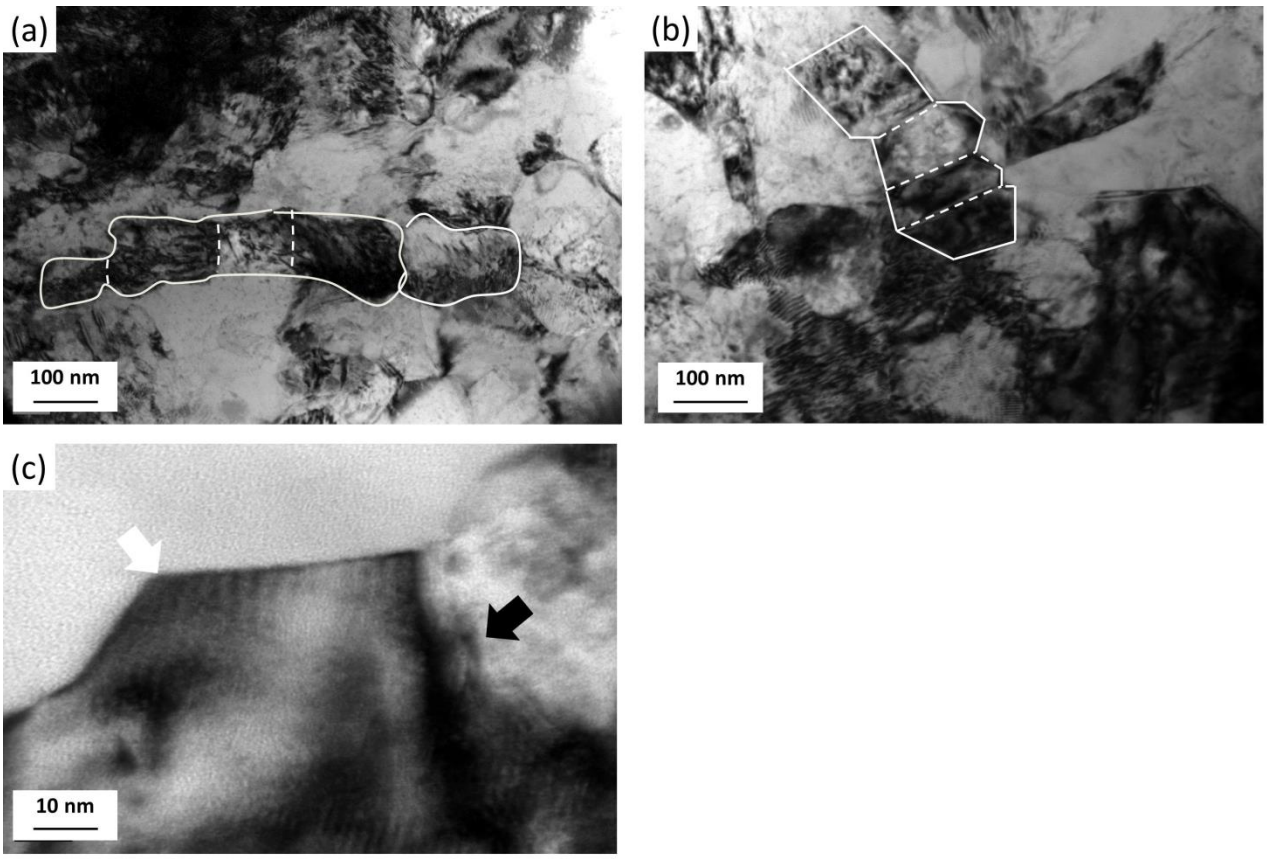

Fig.11. (a), (b) TEM bright-field micrographs of elongated subgrains breaking down into equiaxed subgrains (The route for the breakdown has been delineated by dashed lines). (c) High-angle boundaries marked by the white arrow and low-angle boundaries along the short axis marked by the black arrow.

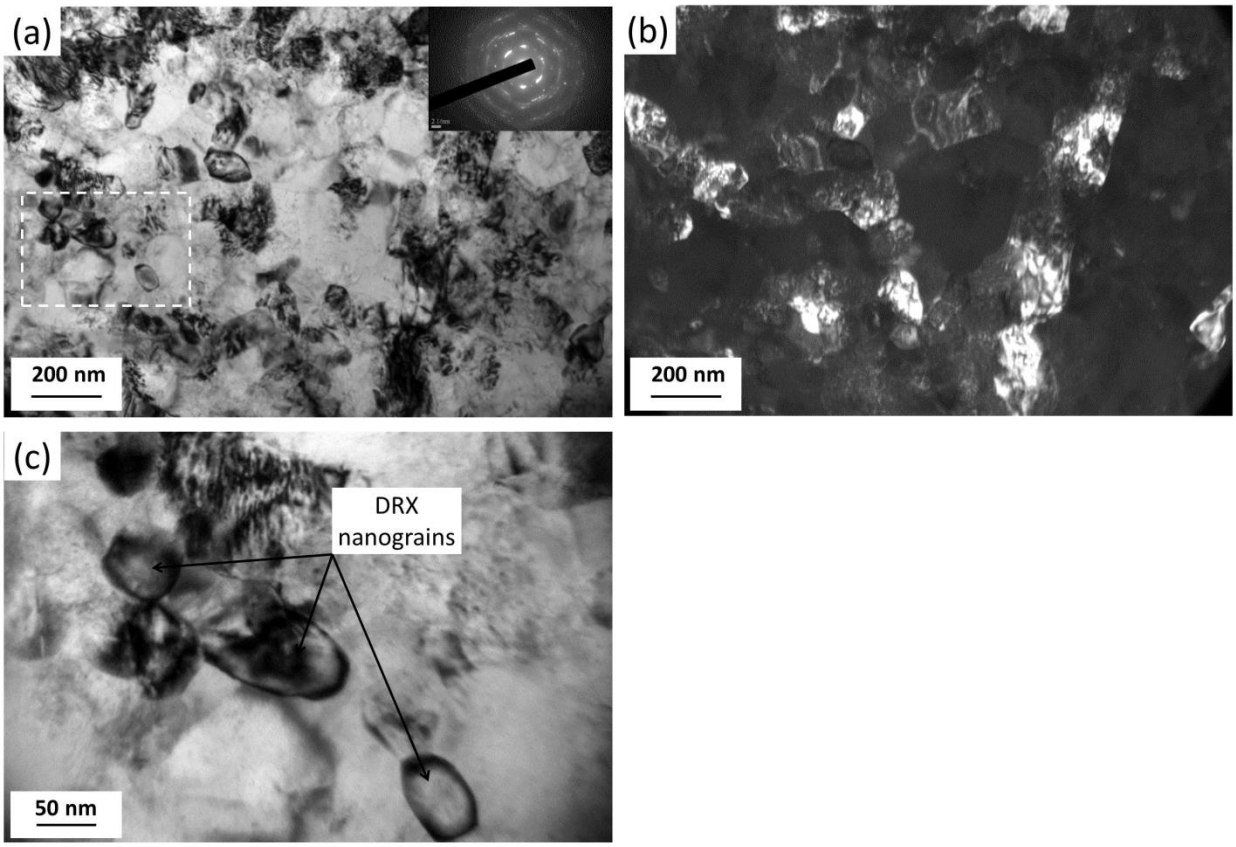

Fig.12. TEM (a) Bright-field and (b) Dark-field micrographs showing the mixture of DRX nanograins and equiaxed subgrains (The inset is the corresponding SAD pattern.), (c) TEM bright-field micrograph corresponding to the dashed area in (a).

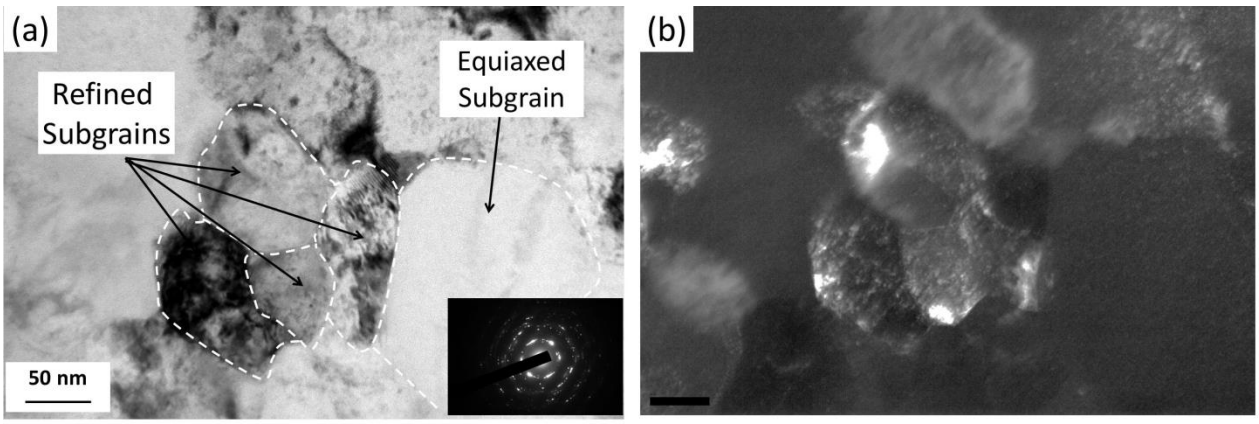

Fig.13. TEM (a) Bright-field and (b) Dark-field micrographs of the subdivision of blocks (The inset shows a corresponding SAD pattern. The subboundaires of equiaxed subgrains and refined subgrains have been delineated by dashed lines.)

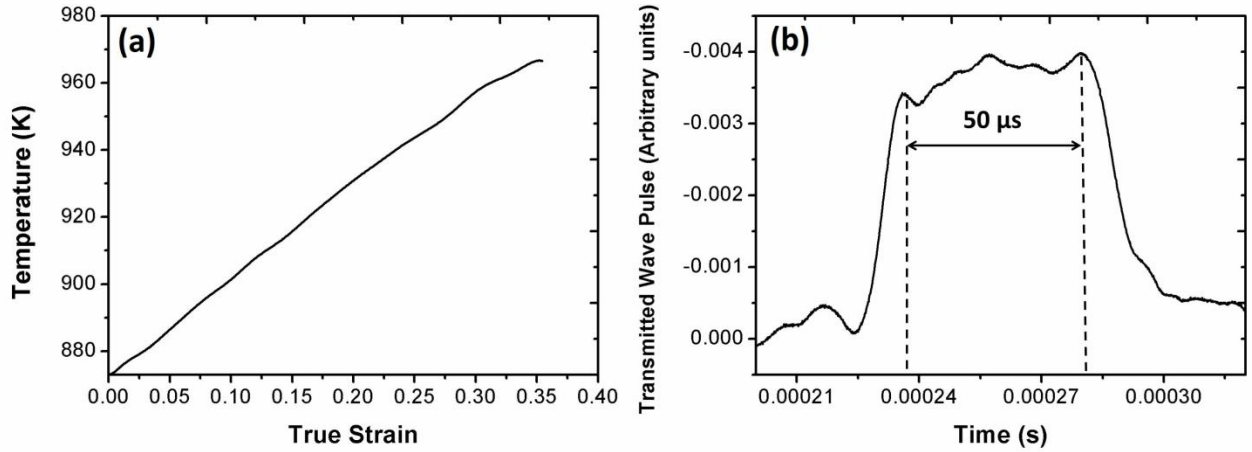

Fig.14. (a) Calculated temperature versus true strain and (b) Transmitted wave pulse versus time, from the SHPB tests at strain rate of 4000 s^{-1} and 873K.

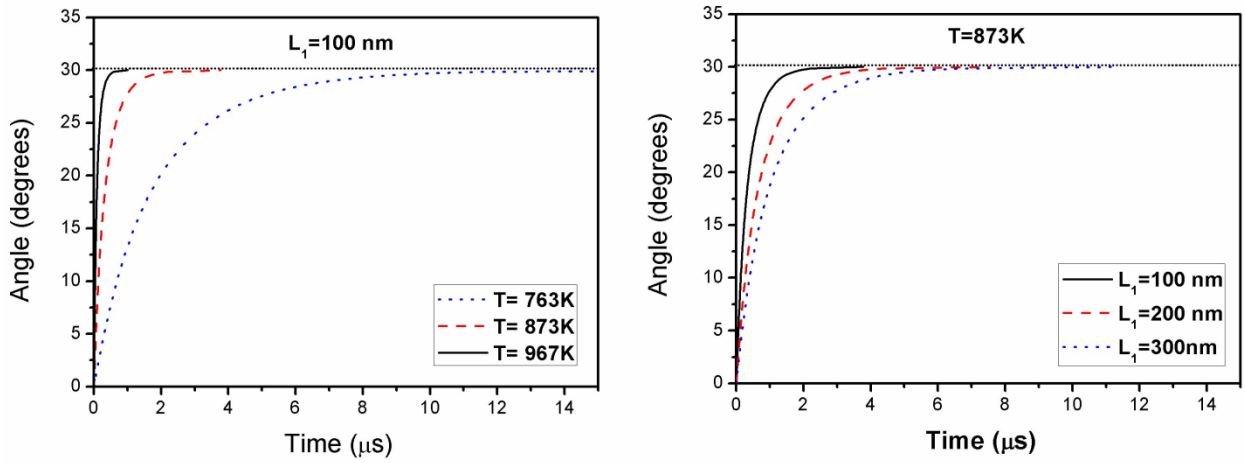

Fig.15. Angle of rotation of subgrain boundary as a function of time for (a) different temperatures for L_1 = 100 nm and (b) different subgrain sizes at 873K.

PAPER 3

Constitutive Modelling of the Flow Behaviour of A β Titanium Alloy at High Strain Rates and Elevated Temperatures Using the Johnson-Cook and Modified Zerilli-Armstrong Models

Hongyi Zhan, Gui Wang, Damon Kent, Matthew Dargusch

Materials Science and Engineering A

2014, Volume 612, Pages 71-79

Constitutive modelling of the flow behaviour of a β titanium alloy at high strain rates and elevated temperatures using the Johnson-Cook and modified Zerilli-Armstrong models

Hongyi Zhan[1,*], Gui Wang[1, 2], Damon Kent[1], Matthew Dargusch[1, 2]

[1]Centre for Advanced Materials Processing and Manufacture, School of Mechanical and Mining Engineering, The University of Queensland, St Lucia, Queensland 4072, Australia

[2]Defence Material Technology Centre, Level 2, 24 Wakefield St, Hawthorn VIC 3122, Australia

[*]h.zhan@uq.edu.au

Abstract

The objectives of this work are to characterize the flow behaviour of the Ti-6Cr-5Mo-5V-4Al (Ti6554) alloy at high strain rates and elevated temperatures using the Johnson-Cook (JC) model and a modified Zerilli-Armstrong (ZA) model, and to make a comparative study on the predictability of these two models. The stress-strain data from Split Hopkinson Pressure Bar (SHPB) tests over a wide range of temperatures (293-1173K) and strain rates (10^3-10^4 s^{-1}) were employed to fit parameters for the JC and the modified ZA models. It is observed that both the JC and the modified ZA models have good capacities of describing the flow behaviour of the Ti6554 alloy at high strain rates and elevated temperatures in terms of the average absolute error. The modified ZA model is able to capture the strain-hardening behaviour of the Ti6554 alloy better as it incorporates the coupling effects of strain and temperature. However, dynamic recovery or dynamic recrystallization that may happen at elevated temperatures should be taken into consideration when selecting data set for parameters fitting for the modified ZA model. Also the modified ZA model requires more stress-strain data for the parameters fitting than the JC model.

Key Words:

β titanium alloys; High strain rate deformation; Johnson-Cook model; Modified Zerilli-Armstrong model

1. Introduction

The usage of the β titanium alloys in the manufacturing of critical load bearing structural parts in the aerospace industry has continued to increase in the past decade owing to their excellent combination of high specific strength, superior fracture toughness and good corrosion resistance. In addition, this category of alloys is deep hardenable through heat treatment processes and has good forgeability which are important features for alloys which are used for manufacturing large section aerospace structures [2, 9, 225, 226]. For instance, forgings of Ti-10V-2Fe-3Al (Ti-10-2-3) are increasingly used in the hub of the main rotor system in helicopters and forgings of Ti-5Al-5Mo-5V-3Cr (Ti-5553) have been used for manufacturing landing gear in the Boeing-787 and Airbus-350 [25]. Knowledge of materials behaviour at high strain rates and elevated temperatures is necessary for applications such as ballistic impacts in armour applications and materials processing such as machining, hot forging, extrusion etc. Understanding and predicting the behaviour of materials under these extreme conditions is important for a number of fields in engineering including modelling of materials processing and structural behaviour under high strain rate deformation conditions using Finite Element Analysis (FEA). In general, the published information on the flow behaviour of β titanium alloys at high strain rates and elevated temperatures is limited. Therefore, it is important to evaluate and predict the flow behaviour of β titanium alloys over a wide range of strain rates and temperatures.

Materials constitutive models are used to describe the relationship between flow stress and strain, strain rate and the temperature of materials. This forms the foundation for FEA modelling of the deformation behaviour of materials. Several constitutive models based on different theories have been proposed and can be sorted into three different types: phenomenological, semi-empirical based and physically based models, respectively. Two physically based models: the Mechanical Threshold Stress (MTS) model [126] and the Bammann-Chiesa-Johnson(BCJ) model [137] are based on specific physical theory and are capable of providing good agreement with the experimental results. However, parameters for these two models are difficult to obtain as they always require some data from strictly controlled experimental conditions. In addition, the accuracy of some material property constants used in these physically based models is still in doubt. Morevoer, these physically based models are not readily available in finite element code. Compared with the physically based models, the Johnson-Cook (JC) model [138], one of the most frequently used empirical models, is preferred by investigators because the parameters for the JC model can be obtained using fewer stress-strain curves due to its simple mathematical form. Also, the JC model can be directly applied to the major commercial finite element packages. In order to improve the

accuracy of the JC model, several modifications have been performed including integration of adiabatic temperature rises [100] and microstructural changes [88, 146, 147] into the model. The main drawback of the JC model lies in its simple mathematical form as it neglects the coupled effects of strain rate and temperature on the flow stress. Also, being an empirical model the average absolute error will increase with increasing deviation of temperature or strain rate from the reference condition defined by the user [139]. Another frequently used constitutive model available in finite element code is the Zerilli-Armstrong (ZA) model [101]. Although the ZA model is based on dislocation dynamics, the parameters for the model are still determined by fitting the model to the stress-strain curves of the materials in a similar way to the JC model. Therefore the ZA model is still a form of semi-empirical model. Some researchers prefer the ZA model to the JC model as the former not only incorporates the coupled effects of strain rate and temperature but also considers dislocation characteristics for particular structures. Even though parameters for the ZA model for the Ti6Al4V alloy and different steels [84, 96, 143, 152-156] have been proposed in recent years, some materials constants for the ZA model are very difficult to validate as they require a stress at 0 K and the athermal stress of the materials. Also, it is not valid to use the ZA model for temperatures above half of the melting temperature of the materials [155]. In order to overcome these barriers, Dipti et al. introduced the reference condition into the ZA model and succeeded in using this modified model to predict the mechanical behaviour of a titanium-modified austenitic stainless steel [157] and a modified 9Cr-1Mo steel [158] at low strain rates and elevated temperatures. However, there is still an uncertainty that if this modified version can be used within the high strain rate domain. Therefore further investigations are required to test its applicability.

So far, investigations into the constitutive models for titanium alloys have mainly focused on the Ti6Al4V alloy and several sets of parameters for the JC model have been developed. Very few studies have been concluded on the constitutive model for metastable β titanium alloys. Hokka et al. [134] has obtained one set of parameters for the JC model applied to the metastable beta titanium alloy Ti-15V-3Cr-3Al-3Sn.

The Ti-6Cr-5Mo-5V-4Al (Ti6554) alloy is a newly-developed metastable β alloy with an ultimate tensile strength (UTS) of around 1250MPa and fracture toughness (KIC) from 80 to 90 MPa $m^{1/2}$ after solution and aging treatments [28, 29]. In terms of damage tolerance, the Ti6554 alloy is promising potential for applications in the aerospace industry. The objective of the current study is to evaluate and predict the flow behaviour of the Ti6554 alloy over a wide range of strain rates at elevated temperatures using the JC and modified ZA constitutive models.

2. Experimental procedures

2.1 Sample Preparation

The Ti–6Cr–5Mo–5V–4Al alloy was casted by multiple vacuum arc melting. Ingots of 620 mm diameter were forged to 60% strain at around 1150℃, and then forged with further 70% deformation in the α/β dual phase zone, reducing the diameter to 110 mm. Cylindrical rods with 10 mm in diameter and 80 mm in length were hot rolled from the forged ingots. The chemical composition of the alloy is listed in Table 1. Hot rolled cylindrical rods of the Ti6554 alloy were solution treated at 1100 K for 1 h in a protective Argon atmosphere and then air cooled. Aging treatments were conducted on the solution treated Ti6554 rods at 833 K for 8 h under ambient atmosphere and then air cooled. Specimens for microstructural observation were wet ground using silicon carbide papers, mechanically polished and ultrasonically cleaned. Specimens for Optical Microscopy (OM) and Scanning Electron Microscopy (SEM) were etched using Kroll's Reagent (2% hydrofluoric acid, 6% nitric acid and 92% distilled water). SEM was performed on a XL30 instrument. The original microstructure of the Ti6554 alloy, consisting of β phase matrix with α phase precipitates, is shown in Fig.1. Cylindrical specimens with a diameter of 5 mm and length of 4 mm for high strain rate tests were cut from rods using electrical discharge machining with a slow cutting speed to minimise the heat affected zone on the samples. For the tests at a strain rate of 10^4 s^{-1}, a smaller cylindrical specimen with a diameter of 2 mm and length of 1.5 mm were required due to equipment limitations. As the aspect ratio was maintained, the effect of specimen dimension will not affect the experimental results.

2.2 High Strain Rate Testing

Mechanical behaviour of the Ti6554 alloy at high strain rates was tested using a Split Hopkinson Pressure Bar (SHPB) arrangement at strain rates from $1000s^{-1}$ to $10000s^{-1}$ and temperatures from 293K to 1173K. The SHPB device consists of a striker bar, an input (or incident) bar and an output (or transmitted) bar as shown in Fig.2. The specimen is sandwiched between the input and output bar. Once the striker bar impacts the input bar, a pulse referred to as the incident pulse will be created going through the input bar into the specimen. When the pulse reaches the interface between the input bar and the specimen, part of the pulse (reflected pulse) will be reflected back to the input bar while the rest (transmitted pulse) will be transmitted to the output bar through the specimen. These pulses are recorded by strain gages mounted on the bars. The flow stress σ, strain ε and strain rate $\dot{\varepsilon}$ are then calculated using the following equations:

$$\sigma = E\frac{A_b}{A_s}\varepsilon_t \quad (1)$$

$$\dot{\varepsilon} = -2\frac{C_0}{L}\varepsilon_R \quad (2)$$

$$\varepsilon = -2\frac{C_0}{L}\int \varepsilon_R \, dt \quad (3)$$

ε_R and ε_t represent the reflected pulse and transmitted pulse, respectively. A_b is the cross-sectional area of the bars, A_s is the cross-sectional area of the specimen and L is the gauge length of the specimen. C_0 is the elastic wave speed in the bars which can be calculated by the equation $\sqrt{E/\rho}$ where E and ρ correspond to Young's modulus and the density of the specimen, respectively.

For the experiments at elevated temperatures, the specimens were heated by an in-situ induction coil and the temperature was regulated by a thermocouple not in contact with the specimen. After reaching the designated temperature, the specimen was maintained at the designated temperature for approximately 2 minutes to ensure a uniform temperature distribution. The incident and transmitted bars were then assembled by a pushing support. The striker bar was launched with the assembly of incident and transmitted bars synchronously to avoid temperature drops in the specimen. The assembly must be completed before the stress wave arrives at the incident bar. The contact time should also be controlled to within 500 ms as the contact between the bars and the specimen will lead to a temperature drop in the specimen. In order to decrease the friction between the contact surfaces of the bars and specimen, molybdenum sulphide was used as a lubricant.

3. Results and discussion

3.1 Flow stress behaviour

Flow curves of the Ti6554 alloy at a range of temperatures (293-1173K) and strain rates (10^3-10^4 s^{-1}) are shown in Fig.3. It could be observed that the flow stress increases with increasing strain rates and decreasing temperatures. Furthermore, flow stress of the Ti6554 alloy is more sensitive to temperature than strain rate. Flow curves at 293K all exhibit a negative strain hardening rate while the strain hardening rate will increase to become positive with increasing temperature, which has been attributed to dynamic strain aging (DSA) caused by the activation of solute Cr atoms in our previous study [30]. The flow curve from the test at 1173K and 4000 s^{-1} in Fig.3 (b) reveals a small peak at a strain of 0.125 followed by a gradual drop of stress towards a plateau, which is the main characteristic of dynamic recrystallization (DRX). This is in accordance with the SEM image shown

in Fig.4 (a) in which some DRX grains have been observed. As the β transus of the Ti6554 alloy is around 1023K, α precipitates have been dissolved into the β matrix in the specimens deformed at 1173K as shown in Fig4 (a) and (b). Specimens deformed at high strain rates and temperatures below 873K all exhibit the similar microstructure as shown in Fig.4 (c) in which α phase precipitates cluster inside the β matrix and nucleate along the β grain boundaries. A kind of string-like α precipitate stretching across some grains has been observed in the samples deformed at strain rates of 4000 s^{-1} and 10000 s^{-1} when the experimental temperature is raised to 873K as shown in Fig.4 (d). This kind of novel α precipitates morphology has been described in detail in our previous study [30]. Though these precipitates of high aspect ratio are supposed to act as barriers to the dislocations movement, no obvious strengthening phenomenon has been observed in flow curves in Fig.3. Hence this microstructural change can be neglected in the constitutive modelling of the flow behaviour of the Ti6654 alloy in order to simplify the establishment of constitutive models.

3.2 Establishment of materials constitutive models

3.2.1 Johnson-Cook model

The basic form of the JC model is defined by the product of three distinctive mathematical terms:

$$\sigma = (A + B\varepsilon^{n})\left(1 + C\ln\frac{\dot{\varepsilon}}{\dot{\varepsilon}_0}\right)\left[1 - \left(\frac{T - T_r}{T_m - T_r}\right)^{m}\right] \quad (4)$$

in which σ is the equivalent flow stress, ε is the equivalent plastic strain, $\dot{\varepsilon}$ is the equivalent plastic strain rate and $\dot{\varepsilon}_0$ is the reference equivalent plastic strain defined by the user (usually defined as 1.0 s^{-1} or 1×10^{-3} s^{-1}). T, T_r and T_m are the workpiece temperature, reference temperature (the minimum temperature under the experiment conditions) and materials melting temperature, respectively. There are five parameters in this model in which A is the yield stress, B and n are used to describe strain hardening effects, C accounts for strain rate hardening and m accounts for thermal softening effects.

The procedures for parameters fitting for the JC model are illustrated below: Taking 293K as the reference temperature and 10^{-3} s^{-1} as the reference strain rate, the dynamic behaviour of the Ti6554 alloy can be represented accurately by the power law equation under the reference condition:

$$\sigma = (A + B\varepsilon^{n}) \quad (5)$$

The value A is the yield stress under the reference condition (or stress at a strain of 0.002). Then plotting of ln(σ-A) vs. lnε gives B from the y-intercept and n from the slope. However, it was observed in our previous study [30] that the flow stress of the Ti6554 alloy tends to increase to a

greater degree beyond a strain rate of 10^3 s^{-1}. Therefore a better approach would be to use a higher strain rate, 10^3 s^{-1}, as the reference strain rate. Following the steps above, A, B and n are calculated out to be 1397.5 MPa, -569.47 MPa and 1.215, respectively.

At the reference temperature of 293K with a fixed strain of 0.10, the JC model can be simplified to:

$$\sigma/\sigma_0 = 1 + C\ln\dot{\varepsilon} \tag{6}$$

where σ_0 is the stress at $\dot{\varepsilon}$= 1000 s^{-1}, T=293K and ε=0.10. Using the flow stress at the same temperature and strain but different strain rates to plot the curve $\{(\sigma/\sigma_0)-1\}$ vs. $\ln\dot{\varepsilon}$ gives C from the slope of the curve. C is calculated to be 0.03052 and the results of fitting are shown in Fig.5 (a).

At a strain rate of 4000 s^{-1} with a fixed strain of 0.10, the JC model can be written as:

$$\sigma/\sigma_b = 1 - T^{*m} \tag{7}$$

where σ_b is the stress at $\dot{\varepsilon}$= 4000 s^{-1}, T=293K and ε=0.10. Using flow stress data at the same strain rate and strain but different temperatures to plot a curve of $\ln(1-\sigma/\sigma_b)$ vs. $\ln T^*$ gives m from the slope of this curve. For high strain rate deformations, it is important to incorporate adiabatic heating into the model. One equation has been extensively used to estimate the temperature elevation during high strain rate deformation:

$$\Delta T = \frac{\eta}{\rho c}\int_{\varepsilon_i}^{\varepsilon_{i+1}} \sigma(\varepsilon_i, \dot{\varepsilon}_i, T_i)\, d\varepsilon \tag{8}$$

in which ρ and c are the density and specific heat capacity of the material, respectively. The integral is the plastic work i.e. the area under the stress-strain curve. η is the heat fraction coefficient. The prevalent perspective is to define η as 0.9 [80, 85, 132]. Following the procedures above, m is calculated out to be 0.91 and the fitting results are shown in Fig.5(b).

Parameters for the Ti6554 alloy to suit the JC model are listed in Table.2. They were derived from the data set shown in Fig.5(a) and Fig.5(b). Another five curves performed under different conditions were used to validate the effectiveness of the JC model for the Ti6554 alloy. The comparison between the predicted curves and experimental curves is shown in Fig.5(c). The average absolute error (Δ) is used to assess the fitting results. Δ is defined as:

$$\Delta = \frac{1}{N}\sum_{N}^{i=N}\left|\frac{\sigma_{exp}^{i} - \sigma_{p}^{i}}{\sigma_{exp}^{i}}\right| \times 100 \tag{9}$$

The average absolute error of the fitting results in Fig.5(c) is 6.0 %.

3.2.2 Modified ZA model

The format of the modified ZA model is modified on the basis of the ZA fcc model [157] :

$$\sigma = (C_1 + C_2\varepsilon^n)\exp\{-(C_3 + C_4\varepsilon)T^* + (C_5 + C_6T^*)\ln\dot{\varepsilon}^*\} \quad (10)$$

$$T^* = T - T_{ref} \quad (11)$$

$$\dot{\varepsilon}^* = \dot{\varepsilon}/\dot{\varepsilon}_{ref} \quad (12)$$

in which σ is the equivalent flow stress, ε is the equivalent plastic strain. $\dot{\varepsilon}$ is the equivalent plastic strain rate and $\dot{\varepsilon}_{ref}$ is the reference equivalent plastic strain defined by user. T and T_{ref} are the workpiece temperature and reference temperature, respectively. $C_1, C_2, C_3, C_4, C_5, C_6$ and n are seven parameters of the modified ZA model. The rationale for the modifications to the ZA model were described in detail in [157] and [158]. The procedures to determine the parameters for the modified ZA model are illustrated below:

A strain rate of 1000 s^{-1} and temperature of 293K were used as the reference strain rate and temperature due to the same reason stated in Section 3.2.1 for the Johnson-Cook model. Under the reference condition, the modified ZA model can be simplified to:

$$\sigma = C_1 + C_2\varepsilon^n \quad (13)$$

C_1 represents the yield stress under the reference condition with C_2 and n accounting for the effects of strain hardening on the flow stress. Then plotting the curve ln(σ-C_1) vs. lnε gives C_2 and n from the y-intercept and slope of the curve, respectively.

Then at the reference strain rate, Eq. (10) can be simplified to:

$$\sigma = (C_1 + C_2\varepsilon^n)\exp[-(C_3 + C_4\varepsilon)T^*] \quad (14)$$

Taking the natural logarithm of Eq.(14), it can be expressed as:

$$\ln\sigma = \ln(C_1 + C_2\varepsilon^n) - (C_3 + C_4\varepsilon)T^* \quad (15)$$

$$S_1 = C_3 + C_4\varepsilon \quad (16)$$

S_1 describes thermal softening effect and C_4 is used to quantify the influence of strain on the thermal softening effect. S_1 can be obtained by the slope of the curve lnσ vs. T*. It is found that the slope of the curve lnσ vs. T*, S_1, becomes smaller as shown in Fig.6 (a) when the data from the testing at 1173K is involved in the fitting. Plotting the curve S_1 vs. ε gives C_3 and C_4 from the y-

intercept and slope of the curve, respectively. By plotting the curve S_1 vs. ε it is found that S_1 decreases much slower with increasing strains (0.05-0.15 in steps of 0.025), as shown in Fig.6 (b), when the data from the test at 1173K is included in the parameters fitting. Considering this difference, it is necessary to clarify the influence of the data set selected for the parameters fitting on the predictability of the modified ZA model.

By taking the natural logarithm of Eq. (10) at a fixed strain, we can get:

$$\ln\sigma = \ln(C_1 + C_2\varepsilon^n) - (C_3 + C_4\varepsilon)T^* + (C_5 + C_6T^*)\ln\dot{\varepsilon}^* \quad (17)$$

$$S_2 = C_5 + C_6T^* \quad (18)$$

S_2 quantifies the strain rate hardening effect and it can be obtained from the slope of the curve $\ln\sigma$ vs. $\dot{\varepsilon}^*$. Plotting the curve S_2 vs. ε gives C_5 and C_6 from the y-intercept and slope of the curve.

Two sets of parameters for the modified ZA model for the Ti6554 alloy have been obtained in Table 3 and Table 4. Fitting results using parameters in Table 3 and Table 4 are shown in Fig.7 and Fig.8, respectively. When the data from tests at 1173K is included in the parameters fitting, the agreement between the predicted data and experimental data is poor as shown in Fig.7. When the data from tests at 1173K is excluded, a much better agreement was observed as shown in Fig.8. A large deviation between the experimental data and calculated data in Fig.8 is only observed at strains larger than 0.125 under the condition of 4000/s and 1173K. This can be attributed to the dynamic recrystallization observed in Fig.4 (a), which cannot be predicted by the modified ZA model. In terms of the fitting results, parameters in Table 4 should be selected to verify the effectiveness of the modified ZA model.

As the parameters in Table 4 were derived from the data set shown in Fig.7 and Fig.8, another three stress-strain curves performed under different conditions were employed to validate the reliability of the modified ZA model. A good agreement has been achieved between experimental data and calculated data as shown in Fig.9. The average absolute error (Δ) of the fitting results in Fig.9 is 5.7%.

3.3 Discussion

One of the main characteristics of the strain hardening behaviour of the Ti6554 alloy at high strain rates over a wide range of temperatures is that flow curves show a negative slope at 293K but the strain hardening rate will increase to become positive with increasing temperature. Both the JC model and the modified ZA model are capable of predicting the dynamic flow behaviour of the

Ti6554 alloy at high strain rates and elevated temperatures in terms of the average absolute error. However, the modified ZA model is able to give a much better description of the strain-hardening behaviour of the Ti6554 alloy than the JC model.

For the JC model, all the predicted curves maintain a negative slope following the curve performed under the reference condition as shown in Fig.5. This can be explained by the format of the strain hardening rate derived from the JC model:

$$d\sigma/d\varepsilon = (Bn\varepsilon^{n-1})\left(1 + C\ln\frac{\dot{\varepsilon}}{\dot{\varepsilon}_0}\right)\left[1 - \left(\frac{T-T_r}{T_m-T_r}\right)^m\right] \quad (19)$$

The sign of the strain hardening rate, dσ/dε, is only determined by parameters B and n which are derived from the stress-strain curve under the reference condition. Therefore the sign of dσ/dε will not change with strain, strain rate or temperature. It is also reported that in the JC model the strain-hardening rate will increase with increasing strain rate but decrease with increasing temperatures [152]. In general, the JC model is inadequate to capture the complex strain hardening behaviour of the Ti6554 alloy. It is also found that the prediction of the JC model is particularly satisfactory when the strain is near to 0.10 which is the fixed strain in the fitting of parameters C and m for the JC model. However, the average absolute error of the fitting results in Fig.5 (c) gradually increases with increasing deviation of strain from 0.10 as shown in Fig.10. This indicates that the JC model is only capable of predicting the dynamic flow behaviour of materials very accurately in a narrow domain near the specific strain which is fixed in the parameters fitting for the JC model. In addition, the parameters C and m for the JC model have been reported to be dependent on the strain that is fixed in the parameters fitting process [139].

The modified ZA model has a better capacity to capture the strain hardening behaviour of the Ti6554 alloy at high strain rates as it incorporates the coupling effects of strain and temperature on the flow stress. The format of $d\ln\sigma/d\varepsilon$ can be derived from the modified ZA model i.e. Eq. (10):

$$d\ln\sigma/d\varepsilon = d\ln(C_1 + C_2\varepsilon^n)/d\varepsilon - C_4T^* \quad (20)$$

According to Eq. (20), the negative sign of C_4 in Table 3 and Table 4 implies that the strain hardening rate will increase with increasing temperature. Comparing parameters in Table 3 with those in Table 4, it is found that a significant difference between these two sets of parameters is that the absolute value of C_4 decreases from 2.22×10^{-3} in Table 4 to 5.2×10^{-4} in Table 3. This indicates that the poor agreement between the predicted and experimental data in Fig.7 is caused by the reduction of C_4. This reduction of C_4 in Table 3 should be caused by the almost zero slope of the flow curve from the test at 1173K. This drop of strain hardening rate at 1173K may be attributed to

dynamic recovery or dynamic recrystallization that happen at elevated temperatures. This indicates that when selecting data set for parameters fitting for the modified ZA model, temperature range should be taken into consideration in order to eliminate the influence of dynamic recovery or dynamic recrystallization on the modelling of strain hardening behaviour.

It should also be kept in mind that the JC model only has 5 parameters to evaluate while the modified ZA model has 7. In addition, the modified ZA model requires more experimental data for parameters fitting than the JC model.

4. Conclusions

Original Johnson-Cook (JC) model and a modified Zerilli-Armstrong (ZA) model have been established to characterize the flow behaviour of the Ti6554 alloy over a wide range of strain rates (10^3-10^4 s^{-1}) and temperatures (293K-1173K) , respectively. Based on this study, following are the conclusions:

1. The main characteristic of the flow behaviour of the Ti6554 alloy at high strain rates is that flow curves exhibit a negative strain hardening rate at 293K while the strain hardening rate will increase to become positive with increasing temperature. The formation of string-like α precipitate can be neglected in the constitutive modelling process as it does not induce extra strengthening effects.

2. The JC model is capable of predicting the dynamic flow behaviour of materials accurately in a narrow domain near the strain value which is fixed in the parameters fitting for the JC model. However the format of the JC model is inadequate to track the complex strain-hardening behaviour of the Ti6554 alloy.

3. The modified ZA model has a much better capacity of describing the strain-hardening rate of the Ti6554 alloy as it incorporate the coupled effects of strain and temperature. However, the temperature range should be controlled when selecting data for parameters fitting for the modified ZA model in order to eliminate the influence of dynamic recovery or dynamic recrystallization.

Acknowledgements

The authors would like to acknowledge the support of the Queensland Centre for Advanced Material Processing and Manufacturing (AMPAM) and the Defence Materials Technology Centre (DMTC). The authors also acknowledge BaoTi Group Ltd., Baoji, China for the provision of the Ti6554 alloy and China Scholarship Council for the scholarship support.

Table 1

Chemical composition (wt. %) of the Ti6554 alloy

Materials	Cr	Mo	V	Al	O
Ti6554	6.05	4.95	5.09	4.20	0.19

Table 2

Parameters of Ti6554 for the JC model

JC model parameter	A(MPa)	B(MPa)	n	C	m
Value	1397.5	-569.47	1.215	0.03052	0.91

Table 3

Parameters for the modified ZA model for Ti6554 with data at 1173K included in fitting process

Parameter	C_1(MPa)	C_2(MPa)	n	C_3	C_4	C_5	C_6
Value	1397.5	-569.47	1.215	0.00113	-5.2×10^{-4}	0.03131	-3.12×10^{-5}

Table 4

Parameters for the modified ZA model for Ti6554 with data at 1173K excluded in fitting process

Parameter	C_1(MPa)	C_2(MPa)	n	C_3	C_4	C_5	C_6
Value	1397.5	-569.47	1.215	0.0012	-0.00222	0.03136	-3.21×10^{-5}

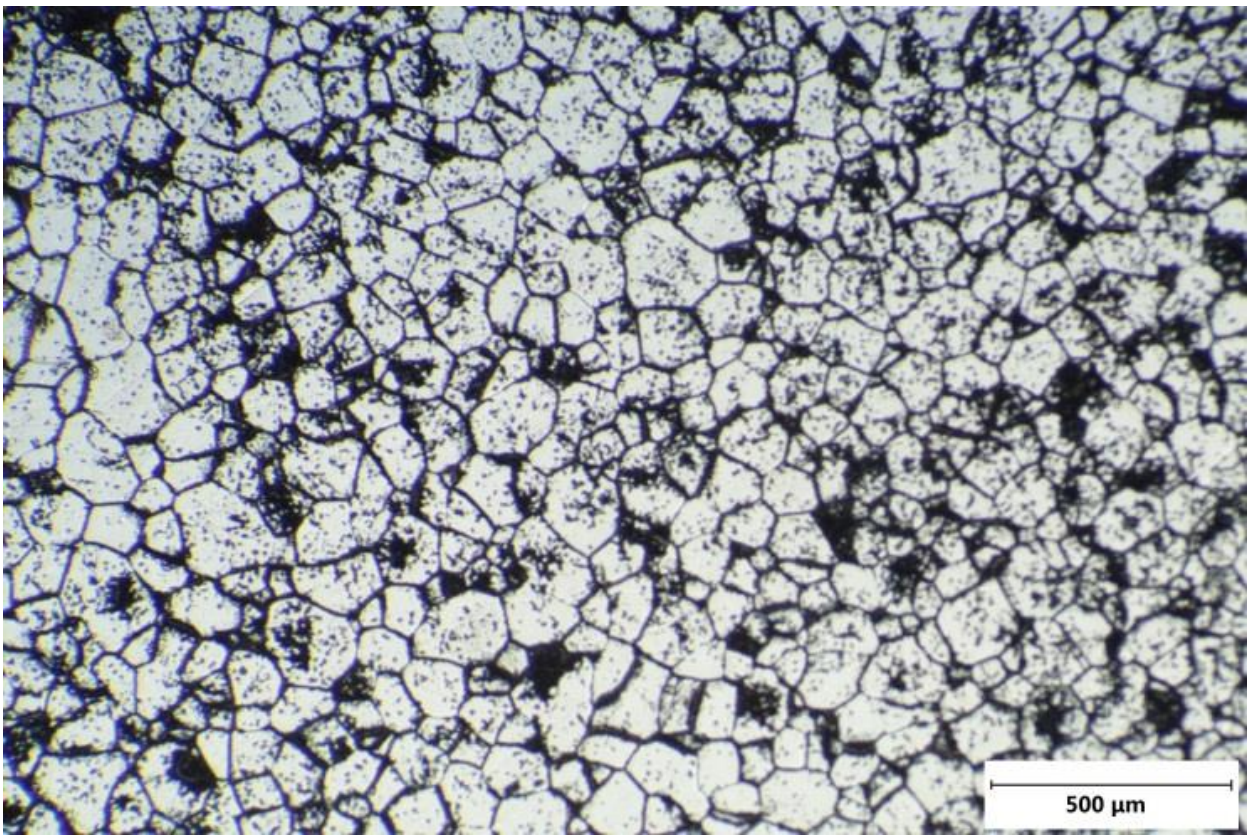

Fig.1. Optical micrograph of the initial microstructure of the Ti6554 alloy

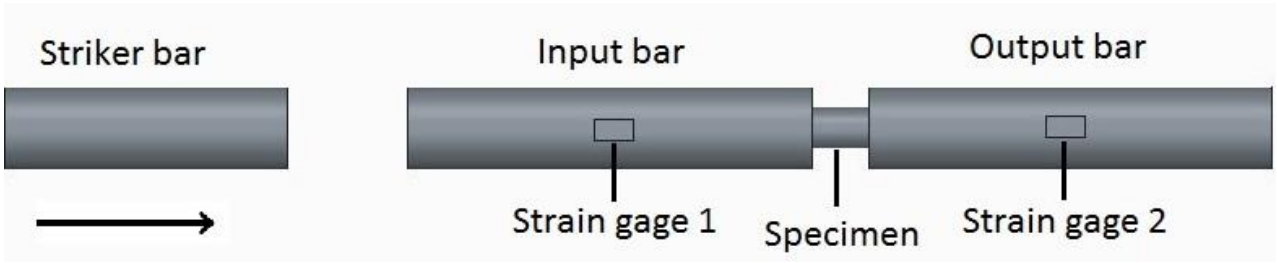

Fig.2. Schematic showing the arrangement of the SHPB device**.**

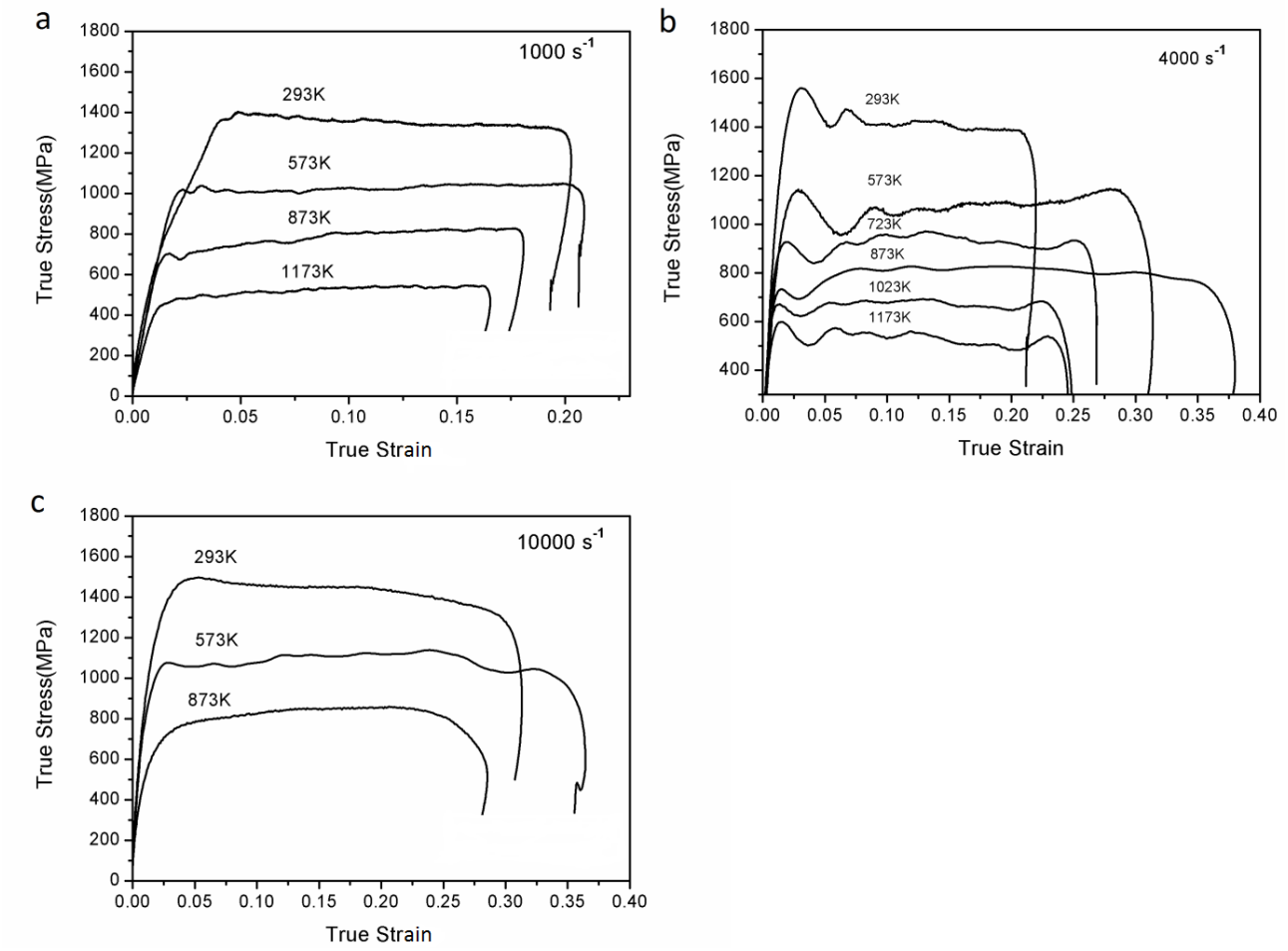

Fig.3. True stress-strain curves of the Ti6554 alloy at various temperatures with strain rate of (a) 1000 s^{-1} (b) 4000 s^{-1} (c) 10000 s^{-1}

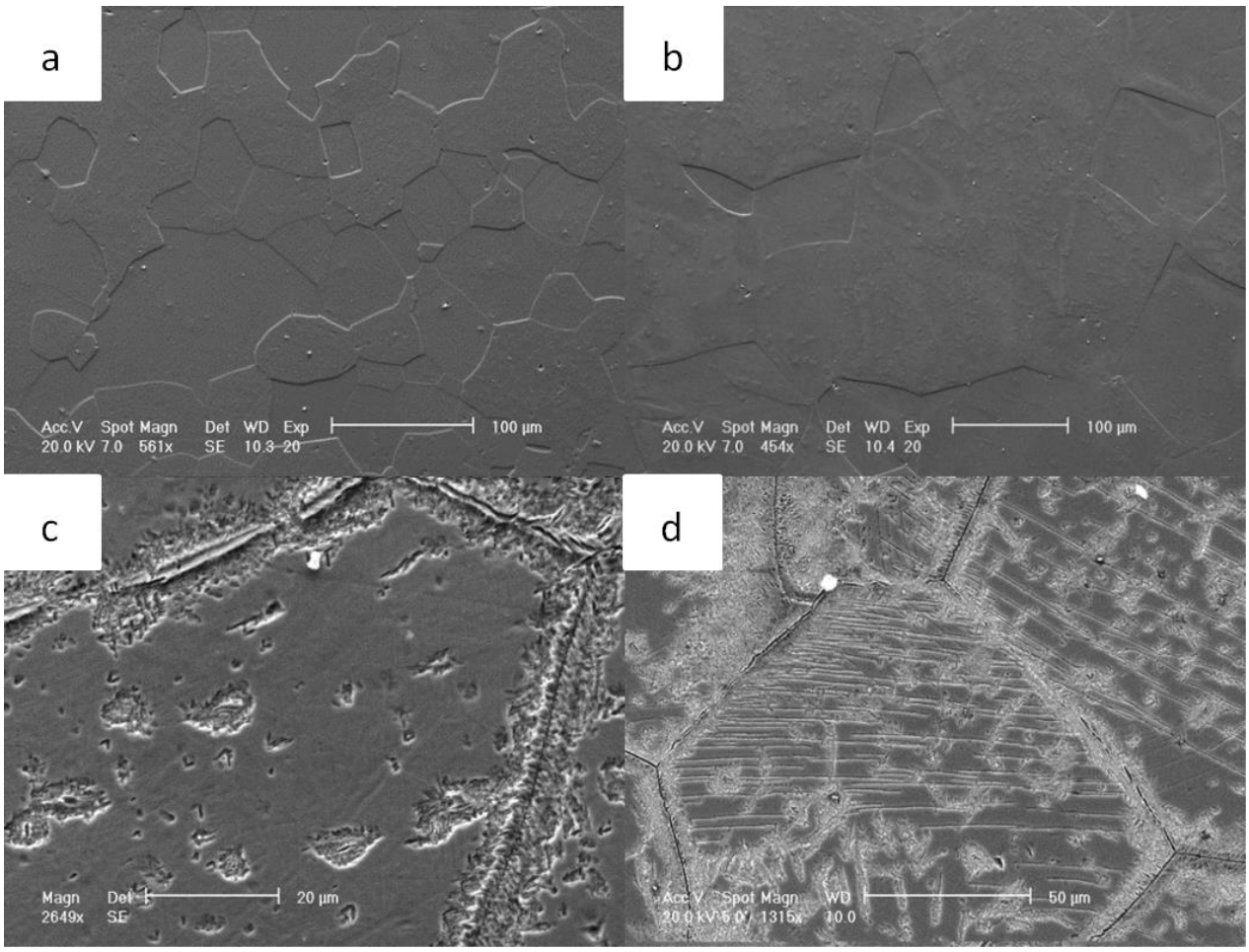

Fig.4. SEM images of samples deformed at**:** (a) 4000 s^{-1}, 1173K; (b) 1000 s^{-1}, 1173K; (c) 4000 s^{-1}, 293K; (d) 4000 s^{-1}, 873K.

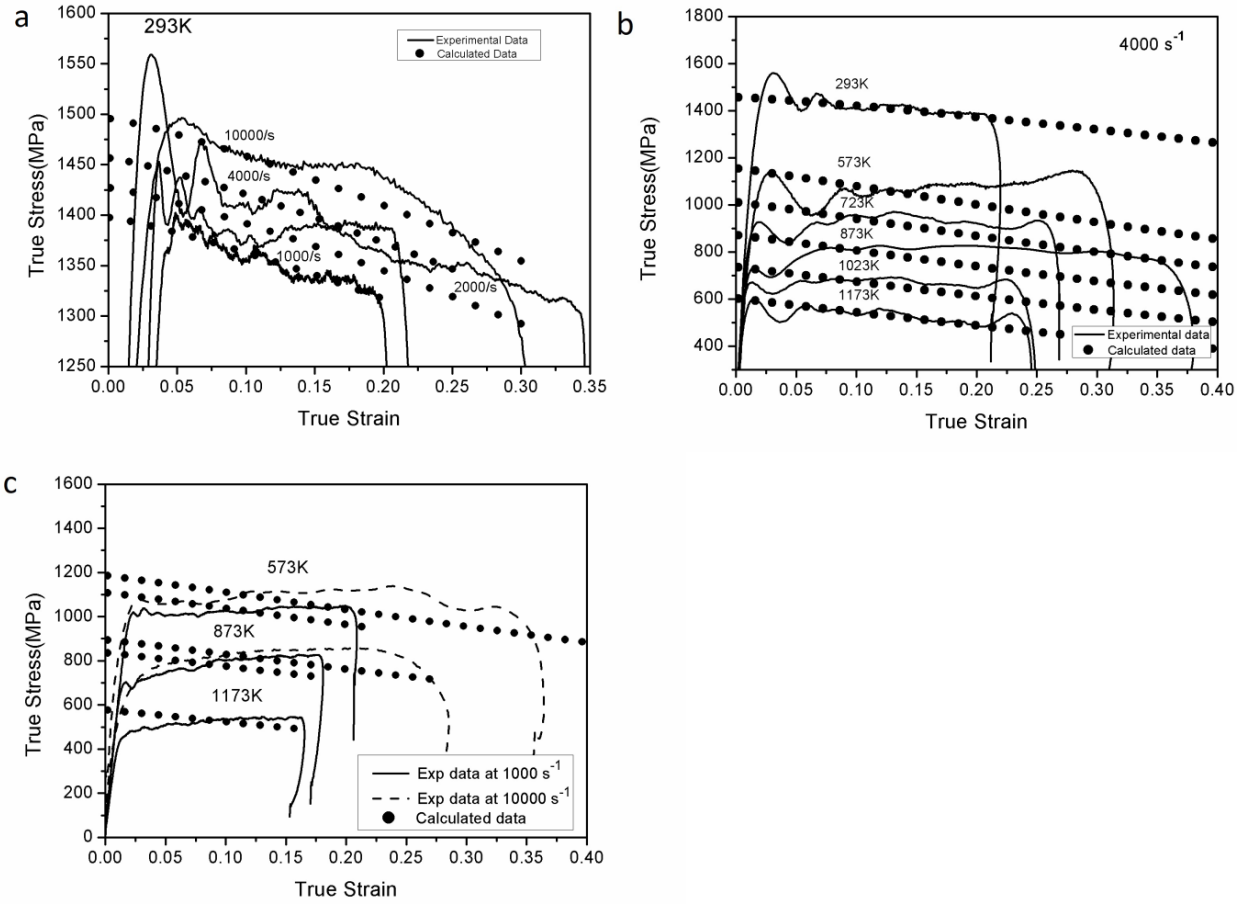

Fig.5. Fitting results using the JC model at (a) 293K (b) 4000 s^{-1}, (c) Validation of the predictability of the JC model

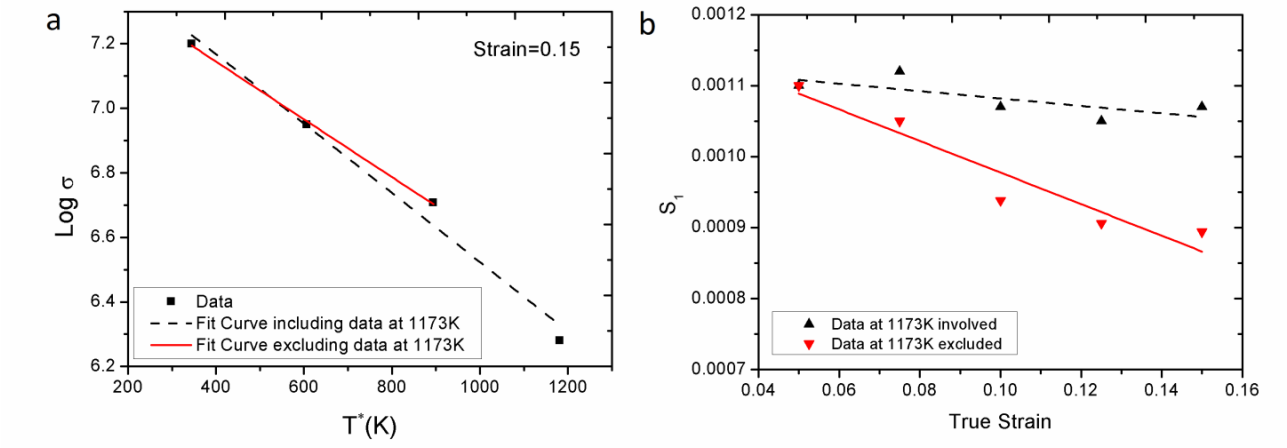

Fig.6. (a) Relationship of logarithmic stress with T^* at a strain of 0.15 (b) Relationship of S_1 with true strain (0.05-0.15 in steps of 0.025).

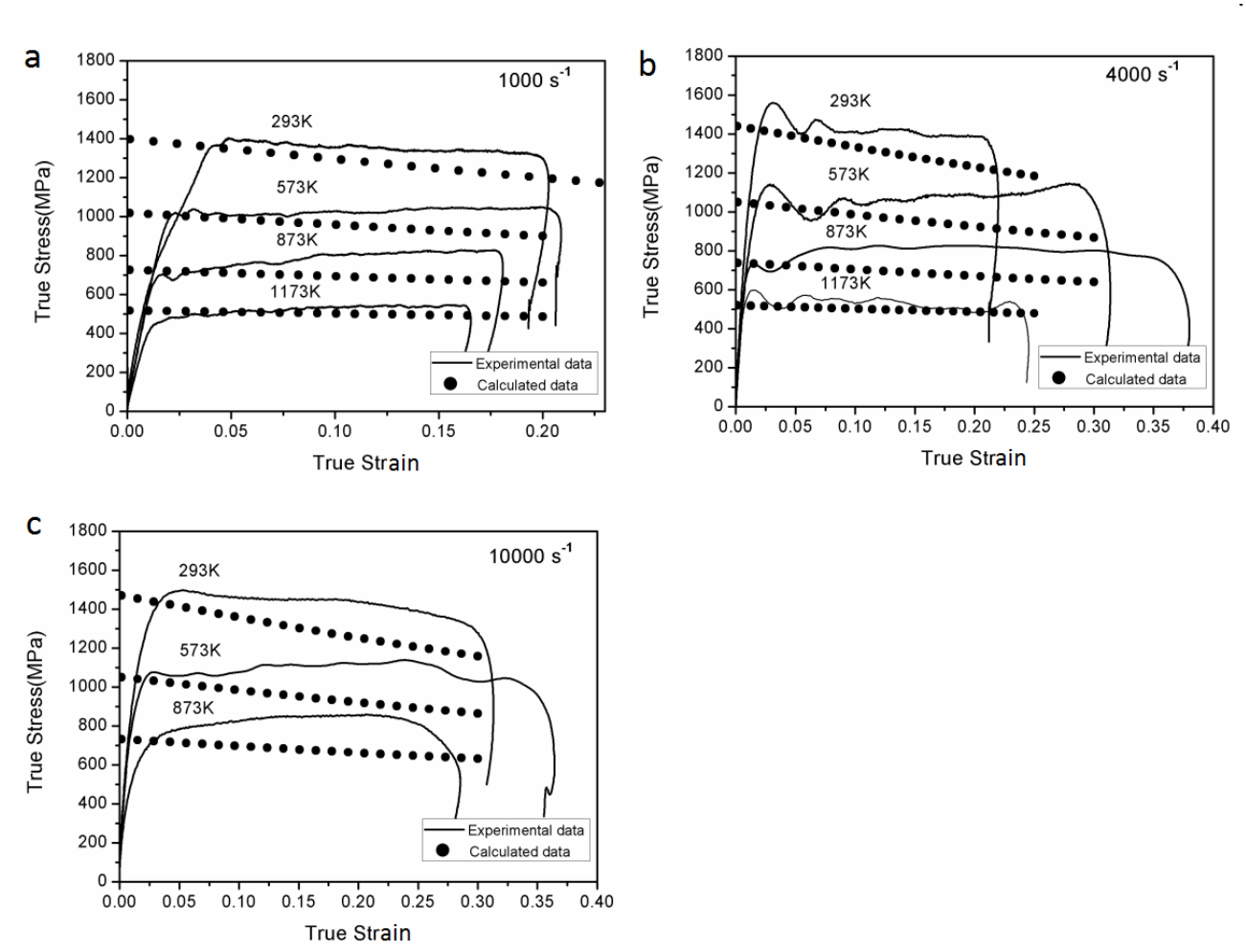

Fig.7. Fitting results using parameters for the modified-ZA model in Table 4: (a) 1000 s^{-1} (b) 4000 s^{-1} (c) 10000 s^{-1}

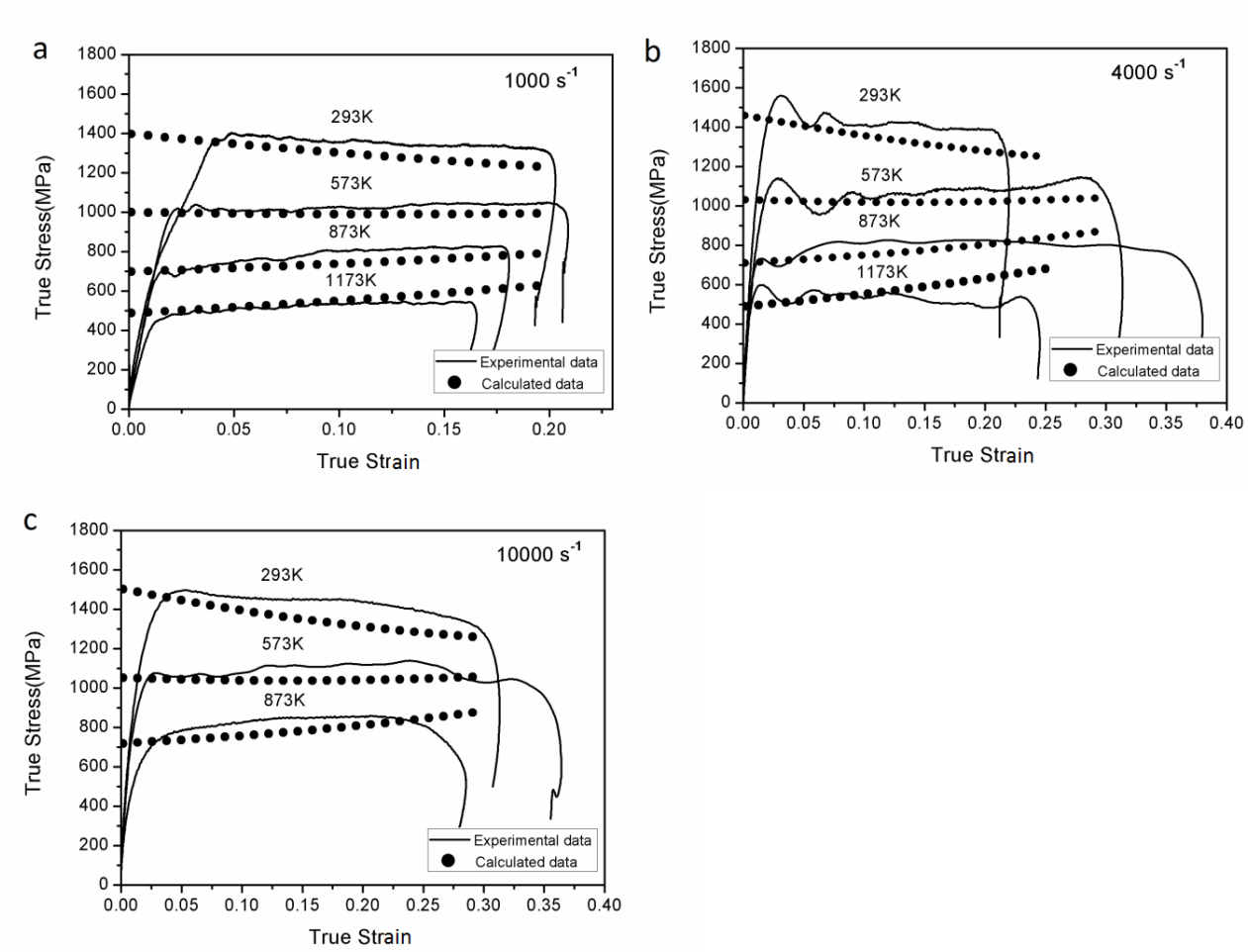

Fig.8. Fitting results using parameters for the modified-ZA model in Table 5: (a) 1000 s^{-1} (b) 4000 s^{-1} (c) 10000 s^{-1}

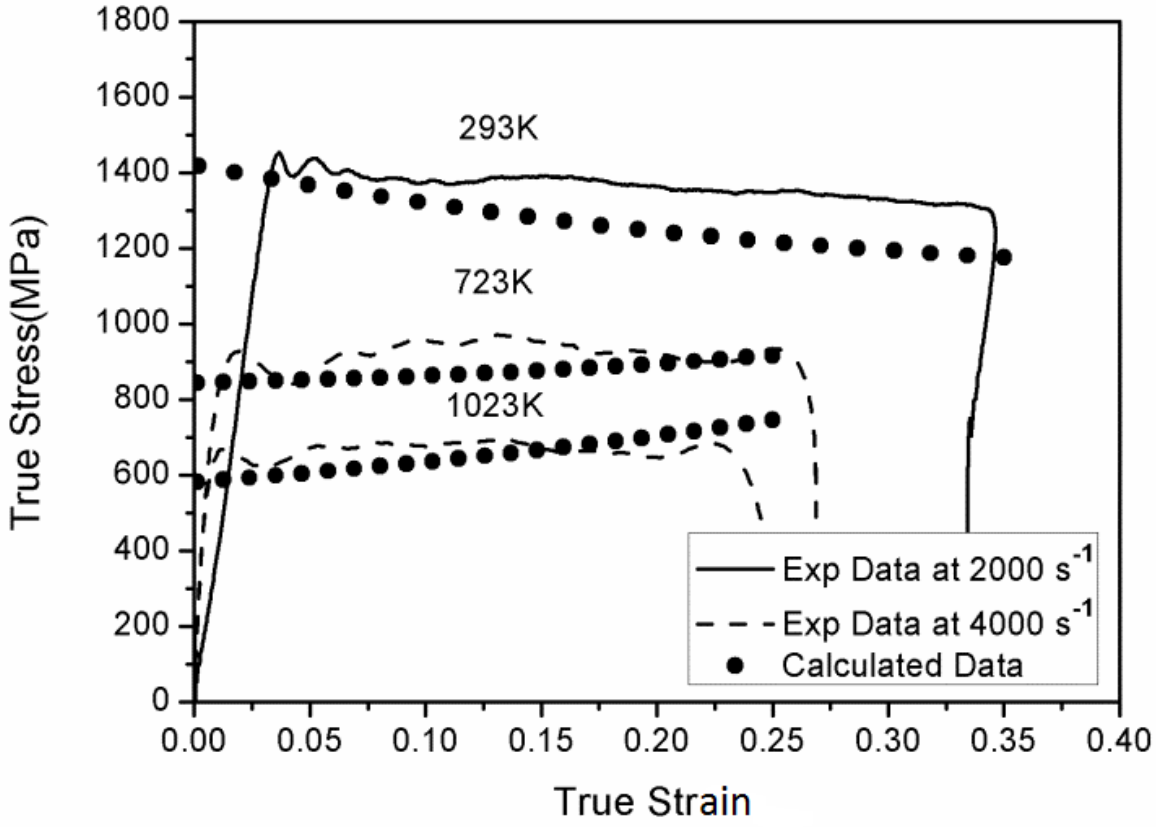

Fig.9. Validation of the predictability for the modified ZA model.

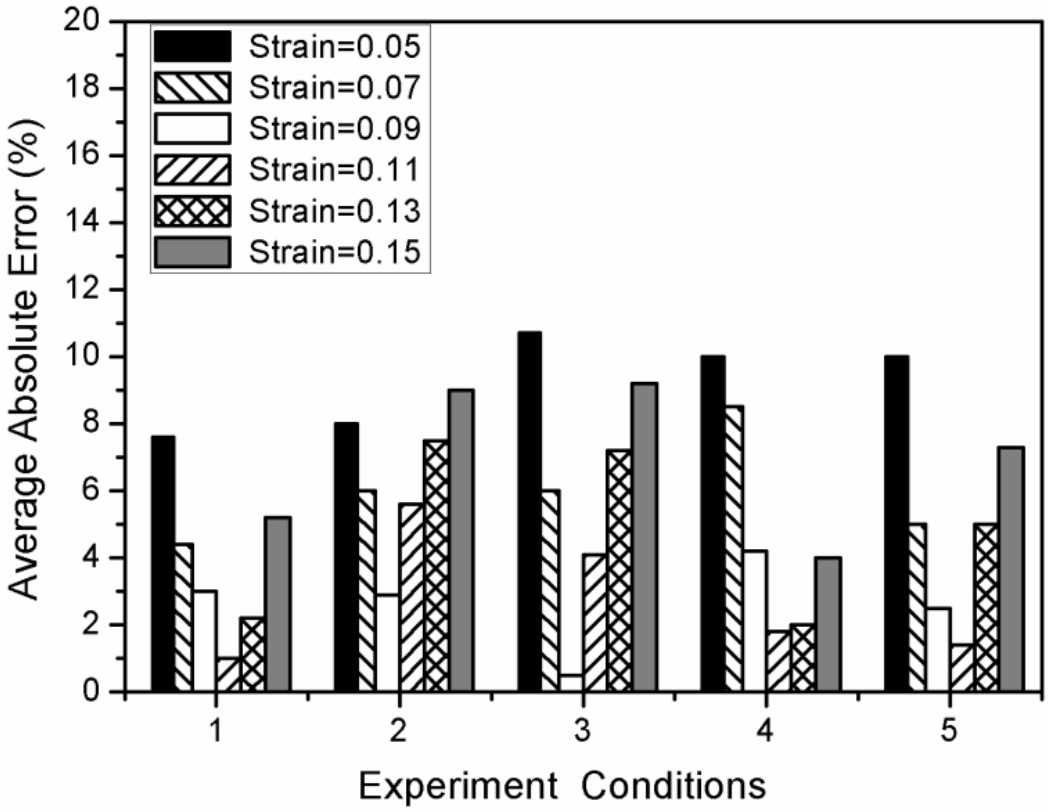

Fig.10. Variation of average absolute error with strains using the JC model: (1)10^3 s^{-1} 573K; (2)10^3 s^{-1}, 873K; (3)10^3 s^{-1},1173K; (4)10^4 s^{-1},573K; (5)10^4 s^{-1},873K.

PAPER 4

On the Deformation Mechanisms and Strain Rate Sensitivity of A Metastable β Ti-Nb Alloy

Hongyi Zhan, Weidong Zeng, Gui Wang, Damon Kent, Matthew Dargusch

Scripta Materialia

2015, Volume 107, Pages 34-37

On the deformation mechanisms and strain rate sensitivity of a metastable β Ti-Nb alloy

Hongyi Zhan[a,*], *Weidong Zeng*[b], *Gui Wang*[a], *Damon Kent*[c], *Matthew Dargusch*[a]

[a]Centre for Advanced Materials Processing and Manufacture, School of Mechanical and Mining Engineering, The University of Queensland, St Lucia, Queensland 4072, Australia

[b]State Key Laboratory of Solidification Processing, School of Materials, Northwestern Polytechnical University, Xi'an 710072, China

[c]School of Science and Engineering, University of the Sunshine Coast, Sippy Downs, Queensland 4575, Australia

*h.zhan@uq.edu.au

Abstract

The Ti-25Nb-3Zr-3Mo-2Sn (wt. %) alloy deforms primarily by {332}<113> twinning with limited {112}<111> twinning and stress-induced phase transformations. For the Ti-25Nb-3Zr-3Mo-2Sn alloy, the yield stress and strain hardening rate are independent of strain rate. It is found that adiabatic heating induced by high strain rate deformations is insufficient to significantly modify the deformation modes. Also the twinning rate and morphologies of {332}<113> twins are independent of strain rate (1×10^{-3} to 1×10^{3} s^{-1}) within the strain range in our experiments.

Keywords

Metastable β titanium alloys; High strain rates; Stress-induced martensitic transformation; Mechanical twinning

In the last decade, a range of metastable β Ti-Nb based alloys with ultralow Young's modulus and superelastic properties have been developed for biomedical implant applications [258-260]. The dominant deformation mechanism for β titanium alloys will change from dislocations slip to twinning and/or stress-induced martensitic (SIM) transformation with decreasing levels of β phase stability [64, 65]. The β phase stability is commonly gauged by the Mo_{eq}, an equivalent binary Ti-

Mo alloy concentration [66]. In recent years, bond order (Bo) and d-orbital energy (Md) have been applied to predict the relationship between plastic deformation behaviour and β phase stability [67, 68]. Decreasing phase stability is reflected by an increase in Md or decrease in Bo. A Bo-Md plot over the range of 2.35 to 2.60 in Md and 2.78 to 2.96 in Bo has been developed based on numerous experimental results [69]. When the β titanium alloys are located within a specific zone in the Bo-Md diagram, different deformation modes including stress-induced martensitic transformation, various types of twinning and/or dislocations slip are reportedly activated simultaneously and their interactions significantly contribute to enhanced strain hardening and higher ductility [73, 74, 261].

For body-centred cubic (bcc) structured metals and alloys, the yield strengths generally have positive strain rate sensitivities as the thermal activation energy required to overcome Peierls stress increases with increasing strain rates. Contrarily, the strain hardening rates decrease with increasing strain rates as thermal softening effects brought by adiabatic heating counteract strain hardening effects when strain rate are beyond 1 s^{-1}. This was shown to be the case for a heavily stabilized β titanium alloy which deformed primarily by dislocations slip [30]. However, deformation modes activated in the metastable β titanium alloys can be complex and the influence of strain rates on the deformation mechanisms and mechanical properties of the metastable β titanium alloys are rarely reported. The Ti-25Nb-3Zr-3Mo-2Sn(wt.%) alloy is particularly promising for biomedical implant applications due to its biocompatible composition, low elastic modulus and good combination of high strength and ductility [57, 262]. High strain rates employed during processes such as machining and high speed forming operations motivate this investigation into the dynamic response of the Ti-25Nb-3Zr-3Mo-2Sn alloy. In the present study, the deformation modes which are activated at different rates of strain and the strain rate sensitivity of the mechanical properties have been investigated for the Ti-Nb-Zr-Mo-Sn alloy.

The Ti-25Nb-3Zr-3Mo-2Sn (wt. %) alloy was produced by vacuum arc remelting. The ingots were hot rolled at a temperature of 1123K to cylindrical rods. Hot rolled rods of the Ti-25Nb-3Zr-3Mo-2Sn alloy were solution treated at 1023K for 1 h in a protective Argon atmosphere and then quenched in water. Specimens for mechanical testing were cut by electro-discharge machining from the rods. Dynamic and quasi-static compressive tests were carried out using Split Hopkinson Pressure Bar (SHPB) tests and an INSTRON machine, respectively. Specimens for electron backscatter diffraction (EBSD) were first wet ground using silicon carbide papers and then mechanically polished. EBSD was performed on a JEOL 6610 instrument equipped with an HKL Channel 5 system operating at 20 kV. Deformed specimens for transmission electron microscopy (TEM) were prepared by mechanical grinding and twinjet polishing using Struers A_3 electrolyte (50

ml perchloric acid, 300 ml butylcellosolve and 500 ml methanol) at an applied voltage of 20V and a temperature of 233 K. TEM investigations were performed using a JEOL 2100 microscope operated at 200 kV. X-ray diffraction (XRD) tests were conducted on a D8 Advance X-ray diffractometer equipped with a graphite monochromators and a Ni-filtered Cu K_α source.

The average Bo and Md of the Ti-Nb-Zr-Mo-Sn alloy are calculated to be 2.846 and 2.441 based on the equation proposed in [69]. Figure 1(a) presents the $\overline{Bo} - \overline{Md}$ diagram showing the Ti-25Nb-3Zr-3Mo-2Sn alloy. This Ti-Nb alloy is located below the boundary M_s (Martensite start temperature) =RT (room temperature) and above the boundary M_f (Martensite finish temperature) =RT, which indicates that the metastable β phase can be retained during water quenching after solution treatment. The EBSD inverse pole figure (IPF) map of the as-received specimens is shown in Figure 1(b). It exhibits a typical equiaxed microstructure with single bcc structured β phase.

The true stress-strain curves of the Ti-25Nb-3Zr-3Mo-2Sn alloys deformed at different strain rates at ambient temperatures are shown in Figure 2(a). The oscillations in the curve from high strain rate deformations are caused by wave dispersion [77, 263]. The yield stress (YS) in this curve can be obtained by the intersection of elastic modulus line with the extended plateau. The strain hardening exponents (n) can be calculated by Hollomon's power law equation: $\sigma = C \times \varepsilon^n$ where σ is the true stress and ε is the true strain. The yield stresses (YS) and strain hardening exponents (n) in quasi-static and high strain rate deformations are listed in the inset of Figure 2(a). It is found that YS is nearly independent of strain rate over strain rates which vary by 6 orders of magnitude. The strain hardening rate for the high strain rate deformation is also pronounced although slightly lower than that under quasi-static conditions. Figure 2(b) presents the XRD patterns of the Ti-Nb-Zr-Mo-Sn alloys after deformation at different strain rates. The diffraction peaks are indexed to be bcc β phase in the undeformed specimens. Diffraction peaks from orthorhombic α" phase can be identified in the deformed specimens, suggesting that some SIM α" formed during the deformation. The intensities of the diffraction peaks related to the SIM α" phase are weak and do not show much variation for the specimens deformed at different rates of strain. It is difficult to quantify the volume fractions of SIM α" in the specimens through XRD results due to its limited peak intensity, preferential grain orientation and peak overlapping.

Different types of deformation products were observed by EBSD and TEM in transverse sections of the specimens deformed at a strain rate of 1×10^{-3} s^{-1} as shown in Figure 3. Most of the plate features within the grains shown in Fig 3(a) have been identified as {332}<113> twins with characteristic 50.5 °misorientation angle as shown in Fig 3(b). {332}<113> twinning is a twining system which is specific to β titanium alloys, for which the coincidence site lattice (CSL) type is Σ11 boundary

[264]. The fraction of Σ11 boundaries in Fig 3(a) is calculated to be 12.7% using HKL Channel 5 software. Some plate like features which are not indexed are coloured black in Fig 3(a). This may be attributed to extensive distortions of the lattice by the deformation. SIM α" is not easily indexed in EBSD mapping as its exact lattice parameters for the Ti-Nb-Zr-Mo-Sn alloy are not precisely known. Finer features can be observed by TEM. A set of parallel lamellae with a thickness of ~100 nm are shown in Figure 3(c). As the diffraction spots relating to the ω phase formed in β titanium alloys are always located at $1/3<112>_{\beta}$ and $2/3<112>_{\beta}$ positions, the lamellar feature in Figure 3(c) can be indexed to the ω phase according to the SAD pattern shown inset. According to their lamellar morphology, they were formed by deformation [72] rather than by quenching. Lath-like stress-induced α" martensite was observed as shown in Figure 3(d), which is in accordance with the XRD results presented in Figure 2(b). Another feature observed by TEM is {112}<111> twins with straight sided plate-like morphologies as shown in Fig 3(e). The CSL type of the {112}<111> twins is Σ3 boundary with a misorientation angle of 60°.

Figure 4 shows EBSD and TEM analysis of the typical microstructure observed in the Ti-Nb-Zr-Mo-Sn alloys deformed at 1×10^{3} s^{-1}. Extensive {332}<113> twins are present as shown in Fig 4(a) by EBSD and the fraction of Σ11 boundaries in Fig 4(a) is calculated to be 13.4%. No obvious difference in twin density and thickness can be observed by EBSD in the microstructures of specimens deformed at different strain rates. Intersections of fine mechanical twins were detected by TEM as shown in Figure 4(c). This twinning system is identified as {112}<111> according to the indexed diagram shown in Figure 4(d). Dark-field images of two different variants of the mechanical twins are shown in Figure 4(e) and (f), respectively. Stress-induced ω phase was also observed as shown in Fig 4(g). Though SIM α" was not observed directly by TEM or EBSD in the specimens deformed at 1×10^{3} s^{-1}, its existence was confirmed by the XRD results (Fig 2(b)).

In contrast to dislocation-dominated deformations in heavily-stabilized β titanium alloys, the yield stress for the Ti-Nb-Zr-Mo-Sn alloy is practically the same at both strain rates of 10^{-3} and 10^{3} s^{-1}. For the metastable β titanium alloys, the critical stress for SIM α" phase transformation and/or {332}<113>twinning is typically lower than that for dislocation slip for quasi-static deformations at an ambient temperature [265, 266]. The critical stress for twinning is normally regarded as insensitive to strain rate due to its diffusionless nature [267]. Li et al [268] and Paradkar et al [269] have discussed the influence of strain rate on the triggering stress of SIM based on the free energy changes associated with the transformation and concluded that the triggering stress increases with increasing strain rate when the strain rate range is within the thermally activated dislocation motion regime. As multiple deformation mechanisms are activated during the deformation, the exact

deformation mode at yield for the different strain rates will be the subject of further investigation.

As the volume fractions of {112}<111> mechanical twinning and stress-induced phases observed in the Ti-25Nb-3Zr-3Mo-2Sn samples after deformation are limited in comparison to {332}<113> twinning, {332}<113> twinning is regarded as the dominant deformation mode. Twins cut across grains and intersect with each other, leading to a decrease in the dislocation mean free path. This phenomenon, referred to as the dynamic Hall-Petch mechanism [264], is able of inducing significant strain hardening rate. The strain hardening rates of the Ti-25Nb-3Zr-3Mo-2Sn alloy for different strain rates are almost identical (Figure 2(a)), which can be explained in two separate aspects. On the one hand, adiabatic heating induced by the high strain rate deformations did not play an important role in stabilizing the β matrix as the dominant deformation mode continues to be {332}<113> twinning according to the EBSD results. Adiabatic heating induced by the high strain rate deformations reportedly stabilize the austenite matrix in austenitic stainless steels [270, 271], supressing SIM transformations and thereby altering the dominant deformation mechanism. Deformation mechanisms of β titanium alloys, as mentioned in the introduction, also change with β phase stability. Variations in the deformation mechanisms will influence the strain hardening behaviour. One equation has been extensively applied to estimate the temperature elevation during high strain rate deformation: $\Delta T = \frac{\eta}{\rho c}\int_{\varepsilon_i}^{\varepsilon_{i+1}} \sigma(\varepsilon_i, \dot{\varepsilon}_i, T_i)\, d\varepsilon$ where the heat capacity of beta titanium alloy is taken as c=0.55 kJ $(kg/K)^{-1}$, the density as ρ=4.67 g cm^{-3} and heat fraction coefficient η is prevalently defined as 0.9 [30]. The integral is the plastic work i.e. the area under the stress-strain curves. A temperature increase of only 38 K is obtained at the end of the deformation for a strain of 0.18 under the high strain rate deformations in our experiments. Considering this relatively small value for adiabatic heating on the β matrix stability it will not be sufficient to modify the dominant deformation mechanism. On the other hand, both density and average thickness of the {332}<113> twins observed in the specimens deformed at different strain rates are similar. This indicates that the twinning rate and morphology of the {332}<113> twins within the strain range of our experiments are strain rate insensitive, which results in similar strain hardening rates for the different strain rates.

In summary, multiple deformation mechanisms including {332}<113> and {112}<111> mechanical twinning, stress-induced martensite and ω phase transformation were activated in the Ti-25Nb-3Zr-3Mo-2Sn alloy and among them {332}<113> twinning was the dominant mechanism at low and high strain rates. The strain hardening behaviour of the Ti-25Nb-3Zr-3Mo-2Sn alloy is strain rate insensitive as adiabatic heating induced by high strain rate deformations is not sufficient to significantly modify the deformation modes and the twinning rate and morphologies of

{332}<113> twins are independent of strain rates (1×10^{-3} to 1×10^{3} s^{-1}) within the strain range in our experiments.

This research is supported by the fund of the State Key Laboratory of Solidification Processing in NWPU, project number: SKLSP201207. The authors also acknowledge the support of the Queensland Centre for Advanced Material Processing and Manufacturing (AMPAM).

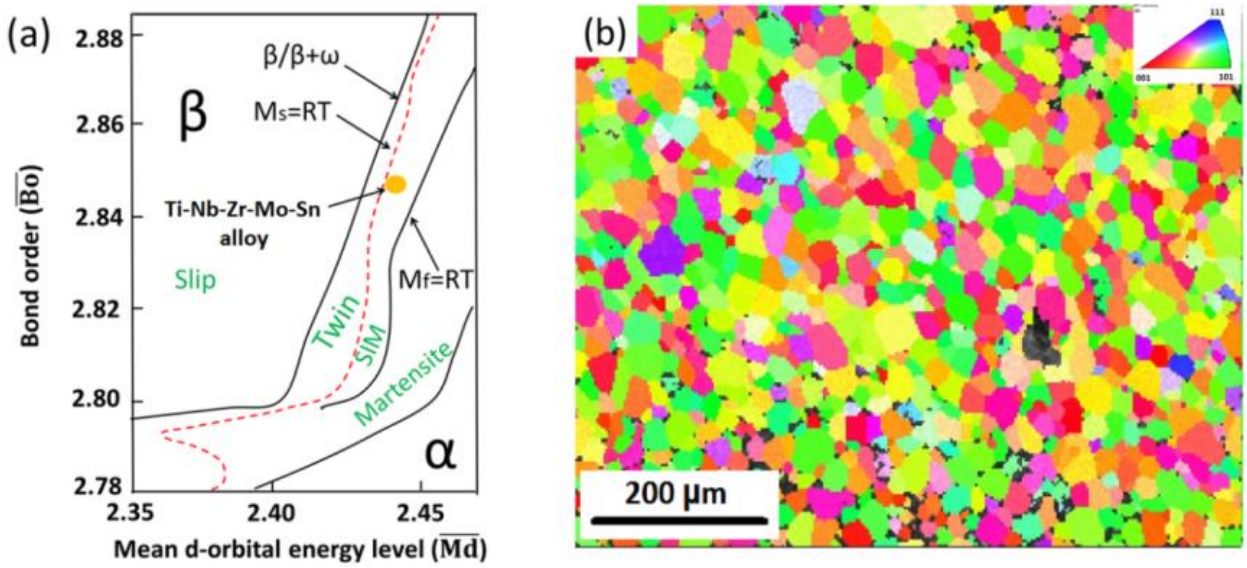

Figure.1. (a) $\overline{Bo} - \overline{Md}$ diagram showing the location of the Ti-Nb-Zr-Mo-Sn alloy. (b) EBSD IPF map relative to the ND (the compressive direction is parallel to ND) of the solution treated Ti-Nb-Zr-Mo-Sn alloy (step size=0.2 μm).

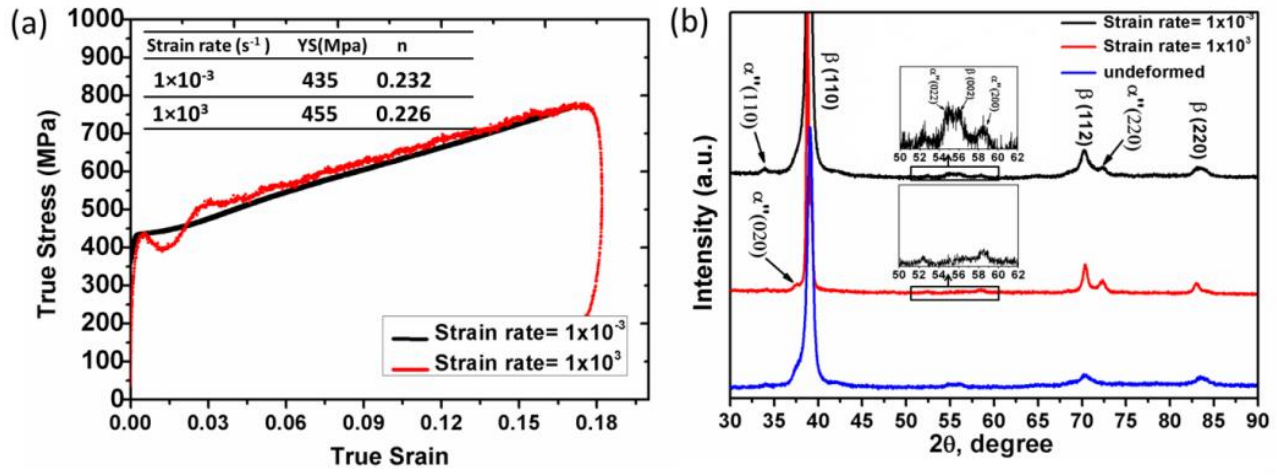

Figure.2. (a) True stress-strain curves (the inset shows yield stress and strain hardening rate for stress-strain curves) and (b) XRD spectrums for specimens deformed at different strain rates.

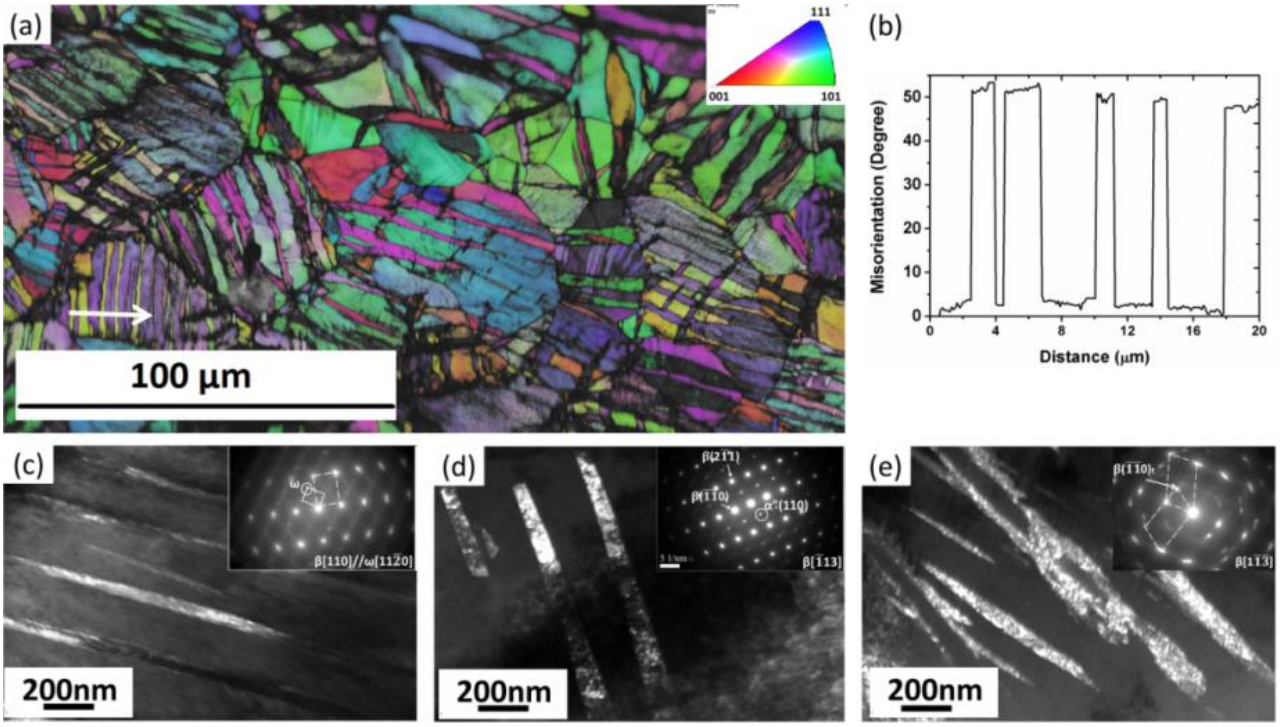

Figure.3. EBSD and TEM analysis of the specimens deformed at 1×10^{-3} s^{-1}: (a) EBSD IPF map relative to the ND (the compressive direction is parallel to ND) with step size of 0.1 µm. (b) Line traces across region arrowed in (a) showing the misorientation angle. TEM dark-field images of (c) ω phase, (d) α" martensite and (e) {112}<111>β twinning. (The inset of (c), (d), and (e) shows corresponding SAD pattern along different zone axis).

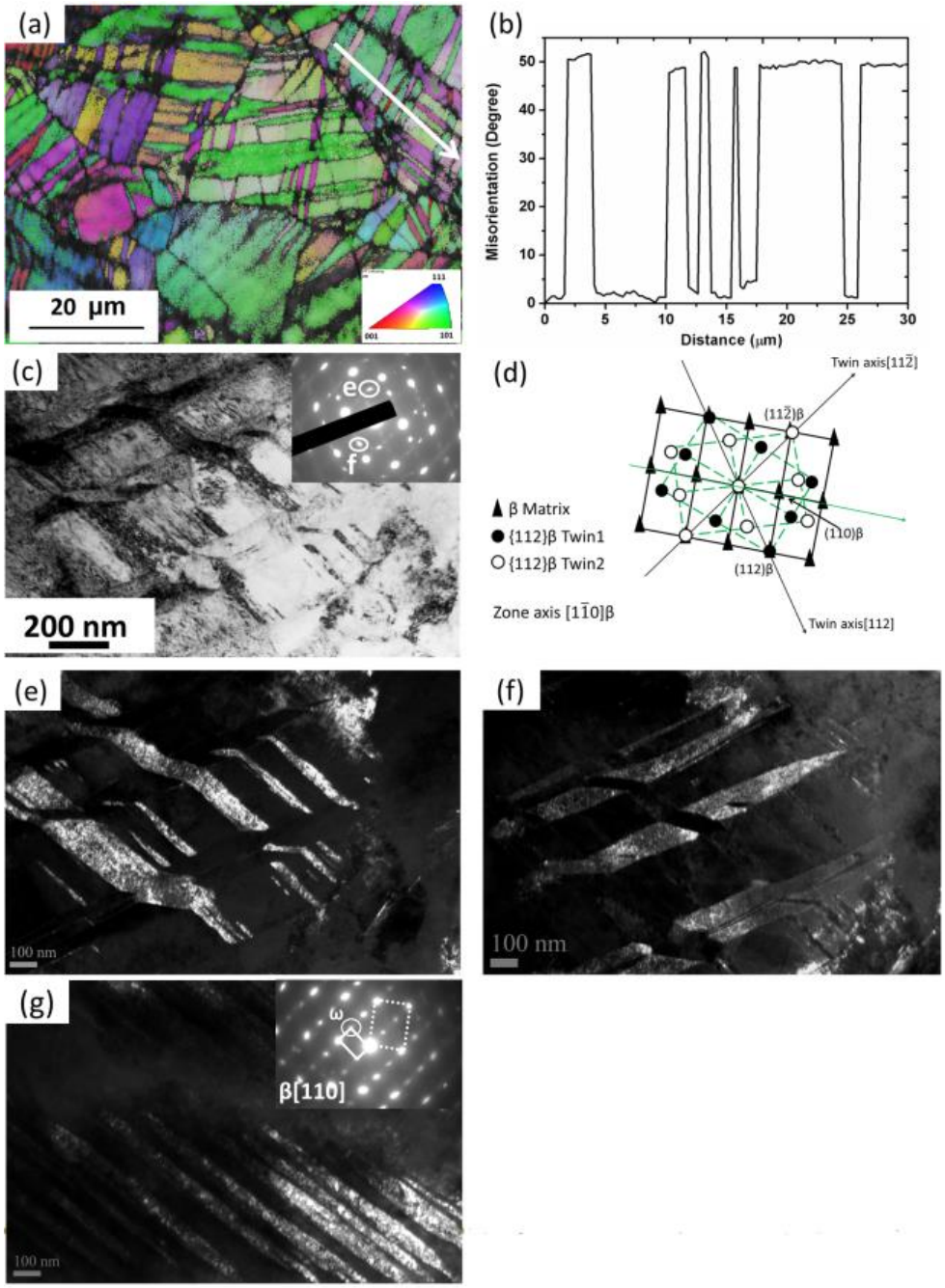

Figure.4. EBSD and TEM analysis of the specimens deformed at 1×10^3 s^{-1}: (a) EBSD IPF map relative to the ND (the compressive direction is parallel to ND) with step size of 0.2 μm (b) Line traces across region arrowed in (a) showing the misorientation angle. (c) Bright-field image of two variants of {112}<111> twinning and corresponding SAD pattern. (d) Indexed diagram corresponding to {112}<111> twins. (e) and (f) Dark-field images of {112}<111>β twins by selecting the diffraction spots highlighted in the inset of (c). (g) TEM dark-field image of ω phase.

PAPER 5

The Dynamic Response of A Metastable β Ti-Nb Alloy to High Strain Rates at Room and Elevated Temperatures

Hongyi Zhan, Gui Wang, Damon Kent, Matthew Dargusch

Acta Materialia

2016, Volume 105, Pages 104-113

The dynamic response of a metastable β Ti-Nb alloy to high strain rates at room and elevated temperatures

Hongyi Zhan[a,*], *Gui Wang*[a], *Damon Kent*[a,b], *Matthew Dargusch*[a]

[a]Centre for Advanced Materials Processing and Manufacture, School of Mechanical and Mining Engineering, The University of Queensland, St Lucia, Queensland 4072, Australia

[b]School of Science and Engineering, University of the Sunshine Coast, Sippy Downs, Queensland 4575, Australia

*h.zhan@uq.edu.au

*Postal Address: Room 634, Building 49, Cooper Road, The University of Queensland, St Lucia, 4072, QLD

Abstract

A metastable β Ti-Nb alloy, Ti-25Nb-3Zr-3Mo-2Sn (wt.%), has been subjected to high strain rate deformations (1000 s^{-1}) at the temperatures of 293K, 573K and 873K by Split Hopkinson Pressure Bar compressive tests. The microstructural evolution and deformation mechanisms of the metastable Ti-Nb-Zr-Mo-Sn alloy have been investigated by X-ray diffraction, electron backscatter diffraction and transmission electron microscopy. Multiple deformation mechanisms including {332} <113> and {112} <111> mechanical twinning, stress-induced α" and ω phase transformations and dislocation slip were identified at 293K. Among them, {332} <113> twinning is the dominant deformation mechanism and induced pronounced strain hardening at 293K. At 573K, {332} <113> and {112} <111> mechanical twinning occur in conjunction with dislocation slip. Though the direct contribution to strengthening by mechanical twinning is relatively small at 573K, it enhances both the multiplication and annihilation of dislocations thereby impacting the strain hardening behaviour of the Ti-Nb-Zr-Mo-Sn alloy. With an increase in temperature to 873K, the plastic strain is accommodated by dislocation slip only. The deformation mechanisms which are active during deformations at different temperatures also influence the development of texture in the Ti-Nb-Zr-Mo-Sn alloy.

Keywords

Metastable β titanium alloys; High strain rates; Mechanical twinning; Strain hardening behaviour

1. Introduction

In the last decade, a range of metastable β Ti-Nb based alloys with ultralow Young's modulus, good biocompatibility and superelastic properties have been developed for biomedical implant applications [258-260, 272, 273]. The dominant deformation mechanism for β titanium alloys varies from dislocation slip to twinning and/or stress-induced martensitic (SIM) transformation with decreasing levels of β phase stability [54, 64, 65]. In recent years, the average bond order (Bo) and d-orbital energies (Md) have been used to predict the relationship between the plastic deformation behaviour and β phase stability [67, 68]. Decreasing β phase stability is reflected by an increase in Md or decrease in Bo. A Bo-Md plot over the range of 2.35 to 2.60 in Md and 2.78 to 2.96 in Bo has been developed on the basis of experimental results [69]. Also, a design principle for development of new β titanium alloys with improved strengths and ductility has been proposed on the basis of the Bo-Md plot [72-74]. When the β titanium alloys are located within a specific region of the Bo-Md diagram, a range of deformation modes including stress-induced martensitic transformation, various types of twinning and/or dislocations slip can be activated simultaneously and their interactions significantly contribute to enhanced strain hardening and higher ductilities [72-74, 261].

The dynamic response of materials at high strain rates and elevated temperatures can be quite different to those under the condition of quasi-static strain at ambient temperatures, with their effects being material-dependent. For most metals the flow stress increases with increasing strain rate but decreases with increasing temperature. However, for TWIP steel [171] and some aluminium alloys [230], the flow stress is mildly sensitive or essentially insensitive to the strain rate. In addition, a strain rate softening behaviour is observed for high manganese steels for strains in the range of ~500-1700 s^{-1} [231]. Khan et al. [133], Nemat-Nasser et al. [132], Hokka et al. [134] and Lee et al. [85, 118, 129] performed dynamic experiments on titanium alloys and observed that the flow stress is sensitive to high strain rates and elevated temperatures. For the Ti6Al4V [129] and Ti15Mo5Zr3Al [85] alloys, it was observed that the flow stress is more sensitive to temperature than strain rate. The deformation mechanisms and mechanical properties of metastable β titanium alloys at high strain rates over a wide range of temperatures are rarely reported.

The Ti-25Nb-3Zr-3Mo-2Sn (wt.%) alloy is particularly promising for biomedical implant applications due to its biocompatible composition, low elastic modulus and good combination of high strength and ductility [57, 262, 274]. The average Bo and Md of the Ti-Nb-Zr-Mo-Sn alloy are calculated to be 2.846 and 2.441 on the basis of the equations proposed in Ref. [69]. It has been shown in Ref. [275] that the Ti-25Nb-3Zr-3Mo-2Sn alloy is located in the region of the $\overline{Bo} - \overline{Md}$ diagram where mechanical twinning and stress-induced phase transformation can take place simultaneously to accommodate plastic strain. Zhang et al. [276] have investigated the effects of cold rolling and annealing on the microstructural evolution and mechanical properties of the Ti-25Nb-3Zr-3Mo-2Sn alloy; while Tian et al. [277] and Bai et al. [278] have studied the hot deformation behaviour of the Ti-25Nb-3Zr-3Mo-2Sn alloy over a narrow temperature range between 1023 K to 1123K with the highest strain rate employed being 50 s^{-1}. The high strain rates and elevated temperatures which are experienced by materials during commercial manufacturing processes such as machining and high speed forming operations motivate this investigation into the dynamic response of the Ti-25Nb-3Zr-3Mo-2Sn alloy at room and elevated temperatures.

In the present study, the stress-strain behaviour of the Ti-Nb-Zr-Mo-Sn alloy was investigated at high strain rates (1000 s^{-1}) at temperatures of 293K, 573K and 873K using Split Hopkinson Pressure Bar compressive tests. The microstructural evolution of the Ti-Nb-Zr-Mo-Sn alloy during the deformations was observed and the interrelationship between the microstructural characteristics and mechanical properties analysed.

2. Experimental

The Ti-25Nb-3Zr-3Mo-2Sn (wt. %) alloy was produced from commercially pure Ti sponge (99.5 wt. % purity), pure Zr bars (99.7 wt. %), pure Sn bars (99.9 wt. %), pure Mo powder (99.8 wt. %) and an intermediate Nb–47 wt. % Ti alloy. The alloys were melted three times by vacuum arc remelting to ensure chemical homogeneity and low levels of impurities. The ingots were hot rolled at a temperature of 1123K into cylindrical rods and solution treated at 1023K (above the β transus) for 1 h in a protective Argon atmosphere followed by quenching into water.

The dynamic mechanical behaviour of the Ti-Nb-Zr-Mo-Sn alloy was tested using a Split Hopkinson Pressure Bar (SHPB) arrangement [80] at a strain rate of 1000 s^{-1} and temperatures of 293K, 573K and 873K. Cylindrical specimens for the high strain rate tests were 5 mm in diameter and 4 mm in height. They were cut from rods using electrical discharge machining with a slow cutting speed to minimise heat effects on the samples. For the experiments performed at elevated

temperatures, the specimens were heated by an in-situ induction coil and the temperature was regulated by a thermocouple which was not in contact with the specimen. After reaching the designated temperature, the specimen was maintained at this temperature for approximately 2 minutes to ensure a uniform temperature distribution. In order to decrease the friction between the contact surfaces of the bars and specimen, molybdenum sulphide was used as a lubricant.

Specimens for electron backscatter diffraction (EBSD) were first wet ground using silicon carbide papers and then mechanically polished. EBSD was performed on a JEOL 6610 instrument equipped with an HKL Channel 5 system operating at 20 kV. EBSD inverse pole figure (IPF) maps covering an area of at least 80000 μm^2 were used to calculate the texture strength and area fraction of twins in specimens deformed at the different temperatures. At least 50 twins were used to calculate the average twin widths. Specimens for transmission electron microscopy (TEM) were prepared by mechanical grinding and twinjet polishing using Struers A_3 electrolyte (50 ml perchloric acid, 300 ml butylcellosolve and 500 ml methanol) at an applied voltage of 20V and a temperature of 233 K. TEM investigations were undertaken using a JEOL 2100 microscope operated at 200 kV. X-ray diffraction (XRD) tests were conducted on a D8 Advance X-ray diffractometer equipped with a graphite monochromator and a Ni-filtered Cu K_α source.

3. Results

3.1. Stress-strain behaviours

True stress-strain curves of the Ti-Nb-Zr-Mo-Sn alloy deformed at 1000 s^{-1} and different temperatures are shown in Figure 1a. None of the deformations resulted in fracture hence the ends of the curves represent unloading rather than fracture. The intense oscillations and characteristic serrations shown in the curves are caused by wave dispersion effects [77, 263]. Plots of the strain hardening rate (θ) vs. true strain are also shown in Figure 1a. The strain hardening rate was determined by differentiating third-order polynomials fitted to the original true stress-strain curves in order to eliminate the wave dispersion effects. The intense oscillations in the stress-strain curves for true strains < 0.05 were not included in the polynomial fitting. The yield stress (σ_y) can be estimated from these plots by the intersection of lines projected from the initial elastic modulus and the slope of the extended plastic deformation plateau. A plot of the yield stress versus temperature is shown in Figure 1b.

The influence of temperature on the yield stress is complex. The yield stress increases as the

deformation temperature is raised from 293K to 573K while it is drastically reduced at 873K (Figure 1b). The strain hardening behaviour of the Ti-Nb-Zr-Mo-Sn alloy is the most pronounced at 293K (Figure 1a) and decreases slowly with increased strain until it remains relatively constant beyond a strain of around 0.10. The strain hardening rate at 573K and 873K are significantly lower and decrease more rapidly in comparison to that at 293K. The strain hardening rate at 573K is higher than that at 873K up to a strain of around 0.15. It should be noted that the stress-strain behaviour described here is for compressive testing, while the behaviours may be different for high strain rate tensile or shear conditions.

3.2. Microstructural evolution

3.2.1. Initial microstructure and XRD results

The EBSD IPF map of the as-received specimens is shown in Figure 2a. It exhibits a typical equiaxed microstructure comprised of the body-centred cubic (bcc) β phase. It is found that the texture in the as-received specimens is weak as shown in Fig 2b. The average grain size is ~22 μm and the fraction of low-angle boundaries (LAB, $2°<\theta<15°$) is ~21% (Figure 2c). Figure 3 presents the XRD spectra from the Ti-Nb-Zr-Mo-Sn alloy after deformations at 1000 s^{-1} at the different temperatures. Diffraction peaks from orthorhombic α" phase can be identified in the specimens deformed at 293K, suggesting that some SIM α" formed during the deformation. The intensities of the diffraction peaks related to the SIM α" phase are weak. It is difficult to quantify the volume fractions of SIM α" in the specimens through XRD due to its limited peak intensity, preferred grain orientations and overlapping of peaks. The diffraction peaks were indexed to the bcc β phase in the specimens deformed at 573K and 873K. Peak intensities for $(110)_{\beta}$, $(002)_{\beta}$ and $(112)_{\beta}$ vary with temperature, indicating that the texture evolution of the Ti-Nb-Zr-Mo-Sn alloy is influenced by temperature.

3.2.2. Microstructures of specimens deformed at 293K

The most prevalent deformation products observed in the specimens deformed at 1000 s^{-1} and 293K are {332} <113> twins as shown in Figure 4. In Figure 4a the plate morphologies have been identified as {332} <113> twins with a characteristic 50.5 °misorientation angle. {332}<113> twinning is a system which is specific to β titanium alloys, for which the coincidence site lattice (CSL) is the Σ11 boundary [264]. The average width of the {332} <113> twins was ~2 μm. The area fraction of {332} <113> twins in the specimens deformed at 293K and 1000 s^{-1} was calculated to be ~46% on the basis of the EBSD analysis. Twin-twin intersections are abundant as shown in Figure 4a. SIM α" is not easily indexed in the EBSD maps as the precise lattice parameters are not

known for the Ti-Nb-Zr-Mo-Sn alloy.

Finer features of the microstructure can be observed by TEM. A network of lamellae with a total width of ~1.8 μm is shown in Figure 4c. Evidence of dislocation slip can be identified by the dislocation forests which surround the twins. The corresponding selected area diffraction pattern (SADP) in Figure 4e has been indexed to be {332} <113> twinning. However, the average width of each {332} <113> twin observed by TEM is ~40 nm, which is much thinner than those observed in the EBSD IPF map. A bundle of {112} <111> twins were also observed by TEM as shown in Figure 5. The average width of the {112} <111> twins is ~120 nm. Unlike {332} <113> twins, the CSL type for the {112} <111> twins is the Σ3 boundary with a misorientation angle of 60 °. Some nano-scale α" martensite was observed to form between the paralleled twins as shown in Figure 5d, which is in accordance with the XRD results. The orientation relationship between α" and β was indexed as $[\bar{1}13]_{\beta}$ // $[002]_{\alpha''}$ as shown in Figure 5e, which has also been reported in previous studies of β titanium alloys [279]. Another feature observed is a set of parallel lamellae with an average width of ~100 nm as shown in Figure 6. Diffraction spots relating to the ω phase formed in β titanium alloys are located at $1/3<112>_{\beta}$ and $2/3<112>_{\beta}$ positions. Therefore, the lamellar feature can be indexed to the ω phase according to the SADP shown in the inset of Figure 6b. In low misfit alloys the athermal ω phase typically forms in the shape of ellipsoidal precipitates [280] while the stress-induced ω phase has a lamellar [72] morphology. Therefore according to the lamellar morphology of these features, they are presumed to form by deformation, rather than during quenching. Similar morphologies of stress-induced ω have been reported in metastable Ti-Nb based alloys in studies conducted by Yang et al. [281], Lai et al. [282] and Talling et al. [283]. Although several different kinds of deformation modes have been found by TEM, the volume fractions of {112} <111> twins and stress-induced phase transformation products are very limited in comparison to the {332} <113> twins.

3.2.3 Microstructures of specimens deformed at 573K and 873K

Obvious twins are observed in the microstructure of specimens deformed at an intermediate temperature of 573K, as shown in Figure 7. Black spots in Figure 7a and b represent unindexed areas. As mentioned previously, the CSL types for the {332} <113> and {112} <111> twin boundaries are Σ11 and Σ3, respectively. Therefore, the boundaries of twins have been delineated with yellow (Σ11) or red (Σ3) colours in the EBSD band contrast map (Figure 7b) and the ratio of Σ3 to Σ11 boundaries is ~0.2. It is found that more {112}<111> twins can be indexed in the EBSD maps for the specimens deformed at 573K compared with those deformed at 293K. This may be related to increased β phase stability at higher temperatures. The area fraction and average width of

mechanical twins in specimens deformed at 1000 s^{-1} and 573K are ~8% and ~6 μm, respectively. The profuse colour variations within grains(Figure 7a) indicates extensive dislocation slip, which is also reflected by the dramatic increase in the fraction of LABs (~50%) as shown in Figure 7c compared to the initial microstructure. Small peaks observed at the misorientation angles from 45-60 degrees in Figure 7c correspond to misorientations across the {332} <113> and/or {112} <111> mechanical twin boundaries. No trace of twins was observed in the microstructures obtained from deformations at the highest temperature of 873K as shown in Figure 8. The LABs are observed around grain boundaries and there are also a few clusters within the grains as shown in Figure 8b. The fraction of LABs increases from 50% at 573 K to 70% at 873K for the deformations at 1000 s^{-1} as shown in Figure 8c.

3.3 Texture evolution

Inverse pole figures viewed along the compressive direction for the specimens deformed at 1000 s^{-1} at temperatures of 293K, 573K and 873K are shown in Figure 9. The value for half width of the contoured IPFs was defined as 10 degrees. Textures for the specimens deformed at the different temperatures are relatively weak due to the limited strain level (~0.2) as shown in Figure 9a, b and c. The fibre texture components were calculated using the HKL Channel 5 software using the "Texture Components" function from their corresponding IPF maps which covered an area of at least 80000 μm^2. It should be noted that an area of 80000 μm^2 does not provide an ideal statistical measure for the texture analysis but can still be used to infer information on the texture evolution in the samples as a result of the deformations. The fractions of fibre texture components for the different deformation conditions are shown in Figure 9d, which were calculated by integrating over an angle of 20 degrees from the ideal <001>, <111> or <011> orientations as suggested by Hörnqvist et al. [284] and Naaman et al. [285]. As the indexing rate for large area IPF maps from the specimens deformed at 293K is much lower than those deformed at 573K and 873K, the fraction of the texture components calculated for the specimens deformed at 293K is not included in Figure 9d. However, Figure 9a suggests that the intensity contours for the specimens deformed at 293K is near the <110> pole. It is observed that the fraction of the texture components varies markedly for the deformations at different temperatures shown in Figure 9d. The fraction of <110> fibre texture decreases rapidly from ~0.35 in the undeformed specimens to ~0.15 in the specimens deformed to a true strain of 0.20 at 873K while the fractions of <001> and <111> fibre texture in the deformed microstructures increase with increasing temperature. These differences in texture development indicate that the texture in the Ti-Nb-Zr-Mo-Sn alloy during high strain rate deformations is dependent on the relative contributions of dislocation slip and mechanical twinning.

As dislocation slip is significant at 573K and 873K, the grain orientation gradually rotates to the preferred softer orientation for the dislocation slip leading to the increment of <001> and <111> fibre texture at 573K and 873K. Similar texture development have been reported in β titanium alloys during hot deformations [286, 287] and uniaxial compressive test [281] . As mechanical twinning is still active in the deformations at 573K, the fraction of <001> fibre texture is lower at 573K compared with that at 873K.

4. Discussion

4.1 Strain hardening behaviour at 293K

It is found that {332} <113> and {112} <111> mechanical twinning, stress-induced α" and ω phase transformations as well as dislocation slip occur concurrently to accommodate the plastic strain at 293K at a strain rate of 1000 s^{-1} for the Ti-Nb-Zr-Mo-Sn alloy. Considering the limited volume fractions of {112} <111> twins and stress-induced phase transformation products observed under TEM and EBSD, it is believed that {332} <113> twinning is the primary deformation mode. In our previous study [275] it was shown that the stress-strain curves for the Ti-Nb-Zr-Mo-Sn alloy deformed at 293K and 1000 s^{-1} shows a pronounced strain hardening which is only slightly lower than that for quasi-static strain conditions. However, for a more heavily stabilized β titanium alloy, the strain hardening rate for deformations at 293K is negative when the strain rate is raised to 1000 s^{-1} due to significant thermal softening effects brought about by adiabatic heating [30]. In this metastable Ti-Nb alloy, profuse {332} <113> mechanical twins cut across grains and intersect with each other leading to a decrease in the dislocation mean free path. This phenomenon, referred to as the dynamic Hall-Petch mechanism [264], is able to induce significant rates of strain hardening in the Ti-Nb-Zr-Mo-Sn alloy even when the strain rate is raised to 1000 s^{-1}.

To quantitatively analyse the hardening effects of the mechanical twins, we assume that the total flow stress can be expressed as:

$$\sigma = \sigma_0 + \Delta\sigma_\rho + \Delta\sigma_t \quad (1)$$

where σ_0 is the friction stress and $\Delta\sigma_\rho$ is the flow stress contributed by dislocation forests. (Note: {112} <111> twins, SIM α" and ω phase transformation have not been considered in the analysis due to their very limited volume fractions.) $\Delta\sigma_t$, the increment of flow stress by {332}<113> mechanical twinning, is always expressed as [288, 289]:

$$\Delta\sigma_t = M\beta Gb/\Lambda \quad (2)$$

Where β is Taylor constant of 0.5 [290] and G is the material shear modulus which is around 30 GPa for the Ti-Nb alloys of low elastic modulus [291, 292]. M is an average Taylor factor of 3.06 and b is the Burgers vector of 2.54 $\times 10^{-10}$ m. Λ *is* the dislocation mean free path (MFP), which can be written as:

$$1/\Lambda = 1/L + 1/D \quad (3)$$

Where L is the average grain size of the as-received microstructures (22μm) and D is the mean twin spacing which can be determined using the volume fraction f and twin thickness d:

$$1/D = f/[2d(1-f)] \quad (4)$$

The volume fraction f can be approximated from the area fraction obtained by EBSD analysis and the twin thickness d can be taken as half of the average twin width (w) based on a stereological relation [264]. For the specimens deformed at 293K and 1000 s^{-1}, f is 46% and d is $w/2=1$ μm on the basis of our EBSD data. However, when taking all these parameters into Eq. (1), (2) and (3), $\Delta\sigma_t$ is calculated to be just 6 MPa. This result does not support the assertion that {332} <113> mechanical twins are the dominant contributor to the significant strain hardening observed. This contradiction can be explained by the fact that due to the limited resolution of EBSD, nano-scale twins cannot be discerned through this analysis technique. It is observed that in TWIP Steels [293], singular mechanical twins observed in EBSD maps are actually bundles of several thin mechanical twins. Eckert et al. also reported similar TEM observations showing that submicron and nanoscale deformation twins arrange to form a filament shape across large length scales [294]. The width of the network of mechanical twins (Figure 4c) observed in our specimens by TEM is also similar to that of the individual twins observed by EBSD (Figure 4a). If we assume that each twin observed in EBSD actually consists of networks of several nano-scale twins with average widths of 40 nm, $\Delta\sigma_t$ is then calculated to be 252 MPa which accounts for around 33% of the total stress for deformations at 293K and 1000 s^{-1} to a true strain of 0.2. Due to a lack of exact values for the shear modulus and average twin width, the calculated value for $\Delta\sigma_t$ is at best a rough estimate but does help to explain the prominent strain hardening behaviour at 293K. The strain hardening rate decreases with increasing strains due to the thickening of twins and slowdown in the primary twining rate, while it remains almost constant for strains above 0.10 probably due to the activation of secondary twinning and twin-twin intersections which further reduce the dislocation mean free path.

4.2 Strain hardening behaviour at 573K and 873K

The main deformation mechanism for the Ti-Nb-Zr-Mo-Sn alloy changes from {332} <113> mechanical twinning at 293K to co-operative {332} <113> mechanical twinning and dislocation slip at 573K, to dislocation slip only at 873K. High temperatures increase β phase stability, which alters the deformation modes at different temperatures.

Elevated temperatures reduce the tendency for mechanical twinning and provide dislocations with the thermal energy necessary to overcome obstacles, resulting in a drastic reduction in the strain hardening rate at 573K and 873K compared with that at 293K. Considering the small volume fraction of mechanical twinning observed in Fig.7 and Fig.8, it is reasonable to conclude that the strain hardening behaviour for high strain rate deformation at 573K and 873K is mainly related to the development of dislocation forests rather than mechanical twinning.

To quantitatively analyse the hardening effects of the dislocation forests on the deformations at 573K and 873K, $\Delta\sigma_\rho$, the flow stress contribution can be expressed as [295, 296]:

$$\Delta\sigma_\rho = M\beta Gb\sqrt{\rho} \tag{5}$$

where ρ is the total dislocation density determined by the competition between dislocation multiplication and annihilation driven by dynamic recovery. Changes in the dislocation density in conjunction with strain can be determined from:

$$d\rho/d\varepsilon = M(k_1\sqrt{\rho} - k_2\rho) \tag{6}$$

where k_1 denotes the dislocation storage rate and k_2 denotes the intensity of dynamic recovery.

For deformations at 573K with a true strain of 0.2, taking the parameters of f is 8% and d is $w/2=3$ μm into Eq. (2), (3) and (4), the $\Delta\sigma_t$ is calculated to be only ~1 MPa. Even if it were to assume that due to the limited resolution of the EBSD mapping the average twin width is an overestimate and the average twin width is similar to that for the deformation at 293K at around 40 nm, regardless of the increased deformation temperatures, the calculated $\Delta\sigma_t$ is only 26 MPa. Therefore, twinning-induced hardening, $\Delta\sigma_t$, can be neglected in Eq. (1). Also, considering that the friction stress σ_0 is insensitive to strain, the equation for strain hardening rate θ can be expressed as:

$$\theta = \frac{d\sigma}{d\varepsilon} = \frac{d(\sigma_0+\Delta\sigma_\rho+\Delta\sigma_t)}{d\varepsilon} = \frac{d\Delta\sigma_\rho}{d\varepsilon} = \frac{d\Delta\sigma_\rho}{d\rho}\times\frac{d\rho}{d\varepsilon} \tag{7}$$

Then taking Eq. (5) and (6) into Eq. (7), θ can be obtained from:

$$\theta = \frac{M^2\beta Gb}{2}k_1 - \frac{M^2\beta Gbk_2}{2}\sqrt{\rho} \tag{8}$$

Therefore a linear relationship exists between the strain hardening rate θ and the stress $\Delta\sigma_\rho$ based on Eq. (5) and (8) can be obtained from:

$$\theta=A-B\Delta\sigma_\rho \quad (9)$$

where,

$$A=\beta GbM^{2}\frac{k_1}{2} \quad (10)$$

$$B=M\frac{k_2}{2} \quad (11)$$

Assuming that the strain hardening is mainly controlled by development of dislocation forest, $\Delta\sigma_\rho$ can be substituted with (σ-σ_y), and the plots of θ vs. (σ-σ_y) for high strain rate deformations at 573K and 873K are shown in Figure 10. After linear curve fitting, *A*, *B* in Eq. (9) for deformations at 573 K and 873 K have been determined to be 1407 MPa, 20 and 920 MPa, 13, respectively.

Using Eq. (8), the parameter k_1 is calculated to be 8×10^9 m^{-1} and 5×10^9 m^{-1} for deformations at 573K and 873K, respectively. k_1 is always regarded as an athermal factor independent of temperature and strain rate [295, 297]. However, k_1 for deformation at 573K is obviously larger than that for the deformations at 873K in our experiments. This contradiction can be attributed to the activation of mechanical twinning for the deformations at 573K. The twin boundaries, similar to grain boundaries, act as sources for the multiplication of dislocations, enhancing the intensity of the dislocation storage rate (k_1). Similar phenomenon has been reported in pure Mg [298] and twinning induced plasticity in steels [297]. Using Eq. (9), the parameter k_2 is calculated to be 13 and 9 for deformations at 573K and 873K, respectively. Unlike k_1, the dynamic recovery rate k_2 is regarded as strain rate and temperature dependent and increases with increasing temperatures. However, k_2 at 873K is contrarily smaller than that at 573K for our experiments. It is reasoned that mechanical twins can absorb dislocations by dissociating them and forming interface ledges, which will enhance the dynamic recovery rate [299]. The difference in k_1 and k_2 for deformations at 573K and 873K is consistent with their strain hardening behaviours shown in Figure 1a. In the early stages of deformation, when dislocation multiplication is the dominant mechanism, the strain hardening rate at 573K is higher than that at 873K because of the larger k_1 value, while the strain hardening rate at 573 K reduces faster than at 873K due to an enhanced dynamic recovery rate due to the presence of mechanical twin boundaries. Therefore, the strain hardening rate at 573K is lower than at 873K when the strain exceeds 0.15. Though the strength contributed by mechanical twinning is relatively small at 573K, the existence of mechanical twins can enhance both the multiplication and annihilation of dislocations thereby influencing the strain hardening behaviour of the Ti-Nb-Zr-Mo-

Sn alloy.

4.3 Yield behaviour

The yield behaviour at 293K is likely related to the stress-induced α", ω phase transformations or to {332} <113> mechanical twinning according to the deformation products observed from the microstructural characterization. It has been observed that the early-stage activation of stress-induced α" [279], ω phase transformations [300] and/or {332} <113> mechanical twinning [301] are related to lower yield stresses. Studies conducted by Sun et al. [72] on a β Ti-12Mo alloy reported that dislocation-induced ω and α" phase transformations along with {332} <113> mechanical twinning take place at the very beginning of the deformation within true strains of around 0.007. However, the exact deformation mechanism at yield point for the deformations at 293K requires further investigation. It is generally thought that the yield stress will decrease with increasing temperatures. However, the yield stress for the Ti-Nb-Zr-Mo-Sn alloy at 573K is higher than that at 293K. The higher yield stress can be related to the more dominant role played by dislocation slip [302]. The significant reduction in the yield stress at 873K is attributed to the cessation of mechanical twinning and to the strong thermal softening effects at the elevated temperatures.

5. Conclusion

In this study, the microstructural evolution and deformation mechanisms of the metastable Ti-Nb-Zr-Mo-Sn alloy at high strain rates (1000 s^{-1}) and temperatures of 293K, 573K and 873K have been investigated systematically. The conclusions can be summarized as follows:

1. The stability of the β phase increases with increasing temperatures and deformation modes activated for the dynamic deformations (1000 s^{-1}) follow the sequence: {332} <113> and {112} <111> mechanical twinning + stress-induced α" and ω phase transformation + dislocations slip at 293K → {332}<113> and {112}<111> mechanical twinning + dislocations slip at 573K → dislocation slip only at 873K.

2. At 293K, the dominant deformation mechanism is {332} <113> mechanical twinning, which induces a much higher strain hardening rate at 293K than at 573K and 873K. At 573K and 873K, dislocation forests control the strain hardening behaviours rather than mechanical twinning. Though the stress contributed by mechanical twinning is relatively small at 573K, the existence of mechanical twinning can enhance both the multiplication and annihilation of dislocations thereby

affecting the strain hardening behaviour of the Ti-Nb-Zr-Mo-Sn alloy.

3. The low yield stress at 293K is likely caused by stress-induced phase transformations and/or {332} <113> mechanical twinning while the enhanced yield stress at 573 K is mainly attributed to the more dominant role played by dislocation slip. The dramatic reduction in yield stress at 873K is due to the cessation of twinning and significant thermal softening brought by elevated temperatures.

4. The texture development in the Ti-Nb-Zr-Mo-Sn alloy is related to the deformation mechanisms active during the plastic deformation. As dislocation slip is dominant at 573K and 873K, the grain orientation gradually rotates to the preferred softer orientation for dislocation slip leading to the formation of more <001> and <111> fibre textures at 573K and 873K.

Acknowledgements

The authors would like to acknowledge the support of the Queensland Centre for Advanced Material Processing and Manufacturing (AMPAM) the facilities and technical assistance from the Australian Microscopy and Microanalysis Research Facility at the Centre for Microscopy and Microanalysis, The University of Queensland. The authors also acknowledge China Scholarship Council for the scholarship supports.

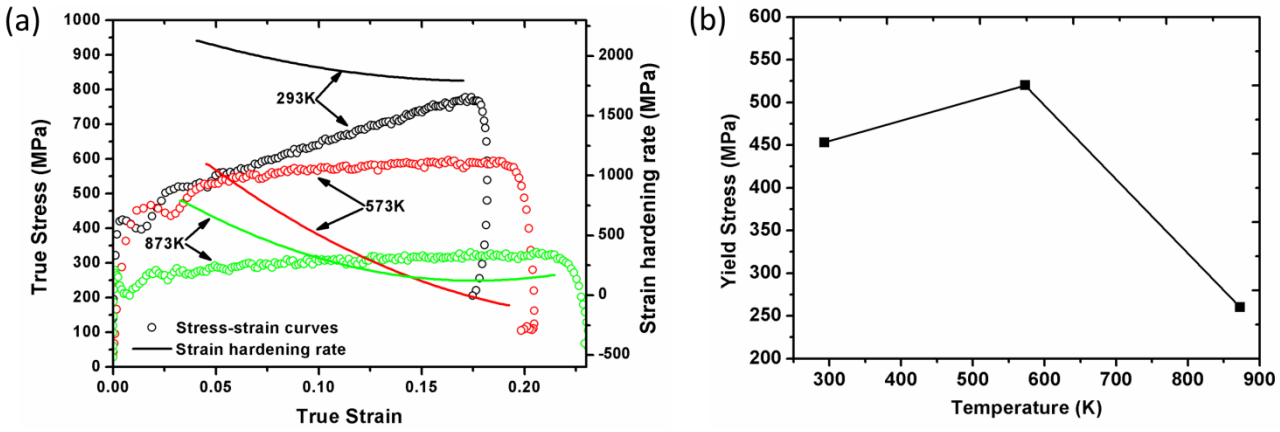

Figure.1. (a) True stress-strain curves and corresponding strain hardening rates. (b) Yield stress for the Ti-Nb-Zr-Mo-Sn alloy deformed at 1000 s^{-1} at different temperatures.

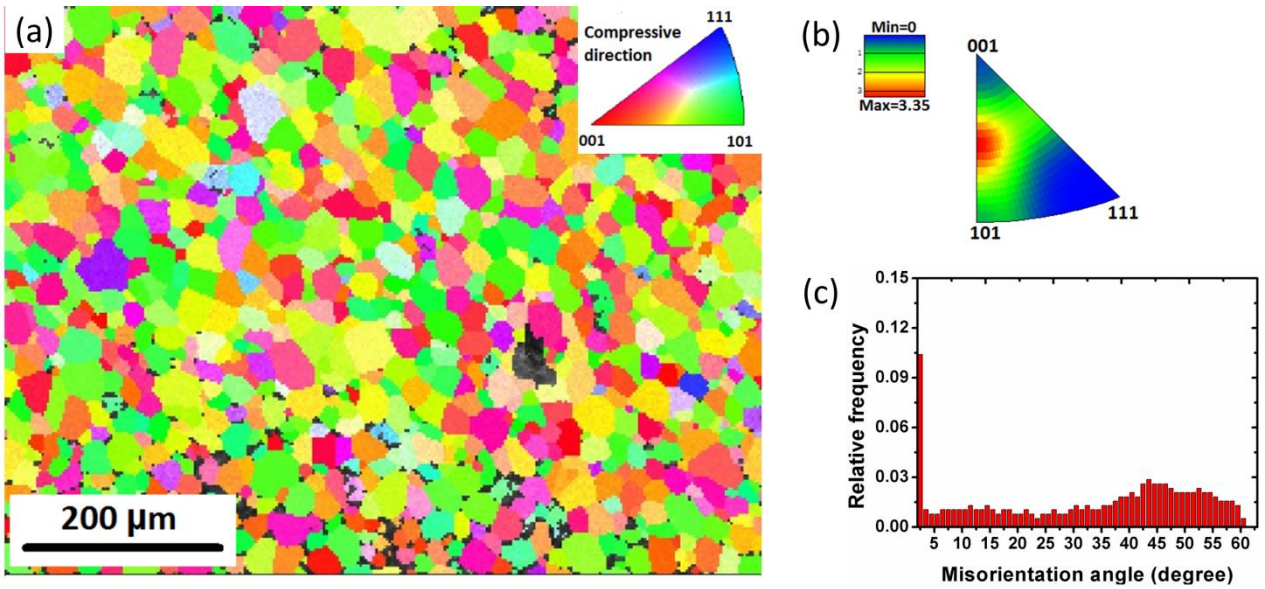

Figure.2. (a) IPF map viewed along the normal direction (ND) (the compressive direction is parallel to ND, step size = 0.2 μm) and corresponding (b) Inverse pole figure, (c) Misorientation distribution histogram for the as-received Ti-Nb-Zr-Mo-Sn alloy.

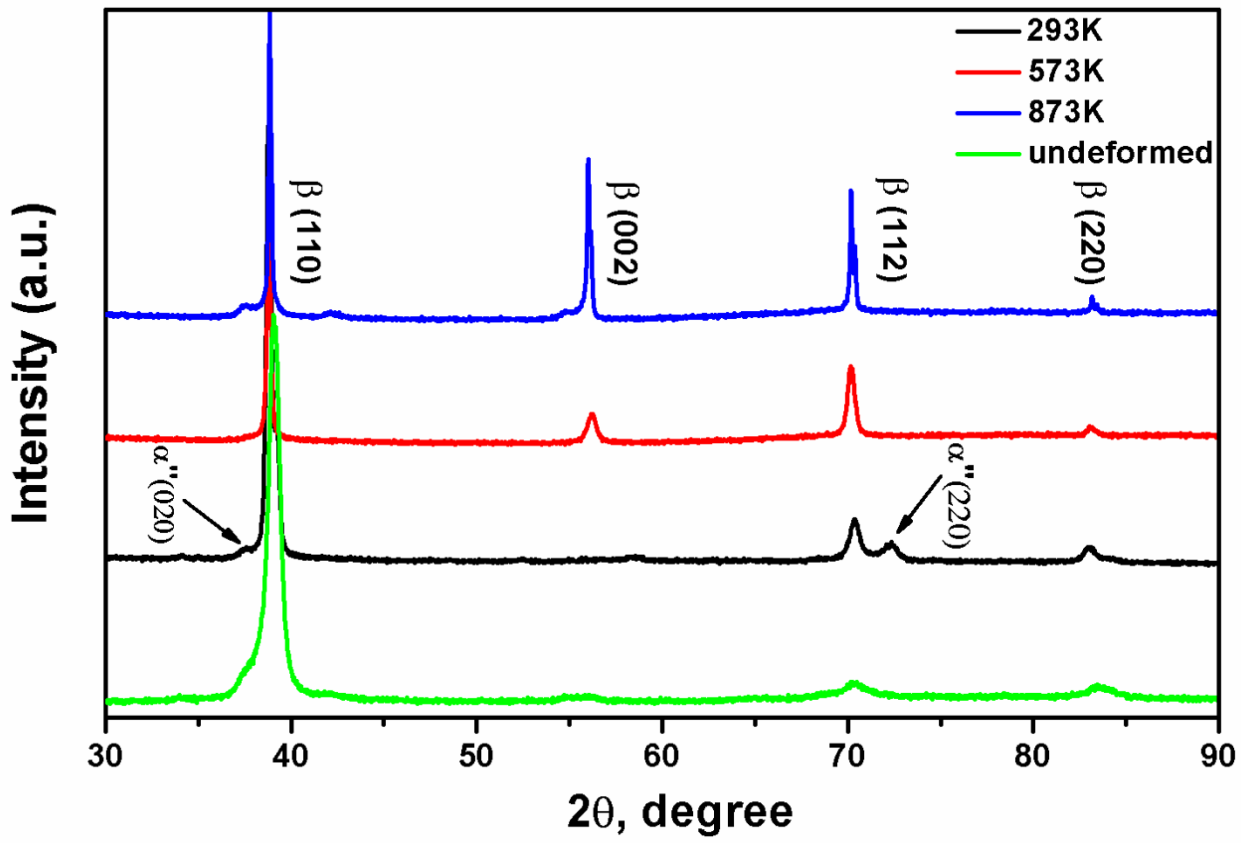

Figure.3. XRD spectra for the Ti-Nb-Zr-Mo-Sn alloy specimens deformed at 1000 s^{-1} to a true strain of 0.2.

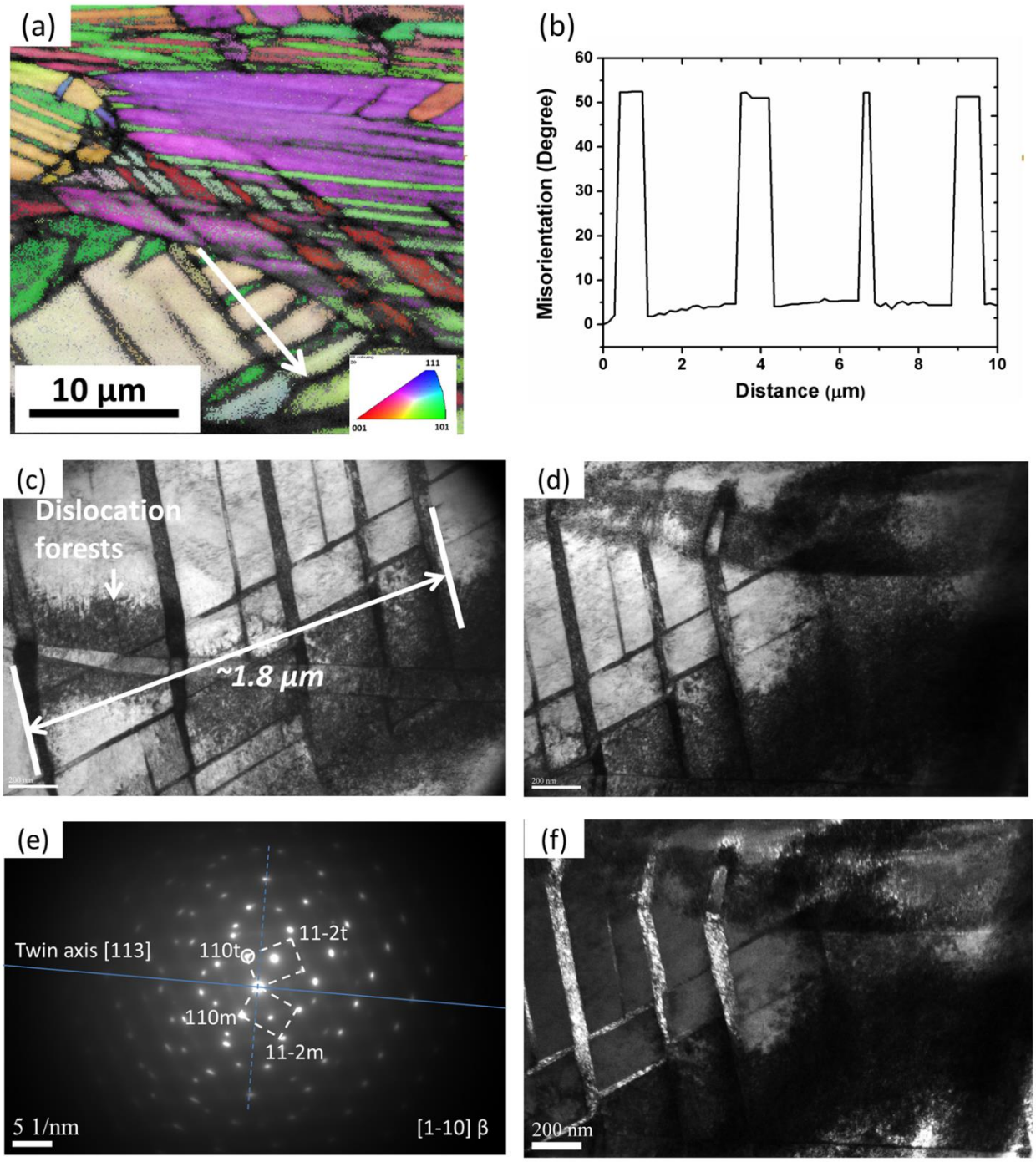

Figure.4. EBSD and TEM analysis of the specimens deformed at 1×10^{3} s^{-1} and 293 K (True strain = 0.2): (a) EBSD IPF map viewed along ND (the compressive direction is parallel to ND, step size = 0.2 µm.) (b) Line trace across region arrowed in (a) showing the misorientation angles of the twins. (c), (d) TEM bright-field images and corresponding (e) selected area diffraction pattern, (f) dark-field image of the {332} <113> twins by selecting diffraction spots circled in (e).

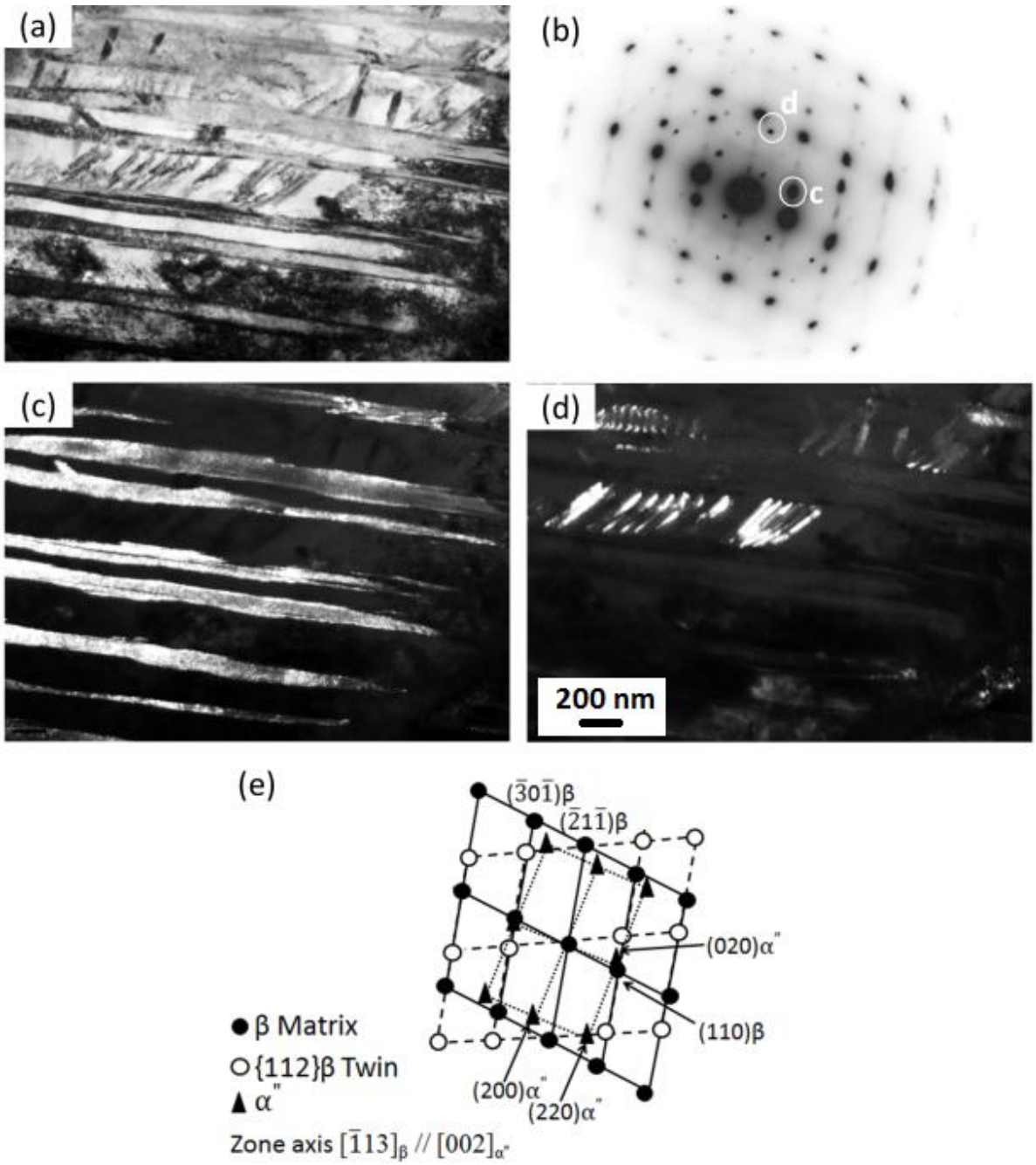

Figure.5. (a) Bright-field image of the specimen deformed at 293K and 1000 s^{-1} (True strain = 0.2) and corresponding (b) SADP. Dark-field images of (c) {112} <111> twins and (d) α" martensite formed by selecting the diffraction spots highlighted in (b). (e) Indexed diagram corresponding to {112} <111> twins and α" martensite.

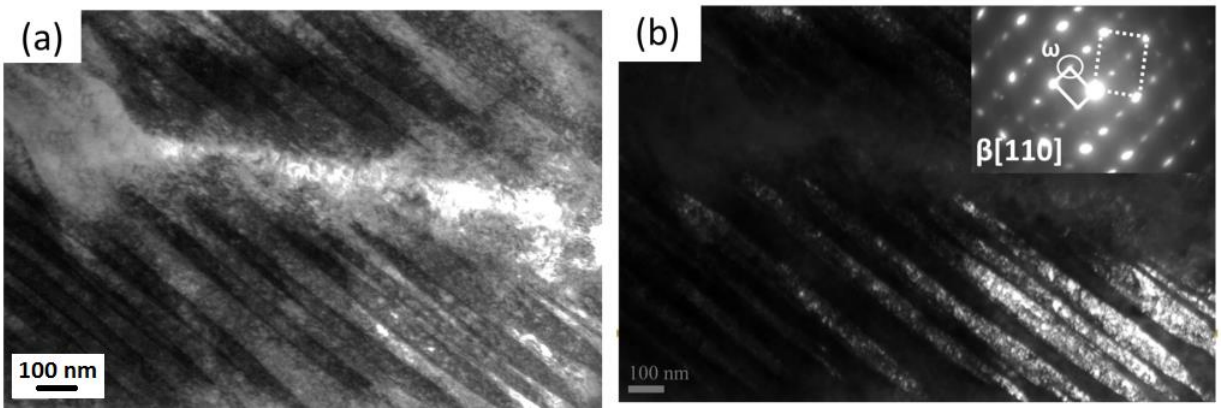

Figure.6. (a) Bright-field and (b) Dark-field images showing stress induced ω phase formed in specimens deformed at 293K and 1000 s^{-1} and the inset of (b) shows the corresponding SADP.

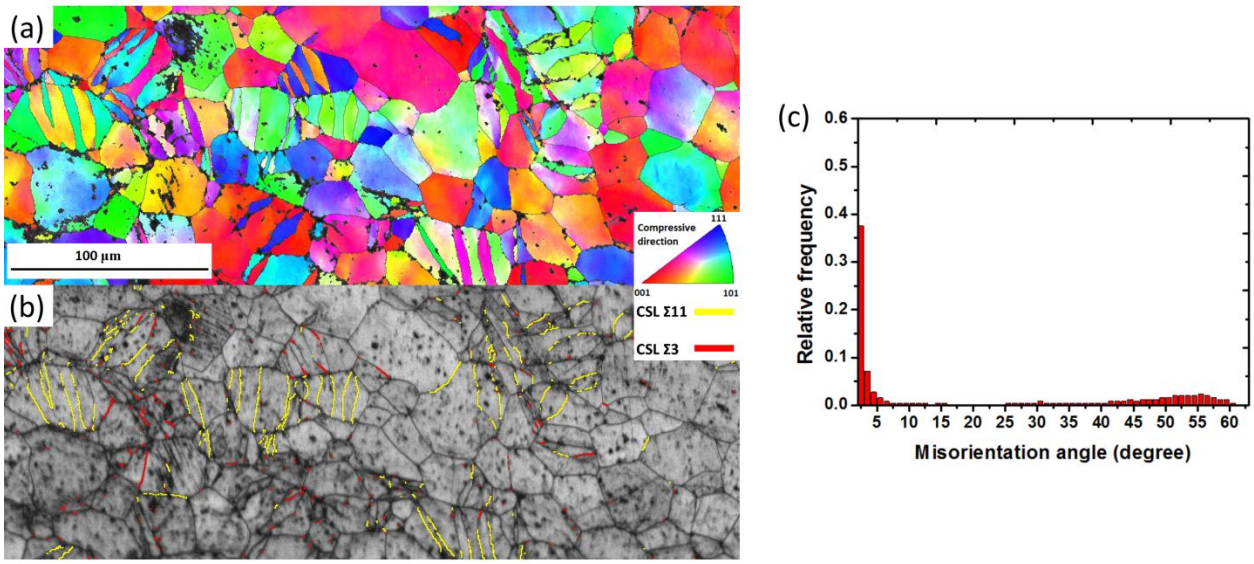

Figure.7. EBSD analysis: (a) IPF map viewed along ND (the compressive direction is parallel to ND, step size = 0.4 μm), (b) band contrast map and (c) corresponding misorientation distribution histogram for the specimens deformed at 1000 s^{-1} and 573K (True strain = 0.2).

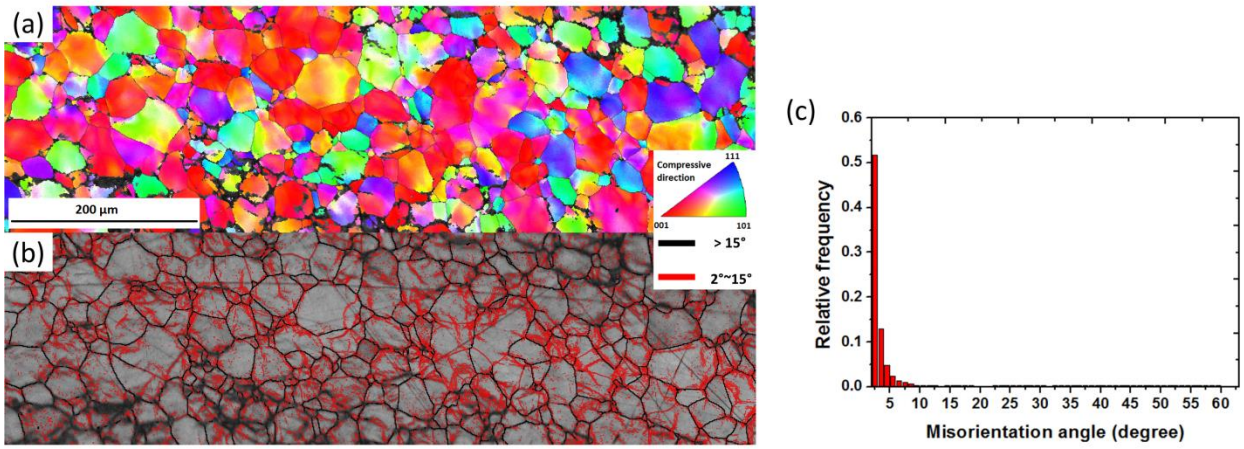

Figure.8. EBSD analysis: (a) IPF map viewed along ND (the compressive direction is parallel to ND, step size = 0.4 μm), (b) band contrast map and (c) corresponding misorientation distribution histogram for the specimens deformed at 1000 s^{-1} and 873K (True strain = 0.2).

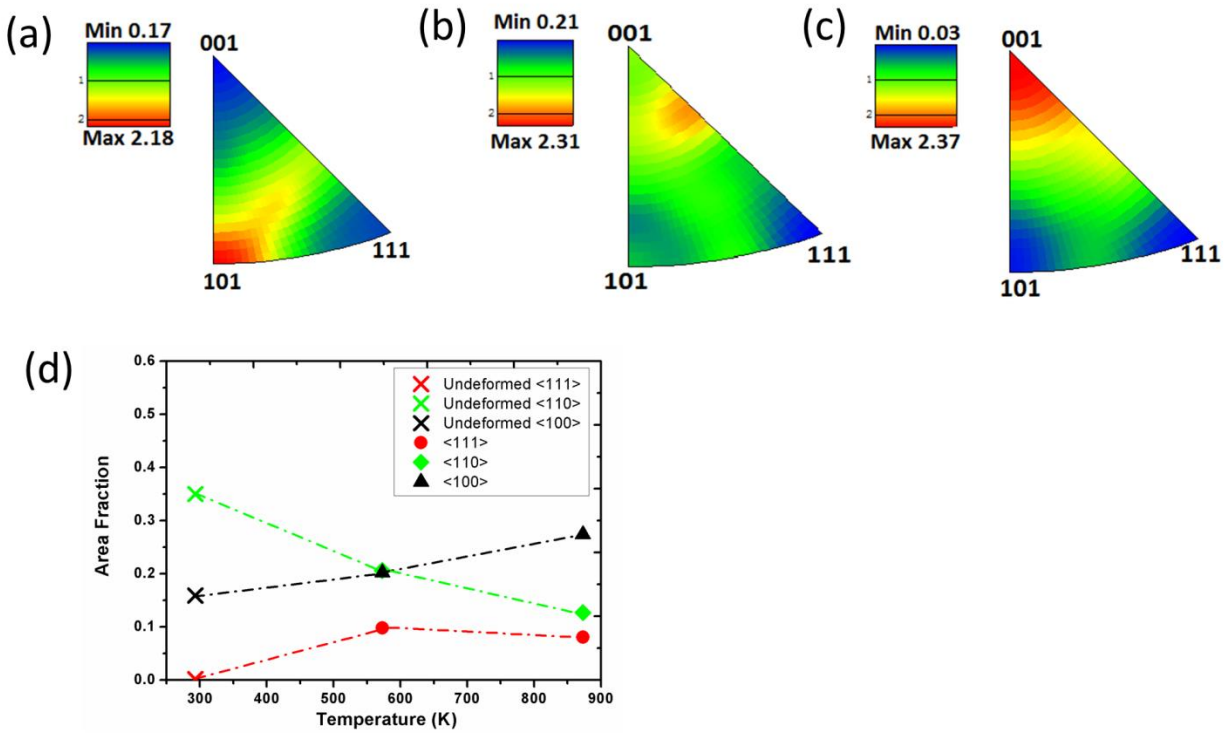

Figure.9. Inverse pole figures (viewed along the compressive direction) from specimens deformed at (a) 1000 s^{-1}, 293K (b) 1000 s^{-1}, 573K (c) 1000 s^{-1}, 873K and (d) Evolution of texture strength with deformation temperature (True strain = 0.2).

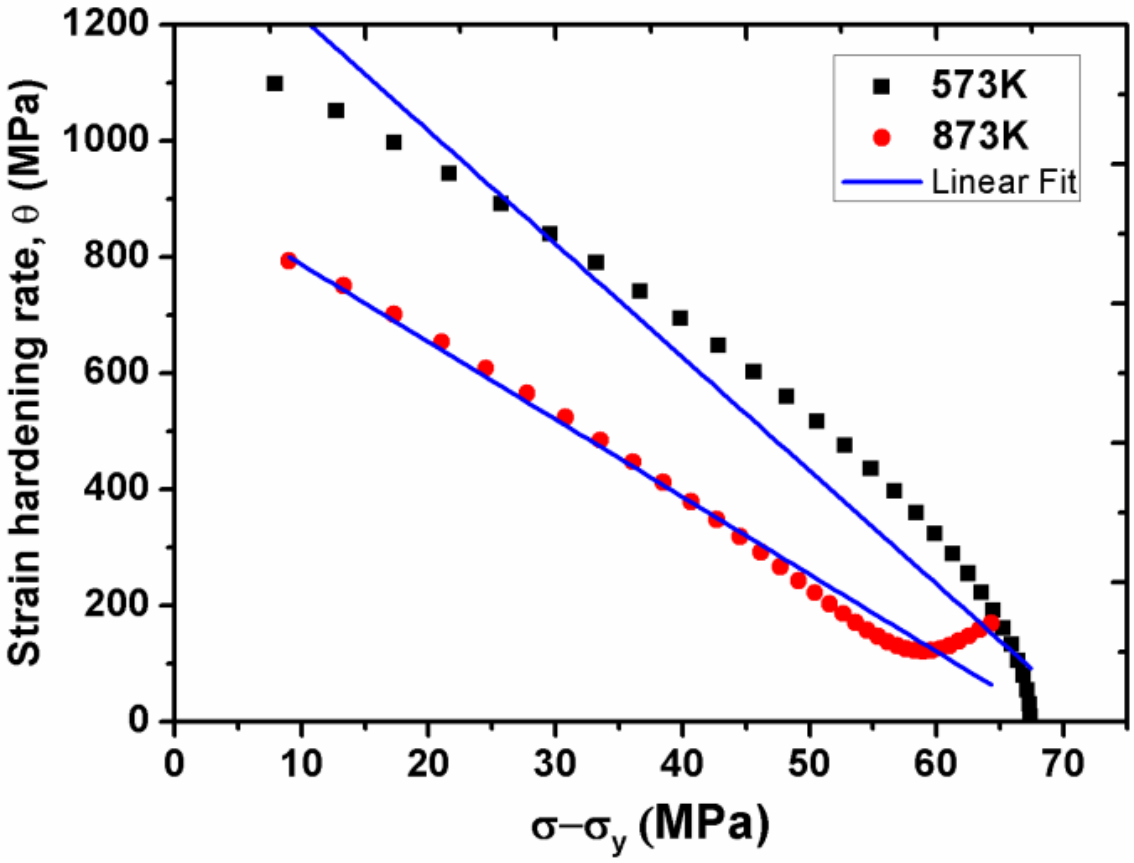

Figure.10. Plot of θ vs. (σ-σ_y) for deformations at 573K and 873K with a strain rate of 1000 s^{-1}.

Chapter 4

Conclusion and Future Work

4.1 Conclusions

In this research the stress-strain behaviour and microstructural evolution of β titanium alloys with different levels of β phase stability have been investigated systematically over a wide range of strain rates and temperatures by Split Hopkinson Pressure Bar testing. Several journal articles have been published during the course of the research. These papers represent an integrated study which contributes to a better understanding of the dynamic response of β titanium alloys to high strain rates at room and elevated temperatures.

The research has demonstrated that β phase stability significantly affects the dynamic response of β titanium alloys at high strain rates. For the Ti-6Cr-5Mo-5V-4Al alloy with Mo_{eq} ~16, dislocation slip is the dominant deformation mechanism under both quasi-static and high strain rate conditions at all testing temperatures. The flow stress of the Ti-6Cr-5Mo-5V-4Al alloy increases with increasing strain rate but decreasing temperature. Also, the alloy is more sensitive to temperature than strain rate. The thermal softening effect brought by adiabatic heating during high strain rate deformations is significant and counteracts the strain hardening effect, resulting in significantly reduced strain hardening rates at high strain rates in contrast to the situation in quasi-static deformation.

For the Ti-25Nb-3Zr-3Mo-2Sn alloy with Mo_{eq} ~10, multiple deformation mechanisms including dislocations slip, {332} <113> and {112} <111> mechanical twinning, stress-induced martensite and ω phase transformations are activated simultaneously at ambient temperatures and among them {332} <113> twinning is dominant, regardless of strain rates. A strong strain hardening rate remains at high strain rates at 293K due to the dynamic Hall-Petch effect induced by extensive mechanical twinning. The stability of the β phase increases with increasing temperatures, thereby the deformation modes activated in the Ti-25Nb-3Zr-3Mo-2Sn alloy deformed at high strain rates vary with temperature. At 573K and 873K, dislocation forests primarily control the strain hardening behaviour in place of mechanical twinning.

Adiabatic shear bands were observed in the Ti-6Cr-5Mo-5V-4Al alloy deformed at strain rates of $4000s^{-1}$ and $10000s^{-1}$ when the deformation temperature was increased to 873K. The tendency for shear bands to form at elevated temperatures in the Ti-6Cr-5Mo-5V-4Al alloy is potentially a consequence of the formation of features with string-like morphologies which only occurred at 873K. The initiation of adiabatic shear bands did not induce a drastic reduction in the flow stress. A high degree of grain refinement was observed by TEM within the shear bands and dynamic recovery played the dominant role in the grain refinement process. The recrystallized nanograins

observed in the core region of the shear bands have been attributed to the action of rotational dynamic recrystallization mechanisms on the basis of kinetic calculations.

In this research the parameters for the Johnson-Cook model and a modified Zerilli-Armstrong model were successfully obtained for the Ti-6Cr-5Mo-5V-4Al alloy. The Johnson-Cook model is capable of predicting the dynamic flow behaviour of materials accurately in a narrow domain near the strain value used in the parameter fitting analysis. Though the Johnson-Cook model is inadequate to track the complex strain hardening behaviour of the Ti-6Cr-5Mo-5V-4Al alloy at high strain rates over a wide range of temperatures due to the limitations in its construction, its applicability has been demonstrated for the finite element simulations of laser-assisted machining of the Ti-6Cr-5Mo-5V-4Al alloy. The modified Zerilli-Armstrong model has a much better capacity than the Johnson-Cook model in tracking the complicated strain hardening behaviour of the Ti-6Cr-5Mo-5V-4Al alloy as the former incorporates the coupled effects of strain and temperature. However, the fitting process for the modified Zerrili-Armstrong model is more complicated and the temperature range must be taken into consideration when selecting data for parameter fitting in order to allow for the influence of dynamic recovery and dynamic recrystallization.

4.2 Future Work

During the course of this research, there were some aspects concerning the dynamic response of β titanium alloys to high strain rates and elevated temperatures, which were identified as warranting further investigation as detailed below:

1. The formation mechanism of the features with string-like morphologies in the Ti-6Cr-5Mo-5V-4Al alloy deformed at high strain rates at 873K.

The features of string-like morphologies were observed in the Ti-6Cr-5Mo-5V-4Al alloy deformed at $4000s^{-1}$ and $10000s^{-1}$ at 873K and were related to the initiation of adiabatic shear bands in Paper 1. However, the formation mechanism for this feature has not been clarified. Whether they were formed by displacive, diffusional or mixed mode mechanisms remains unclear. Investigations on the formation mechanisms of the feature will be beneficial for the control of microstructures and then optimization of properties for the Ti-6Cr-5Mo-5V-4Al alloy.

2. The microstructural evolution within adiabatic shear bands in the Ti-25Nb-3Zr-3Mo-2Sn alloy and corresponding formation mechanisms.

For the Ti-6Cr-5Mo-5V-4Al alloy, dislocation motion and dynamic recovery played important roles in the formation of refined grains within the adiabatic shear bands. As multiple deformation mechanisms were observed in the Ti-25Nb-3Zr-3Mo-2Sn alloy deformed at high strain rates as described in Paper 4 and 5, the microstructural evolution within the shear bands in the Ti-25Nb-3Zr-3Mo-2Sn alloy and their corresponding formation mechanisms remain unclear and warrant further investigation.

3. The establishment of constitutive models for the Ti-25Nb-3Zr-3Mo-2Sn alloy.

The dynamic response of the Ti-25Nb-3Zr-3Mo-2Sn alloy to high strain rates at room and elevated temperatures is more complicated than the Ti-6Cr-5Mo-5V-4Al alloy. Therefore, empirical constitutive models such as the Johnson-Cook model and Zerilli-Armstrong model are not appropriate to predict the flow stress of the Ti-25Nb-3Zr-3Mo-2Sn alloy. To the authors' best knowledge, to date no constitutive model has ever been established for the Ti-Nb based β titanium alloys. The establishment of physically-based constitutive models, which include the effects of mechanical twinning, may be suitable to predict their deformation behaviours.

Appendix

Numerical Modeling of Laser Assisted Machining of a Beta Titanium Alloy

Yao Xi[1,2,a], Hongyi Zhan[1,b], R. A. Rahman Rashid[2,3,c], Gui Wang[1,2,d], Shoujin Sun[4,e], Matthew Dargusch[1,2,f]

[1]Centre for Advanced Materials Processing and Manufacture, School of Mechanical and Mining Engineering, The University of Queensland, St Lucia, Queensland 4072, Australia

[2]Defence Materials Technology Centre, Level 2, 24 Wakefield St, Hawthorn VIC 3122, Australia

[3]Faculty of Science, Engineering and Technology, Swinburne University of Technology, Hawthorn, Victoria 3122

[4]School of Aerospace, Mechanical and Manufacturing Engineering, RMIT university, Melbourne, VIC 3000, Australia

[a]y.xi@uq.edu.au, [b]h.zhan@uq.edu.au, [c]rrahmanrashid@swin.edu.au, [d]gui.wang@uq.edu.au, [e]shoujin.sun@rmit.edu.au, [f]m.dargusch@uq.edu.au

Abstract: Laser assisted machining is a promising new machining technology that can be used to assist with the fabrication of components from difficult to machine materials such as Beta titanium alloys. To understand the mechanism behind this process, a reliable numerical machining model is needed. This study employed an SPH method to the problem of laser assisted machining of Ti-6Cr-5Mo-5V-4Al alloy. The SPH method has several advantages when dealing with large-deformation problems compared with traditional finite element methods. A laser scanning model was developed beforehand to predict the temperature elevation due to laser heating and the temperature results were used as initial conditions for the SPH/FE machining models. Johnson-Cook parameters and Zerilli-Armstrong parameters of Ti-6Cr-5Mo-5V-4Al alloy were acquired based on experimental data from the Split Hopkinson Pressure Bar (SHPB) test and were implemented in the machining models. The cutting force predictions of machining models using these two material models were discussed in this study. Both conventional machining (CM) and laser assisted machining (LAM) were simulated. The main cutting force predictions and the temperature predictions were compared with experimental results to validate the models.

Keywords: Laser assisted machining; SPH method; Material constitutive model

1. Introduction

Owing to their inherent properties such as high strength to weight ratio, high fracture toughness and excellent corrosion resistance, beta titanium alloys are widely used in the aerospace industry for applications such as landing gear, springs, nacelle and empennage structure [303]. However, the machining cost of beta titanium alloys is very high due to their unique properties such as low thermal conductivity, strong alloying tendency with some material in the cutting tool, and relatively low modulus of elasticity. Thus some advanced machining technologies have been developed to improve the machinability of Beta titanium alloys in order to lower the manufacturing cost and increase productivity in order to meet the growing demand for products manufactured from beta titanium alloys. One of these advanced machining technologies being investigated is laser assisted machining (LAM).

The basic idea of LAM is to introduce a laser beam into the conventional machining system as a heat source in order to locally heat and soften the workpiece material before the cutting tool removes the unwanted section. As a result of the laser heating, the yield strength and hardness of the workpiece material is reduced which should allow the material to be machined with lower power consumption and higher material removal rate and therefore greater productivity [304]. This method has been studied by some researchers and is believed to be a promising method to reduce the machining cost of difficult to machine materials. Sun et al. [305] carried out a parametric investigation on laser assisted machining of commercially pure titanium, compared to conventional machining. In this study both a lower magnitude and lower variation of cutting forces and a smoother surface finish were achieved. Dandekar et al. [306] reported a significant machinability improvement for the Ti-6Al-4V alloy during laser assisted machining, with reduced specific cutting energy and improved surface roughness compared to conventional machining. Rahman Rashid et al. [307, 308] conducted experimental studies on laser assisted machining of the beta titanium alloy Ti-6Cr-5Mo-5V-4Al. It was found through this work that cutting force can be reduced by up to 15% under LAM when compared with conventional machining, and the optimum feed rate, cutting speed and laser power for LAM of Ti-6Cr-5Mo-5V-4Al alloy was 0.15-0.25 mm/rev, 25-125 m/min and 1200-1600 W, respectively.

Experimental studies of laser assisted machining can be time consuming and expensive because it is a process with complex thermo-mechanical and highly dynamic features, and a large amount of heating and cutting parameters can potentially affect the process dramatically. Therefore, it is essential to have reliable numerical models to conduct parametric studies on laser assisted machining in order to understand the mechanism behind the process and optimize the machining

parameters.

Simulation of conventional machining processes have been widely studied by researchers [309-313], and most of this reported work adopted finite element methods. However, as the machining process is a large deformation process with complex physical and chemical features, the traditional finite element method has some difficulties in simulating the machining process due to issues such as mesh tangling and distortion. To overcome these problems, some researchers have introduced a new method in their studies to simulate the machining process, which is the smoothed particle hydrodynamics (SPH) method.

The SPH method is a mesh-free Lagrangian numerical method originally developed in 1977 for astrophysics applications, and has since been applied in mechanics problems over the past three decades. Applying the SPH method to machining models involves several advantages compared to the traditional finite element method. First, the mesh-free SPH method does not have the mesh tangling and distortion problems which usually happen in traditional finite element analyses involving large deformation. Another advantage of the SPH method is that it does not need to use chip separation criterion or predefine the cutting path to allow the chip to separate from the workpiece. In SPH machining models, the chip will naturally separate from the workpiece, and the creation of the new free faces can be directly managed by the SPH method. Limido et al. [314] applied the SPH method to simulate high speed metal cutting. The results of the SPH model were compared with experimental and numerical data in terms of the chip morphology and the cutting forces. The comparison showed that the SPH model is able to predict continuous and serrated chips and also the cutting forces. However, in order to reduce the model size and the computational time, the tool velocity in the SPH model is assumed to be ten times higher than the real velocity, which in reality is valid only for limited situations. Calamz et al. [315] used an SPH metal cutting model to analyze the chip formation and cutting forces with and without tool wear. The tool wear was modeled by the change of the tool geometry. The predicted results were compared with experimental data which showed good agreement for chip formation comparisons. The model correctly predicted the variation of the cutting forces induced by the tool wear but not the magnitude of the cutting forces. In a similar way to Limido's work [314], the tool velocity was also assumed to be ten times higher than the real velocity in this study. Zahedi et al. [316] have also reported an SPH machining model which can be used to study a micro-machining process in a similar way as other reported SPH machining models, this work also simulated orthogonal cutting with a relatively simple shaped workpiece.

Simulation of conventional machining has been widely studied by researchers, but only a few

studies have addressed the simulation of laser assisted machining. Singh et al. [317] reported a 3D transient finite element model of a moving Gaussian laser heat source to characterize and predict the heat affected zone of the workpiece material in the laser assisted micro-grooving process. The Gaussian distribution of laser power intensity $P_{x,y}$ at location (x, y) is given by:

$$P_{x,y} = \frac{2P_{tot}}{\pi r_b^2} \exp\left(-\frac{2r^2}{r_b^2}\right) \tag{1}$$

where $r = \sqrt{x^2 + y^2}$ is the distance measured from the laser beam center and r_b is the laser beam radius, $P_{tot} = \eta P_{incident}$, where P_{tot} is the total power absorbed, $P_{incident}$ is the incident laser power, and η is the average absorptivity of the workpiece material. In the center of the laser beam, when the temperature exceeds the melting point the node was assumed to remain in the mesh and the latent heat of fusion was simulated by artificially increasing the liquid specific heat. Corresponding experiments were conducted to validate the model. The experimental results were compared with the predicted results, where a prediction error of 5%-15% was found with most of the predicted results falling within 10% of the measured results.

Yang et al. [318] also developed a 3D transient finite element thermal model to predict the depth and width of the heat affect zone in a Ti6Al4V workpiece caused by laser heating. The model was developed using the commercial finite element software ANSYS and the laser beam were simulated by a Gaussian heat source. The material emissivity ε and absorptivity η used in the model were calculated based on the experimental data using Equation 2 and 3.

$$\varepsilon = \left(\frac{T_r}{T_s}\right)^4 \tag{2}$$

where T_s and T_r are the sample and its radiance temperature, respectively,

$$\eta = \frac{K\Delta T}{2P_{incident}} \sqrt{\frac{\pi^3 r_b^3 U}{2\alpha}} \tag{3}$$

where k is the thermal conductivity, ΔT is the measured maximum temperature on the top surface of the workpiece material, $P_{incident}$ is the incident laser power, r_b is the laser beam radius, U is the laser scanning speed, α is the thermal diffusivity. To achieve higher model efficiency, a plane of symmetry was used and therefore only half of the workpiece was modeled. Comparisons of the simulated and measured maximum depth and width of the heat affected zone for various laser

powers and laser scanning speeds were carried out, and very close correlations between simulation and experimental results were observed.

Shen [319] developed a 3D thermal model using the finite element analysis software ANSYS to predict the temperature distribution in a silicon nitride workpiece during laser assisted milling. The top-hat distribution of laser intensity was used in this study. An approximately uniform heat flux was applied to the elements within an elliptic spot on the top surface of the workpiece. Material removal was taken into account in this study by deactivating the elements that had been removed. Heat generation associated with machining was also considered in the model, however, a later detailed study performed by the author showed that the heat generation associated with machining is negligible compared to the heat flux input from the laser source. The thermal model was validated through experiments, the predicted temperature histories were in good agreement with those measured. The minimum temperature in the cutting zone predicted by the thermal model was used as the initial workpiece temperature for a 2D distinct element machining model which well depicted the brittle behavior of the material removal process of silicon nitride ceramics during laser assisted milling.

In this study, both a traditional finite element method and the SPH method embedded in LS-DYNA were used to simulate the laser assisted turning of the beta titanium alloy Ti-6Cr-5Mo-5V-4Al. A finite element thermal model was developed to predict the cutting area temperature distribution after the laser heated the workpiece material. The laser spot was modeled by an approximately uniform heat flux which was applied to elements within a circular spot on the top surface of the workpiece. A similar method was adopted in Shen's study [319]. The temperature distribution result predicted by the thermal model was used as an initial condition for a SPH/FE turning model to study the LAM process. To develop the machining model, a material constitutive model is necessary, therefore a set of Johnson-Cook model parameters and a set of Zerilli–Armstrong model parameters for the Ti-6Cr-5Mo-5V-4Al alloy were obtained based on the experimental data from the Split Hopkinson pressure bar (SHPB) tests, both sets of parameters were employed in the machining simulation. In this study, the laser scanning and the SPH/FE machining models were validated by comparing the simulation results with the experimental results.

2. Model descriptions

2.1 Geometry and mesh

A 3D FE/SPH turning model was developed in this study. The machining parameters were chosen based on the laser assisted machining and conventional machining experiments previously conducted by the authors' research group [308]. The machining parameters are listed in Table 1.

The cutting tool was assumed to be a rigid body in this study. Details of cutting tool geometry and its effect on the workpiece geometry were taken into consideration in the simulation, the cutting tool used in the turning experiments was a Sandvik CNMX1204 A2-SMH13A tool, the rake angle, clearance angle and tool nose radius of this tool are 15 °, 6 ° and 0.4 mm, respectively. Fig.1 shows the geometry modeling approach to determine the uncut chip cross-section based on the tool nose radius, depth of cut, and feed. Similar geometry setup for the turning process can be found in the literature [320-322].

As shown in Fig.1, the workpiece was divided into two parts, the bottom part was meshed using traditional finite elements while the upper part where the chip would be generated and large deformation would occur was modeled by SPH particles. SPH method was selected here due to its strong ability to handle large deformation problem and chip can separate from the workpiece naturally in SPH machining model without predefining any separation line or using any arbitrary chip separation criterion. The basic principles of SPH method are discussed below [316, 323]:

SPH uses a set of particles to represent a continuum, material properties and state variables are approximated at these finite particles, which move with material deformation. Each particle interacts with all other particles that are within a given distance from it, the distance is usually assumed to be 2*h*, where *h* is called the smoothing length. The value of a continuous function, or its derivative, can be estimated at any particle based on known values at the surrounding particles using the following kernel estimates:

$$f(x) = \int_{\Omega} f(x')W(x - x', h)dx' \tag{4}$$

where *f(x)* is a function of the three-dimensional position vector *x*, *Ω* is the volume of the integral that contains x, dx' is a differential volume element, *W* is the kernel function that weights the particles interactions and is defined using the function θ by the relation:

$$W(x - x', h) = \frac{1}{h^d}\theta\left(\frac{\|x - x'\|}{h}\right) \tag{5}$$

where *d* is the number of space dimensions. *W(x,h)* should be a centrally peaked function. The most common function used by the SPH community is the cubic B-spline which is defined by choosing *y*

as:

$$\theta(y) = C \times \begin{cases} 1 - \frac{3}{2}y^2 + \frac{3}{4}y^3 & for\ y \le 0, \\ \frac{1}{4}(2-y)^3 & for\ 1 \le y \le 2, \\ 0 & for\ y > 2, \end{cases} \tag{6}$$

where C is a constant of normalization that depends on the number of space dimensions.

Then, the smoothing function W satisfies the following conditions:

- Normalization condition:

$$\int_{\Omega} W(x - x', h)dx' = 1 \tag{7}$$

- Delta function property:

$$\lim_{h \to 0} W(x - x', h) = \delta(x - x') \tag{8}$$

where δ is the Dirac delta function.

- Compact support condition:

$$W(x - x', h) = 0 \quad \text{when} \quad |x - x'| > h. \tag{9}$$

After several steps of derivation and by converting the continuous volume integrals to sums over discrete interpolation points, the equations can be expressed as follows:

$$f(x_i) = \sum_j \frac{m_j}{\rho_j} f(x_i) W(x - x', h) \tag{10}$$

where m_j is the mass of particle j and ρ_j is the density of particle j. The value of a function at particle i is approximated using the values of the functions at all the particles that interact with particle i.

2.2 Material constitutive model

In the machining models, a material constitutive model is required in order to describe the relationship between flow stress, strain, strain rate and temperature. The Johnson-Cook (JC)

material model [324] is the most widely used material model [325-327] as it requires fewer material constants and also few experiments to evaluate these constants. The Johnson-Cook constitutive model can be represented by Equation 11:

$$\sigma = (A + B\varepsilon^n)\left(1 + C\ln\frac{\dot{\varepsilon}}{\dot{\varepsilon}_0}\right)\left[1 - \left(\frac{T - T_r}{T_m - T_r}\right)^m\right] \tag{11}$$

where σ is the equivalent flow stress, ε is the equivalent plastic strain, $\dot{\varepsilon}$ is the equivalent plastic strain rate, $\dot{\varepsilon}_0$ is the reference equivalent plastic strain rate, T is the workpiece temperature, T_m is the material melting temperature and, T_r is the room temperature, *A*, *B*, *n*, *m* and *C* are material constants.

Another frequently used material constitutive material model in finite element simulation is Zerilli-Armstrong (ZA) material model, which is a semi-empirical model based on the theory of dislocation dynamics [105]. The model can be expressed by equation as follows:

$$\sigma = C_1 + C_2^{(-C_3T + C_4T\ln\dot{\varepsilon})} + C_5\varepsilon^n \tag{12}$$

where σ is the equivalent flow stress, ε is the equivalent plastic strain, $\dot{\varepsilon}$ is the equivalent plastic strain rate and *T* is the workpiece temperature. C_1, C_2, C_3, C_4, C_5 and *n* are the material constants for ZA model.

Both the Johnson-Cook and Zerilli-Armstrong material constitutive models were used in this study to describe the material behaviour of the Ti-6Cr-5Mo-5V-4Al alloy. In order to acquire the JC and ZA material constants for the Ti-6Cr-5Mo-5V-4Al alloy, Split Hopkinson Pressure Bar (SHPB) experiments were carried out. The results from these experiments were used by the authors' research group in order to calculate the constants in the JC and ZA material models for the Ti-6Cr-5Mo-5V-4Al alloy [328]. The calculated JC and ZA parameters are listed in Table 2.

2.3 Contact and boundary conditions

A node to solid contact algorithm was adopted in this model, which is a contact type used particularly for SPH particles with solid elements using the plane stress, plane strain or axisymmetric formulation. The "tied" option was switched on for the contact interface between the SPH part and the bottom part of the workpiece to eliminate the gap between these two parts. The Coulomb friction model was implemented in this study. The friction coefficient was calculated

using Equation 13 [329, 330]:

$$\mu = \frac{F_t + F_c \tan\alpha}{F_c - F_t \tan\alpha} \tag{13}$$

where F_t and F_c are the thrust force and cutting force, respectively and α is the rake angle. The data used for the calculation was obtained from the laser assisted machining experiments. Calculation results showed that the friction coefficients vary from 0.58 to 0.70. An average value of 0.61 was used for the following machining simulations.

The nodes on the bottom surface of the workpiece were fixed in all directions so that the workpiece would not move during the machining simulation. The initial workpiece temperature was set to room temperature (20 ℃) in order to perform the conventional machining simulation first, and then the thermal results from a laser heating model which will be discussed below were used as the initial thermal condition for the machining model in order to simulate the laser assisted machining process.

2.4 Laser heating thermal model

A laser heating thermal model was developed to predict the temperature distribution in the cutting area of the workpiece material. The laser heating process was realized by a user-defined subroutine where the laser spot was defined by a heat flux *fl* which in LS-DYNA is defined as heat (energy) per time and per surface area, which can be expressed as:

$$fl = \frac{q_{tot}}{t \cdot A} \tag{14}$$

where q_{tot} is the total absorbed laser energy by the elements within the area A per time t. In this study, the radius of the laser spot was 1 mm, q_{tot} is decided by the incident laser power and absorptivity. Here, the incident laser power was assumed to be 1200 W which is reported as the optimum laser power for laser assisted machining of beta titanium alloy Ti-6Cr-5Mo-5V-4Al [307]. Absorptivity is an important parameter that affects the efficiency and reliability of laser heating, but only limited work to address this subject has been reported. The previously mentioned analytical method developed by Yang et al. [318] was adopted in this work to calculate the absorptivity of the workpiece material. The method is expressed as Equation 3, and the data used for the absorptivity calculation comes from the experimental work conducted by the authors' group [307, 308].

Five sets of laser scanning speeds were simulated, these speeds were chosen based on previous

parametric studies on laser assisted machining of titanium alloys [305, 307]. The laser scanning speeds and the corresponding absorptivity are listed in Table 3. Other assumptions of the thermal model included:

1) The size of the workpiece was 211×20×5 mm.
2) The workpiece material was assumed to be homogeneous.
3) The ambient temperature was 20 ℃.
4) Air convention was ignored in this model.
5) The workpiece density is 4.67×10^3 kg/m^3, the temperature-dependent conductivity and heat capacity were measured (see Fig.2.) and used in the simulation.

2.5 Experimental validation

The details of laser assisted machining of Ti-6Cr-5Mo-5V-4Al alloy experiments have been reported by the authors' research group [308]. Both the thermal model and the machining model developed in this work were validated by comparing the simulation results with this experimental data. The basic experiment setup is shown in Fig.3. Laser assisted machining of the Ti-6Cr-5Mo-5V-4Al alloy was performed on a 3.5 hp Hafco Metal Master lathe (Model AL540). A 2.5 kW Nd:YAG laser delivered by a 15 m long laser optical fibre connected to the lathe was used to heat the workpiece material. The laser beam was focused by an optical lens with focal length of 200 mm at an angle of 40°±5°onto the workpiece which was placed at a distance of 208 ±5 mm from the laser. The diameter of the laser spot was 2 mm. A PCB force sensor (Model 260A01) with an upper frequency limit of 90 kHz was used to measure the cutting force. The force signal was recorded and analysed by Scope® software, a noise of 10 N was observed. An infrared thermal camera FLIR A40 was placed 350 mm vertically above the cutting tool to measure the temperature during the machining processes. The cutting tool used in the experiments was an uncoated tungsten carbide tool CNMX1204A2-SMH13A with a 15° rake angle and 6° clearance angle. The machining parameters are listed in Table 1.

3. Results

3.1 Thermal results

The temperature distribution on the workpiece after laser scanning is predicted by the laser heating

model, as shown in Fig.4. The maximum temperature in the laser spot under various laser scanning speeds is shown in Fig.5, it can be seen that the maximum temperature reduced when the laser scanning speed increased. The drop in the maximum temperature is possibly due to the shorter laser exposure time that resulted from higher laser scanning speed.

In Fig.5 (a), the predicted maximum temperature in the laser spot is compared with the maximum temperature in the laser spot measured in experiments, where a good correlation can be obtained, with a maximum error of 9%.

In the laser assisted machining process, the distance between the laser spot and the cutting tool is 25 mm. Therefore, the temperature distribution at the cutting tool position which is 25 mm away from the laser spot (see Fig.4) was used as the initial workpiece temperature condition for the laser assisted machining model. The vertical temperature gradient at the cutting tool position after laser heating is shown in Fig.5 (b).

3.2 Cutting temperature

Temperature in the cutting area was predicted by the machining models and the results are shown in Fig.6. The cutting temperature predicted by the machining model using ZA material parameters is higher and more accurate than that predicted by the machining model using JC material parameters. A large amount of heat has localized on the chips in the simulated results for the machining model using ZA parameters, which shows good agreement with the experimental measurement.

3.3 Cutting force results

The main cutting forces predicted by the machining model during conventional machining and laser assisted machining are compared with the experimental results in Fig.7. Both the simulation results and experimental results indicated that the main cutting force is only slightly influenced by the cutting speed within the tested range. However, the results indicated that machining model using JC material parameters produced much more accurate predictions with an average error of 5.93%, while the predictions from machining model using ZA material parameters has an average error of 32.04% comparing to the experimental measurements.

When machining with the assistance of laser heating, the machining model using JC parameters predicted a maximum 17.40% decrease in the main cutting forces while the experimental results showed a maximum 15.07% reduction in the main cutting force. The predicted average main cutting force reduction within the tested cutting speed range is 13.79% which is also in good agreement

with the experimental results 11.64%, see Fig.8.

However, the machining model using ZA parameters offered a totally different prediction which showed almost no change in cutting force when the laser assistance was added into the machining process.

Cutting forces predicted by the machining model in this study generally showed good agreement with the experimental results. However, machining models that employed ZA parameters failed in predicting the cutting force change caused by laser assistance in the machining process, therefore, the predictions produced by the machining model using JC parameters would be more reliable for this study.

The machining model using JC parameters produced more reasonable results in this study, but all its predictions were slightly smaller than the experimental measurements. The possible reason for this is that the material constants were acquired based on the experimental data from Split Hopkinson Pressure Bar (SHPB) test results, and the SHPB tests produced less than 0.5 of strain which is obviously much smaller than the strain generated in the machining process. It is possible that the JC parameters acquired from this experimental data with lower strain results may lead to an underestimation of the cutting force in the machining simulation.

4. Conclusion

Laser assisted machining of Ti-6Cr-5Mo-5V-4Al alloy models have been developed in this work. A laser scanning model was established beforehand to predict the temperature in the cutting area due to laser heating. The SPH method was used in this study to develop metal cutting models. The machining simulation employed a set of Johnson-Cook parameters which were calculated based on the experimental data of Split Hopkinson Pressure bar (SHPB) Test. Both conventional machining (CM) and laser assisted machining (LAM) were modeled, and the predicted cutting force results from the machining models and the temperature results from the thermal models were compared with the results obtained from CM and LAM experiments in order to validate the simulations. The main findings of this work include:

- The laser scanning model produced accurate predictions of the maximum temperature in the laser spot, it can be seen from both simulation and experimental results that the maximum temperature within the material subjected to the laser spot decreased when the

laser scanning speed increased.

- A SPH approach may be able to model workpieces with relatively complex shapes, and both JC parameters and ZA parameters can be used in the machining simulations. The main cutting forces predicted by the machining model using JC parameters is much more accurate than that predicted by machining model using ZA parameters. Moreover, the machining model using ZA parameters failed in predicting the cutting force change caused by the laser assistance in the machining process.

- Both the results obtained from the machining model using JC parameters and the experimental data indicate that the cutting speed only slightly affects the main cutting force within the tested range. Both simulation and experiment showed that the main cutting force drops when machining with the assistance of the laser. The maximum main cutting force reduction predicted by the simulation is 17.40% while the experimental result is 15.07%.

- Although the main cutting forces predicted by the machining model using JC parameters are smaller than the experimental results, the good agreement between the main cutting force predictions and the experimental results might indicate that the reported Johnson-Cook parameters are suitable for implementation in Ti-6Cr-5Mo-5V-4Al alloy machining simulations for cutting force studies.

Acknowledgment

The authors acknowledge the support of the Queensland Centre for Advanced Material Processing and Manufacturing. The authors would also like to acknowledge the support of the Defence Material Technology Centre.

Table 1. Machining parameters

	Conventional machining	Laser assisted machining
Laser Power	N/A	1200 w
Laser Spot Diameter	N/A	2 mm
Laser-Tool Distance	N/A	25 mm
Cutting Speed (m/min)	51, 66, 78, 103, 118	54, 69, 81, 107, 123
Feed	0.19mm/rev	
Depth of Cut	1 mm	

Table 2. Johnson-Cook parameters and Zerilli-Armstrong parameters for Ti-6Cr-5Mo-5V-4Al alloy

Johnson-Cook model	Zerilli-Armstrong model
A=1397 MPa	C_1=1397 Mpa
B=-569 MPa	C_2=-569 MPa
C=0.031	C_3=0.00113
n=1.215	C_4=-5.2×10^{-4}
m=0.91	C_5=0.0302
	n=1.215

Table 3. Laser scanning speed and corresponding absorptivity.

Laser scanning speed (m/min)	Absorptivity
54	0.647
69	0.685
81	0.674
107	0.694
123	0.712

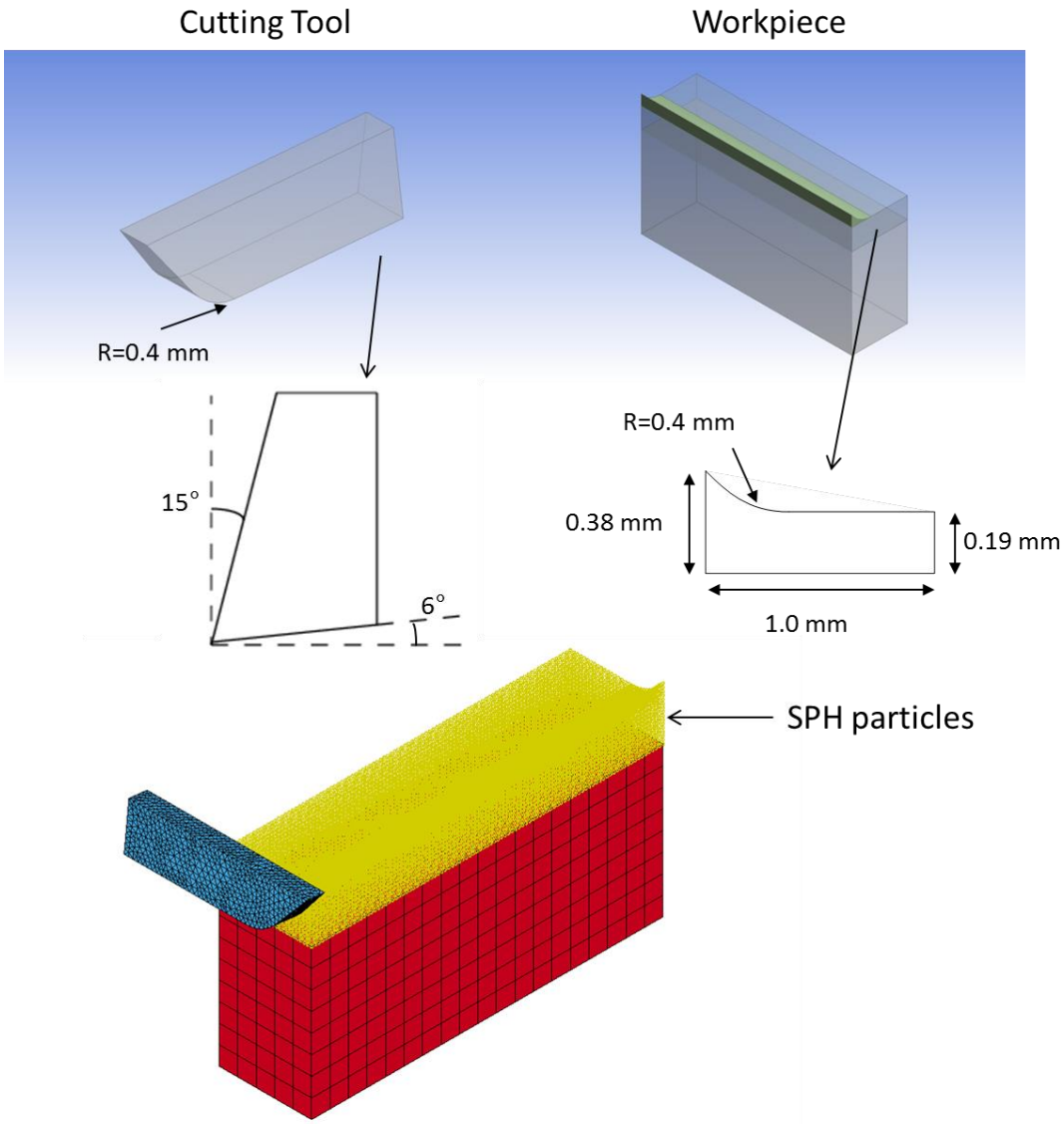

Figure 1. Machining model with detailed cutting tool and workpiece geometry

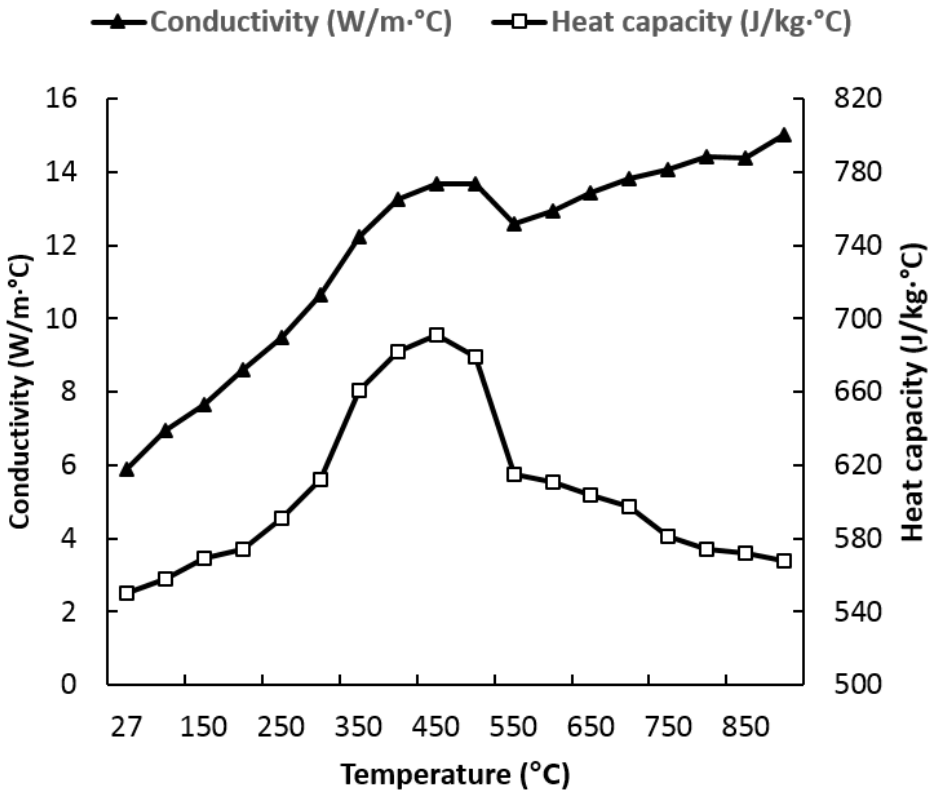

Figure 2. Temperature-dependent conductivity and heat capacity of Ti-6Cr-5Mo-5V-4Al alloy

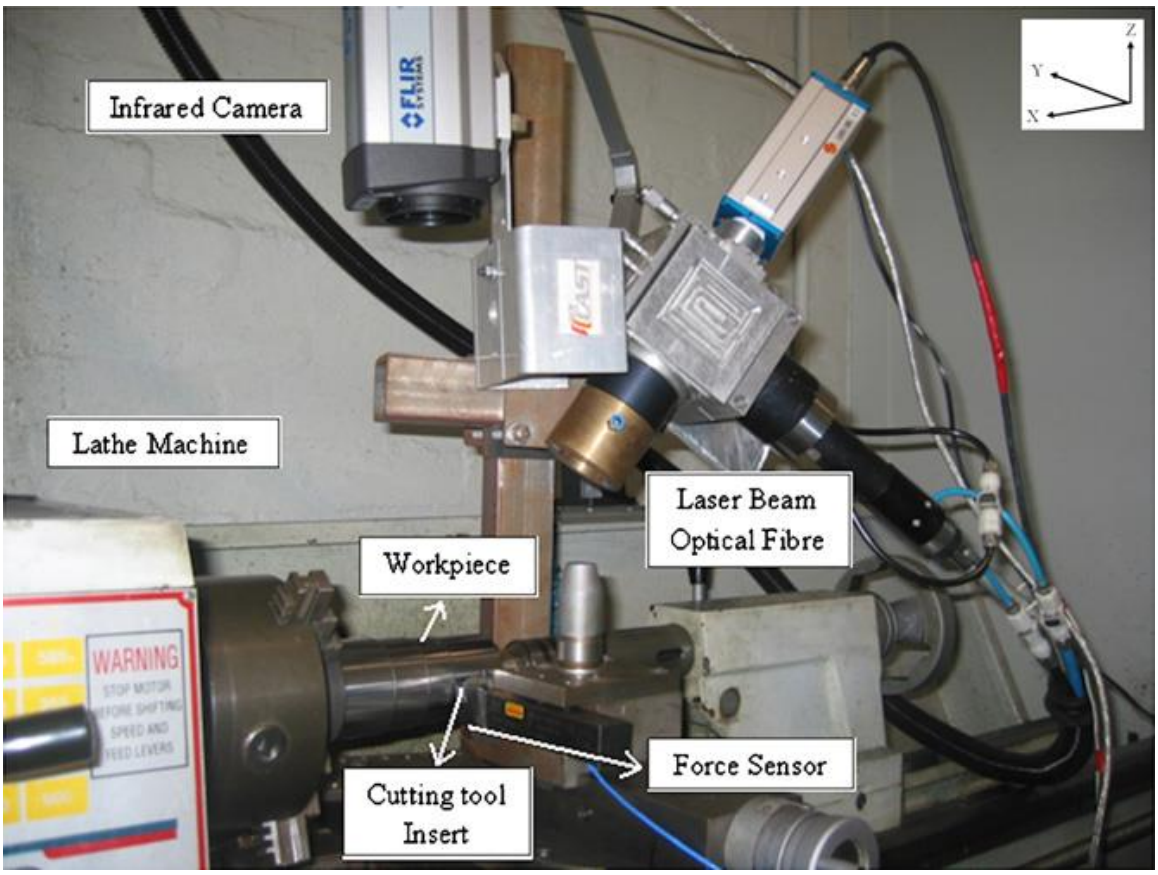

Figure 3. Experiment setup for the machining trials.

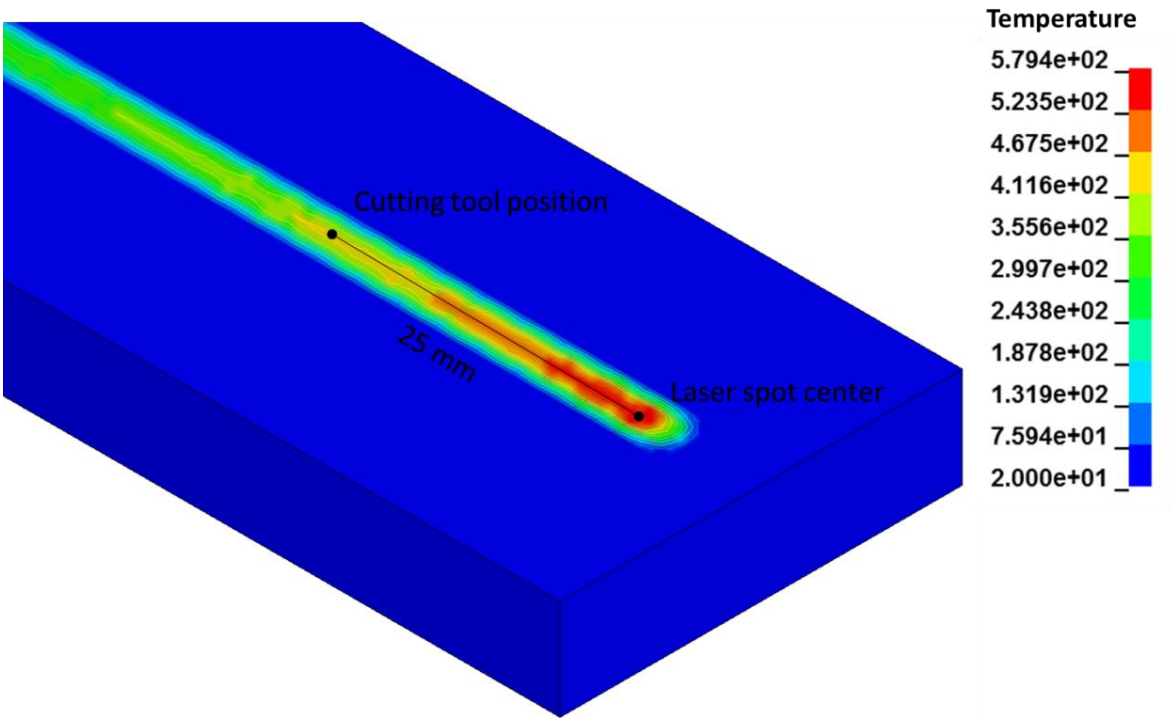

Figure 4. Laser scanning simulation, laser scanning speed 123 m/min.

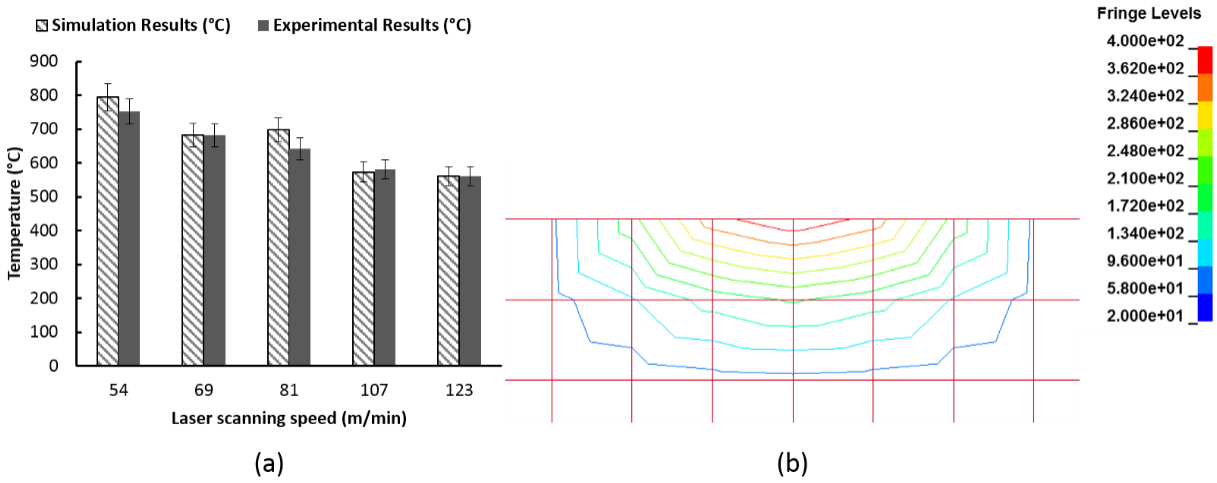

Figure 5. Temperature results from the laser scanning model. (a) Maximum temperature in the laser spot. (b) Vertical temperature gradient resulted from laser heating at the cutting tool position, laser power: 1200 w, laser scanning speed: 54 m/min, mesh size: 0.5 mm

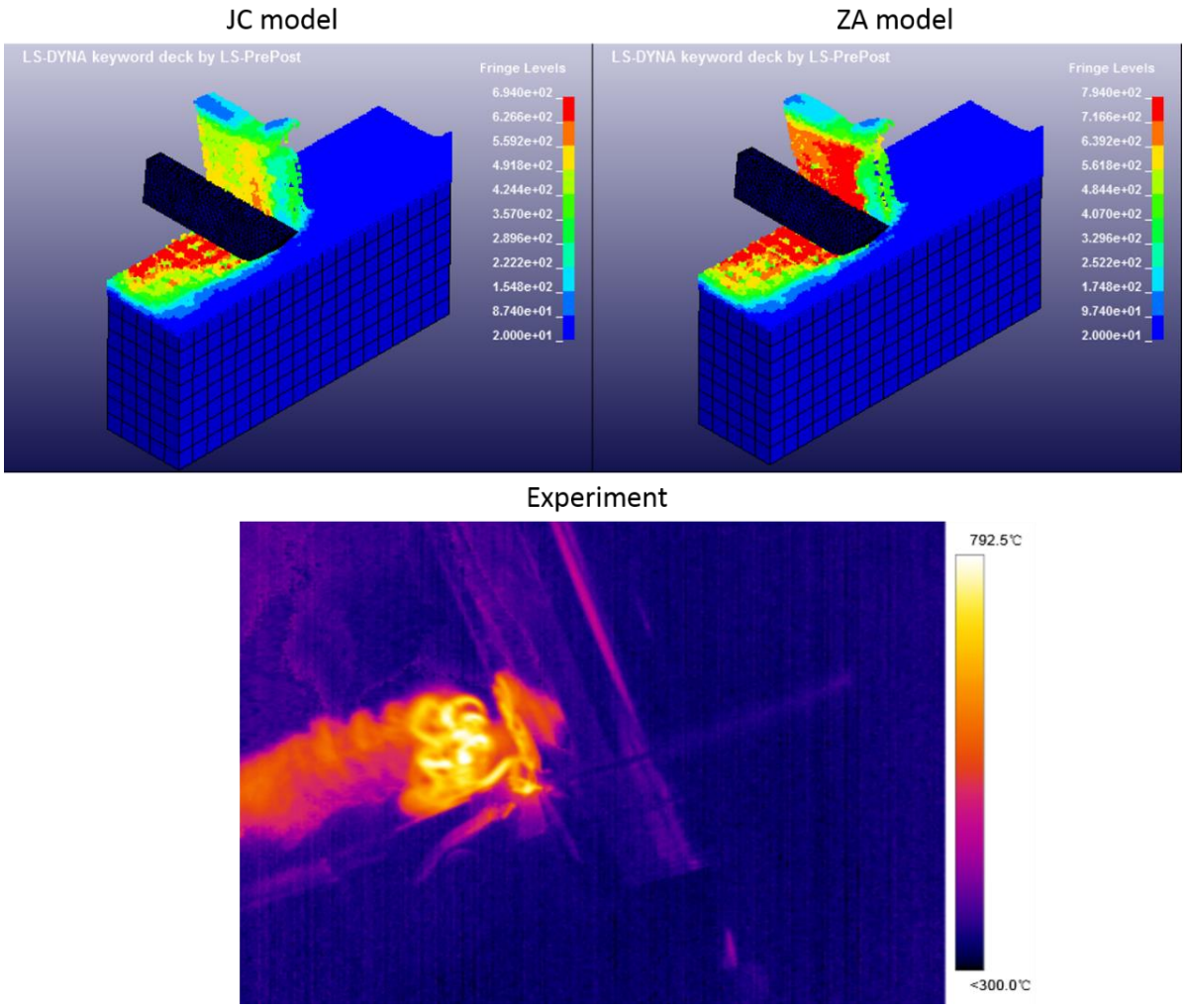

Figure 6. Cutting temperature comparison, conventional machining, 51 m/min.

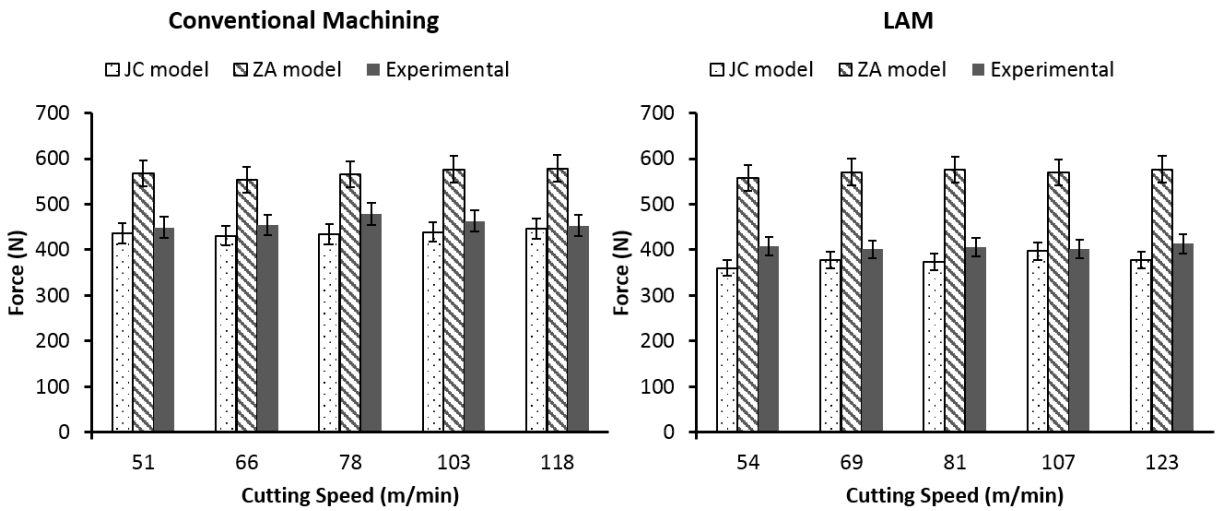

Figure 7. Predicted main cutting force compared with the experimental measurements

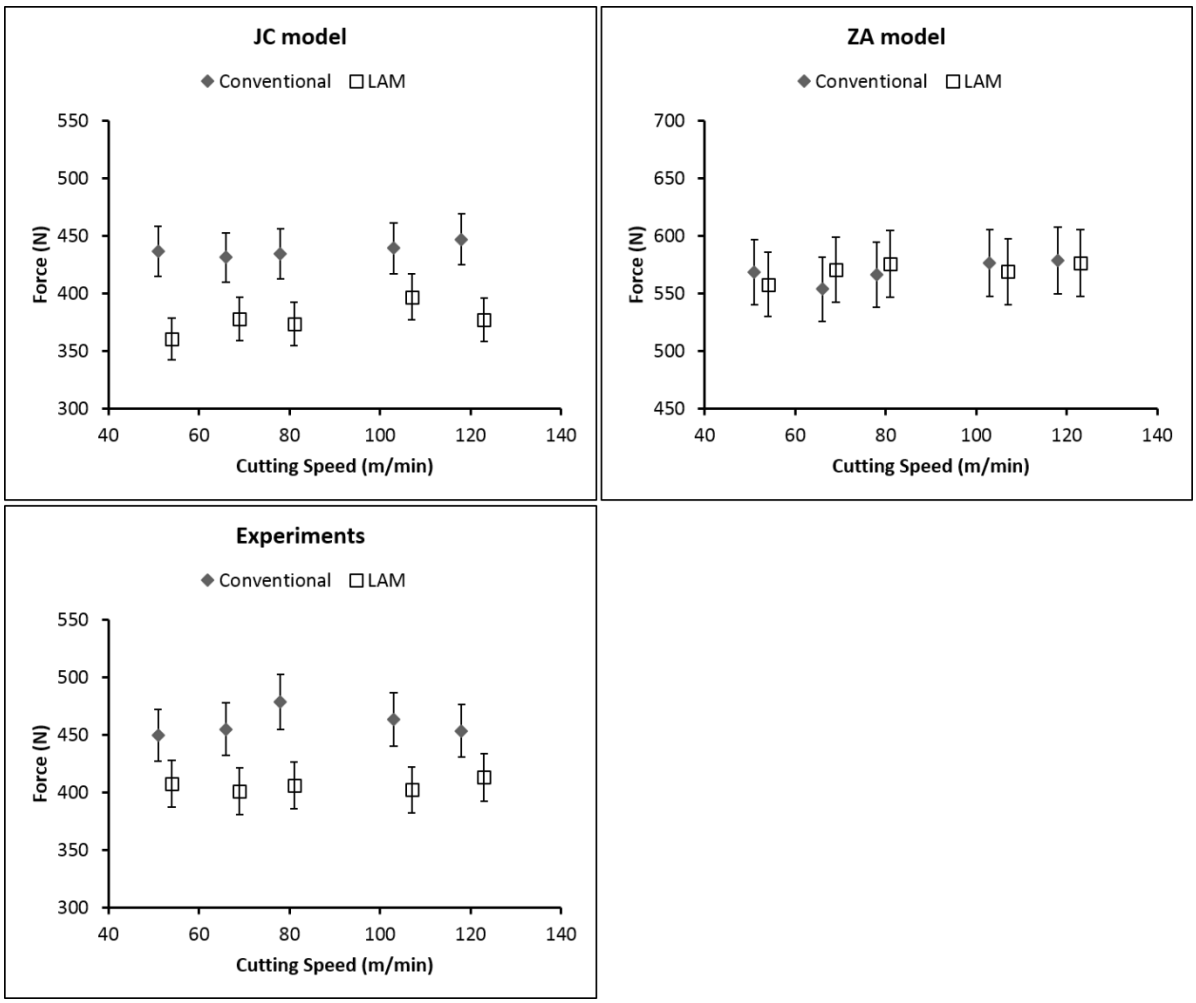

Figure 8. Cutting force reduction with the assistance of laser

References

[1] Lütjering G, Williams JC. Titanium: Springer; 2007.

[2] Leyens C, Peters M. Titanium and titanium alloys: Wiley Online Library; 2003.

[3] Joshi VA. Titanium alloys: an atlas of structures and fracture features: CRC Press; 2006.

[4] Yang X, Richard Liu C. Machining titanium and its alloys. Mach Sci Technol 1999;3:107-39.

[5] Boyer R. Titanium for aerospace: rationale and applications. Advanced Performance Materials 1995;2:349-68.

[6] Yang X, Liu CR. Machining titanium and its alloys. Mach Sci Technol 1999;3:107-39.

[7] Ezugwu E, Bonney J, Yamane Y. An overview of the machinability of aeroengine alloys. Journal of Materials Processing Technology 2003;134:233-53.

[8] Rahman M, Wong YS, Zareena AR. Machinability of Titanium Alloys. JSME International Journal Series C 2003;46:107-15.

[9] Boyer R, Briggs R. The use of β titanium alloys in the aerospace industry. J Mater Eng Perform 2005;14:681-5.

[10] Davim JP. Machining of Titanium Alloys: Springer; 2014.

[11] Rohde R. Metallurgical effects at high strain rates: Springer Science & Business Media; 2012.

[12] Shih-Chieh L, Duffy J. J Mech Phys Solids 1998;46:2201-31.

[13] Xue Q, Meyers MA, Nesterenko VF. Self-organization of shear bands in titanium and Ti-6Al-4V alloy. Acta Mater 2002;50:575-96.

[14] Hopkinson B. A method of measuring the pressure produced in the detonation of high explosives or by the impact of bullets. Philos T R Soc Lond 1914;213:437-56.

[15] Sun J, Guo YB. Material flow stress and failure in multiscale machining titanium alloy Ti-6Al-4V. Int J Adv Manuf Tech 2009;41:651-9.

[16] Gray III GT. High-strain-rate deformation: mechanical behavior and deformation substructures induced. Annual Review of Materials Research 2012;42:285-303.

[17] Meyers MA. Dynamic behavior of materials: Wiley-Interscience; 1994.

[18] Kahraman N, Gülenç B, Findik F. Joining of titanium/stainless steel by explosive welding and effect on interface. Journal of Materials Processing Technology 2005;169:127-33.

[19] Akbari Mousavi SAA, Farhadi Sartangi P. Experimental investigation of explosive welding of cp-titanium/AISI 304 stainless steel. Mater Design 2009;30:459-68.

[20] Habib MA, Keno H, Uchida R, Mori A, Hokamoto K. Cladding of titanium and magnesium alloy plates using energy-controlled underwater three layer explosive welding. Journal of Materials Processing Technology 2015;217:310-6.

[21] Mynors DJ, Zhang B. Applications and capabilities of explosive forming. Journal of Materials Processing Technology 2002;125–126:1-25.

[22] Thakur A, Gangopadhyay S. State-of-the-art in surface integrity in machining of nickel-based super alloys. International Journal of Machine Tools and Manufacture 2016;100:25-54.

[23] Duan CZ, Zhang LC. Adiabatic shear banding in AISI 1045 steel during high speed machining: Mechanisms of microstructural evolution. Materials Science and Engineering: A 2012;532:111-9.

[24] Mishra B, Mondal C, Goyal R, Ghosal P, Kumar KS, Madhu V. Plastic flow behavior of 7017 and 7055 aluminum alloys under different high strain rate test methods. Materials Science and Engineering: A 2014;612:343-53.

[25] Jones NG, Dashwood RJ, Dye D, Jackson M. Thermomechanical processing of Ti-5A1-5Mo-5V-3Cr. Mat Sci Eng a-Struct 2008;490:369-77.

[26] Zhan H, Wang G, Kent D, Dargusch M. Constitutive modelling of the flow behaviour of a β titanium alloy at high strain rates and elevated temperatures using the Johnson–Cook and modified Zerilli–Armstrong models. Materials Science and Engineering: A 2014;612:71-9.

[27] Fan J, Li J, Kou H, Hua K, Tang B, Zhang Y. Influence of solution treatment on microstructure and mechanical properties of a near β titanium alloy Ti-7333. Materials & Design 2015;83:499-507.

[28] Yang YL, Wang WQ, Li FL, Zhang YQ, Yang HL, Zhang PH. The Microstructure and Mechanical Properties of High-Strength and High-Toughness Titanium Alloy BTi-6554 Bar. Materials science forum: Trans Tech Publ; 2009. p. 173-6.

[29] Wang YQ, Wang G, Wang WQ, Kent D, Dargusch MS. The aging response of a metastable β Ti alloy, BTi-6554. Materials science forum: Trans Tech Publ; 2011. p. 29-32.

[30] Zhan H, Kent D, Wang G, Dargusch MS. The dynamic response of a β titanium alloy to high strain rates and elevated temperatures. Materials Science and Engineering: A 2014;607:417-26.

[31] Shekhar S, Sarkar R, Kar SK, Bhattacharjee A. Effect of solution treatment and aging on microstructure and tensile properties of high strength beta titanium alloy, Ti-5Al-5V-5Mo-3Cr. Materials & Design 2015;66:596-610.

[32] Ahmed M, Savvakin DG, Ivasishin OM, Pereloma EV. The effect of ageing on microstructure and mechanical properties of powder Ti-5Al-5Mo-5V-1Cr-1Fe alloy. Mat Sci Eng a-Struct 2014;605:89-97.

[33] Fan JK, Li JS, Kou HC, Hua K, Tang B, Zhang YD. Influence of solution treatment on microstructure and mechanical properties of a near beta titanium alloy Ti-7333. Materials & Design 2015;83:499-507.

[34] Li CL, Mi XJ, Ye WJ, Hui SX, Yu Y, Wang WQ. Effect of solution temperature on microstructures and tensile properties of high strength Ti-6Cr-5Mo-5V-4Al alloy. Mat Sci Eng a-

Struct 2013;578:103-9.

[35] Zheng Y, Williams RE, Sosa JM, Alam T, Wang Y, Banerjee R, et al. The indirect influence of the ω phase on the degree of refinement of distributions of the α phase in metastable β-Titanium alloys. Acta Materialia 2016;103:165-73.

[36] Ahmed M, Li T, Casillas G, Cairney JM, Wexler D, Pereloma EV. The evolution of microstructure and mechanical properties of Ti–5Al–5Mo–5V–2Cr–1Fe during ageing. Journal of Alloys and Compounds 2015;629:260-73.

[37] Coakley J, Vorontsov VA, Jones NG, Radecka A, Bagot PA, Littrell KC, et al. Precipitation processes in the beta-titanium alloy Ti–5Al–5Mo–5V–3Cr. Journal of Alloys and Compounds 2015;646:946-53.

[38] Nag S, Zheng Y, Williams R, Devaraj A, Boyne A, Wang Y, et al. Non-classical homogeneous precipitation mediated by compositional fluctuations in titanium alloys. Acta Materialia 2012;60:6247-56.

[39] Ning YQ, Xie BC, Liang HQ, Li H, Yang XM, Guo HZ. Dynamic softening behavior of TC18 titanium alloy during hot deformation. Materials & Design 2015;71:68-77.

[40] Liang H, Guo H, Nan Y, Qin C, Peng X, Zhang J. The construction of constitutive model and identification of dynamic softening mechanism of high-temperature deformation of Ti–5Al–5Mo–5V–1Cr–1Fe alloy. Materials Science and Engineering: A 2014;615:42-50.

[41] Nan Y, Ning Y, Liang H, Guo H, Yao Z, Fu MW. Work-hardening effect and strain-rate sensitivity behavior during hot deformation of Ti–5Al–5Mo–5V–1Cr–1Fe alloy. Materials & Design 2015;82:84-90.

[42] Hua K, Xue XY, Kou HC, Fan JK, Tang B, Li JS. Characterization of hot deformation microstructure of a near beta titanium alloy Ti-5553. Journal of Alloys and Compounds 2014;615:531-7.

[43] Fan J, Kou H, Lai M, Tang B, Chang H, Li J. Characterization of hot deformation behavior of a new near beta titanium alloy: Ti-7333. Materials & Design 2013;49:945-52.

[44] Miyazaki S, Otsuka K. Development of shape memory alloys. ISIJ International 1989;29:353-77.

[45] Miyazaki S, Ohmi Y, Otsuka K, Suzuki Y. Characteristics of deformation and transformation pseudoelasticity in Ti-Ni alloys. Le Journal de Physique Colloques 1982;43:C4-255-C4-60.

[46] Köster R, Vieluf D, Kiehn M, Sommerauer M, Kähler J, Baldus S, et al. Nickel and molybdenum contact allergies in patients with coronary in-stent restenosis. The Lancet 2000;356:1895-7.

[47] Sun F, Zhang JY, Marteleur M, Brozek C, Rauch EF, Veron M, et al. A new titanium alloy

with a combination of high strength, high strain hardening and improved ductility. Scripta Mater 2015;94:17-20.

[48] Froimson MI, Garino J, Machenaud A, Vidalain JP. Minimum 10-year Results of a Tapered, Titanium, Hydroxyapatite-Coated Hip Stem. An Independent Review. Journal of Arthroplasty 2007;22:1-7.

[49] Kent D, Wang G, Yu Z, Dargusch MS. Corrigendum to "Pseudoelastic behaviour of a β Ti–25Nb–3Zr–3Mo–2Sn alloy" [Mater. Sci. Eng. A 527 (2010) 2246–2252]. Materials Science and Engineering: A 2010;527:4524.

[50] Niinomi M. Mechanical biocompatibilities of titanium alloys for biomedical applications. Journal of the Mechanical Behavior of Biomedical Materials 2008;1:30-42.

[51] Tane M, Akita S, Nakano T, Hagihara K, Umakoshi Y, Niinomi M, et al. Low Young's modulus of Ti–Nb–Ta–Zr alloys caused by softening in shear moduli c′ and c44 near lower limit of body-centered cubic phase stability. Acta Materialia 2010;58:6790-8.

[52] Tane M, Nakano T, Kuramoto S, Hara M, Niinomi M, Takesue N, et al. Low Young's modulus in Ti–Nb–Ta–Zr–O alloys: Cold working and oxygen effects. Acta Materialia 2011;59:6975-88.

[53] Chang LL, Wang YD, Ren Y. In-situ investigation of stress-induced martensitic transformation in Ti–Nb binary alloys with low Young's modulus. Materials Science and Engineering: A 2016;651:442-8.

[54] Ankem S, Greene CA. Recent developments in microstructure/property relationships of beta titanium alloys. Mat Sci Eng a-Struct 1999;263:127-31.

[55] Li SJ, Cui TC, Hao YL, Yang R. Fatigue properties of a metastable beta-type titanium alloy with reversible phase transformation. Acta Biomater 2008;4:305-17.

[56] Hao YL, Li SJ, Sun SY, Zheng CY, Yang R. Elastic deformation behaviour of Ti-24Nb-4Zr-7.9Sn for biomedical applications. Acta Biomater 2007;3:277-86.

[57] Kent D, Wang G, Yu Z, Dargusch MS. Pseudoelastic behaviour of a β Ti–25Nb–3Zr–3Mo–2Sn alloy. Materials Science and Engineering: A 2010;527:2246-52.

[58] Obbard EG, Hao YL, Akahori T, Talling RJ, Niinomi M, Dye D, et al. Mechanics of superelasticity in Ti–30Nb–(8–10)Ta–5Zr alloy. Acta Mater 2010;58:3557-67.

[59] Al-Zain Y, Kim HY, Hosoda H, Nam TH, Miyazaki S. Shape memory properties of Ti–Nb–Mo biomedical alloys. Acta Materialia 2010;58:4212-23.

[60] Kim HY, Ikehara Y, Kim JI, Hosoda H, Miyazaki S. Martensitic transformation, shape memory effect and superelasticity of Ti–Nb binary alloys. Acta Mater 2006;54:2419-29.

[61] Farooq MU, Khalid FA, Zaigham H, Abidi IH. Superelastic behaviour of Ti–Nb–Al ternary

shape memory alloys for biomedical applications. Materials Letters 2014;121:58-61.

[62] Fu J, Yamamoto A, Kim HY, Hosoda H, Miyazaki S. Novel Ti-base superelastic alloys with large recovery strain and excellent biocompatibility. Acta Biomaterialia 2015;17:56-67.

[63] Tahara M, Kim HY, Hosoda H, Miyazaki S. Cyclic deformation behavior of a Ti–26 at.% Nb alloy. Acta Materialia 2009;57:2461-9.

[64] Yang Y, Li GP, Cheng GM, Li YL, Yang K. Multiple deformation mechanisms of Ti-22.4Nb-0.73Ta-2.0Zr-1.34O alloy. Appl Phys Lett 2009;94.

[65] Sakaguchi N, Niinomi M, Akahori T, Takeda J, Toda H. Relationships between tensile deformation behavior and microstructure in Ti-Nb-Ta-Zr system alloys. Mater Sci Eng C-Biomimetic Supramol Syst 2005;25:363-9.

[66] Kent D, Wang G, Dargusch M. Effects of phase stability and processing on the mechanical properties of Ti–Nb based β Ti alloys. J Mech Behav Biomed 2013;28:15-25.

[67] Abdel-Hady M, Fuwa H, Hinoshita K, Kimura H, Shinzato Y, Morinaga M. Phase stability change with Zr content in β-type Ti-Nb alloys. Scripta Mater 2007;57:1000-3.

[68] Morinaga M, Yukawa N, Maya T, Sone K, Adachi H. Theoretical design of titanium alloys. Sixth World Conference on Titanium III1988. p. 1601-6.

[69] Abdel-Hady M, Hinoshita K, Morinaga M. General approach to phase stability and elastic properties of β-type Ti-alloys using electronic parameters. Scripta Mater 2006;55:477-80.

[70] Laheurte P, Prima F, Eberhardt A, Gloriant T, Wary M, Patoor E. Mechanical properties of low modulus titanium alloys designed from the electronic approach. J Mech Behav Biomed 2010;3:565-73.

[71] Kuroda D, Niinomi M, Morinaga M, Kato Y, Yashiro T. Design and mechanical properties of new β type titanium alloys for implant materials. Materials Science and Engineering A 1998;243:244-9.

[72] Sun F, Zhang JY, Marteleur M, Gloriant T, Vermaut P, Laillé D, et al. Investigation of early stage deformation mechanisms in a metastable β titanium alloy showing combined twinning-induced plasticity and transformation-induced plasticity effects. Acta Mater 2013;61:6406-17.

[73] Marteleur M, Sun F, Gloriant T, Vermaut P, Jacques PJ, Prima F. On the design of new β-metastable titanium alloys with improved work hardening rate thanks to simultaneous TRIP and TWIP effects. Scripta Mater 2012;66:749-52.

[74] Sun F, Zhang JY, Marteleur M, Brozek C, Rauch EF, Veron M, et al. A new titanium alloy with a combination of high strength, high strain hardening and improved ductility. Scripta Mater 2015;94:17-20.

[75] Min XH, Tsuzaki K, Emura S, Tsuchiya K. Heterogeneous twin formation and its effect on

tensile properties in Ti–Mo based β titanium alloys. Materials Science and Engineering: A 2012;554:53-60.

[76] Min XH, Tsuzaki K, Emura S, Tsuchiya K. Enhancement of uniform elongation in high strength Ti-Mo based alloys by combination of deformation modes. Mat Sci Eng a-Struct 2011;528:4569-78.

[77] Marais S, Tait R, Cloete T, Nurick G. Material testing at high strain rate using the split Hopkinson pressure bar. Latin American Journal of Solids and Structures 2004;1:219-339.

[78] Kim JH, Kim D, Han HN, Barlat F, Lee MG. Strain rate dependent tensile behavior of advanced high strength steels: Experiment and constitutive modeling. Mat Sci Eng a-Struct 2013;559:222-31.

[79] Peirs J, Verleysen P, Tirry W, Rabet L, Schryvers D, Degrieck J. Dynamic shear localization in Ti6Al4 V. Procedia Engineering 2011;10:2342-7.

[80] Sasso M, Newaz G, Amodio D. Material characterization at high strain rate by Hopkinson bar tests and finite element optimization. Mat Sci Eng a-Struct 2008;487:289-300.

[81] Davies RM. A Critical Study of the Hopkinson Pressure Bar. Philos Tr R Soc S-A 1948;240:375-457.

[82] KOLSKY H. An Investigation of the Mechanical Properties of Materials at Very High Rates of Loading. Proc Phys Soc, B1949. p. 676-700.

[83] Marais S, Tait R, Cloete T, Nurick G. Material testing at high strain rate using the split Hopkinson pressure bar. Latin American Journal of Solids and Structures, an ABCM Journal 2004;1:219-339.

[84] Macdougall DAS, Harding J. A constitutive relation and failure criterion for Ti6Al4V alloy at impact rates of strain. J Mech Phys Solids 1999;47:1157-85.

[85] Lee WS, Chen TH, Lin CF, Lee NW. High strain rate shear deformation and fracture behaviour of biomedical titanium alloy. Mater Sci Tech-Lond 2010;26:1079-87.

[86] Gilat A, Cheng CS. Modeling torsional split Hopkinson bar tests at strain rates above 10,000 s(-1). Int J Plasticity 2002;18:787-99.

[87] Meyers MA, Murr LE. Shock Waves and High-Strain-Rate Phenomena in Metals. Concepts and Applications. DTIC Document; 1981.

[88] Seo S, Min O, Yang H. Constitutive equation for Ti-6Al-4V at high temperatures measured using the SHPB technique. Int J Impact Eng 2005;31:735-54.

[89] Vergani L, Guagliano M, Peirs J, Verleysen P, Tirry W, Rabet L, et al. 11th International Conference on the Mechanical Behavior of Materials (ICM11)Dynamic shear localization in Ti6Al4V. Procedia Engineering 2011;10:2342-7.

[90] Hines J, Vecchio K. Recrystallization kinetics within adiabatic shear bands. Acta Mater 1997;45:635-49.

[91] Bertholf LD, Karnes CH. Two-dimensional analysis of the split hopkinson pressure bar system. J Mech Phys Solids 1975;23:1-19.

[92] Vergani L, Guagliano M, Tekalur SA, Sen O. 11th International Conference on the Mechanical Behavior of Materials (ICM11)Effect of Specimen Size in the Kolsky Bar. Procedia Engineering 2011;10:2663-71.

[93] Rodríguez J, Cortés R, Martínez MA, Sánchez-Gálvez V, Navarro C. Numerical study of the specimen size effect in the split Hopkinson pressure bar tests. J Mater Sci 1995;30:4720-5.

[94] Khan AS, Suh YS, Kazmi R. Quasi-static and dynamic loading responses and constitutive modeling of titanium alloys. Int J Plasticity 2004;20:2233-48.

[95] Lesuer DR. EXPERIMENTAL INVESTIGATIONS OF MATERIAL MODELS FOR TI-6A1-4V TITANIUM AND 2024-T3 ALUMINUM. 2000.

[96] Macdougall D, Harding J. A constitutive relation and failure criterion for Ti6Al4V alloy at impact rates of strain. J Mech Phys Solids 1999;47:1157-85.

[97] Nemat-Nasser S, Guo W-G, Nesterenko VF, Indrakanti S, Gu Y-B. Dynamic response of conventional and hot isostatically pressed Ti–6Al–4V alloys: experiments and modeling. Mech Mater 2001;33:425-39.

[98] Johnson G, Holmquist T. Test data and computational strength and fracture model constants for 23 materials subjected to large strains, high strain rates, and high temperatures. Los Alamos National Laboratory, Los Alamos, NM, Report No LA-11463-MS 1989.

[99] Seo S, Min O, Yang H. Constitutive equation for Ti–6Al–4V at high temperatures measured using the SHPB technique. Int J Impact Eng 2005;31:735-54.

[100] Lee W-S, Lin C-F. Plastic deformation and fracture behaviour of Ti–6Al–4V alloy loaded with high strain rate under various temperatures. Materials Science and Engineering: A 1998;241:48-59.

[101] Zerilli FJ, Armstrong RW. Dislocation-mechanics-based constitutive relations for material dynamics calculations. J Appl Phys 1987;61:1816-25.

[102] Kocks U, Argon A, Ashby M, Chalmers B, Christian J, Massalski T. Progr. Mater. Sci. Pergamon Press Oxford, United Kingdom; 1975.

[103] Lennon AM, Ramesh KT. The influence of crystal structure on the dynamic behavior of materials at high temperatures. Int J Plasticity 2004;20:269-90.

[104] Taylor G. Thermally-activated deformation of BCC metals and alloys. Prog Mater Sci 1992;36:29-61.

[105] Zerilli FJ, Armstrong RW. Dislocation-Mechanics-Based Constitutive Relations for Material Dynamics Calculations. Journal of Applied Physics 1987;61:1816-25.

[106] Meyers MA, Chen YJ, Marquis FDS, Kim DS. HIGH-STRAIN, HIGH-STRAIN-RATE BEHAVIOR OF TANTALUM. Metall Mater Trans A 1995;26:2493-501.

[107] Nemat-Nasser S, Li Y. Flow stress of f.c.c. polycrystals with application to OFHC Cu. Acta Mater 1998;46:565-77.

[108] Lee W-S, Liu C-Y, Sun T-N. Dynamic impact response and microstructural evolution of inconel 690 superalloy at elevated temperatures. Int J Impact Eng 2005;32:210-23.

[109] Smerd R, Winkler S, Salisbury C, Worswick M, Lloyd D, Finn M. High strain rate tensile testing of automotive aluminum alloy sheet. Int J Impact Eng 2005;32:541-60.

[110] Ulacia I, Dudamell N, Gálvez F, Yi S, Pérez-Prado M, Hurtado I. Mechanical behavior and microstructural evolution of a Mg AZ31 sheet at dynamic strain rates. Acta Mater 2010;58:2988-98.

[111] Shen J, Kondoh K, Jones T, Mathaudhu S, Kecskes L, Wei Q. Effect of strain rate on the mechanical properties of magnesium alloy AMX602. Materials Science and Engineering: A 2016;649:338-48.

[112] Gurao N, Kapoor R, Suwas S. Deformation behaviour of commercially pure titanium at extreme strain rates. Acta Mater 2011;59:3431-46.

[113] Lee S, Estrin Y, De Cooman BC. Effect of the Strain Rate on the TRIP-TWIP Transition in Austenitic Fe-12 pct Mn-0.6 pct C TWIP Steel. Metall Mater Trans A 2014;45A:717-30.

[114] Yang HK, Zhang ZJ, Dong FY, Duan QQ, Zhang ZF. Strain rate effects on tensile deformation behaviors for Fe-22Mn-0.6C-(1.5Al) twinning-induced plasticity steel. Mat Sci Eng a-Struct 2014;607:551-8.

[115] Bintu A, Vincze G, Picu CR, Lopes AB, Gracio JJ, Barlat F. Strain hardening rate sensitivity and strain rate sensitivity in TWIP steels. Mat Sci Eng a-Struct 2015;629:54-9.

[116] Russel M, Martin S, Kruger L, Kreuzer W. High strain rate behavior, transformation-induced plasticity and fracture toughness characterization of cast and additionally tempered Fe85Cr4Mo8V2C1 alloy manufactured using a rapid solidification technique. J Mater Sci 2012;47:6915-28.

[117] Kumar N, Ying Q, Nie X, Mishra RS, Tang Z, Liaw PK, et al. High strain-rate compressive deformation behavior of the Al0.1CrFeCoNi high entropy alloy. Mater Design 2015;86:598-602.

[118] Lee WS, Chen TH, Hwang HH. Impact response and microstructural evolution of biomedical titanium alloy under various temperatures. Metall Mater Trans A 2008;39A:1435-48.

[119] Lee WS, Chen TH, Lin CF, Lu GT. Adiabatic Shearing Localisation in High Strain Rate Deformation of Al-Sc Alloy. Mater Trans 2010;51:1216-21.

[120] Lee WS, Liu CY, Sun TN. Dynamic impact response and microstructural evolution of Inconel 690 superalloy at elevated temperatures. Int J Impact Eng 2005;32:210-23.

[121] Lee WS, Lin CF, Chen TH, Luo WZ. High temperature deformation and fracture behaviour of 316L stainless steel under high strain rate loading. J Nucl Mater 2012;420:226-34.

[122] Lee WS, Lin CF, Liu TJ. Impact and fracture response of sintered 316L stainless steel subjected to high strain rate loading. Mater Charact 2007;58:363-70.

[123] El-Magd E, Abouridouane M. Characterization, modelling and simulation of deformation and fracture behaviour of the light-weight wrought alloys under high strain rate loading. Int J Impact Eng 2006;32:741-58.

[124] Kalthoff JF, Burgel A. Influence of loading rate on shear fracture toughness for failure mode transition. Int J Impact Eng 2004;30:957-71.

[125] Lee WS, Lin CF, Chen TH, Yang MC. Effects of prestrain on high temperature impact properties of 304L stainless steel. J Mater Res 2010;25:754-63.

[126] Follansbee PS, Kocks UF. A constitutive description of the deformation of copper based on the use of the mechanical threshold stress as an internal state variable. Acta Metallurgica 1988;36:81-93.

[127] Lee WS, Lin CF. Comparative study of the impact response and microstructure of 304L stainless steel with and without prestrain. Metallurgical and Materials Transactions A: Physical Metallurgy and Materials Science 2002;33:2801-10.

[128] Zerilli FJ, Armstrong RW. The effect of dislocation drag on the stress-strain behavior of F.C.C. metals. Acta Metall Mater 1992;40:1803-8.

[129] Lee WS, Lin CF. High-temperature deformation behaviour of Ti6Al4V alloy evaluated by high strain-rate compression tests. Journal of Materials Processing Technology 1998;75:127-36.

[130] Nemat-Nasser S, Guo WG, Cheng JY. Mechanical properties and deformation mechanisms of a commercially pure titanium. Acta Mater 1999;47:3705-20.

[131] Nemat-Nasser S, Guo WG, Kihl DP. Thermomechanical response of AL-6XN stainless steel over a wide range of strain rates and temperatures. J Mech Phys Solids 2001;49:1823-46.

[132] Nemat-Nasser S, Guo WG, Nesterenko VF, Indrakanti SS, Gu YB. Dynamic response of conventional and hot isostatically pressed Ti-6Al-4V alloys: experiments and modeling. Mech Mater 2001;33:425-39.

[133] Khan AS, Sung Suh Y, Kazmi R. Quasi-static and dynamic loading responses and constitutive modeling of titanium alloys. Int J Plasticity 2004;20:2233-48.

[134] Hokka M, Leemet T, Shrot A, Baeker M, Kuokkala VT. Characterization and numerical modeling of high strain rate mechanical behavior of Ti-15-3 alloy for machining simulations. Mat

Sci Eng a-Struct 2012;550:350-7.

[135] Song WQ, Sun S, Zhu S, Wang G, Wang J, Dargusch MS. Compressive deformation behavior of a near-beta titanium alloy. Mater Design 2012;34:739-45.

[136] Farghadany E, Zarei-Hanzaki A, Abedi HR, Dietrich D, Yadegari MR, Lampke T. The coupled temperature-strain rate sensitivity of Ti-29Nb-13Ta-4.6Zr alloy. Mat Sci Eng a-Struct 2014;610:258-62.

[137] Guo YB, Wen Q, Horstemeyer MF. An internal state variable plasticity-based approach to determine dynamic loading history effects on material property in manufacturing processes. Int J Mech Sci 2005;47:1423-41.

[138] Johnson GR, Cook WH. A constitutive model and data for metals subjected to large strains, high strain rates and high temperatures. Proceedings of the 7th International Symposium on Ballistics: The Hague, Netherlands: International Ballistics Committee; 1983. p. 541-7.

[139] Samantaray D, Mandal S, Bhaduri AK. A comparative study on Johnson Cook, modified Zerilli-Armstrong and Arrhenius-type constitutive models to predict elevated temperature flow behaviour in modified 9Cr-1Mo steel. Comp Mater Sci 2009;47:568-76.

[140] Vijay Sekar KS, Pradeep Kumar M. Finite element simulations of Ti6Al4V titanium alloy machining to assess material model parameters of the Johnson-Cook constitutive equation. J Braz Soc Mech Sci 2011;33:203-11.

[141] Lee WS, Lin CF. Plastic deformation and fracture behaviour of Ti-6Al-4V alloy loaded with high strain rate under various temperatures. Mat Sci Eng a-Struct 1998;241:48-59.

[142] Yang Y, Jiang F, Zhou BM, Li XM, Zheng HG, Zhang QM. Microstructural characterization and evolution mechanism of adiabatic shear band in a near beta-Ti alloy. Mat Sci Eng a-Struct 2011;528:2787-94.

[143] Meyer HW, Kleponis DS. Modeling the high strain rate behavior of titanium undergoing ballistic impact and penetration. Int J Impact Eng 2001;26:509-21.

[144] Holmquist TJ, Johnson GR. Determination of Constants and Comparison of Results for Various Constitutive Models. J Phys Iv 1991;1:853-60.

[145] Arsecularatne JA, Zhang LC. Assessment of constitutive equations used in machining. 2004. p. 277-82.

[146] Sima M, Ozel T. Modified material constitutive models for serrated chip formation simulations and experimental validation in machining of titanium alloy Ti-6Al-4V. Int J Mach Tool Manu 2010;50:943-60.

[147] Calamaz M, Coupard D, Girot F. A new material model for 2D numerical simulation of serrated chip formation when machining titanium alloy Ti-6Al-4V. Int J Mach Tool Manu

2008;48:275-88.

[148] Lin YC, Chen XM, Liu G. A modified Johnson-Cook model for tensile behaviors of typical high-strength alloy steel. Mat Sci Eng a-Struct 2010;527:6980-6.

[149] He A, Xie GL, Zhang HL, Wang XT. A comparative study on Johnson-Cook, modified Johnson-Cook and Arrhenius-type constitutive models to predict the high temperature flow stress in 20CrMo alloy steel. Mater Design 2013;52:677-85.

[150] Li HY, Li YH, Wang XF, Liu JJ, Wu Y. A comparative study on modified Johnson Cook, modified Zerilli-Armstrong and Arrhenius-type constitutive models to predict the hot deformation behavior in 28CrMnMoV steel. Mater Design 2013;49:493-501.

[151] Tan JQ, Zhan M, Liu S, Huang T, Guo J, Yang H. A modified Johnson-Cook model for tensile flow behaviors of 7050-T7451 aluminum alloy at high strain rates. Mat Sci Eng a-Struct 2015;631:214-9.

[152] Liang R, Khan AS. A critical review of experimental results and constitutive models for BCC and FCC metals over a wide range of strain rates and temperatures. Int J Plasticity 1999;15:963-80.

[153] Lee W-S, Liu C-Y. The effects of temperature and strain rate on the dynamic flow behaviour of different steels. Materials Science and Engineering: A 2006;426:101-13.

[154] Chiou S-T, Cheng W-C, Lee W-S. Strain rate effects on the mechanical properties of a Fe–Mn–Al alloy under dynamic impact deformations. Materials Science and Engineering: A 2005;392:156-62.

[155] Lennon A, Ramesh K. The influence of crystal structure on the dynamic behavior of materials at high temperatures. Int J Plasticity 2004;20:269-90.

[156] Dey S, Børvik T, Hopperstad O, Langseth M. On the influence of constitutive relation in projectile impact of steel plates. Int J Impact Eng 2007;34:464-86.

[157] Samantaray D, Mandal S, Borah U, Bhaduri A, Sivaprasad P. A thermo-viscoplastic constitutive model to predict elevated-temperature flow behaviour in a titanium-modified austenitic stainless steel. Materials Science and Engineering: A 2009;526:1-6.

[158] Samantaray D, Mandal S, Bhaduri A. A comparative study on Johnson Cook, modified Zerilli–Armstrong and Arrhenius-type constitutive models to predict elevated temperature flow behaviour in modified 9Cr–1Mo steel. Comp Mater Sci 2009;47:568-76.

[159] He A, Xie GL, Zhang HL, Wang XT. A modified Zerilli-Armstrong constitutive model to predict hot deformation behavior of 20CrMo alloy steel. Mater Design 2014;56:122-7.

[160] Shamsolhodaei A, Zarei-Hanzaki A, Ghambari M, Moemeni S. The high temperature flow behavior modeling of NiTi shape memory alloy employing phenomenological and physical based constitutive models: A comparative study. Intermetallics 2014;53:140-9.

[161] Zhang HJ, Wen WD, Cui HT, Xu Y. A modified Zerilli-Armstrong model for alloy IC10 over a wide range of temperatures and strain rates. Mat Sci Eng a-Struct 2009;527:328-33.

[162] Lesuer D. Experimental investigation of material models for Ti-6Al-4V and 2024-T3. US Department of Transportation, Report No DOT/FAA/AR-00/25 2000.

[163] Gao ZG, Zhang XM, Chen MA. Influence of strain rate on the precipitate microstructure in impacted aluminum alloy. Scripta Mater 2008;59:983-6.

[164] Zaera R, Rodriguez-Martinez JA, Casado A, Fernandez-Saez J, Rusinek A, Pesci R. A constitutive model for analyzing martensite formation in austenitic steels deforming at high strain rates. Int J Plasticity 2012;29:77-101.

[165] Ahmed M, Wexler D, Casillas G, Savvakin DG, Pereloma EV. Strain rate dependence of deformation-induced transformation and twinning in a metastable titanium alloy. Acta Mater 2016;104:190-200.

[166] Li C, Chen JH, Wu X, van der Zwaag S. Effect of strain rate on stress-induced martensitic formation and the compressive properties of Ti-V-(Cr,Fe)-Al alloys. Mat Sci Eng a-Struct 2013;573:111-8.

[167] Lee WS, Lin CF, Chen TH, Yang MC. High temperature microstructural evolution of 304L stainless steel as function of pre-strain and strain rate. Mat Sci Eng a-Struct 2010;527:3127-37.

[168] Grassel O, Kruger L, Frommeyer G, Meyer LW. High strength Fe-Mn-(Al, Si) TRIP/TWIP steels development - properties - application. Int J Plasticity 2000;16:1391-409.

[169] Lee W-S, Lin C-F, Chen T-H, Yang M-C. High temperature microstructural evolution of 304L stainless steel as function of pre-strain and strain rate. Materials Science and Engineering: A 2010;527:3127-37.

[170] Dudamell NV, Ulacia I, Galvez F, Yi S, Bohlen J, Letzig D, et al. Twinning and grain subdivision during dynamic deformation of a Mg AZ31 sheet alloy at room temperature. Acta Mater 2011;59:6949-62.

[171] Li DZ, Wei YH, Liu CY, Hou LF, Liu DF, Jin XZ. Effects of High Strain Rate on Properties and Microstructure Evolution of TWIP Steel Subjected to Impact Loading. J Iron Steel Res Int 2010;17:67-73.

[172] Podurets AM, Raevskii VA, Khanzhin VG, Lebedev AI, Aprelkov ON, Igonin VV, et al. Twin Structures in Copper after Shock and Shockless High-Rate Loading. Combust Explo Shock+ 2011;47:606-14.

[173] Xu F, Zhang XY, Ni HT, Liu Q. {1 1 (2)over-bar 4} deformation twinning in pure Ti during dynamic plastic deformation. Mat Sci Eng a-Struct 2012;541:190-5.

[174] Wang TB, Li BL, Li MA, Li YC, Wang ZQ, Nie ZR. Effects of strain rates on deformation

twinning behavior in alpha-titanium. Mater Charact 2015;106:218-25.

[175] Xu F, Zhang XY, Ni HT, Cheng YM, Zhu YT, Liu Q. Effect of twinning on microstructure and texture evolutions of pure Ti during dynamic plastic deformation. Mat Sci Eng a-Struct 2013;564:22-33.

[176] Knezevic M, Zecevic M, Beyerlein IJ, Bingert JF, McCabe RJ. Strain rate and temperature effects on the selection of primary and secondary slip and twinning systems in HCP Zr. Acta Mater 2015;88:55-73.

[177] Gray GT. High-Strain-Rate Deformation: Mechanical Behavior and Deformation Substructures Induced. Annu Rev Mater Res 2012;42:285-303.

[178] Zener C, Hollomon J. Effect of strain rate upon plastic flow of steel. J Appl Phys 1944;15:22-32.

[179] Bassim MN. Study of the formation of adiabatic shear bands in steels. Journal of Materials Processing Technology 2001;119:234-6.

[180] Bassim MN, Panic N. J Mater Proc Technol 1999:481-5.

[181] Odeshi AG, Al-Ameeri S, Bassim MN. Effect of high strain rate on plastic deformation of a low alloy steel subjected to ballistic impact. Journal of Materials Processing Technology 2005;162-163:385-91.

[182] Odeshi AG, Al-ameeri S, Mirfakhraei S, Yazdani F, Bassim MN. Deformation and failure mechanism in AISI 4340 steel under ballistic impact. Theoretical and Applied Fracture Mechanics 2006;45:18-24.

[183] Li Q, Xu Y, Bassim MN. Mater Sci Eng A 2003;358:128-33.

[184] Shahan AR, Taheri AK. Adiabatic shear bands in titanium and titanium alloys: a critical review. Materials & Design 1993;14:243-50.

[185] Xu YB, Bai YL, Meyers MA. Deformation, phase transformation and recrystallization in the shear bands induced by high-strain rate loading in titanium and its alloys. J Mater Sci Technol 2006;22:737-+.

[186] Peirs J, Tirry W, Amin-Ahmadi B, Coghe F, Verleysen P, Rabet L, et al. Microstructure of adiabatic shear bands in Ti6Al4V. Mater Charact 2013;75:79-92.

[187] Murr L, Ramirez A, Gaytan S, Lopez M, Martinez E, Hernandez D, et al. Microstructure evolution associated with adiabatic shear bands and shear band failure in ballistic plug formation in Ti–6Al–4V targets. Materials Science and Engineering: A 2009;516:205-16.

[188] Martinez F, Murr L, Ramirez A, Lopez M, Gaytan S. Dynamic deformation and adiabatic shear microstructures associated with ballistic plug formation and fracture in Ti–6Al–4V targets. Materials Science and Engineering: A 2007;454:581-9.

[189] Liu X, Tan C, Zhang J, Hu Y, Ma H, Wang F, et al. Influence of microstructure and strain rate on adiabatic shearing behavior in Ti–6Al–4V alloys. Materials Science and Engineering: A 2009;501:30-6.

[190] Meyers M, Pak H-R. Observation of an adiabatic shear band in titanium by high-voltage transmission electron microscopy. Acta Metallurgica 1986;34:2493-9.

[191] Yang Y, Wang B. Dynamic recrystallization in adiabatic shear band in α-titanium. Mater Lett 2006;60:2198-202.

[192] Mebar Y, Shechtman D. ON THE ADIABATIC SHEAR OF TI-6AL-4V BALLISTIC TARGETS. Materials Science and Engineering 1983;58:181-8.

[193] Xu YB, Zhang JH, Bai YL, Meyers MA. Shear localization in dynamic deformation: Microstructural evolution. Metall Mater Trans A 2008;39A:811-43.

[194] Semiatin S, Lahoti G, Oh S. Material behavior under high stress and ultrahigh loading rates. Proceedings of Sagamore Almy Materials Research Conference New York: Plenum Press1983. p. 119-60.

[195] Boakye-Yiadom S, Khan AK, Bassim N. A systematic study of grain refinement during impact of 4340 steel. Materials Science and Engineering: A 2014;605:270-85.

[196] Odeshi AG, Bassim MN. Evolution of adiabatic shear bands in a dual-phase steel at very high strain rates. Mat Sci Eng a-Struct 2008;488:235-40.

[197] Odeshi AG, Al-ameen S, Bassim MN. Effect of high strain rate on plastic deformation of a low alloy steel subjected to ballistic impact. Journal of Materials Processing Technology 2005;162:385-91.

[198] Boakye Yiadom S, Khaliq Khan A, Bassim N. Effect of microstructure on the nucleation and initiation of adiabatic shear bands (ASBs) during impact. Materials Science and Engineering: A 2014;615:373-94.

[199] Meyers MA, Pak HR. OBSERVATION OF AN ADIABATIC SHEAR BAND IN TITANIUM BY HIGH-VOLTAGE TRANSMISSION ELECTRON-MICROSCOPY. Acta Metallurgica 1986;34:2493-9.

[200] Andrade U, Meyers MA, Vecchio KS, Chokshi AH. Dynamic Recrystallization in High-Strain, High-Strain-Rate Plastic-Deformation of Copper. Acta Metall Mater 1994;42:3183-95.

[201] Nemat-Nasser S, Isaacs JB, Liu MQ. Microstructure of high-strain, high-strain-rate deformed tantalum. Acta Mater 1998;46:1307-25.

[202] Lins JFC, Sandim HRZ, Kestenbach HJ, Raabe D, Vecchio KS. A microstructural investigation of adiabatic shear bands in an interstitial free steel. Materials Science and Engineering: A 2007;457:205-18.

[203] Tang L, Chen Z, Zhan C, Yang X, Liu C, Cai H. Microstructural evolution in adiabatic shear bands of copper at high strain rates: Electron backscatter diffraction characterization. Mater Charact 2012;64:21-6.

[204] Martinez F, Murr LE, Ramirez A, Lopez MI, Gaytan SM. Dynamic deformation and adiabatic shear microstructures associated with ballistic plug formation and fracture in Ti–6Al–4V targets. Materials Science and Engineering: A 2007;454–455:581-9.

[205] Xue Q, Bingert JF, Henrie BL, Gray Iii GT. EBSD characterization of dynamic shear band regions in pre-shocked and as-received 304 stainless steels. Materials Science and Engineering: A 2008;473:279-89.

[206] Meyers MA, Nesterenko VF, LaSalvia JC, Xu YB, Xue Q. Observation and modeling of dynamic recrystallization in high-strain, high-strain rate deformation of metals. J Phys IV 2000;10:51-6.

[207] Yang Y, Wang BF. Dynamic recrystallization in adiabatic shear band in alpha-titanium. Mater Lett 2006;60:2198-202.

[208] Wang BF, Yang Y. Microstructure evolution in adiabatic shear band in fine-grain-sized Ti-3Al-5Mo-4.5V alloy. Mat Sci Eng a-Struct 2008;473:306-11.

[209] Xue Q, Liao XZ, Zhu YT, Gray GT. Formation mechanisms of nanostructures in stainless steel during high-strain-rate severe plastic deformation. Mat Sci Eng a-Struct 2005;410:252-6.

[210] Sun HQ, Shi YN, Zhang MA, Lu K. Plastic strain-induced grain refinement in the nanometer scale in a Mg alloy. Acta Mater 2007;55:975-82.

[211] Tao NR, Lu K. Nanoscale structural refinement via deformation twinning in face-centered cubic metals. Scripta Mater 2009;60:1039-43.

[212] Yin DL, Zhang KF, Wang GF, Han WB. Warm deformation behavior of hot-rolled AZ31 Mg alloy. Mat Sci Eng a-Struct 2005;392:320-5.

[213] Tang L, Chen ZY, Zhan CK, Yang XY, Liu CM, Cai HN. Microstructural evolution in adiabatic shear bands of copper at high strain rates: Electron backscatter diffraction characterization. Mater Charact 2012;64:21-6.

[214] Zou DL, Luan BF, Liu Q, Chai LJ, Chen JW. Characterization of adiabatic shear bands in the zirconium alloy impacted by split Hopkinson pressure bar at a strain rate of 6000 s−1. Materials Science and Engineering: A 2012;558:517-24.

[215] Hines JA, Vecchio KS, Ahzi S. A model for microstructure evolution in adiabatic shear bands. Metallurgical and Materials Transactions A: Physical Metallurgy and Materials Science 1998;29:191-203.

[216] Lins JFC, Sandim HRZ, Kestenbach H, Raabe D, Vecchio KS. A microstructural

investigation of adiabatic shear bands in an interstitial free steel. Mat Sci Eng a-Struct 2007;457:205-18.

[217] Rhim S-H, Oh S-I. Prediction of serrated chip formation in metal cutting process with new flow stress model for AISI 1045 steel. Journal of Materials Processing Technology 2006;171:417-22.

[218] Nesterenko VF, Meyers MA, LaSalvia JC, Bondar MP, Chen YJ, Lukyanov YL. Shear localization and recrystallization in high-strain, high-strain-rate deformation of tantalum. Mat Sci Eng a-Struct 1997;229:23-41.

[219] Meyers MA, Xu YB, Xue Q, Perez-Prado MT, McNelley TR. Microstructural evolution in adiabatic shear localization in stainless steel. Acta Mater 2003;51:1307-25.

[220] Meyers M, Nesterenko V, Benson D, Cao B, Xu Y. Shear localization-martensitic transformation interactions in Fe-Cr-Ni monocrystal. Metallurgical and Materials Transactions A 2004;35:2575-86.

[221] Bayoumi AE, Xie JQ. Some Metallurgical Aspects of Chip Formation in Cutting Ti-6wt-Percent-Al-4wt-Percent-V Alloy. Mat Sci Eng a-Struct 1995;190:173-80.

[222] Wang B, Sun J, Wang X, Fu A. Adiabatic shear localization in a near beta Ti–5Al–5Mo–5 V–1Cr–1Fe alloy. Materials Science and Engineering: A 2015;639:526-33.

[223] Timothy S, Hutchings I. The structure of adiabatic shear bands in a titanium alloy. Acta Metallurgica 1985;33:667-76.

[224] Zhang J, Tan C-w, Ren Y, Yu X-d, Ma H-l, Wang F-c, et al. Adiabatic shear fracture in Ti-6Al-4V alloy. Transactions of Nonferrous Metals Society of China 2011;21:2396-401.

[225] Boyer RR. Titanium for aerospace: Rationale and applications. Advanced Performance Materials 1995;2:349-68.

[226] Nyakana S, Fanning J, Boyer R. Quick reference guide for β titanium alloys in the 00s. J Mater Eng Perform 2005;14:799-811.

[227] Li C, Mi X, Ye W, Hui S, Yu Y, Wang W. A study on the microstructures and tensile properties of new beta high strength titanium alloy. Journal of Alloys and Compounds 2012.

[228] Pinghui Z, Chenglin L, Songxiao H, Weiqi W, Yulan Y. Effect of Solution Treatment on Microstructure and Tensile Properties of Ti-6Cr-5Mo-5V-4Al Alloy. Chinese Journal of Rare Metals 2011;5:002.

[229] Kent D, Wang G, Wang W, Dargusch MS. Influence of ageing temperature and heating rate on the properties and microstructure of beta Ti alloy, Ti-6Cr-5Mo-5V-4Al. Mat Sci Eng a-Struct 2012;531:98-106.

[230] Smerd R, Winkler S, Salisbury C, Worswick M, Lloyd D, Finn M. High strain rate tensile

testing of automotive aluminum alloy sheet. Int J Impact Eng 2005;32:541-60.

[231] Khosravifard A, Moshksar MM, Ebrahimi R. High strain rate torsional testing of a high manganese steel: Design and simulation. Mater Design 2013;52:495-503.

[232] Lee WS, Kao HC. High temperature deformation behaviour of Haynes 188 alloy subjected to high strain rate loading. Mat Sci Eng a-Struct 2014;594:292-301.

[233] Dehghan-Manshadi A, Dippenaar RJ. Development of alpha-phase morphologies during low temperature isothermal heat treatment of a Ti-5Al-5Mo-5V-3Cr alloy. Mat Sci Eng a-Struct 2011;528:1833-9.

[234] Rittel D, Wang ZG. Thermo-mechanical aspects of adiabatic shear failure of AM50 and Ti6Al4V alloys. Mech Mater 2008;40:629-35.

[235] Jones N, Dashwood R, Dye D, Jackson M. The flow behavior and microstructural evolution of Ti-5Al-5Mo-5V-3Cr during subtransus isothermal forging. Metallurgical and Materials Transactions A 2009;40:1944-54.

[236] Jones N, Dashwood R, Jackson M, Dye D. Development of chevron-shaped α precipitates in Ti–5Al–5Mo–5V–3Cr. Scripta Mater 2009;60:571-3.

[237] Furuhara T, Maki T. Variant selection in heterogeneous nucleation on defects in diffusional phase transformation and precipitation. Materials Science and Engineering: A 2001;312:145-54.

[238] Ohyama H, Nakamori H, Ashida Y, Maki T. Effects of Cold Deformation on the Morphology of. ALPHA. Precipitates in. BETA. Titanium Alloys. Isij Int 1992;32:222-31.

[239] Jones NG, Dashwood RJ, Dye D, Jackson M. The Flow Behavior and Microstructural Evolution of Ti-5Al-5Mo-5V-3Cr during Subtransus Isothermal Forging. Metall Mater Trans A 2009;40A:1944-54.

[240] Kim C, Batra R. Effect of initial temperature on the initiation and growth of shear bands in a plain carbon steel. International journal of non-linear mechanics 1992;27:279-91.

[241] Ghomi HM, Odeshi AG. The effects of microstructure, strain rates and geometry on dynamic impact response of a carbon-manganese steel. Mat Sci Eng a-Struct 2012;532:308-15.

[242] Kad BK, Gebert JM, Perez-Prado MT, Kassner ME, Meyers MK. Ultrafine-grain-sized zirconium by dynamic deformation. Acta Mater 2006;54:4111-27.

[243] Perez-Prado MT, Hines JA, Vecchio KS. Microstructural evolution in adiabatic shear bands in Ta and Ta-W alloys. Acta Mater 2001;49:2905-17.

[244] Boakye-Yiadom S, Khan AK, Bassim N. A systematic study of grain refinement during impact of 4340 steel. Mat Sci Eng a-Struct 2014;605:270-85.

[245] Li DH, Yang Y, Xu T, Zheng HG, Zhu QS, Zhang QM. Observation of the microstructure in the adiabatic shear band of 7075 aluminum alloy. Mat Sci Eng a-Struct 2010;527:3529-35.

[246] Meyers M, Nesterenko V, LaSalvia J, Xu Y, Xue Q. Observation and modeling of dynamic recrystallization in high-strain, high-strain rate deformation of metals. Le Journal de Physique IV 2000;10:Pr9-51-Pr9-6.

[247] Yang DK, An Y, Cizek P, Hodgson P. Development of adiabatic shear band in cold-rolled titanium. Mat Sci Eng a-Struct 2011;528:3990-7.

[248] Wang G. The Effect of Temperature on the Microstructure of a Metastable β Ti Alloy. Materials science forum 2010;654-656:847-50.

[249] Xu Y, Zhang J, Bai Y, Meyers MA. Shear localization in dynamic deformation: microstructural evolution. Metallurgical and Materials Transactions A 2008;39:811-43.

[250] Yang DK, Cizek P, Hodgson PD, Wen CE. Microstructure evolution and nanograin formation during shear localization in cold-rolled titanium. Acta Mater 2010;58:4536-48.

[251] Xue Q, Cerreta EK, Gray GT. Microstructural characteristics of post-shear localization in cold-rolled 316L stainless steel. Acta Mater 2007;55:691-704.

[252] Li YS, Tao NR, Lu K. Microstructural evolution and nanostructure formation in copper during dynamic plastic deformation at cryogenic temperatures. Acta Mater 2008;56:230-41.

[253] Huang LJ, Geng L, Li AB, Cui XP, Li HZ, Wang GS. Characteristics of hot compression behavior of Ti–6.5Al–3.5Mo–1.5Zr–0.3Si alloy with an equiaxed microstructure. Materials Science and Engineering: A 2009;505:136-43.

[254] Xue Q, Shen L, Bai Y. A modified split Hopkinson torsional bar in studying shear localization. Measurement Science and Technology 1995;6:1557.

[255] Xue Q, Gray GT. Development of adiabatic shear bands in annealed 316L stainless steel: Part I. Correlation between evolving microstructure and mechanical behavior. Metall Mater Trans A 2006;37A:2435-46.

[256] Tao NR, Wang ZB, Tong WP, Sui ML, Lu J, Lu K. An investigation of surface nanocrystallization mechanism in Fe induced by surface mechanical attrition treatment. Acta Mater 2002;50:4603-16.

[257] Xue Q, Gray GT. Development of adiabatic shear bands in annealed 316L stainless steel: Part II. TEM studies of the evolution of microstructure during deformation localization. Metall Mater Trans A 2006;37A:2447-58.

[258] Sun F, Nowak S, Gloriant T, Laheurte P, Eberhardt A, Prima F. Influence of a short thermal treatment on the superelastic properties of a titanium-based alloy. Scripta Mater 2010;63:1053-6.

[259] Hao YL, Li SJ, Prima F, Yang R. Controlling reversible martensitic transformation in titanium alloys with high strength and low elastic modulus. Scripta Mater 2012;67:487-90.

[260] Al-Zain Y, Kim HY, Koyano T, Hosoda H, Nam TH, Miyazaki S. Anomalous temperature

dependence of the superelastic behavior of Ti-Nb-Mo alloys. Acta Mater 2011;59:1464-73.

[261] Min XH, Tsuzaki K, Emura S, Tsuchiya K. Enhancement of uniform elongation in high strength Ti–Mo based alloys by combination of deformation modes. Materials Science and Engineering: A 2011;528:4569-78.

[262] Paladugu M, Kent D, Wang G, Yu ZT, Dargusch MS. Strengthening of cast Ti-25Nb-3Mo-3Zr-2Sn alloy through precipitation of alpha in two discrete crystallographic orientations. Mat Sci Eng a-Struct 2010;527:6601-6.

[263] Follansbee PS, Frantz C. WAVE-PROPAGATION IN THE SPLIT HOPKINSON PRESSURE BAR. J Eng Mater-T Asme 1983;105:61-6.

[264] Min X, Chen X, Emura S, Tsuchiya K. Mechanism of twinning-induced plasticity in β-type Ti–15Mo alloy. Scripta Mater 2013;69:393-6.

[265] Laheurte P, Eberhardt A, Philippe MJ. Influence of the microstructure on the pseudoelasticity of a metastable beta titanium alloy. Materials Science and Engineering: A 2005;396:223-30.

[266] Hao Y, Yang R, Niinomi M, Kuroda D, Zhou Y, Fukunaga K, et al. Young's modulus and mechanical properties of Ti-29Nb-13Ta-4.6 Zr in relation to α ″martensite. Metallurgical and Materials Transactions A 2002;33:3137-44.

[267] Brown DW, Beyerlein IJ, Sisneros TA, Clausen B, Tomé CN. Role of twinning and slip during compressive deformation of beryllium as a function of strain rate. Int J Plasticity 2012;29:120-35.

[268] Li C, Chen JH, Wu X, van der Zwaag S. Effect of strain rate on stress-induced martensitic formation and the compressive properties of Ti–V–(Cr,Fe)–Al alloys. Materials Science and Engineering: A 2013;573:111-8.

[269] Paradkar A, Kamat SV. The effect of strain rate on trigger stress for stress-induced martensitic transformation and yield strength in Ti–18Al–8Nb alloy. Journal of Alloys and Compounds 2010;496:178-82.

[270] Das A, Tarafder S, Chakraborti PC. Estimation of deformation induced martensite in austenitic stainless steels. Materials Science and Engineering: A 2011;529:9-20.

[271] Talonen J, Nenonen P, Pape G, Hanninen H. Effect of strain rate on the strain-induced gamma ->alpha '-martensite transformation and mechanical properties of austenitic stainless steels. Metall Mater Trans A 2005;36A:421-32.

[272] Miyazaki S, Kim HY, Hosoda H. Development and characterization of Ni-free Ti-base shape memory and superelastic alloys. Materials Science and Engineering A 2006;438-440:18-24.

[273] Hao YL, Li SJ, Sun SY, Zheng CY, Yang R. Elastic deformation behaviour of Ti–24Nb–4Zr–7.9Sn for biomedical applications. Acta Biomater 2007;3:277-86.

[274] Yu S, Yu Z, Wang G, Han J, Ma X, Dargusch MS. Biocompatibility and osteoconduction of active porous calcium–phosphate films on a novel Ti–3Zr–2Sn–3Mo–25Nb biomedical alloy. Colloids and Surfaces B: Biointerfaces 2011;85:103-15.

[275] Zhan H, Zeng W, Wang G, Kent D, Dargusch M. On the deformation mechanisms and strain rate sensitivity of a metastable β Ti–Nb alloy. Scripta Mater 2015.

[276] Zhang Y, Kent D, Wang G, St John D, Dargusch M. Evolution of the microstructure and mechanical properties during fabrication of mini-tubes from a biomedical β-titanium alloy. J Mech Behav Biomed 2015;42:207-18.

[277] Tian YX, Wang G, Yu S, Yu ZT. Microstructure characteristics and strain rate sensitivity of a biomedical Ti–25Nb–3Zr–3Mo–2Sn titanium alloy during thermomechanical processing. J Mater Sci 2015;50:5165-73.

[278] Bai XF, Zhao YQ, Zeng WD, Jia ZQ, Zhang YS. Characterization of hot deformation behavior of a biomedical titanium alloy TLM. Materials Science and Engineering: A 2014;598:236-43.

[279] Xu W, Kim KB, Das J, Calin M, Eckert J. Phase stability and its effect on the deformation behavior of Ti–Nb–Ta–In/Cr β alloys. Scripta Mater 2006;54:1943-8.

[280] Nag S, Banerjee R, Srinivasan R, Hwang J, Harper M, Fraser H. ω-Assisted nucleation and growth of α precipitates in the Ti–5Al–5Mo–5V–3Cr–0.5 Fe β titanium alloy. Acta Mater 2009;57:2136-47.

[281] Yang Y, Wu SQ, Li GP, Li YL, Lu YF, Yang K, et al. Evolution of deformation mechanisms of Ti–22.4Nb–0.73Ta–2Zr–1.34O alloy during straining. Acta Mater 2010;58:2778-87.

[282] Lai MJ, Tasan CC, Zhang J, Grabowski B, Huang LF, Raabe D. Origin of shear induced β to ω transition in Ti–Nb-based alloys. Acta Mater 2015;92:55-63.

[283] Talling RJ, Dashwood RJ, Jackson M, Dye D. On the mechanism of superelasticity in Gum metal. Acta Mater 2009;57:1188-98.

[284] Hörnqvist M, Mortazavi N, Halvarsson M, Ruggiero A, Iannitti G, Bonora N. Deformation and texture evolution of OFHC copper during dynamic tensile extrusion. Acta Mater 2015;89:163-80.

[285] Naaman H, Talreja R, Jensen DJ, Hansen N. Development of deformation textures in polycrystalline copper experiments and model predictions. Texture, Stress, and Microstructure 1987;7:149-70.

[286] Li P, Duan YP, Xue KM, Wang XX, Gan GQ. Microstructures and textures of TB8 titanium alloy after hot deformation. Zhongguo Youse Jinshu Xuebao/Chinese Journal of Nonferrous Metals 2010;20:872-7.

[287] Fan JK, Kou HC, Lai MJ, Tang B, Chang H, Li JS. Hot deformation mechanism and microstructure evolution of a new near β titanium alloy. Materials Science and Engineering: A 2013;584:121-32.

[288] Shen YF, Wang YD, Liu XP, Sun X, Lin Peng R, Zhang SY, et al. Deformation mechanisms of a 20Mn TWIP steel investigated by in situ neutron diffraction and TEM. Acta Mater 2013;61:6093-106.

[289] Dini G, Ueji R, Najafizadeh A, Monir-Vaghefi SM. Flow stress analysis of TWIP steel via the XRD measurement of dislocation density. Materials Science and Engineering: A 2010;527:2759-63.

[290] Ning YQ, Xie BC, Liang HQ, Li H, Yang XM, Guo HZ. Dynamic softening behavior of TC18 titanium alloy during hot deformation. Mater Design 2015;71:68-77.

[291] Karre R, Niranjan MK, Dey SR. First principles theoretical investigations of low Young's modulus beta Ti–Nb and Ti–Nb–Zr alloys compositions for biomedical applications. Materials Science and Engineering: C 2015;50:52-8.

[292] Tane M, Akita S, Nakano T, Hagihara K, Umakoshi Y, Niinomi M, et al. Peculiar elastic behavior of Ti–Nb–Ta–Zr single crystals. Acta Mater 2008;56:2856-63.

[293] Jeong K, Jin J-E, Jung Y-S, Kang S, Lee Y-K. The effects of Si on the mechanical twinning and strain hardening of Fe–18Mn–0.6C twinning-induced plasticity steel. Acta Mater 2013;61:3399-410.

[294] Eckert J, Das J, Xu W, Theissmann R. Nanoscale mechanism and intrinsic structure related deformation of Ti-alloys. Materials Science and Engineering: A 2008;493:71-8.

[295] Liang ZY, Wang X, Huang W, Huang MX. Strain rate sensitivity and evolution of dislocations and twins in a twinning-induced plasticity steel. Acta Mater 2015;88:170-9.

[296] Hutchinson B, Ridley N. On dislocation accumulation and work hardening in Hadfield steel. Scripta Mater 2006;55:299-302.

[297] Shterner V, Molotnikov A, Timokhina I, Estrin Y, Beladi H. A constitutive model of the deformation behaviour of twinning induced plasticity (TWIP) steel at different temperatures. Materials Science and Engineering: A 2014;613:224-31.

[298] Qiao Y, Wang X, Liu Z, Wang E. Effects of grain size, texture and twinning on mechanical properties and work-hardening behaviors of pure Mg. Materials Science and Engineering: A 2013;578:240-6.

[299] Koike J, Kobayashi T, Mukai T, Watanabe H, Suzuki M, Maruyama K, et al. The activity of non-basal slip systems and dynamic recovery at room temperature in fine-grained AZ31B magnesium alloys. Acta Mater 2003;51:2055-65.

[300] Wang XL, Li L, Xing H, Ou P, Sun J. Role of oxygen in stress-induced ω phase transformation and {3 3 2}〈1 1 3〉 mechanical twinning in βTi–20V alloy. Scripta Mater 2015;96:37-40.

[301] Min XH, Tsuzaki K, Emura S, Sawaguchi T, Ii S, Tsuchiya K. {332}〈113〉 Twinning system selection in a β-type Ti–15Mo–5Zr polycrystalline alloy. Materials Science and Engineering: A 2013;579:164-9.

[302] Min XH, Tsuzaki K, Emura S, Tsuchiya K. Heterogeneous twin formation and its effect on tensile properties in Ti–Mo based β titanium alloys. Materials Science and Engineering: A 2012;554:53-60.

[303] Boyer RR, Briggs RD. The use of β titanium alloys in the aerospace industry. J of Materi Eng and Perform 2005;14:681-5.

[304] Sun S, Brandt M, Dargusch MS. Thermally enhanced machining of hard-to-machine materials--A review. International Journal of Machine Tools and Manufacture 2010;50:663-80.

[305] Sun S, Harris J, Brandt M. Parametric Investigation of Laser-Assisted Machining of Commercially Pure Titanium. Advanced Engineering Materials 2008;10:565-72.

[306] Dandekar CR, Shin YC, Barnes J. Machinability improvement of titanium alloy (Ti-6Al-4V) via LAM and hybrid machining. International Journal of Machine Tools and Manufacture 2010;50:174-82.

[307] Rahman Rashid RA, Sun S, Wang G, Dargusch MS. The effect of laser power on the machinability of the Ti-6Cr-5Mo-5V-4Al beta titanium alloy during laser assisted machining. International Journal of Machine Tools and Manufacture 2012;63:41-3.

[308] Rahman Rashid RA, Sun S, Wang G, Dargusch MS. An investigation of cutting forces and cutting temperatures during laser-assisted machining of the Ti–6Cr–5Mo–5V–4Al beta titanium alloy. International Journal of Machine Tools and Manufacture 2012;63:58-69.

[309] Mitrofanov AV, Babitsky VI, Silberschmidt VV. Finite element simulations of ultrasonically assisted turning. Computational Materials Science 2003;28:645-53.

[310] Monaghan J, MacGinley T. Modelling the orthogonal machining process using coated carbide cutting tools. Computational Materials Science 1999;16:275-84.

[311] Bil H, Kılıç SE, Tekkaya AE. A comparison of orthogonal cutting data from experiments with three different finite element models. International Journal of Machine Tools and Manufacture 2004;44:933-44.

[312] List G, Sutter G, Bouthiche A. Cutting temperature prediction in high speed machining by numerical modelling of chip formation and its dependence with crater wear. International Journal of Machine Tools and Manufacture 2012;54–55:1-9.

[313] Sima M, Özel T. Modified material constitutive models for serrated chip formation simulations and experimental validation in machining of titanium alloy Ti–6Al–4V. International Journal of Machine Tools and Manufacture 2010;50:943-60.

[314] Limido J, Espinosa C, Salaün M, Lacome JL. SPH method applied to high speed cutting modelling. International Journal of Mechanical Sciences 2007;49:898-908.

[315] Calamaz M, Limido J, Nouari M, Espinosa C, Coupard D, Salaün M, et al. Toward a better understanding of tool wear effect through a comparison between experiments and SPH numerical modelling of machining hard materials. International Journal of Refractory Metals and Hard Materials 2009;27:595-604.

[316] Abolfazl Zahedi S, Demiral M, Roy A, Silberschmidt VV. FE/SPH modelling of orthogonal micro-machining of f.c.c. single crystal. Computational Materials Science 2013;78:104-9.

[317] Singh R, Alberts MJ, Melkote SN. Characterization and prediction of the heat-affected zone in a laser-assisted mechanical micromachining process. International Journal of Machine Tools and Manufacture 2008;48:994-1004.

[318] Yang J, Sun S, Brandt M, Yan W. Experimental investigation and 3D finite element prediction of the heat affected zone during laser assisted machining of Ti6Al4V alloy. Journal of Materials Processing Technology 2010;210:2215-22.

[319] Shen X. Numerical modeling and experimental investigation of laser-assisted machining of silicon nitride ceramics. Manhattan, Kansas: Kansas state university; 2010.

[320] Li R, Shih AJ. Finite element modeling of 3D turning of titanium. International journal of advanced manufacturing technology 2006;29:253-61.

[321] Guo YB, Liu CR. 3D FEA Modeling of Hard Turning. Journal of Manufacturing Science and Engineering 2002;124:189-99.

[322] Tugrul Ö. Computational modelling of 3D turning: Influence of edge micro-geometry on forces, stresses, friction and tool wear in PcBN tooling. Journal of Materials Processing Technology 2009;209:5167-77.

[323] Xi Y, Bermingham M, Wang G, Dargusch M. SPH/FE modeling of cutting force and chip formation during thermally assisted machining of Ti6Al4V alloy. Computational Materials Science 2014;84:188-97.

[324] Johnson GR, Cook WH. A constitutive model and data for metals. 7th International Symposium on Ballistics1983. p. 541-7.

[325] Xi Y, Bermingham M, Wang G, Dargusch M. Finite Element Modeling of Cutting Force and Chip Formation During Thermally Assisted Machining of Ti6Al4V Alloy. Journal of Manufacturing Science and Engineering 2013;135:061014-.

[326] Huang Y, Liang SY. Cutting forces modeling considering the effect of tool thermal property--application to CBN hard turning. International Journal of Machine Tools and Manufacture 2003;43:307-15.

[327] Ahmed N, Mitrofanov AV, Babitsky VI, Silberschmidt VV. 3D finite element analysis of ultrasonically assisted turning. Computational Materials Science 2007;39:149-54.

[328] Zhan H, Kent D, Wang G, Dargusch M. Semi-empirical constitutive modelling of dynamic stress-strain behaviour for a beta-titanium alloy at high strain rates over a wide range of temperatures 2014.

[329] Trent EM, Wright PK. Metal Cutting. 4th ed. Woburn: Butterworth-Heinemann; 2000.

[330] ASM handbook, volume 16: machining. 9th ed. Materials Park, OH: ASM International; 1995.